University of Cyprus

DEPARTMENT OF CHEMISTRY

Spectroscopic studies of molecular conformations of conjugated polymers for OPV applications

Doctor of philosophy dissertation

EIRINI LARIOU

December 2019

University of Cyprus
Department of Chemistry

Spectroscopic studies of molecular conformations of conjugated polymers for OPV applications

EIRINI LARIOU

Dissertation submitted for fulfilment of the requirements for a Doctoral Degree at the University of Cyprus

December 2019

VALIDATION PAGE

Doctoral Candidate: Eirini Lariou

Doctoral Thesis Title: Spectroscopic studies of molecular conformations of conjugated polymers for OPV applications

*The present Doctoral Dissertation was submitted in partial fulfillment of the requirements for the degree of Doctor of Philosophy at the **Department of Chemistry** and was approved on the 17/12/2019 by the members of the **Examination Committee**.*

Examination Committee

- **Sophia C. Hayes**
  Associate Professor, Department of Chemistry, University of Cyprus (Research supervisor)

- **Epameinondas Leontidis**
  Professor, Department of Chemistry, University of Cyprus

- **Anastasios Keramidas**
  Professor, Department of Chemistry, University of Cyprus

- **Grigorios Itskos**
  Associate Professor, Department of Physics, University of Cyprus

- **Gitti Frey**
  Professor, Department of Materials Science and Engineering, Technion Israel Institute of Technology

DECLARATION OF AUTHORSHIP

The present doctoral dissertation was submitted in partial fulfillment of the requirements for the degree of Doctor of Philosophy of the University of Cyprus. It is a product of original work of my own, conducted at the Molecular Spectroscopy Laboratory under the supervision of Associate Prof. Sophia C. Hayes.

Exceptions:

- *Absorption and PL experiments on P3HT derivatives were performed by Dr. Matthew Dyson at the Department of Materials, Imperial College London.*
- *Experiments performed on OPV devices and discussed in chapter 6. The work of others is clearly quoted.*
- *Temperature dependent Absorption experiments on PCE11 were performed by Konstantin Schötz at the Department of Physics, University of Bayreuth.*
- *DFT calculations on PCE11 where performed at the Department of Chemistry, University of Mons by Rishat Dilmurat.*

DATE: 17/12/2019

SIGNATURE:

Acknowledgments

The present doctoral dissertation was carried out at the department of Chemistry of the University of Cyprus, during the time period of January 2016 – December 2019. I gratefully acknowledge the funding from the European Union's Horizon 2020 research and innovation program **'INFORM'** under the Marie Sklodowska-Curie grant agreement No 675867.

I would like to express my deepest appreciation to all those amazing individuals that made the Ph.D journey so special and truly memorable.

First and foremost, I am thankful to my advisor Associate **Prof. Sophia C. Hayes** for being constantly supportive and helpful to confront all the obstacles that unavoidably arose during this process. Thank you Sophia for trusting me, giving me so many valuable opportunities, keeping me constantly motivated and standing as a mentor. Your genuine enthusiasm for science, your patience to obtain reliable results as well as your great attention to detail inspired me to develop those skills as well.

My appreciation extends to the rest of my thesis committee: **Prof. Epameinondas Leontidis** for his participation to all of my scientific exams and for his constructive comments at every stage of my research**. Prof. Anastasios Keramidas** and Assosiate **Prof. Grigorios Itskos** for kindly accepting the invitation to take part in my examination committee**. Prof. Gitti Frey**, for the nice discussions that we had within the INFORM meetings and for honouring me by coming to Cyprus for my Ph.D defence. I thank you all for taking the time to read my dissertation, providing valuable comments and scientific counselling.

Special thanks go to all people that were (directly or indirectly) involved in the 'INFORM' project and especially those with whom I collaborated more closely:

- **Dr. Basel Shamieh** from Technion Israel Institute of technology, for providing samples to us and for the excellent collaboration that we had under the supervision of Prof. Gitti Frey.
- **Dr. Matthew Dyson** and **Dr. Giovani Maria Matrone** from Imperial College London for the fruitful collaboration under the supervision of Prof. Natalie Stingelin, for providing samples to us and for welcoming me to their lab.
- **Konstantin Schötz** from the University of Bayreuth for the kind hospitality in Bayreuth and for performing temperature dependent absorption measurements under the supervision of Prof. Anna Köhler.

Additionally, I wish to thank Assistant **Prof. Keivanidis** from Cyprus University of Technology for the fruitful collaboration that we had as well as **Rishat Dilmurat** from the University of Mons for running DFT calculations under the supervision of Prof David Beljonne.

I take the opportunity to thank also the personnel of the Department of Chemistry that happily helped me out when needed, Niki and Elena for dealing with bureaucratic issues as well as Georgia, Savvas and Panikos for their technical support.

A warm word of thanks for my lab mates: Elisa Alloa and Eliana Nikolaidou, as well as the girls that we shared the office: Marina, Sotiroula and Mikela, for being a major source of support and encouragement and for making the working environment so pleasant with their presence.

Last but not least, I owe sincere thanks to my ever-present and beloved friends for their invaluable moral support during this process. As for my family, there are no proper words to describe my gratitude for their unconditional love and support. Making them proud is the greatest reward possible for my efforts.

Nicosia, December 2019

"...και πολλά μέλλει να μάθεις

αν το Ασήμαντο εμβαθύνεις"

Odysseas Elytis

ABSTRACT

Organic electronics is a scientific field that emerged as an attractive alternative to silicon-based technology because organic materials can significantly reduce fabrication cost, energy consumption and enable additional functionalities such as flexibility of the devices. Moreover, their optolelectronic properties can be easily altered to meet specific end applications. In this study emphasis is given on organic semiconductors targeting organic photovoltaic (OPV) applications, where a key -yet poorly understood- factor in optimising device performance is molecular conformation of the polymeric chains within the film. Thus it is essential to establish a concrete connection between structure and properties in order to access the full potential of OPVs as a sustainable and cost-effective renewable energy source.

Starting from a fundamental level, this work systematically investigates the impact of specific processing parameters on molecular conformation of the organic semiconductors, explores in which ways we can achieve controlled manipulation of this local ordering and discusses the potential correlation to macroscopic properties. P3HT is employed as a reference material and is compared with two of its more polar derivatives P3HT-b-PEO and P3BEOT to elucidate the impact of chemical substitution with side chains on backbone planarity. Resonance Raman (RR) spectroscopy was chosen as a sensitive probe of chain ordering and revealed that polarity difference between the semiconductor backbone and its side chains can substantially disrupt backbone planarity. However, blending those samples with insulating commodity plastics such as PEO proved a reliable approach to minimise this effect and sustain backbone order as the compatibility between certain moieties of the blend components is polarity dependent. To complete this study, the exposure to polar environments such as water vapour was investigated and showed to facilitate backbone realignment towards specific chain arrangements.

To develop this fundamental study of organic semiconductors a step further towards its application in OPVs it's important to explore the conformation of polymers combined with acceptor materials that constitute the active layer of such devices. By focusing on P3HT:PCBM blends the effect of two different types of structural polymorphs of P3HT, densely packed and non-densely packed, is investigated. Resonance Raman experimental data reveals that the energetic disorder in the P3HT:PCBM is higher in the absence of the

densely-packed P3HT polymorph and the potential impact of this on the performance of the OPV device is discussed considering data from transient absorption (TA) and time-delayed collection field (TDCF) measurements. Semi-complete OPV devices are also employed, to explore the interface between silver electrode and P3HT:PCBM blends from a structural point of view. The buried organic/metal interface is experimentally accessible through Surface Enhanced Resonance Raman Spectroscopy (SERRS) and reveals a clear distortion of planarity of the polymeric chains at the interface with silver. However, this can be prevented by the presence of specific additives in the P3HT:PCBM blend. The two additives chosen, HEG-DT and BDMT, due to their thiol end groups are attracted to silver forming an interlayer between the polymer blend and the electrode.

Finally, as research in OPVs is becoming oriented towards the development of non-fullerene acceptors, compatible materials for this new generation of OPV devices are studied in order to sustain and exceed the efficiencies achieved with fullerenes. An interesting candidate material is the donor-acceptor type polymer PCE11 that together with its compatibility with non-fullerene acceptors its properties are highly sensitive to processing conditions. Resonance Raman spectroscopy provided valuable insights on the effect of molecular weight and processing conditions on the molecular conformation of PCE11. Among the samples studied, high molecular weight films showed consistently increased chain planarity –verified by DFT calculations- compared to low molecular weight ones and were investigated further. Temperature dependent Resonance Raman Spectroscopy (RRS) was employed to develop a basic understanding on the polymer conformation. The data obtained were combined with temperature dependent absorption measurements through Resonance Raman Intensity Analysis (RRIA) to provide access to a quantitative picture of the excited state geometry, distinguish the relative contribution from each vibrational mode to these geometry changes and extract values for the mode specific reorganisation energy.

ΠΕΡΙΛΗΨΗ

Τα οργανικά ηλεκτρονικά είναι ένας επιστημονικός κλάδος που προέκυψε ως μια ελκυστική εναλλακτική πρόταση στην τεχνολογία πυριτίου λόγω του σημαντικά μειωμένου κόστους παραγωγής καθώς και κάποιων επιπλέον δυνατοτήτων που προσφέρουν οι συσκευές αυτές όπως η ευκαμψία και το μειωμένο βάρος. Επιπλέον, οι οπτοηλεκτρονικές ιδιότητες των οργανικών ημιαγωγών -σε αντίθεση με τους ανόργανους- μπορούν εύκολα να τροποποιηθούν ανάλογα με τις ανάγκες της εκάστοτε εφαρμογής. Η παρούσα μελέτη θα εστιαστεί στους οργανικούς ημιαγωγούς που προορίζονται για οργανικές φωτοβολταϊκές εφαρμογές, όπου παράγοντας κλειδί στη βελτιστοποίηση της απόδοσης των συσκευών – ελάχιστα κατανοητός ωστόσο- είναι η μοριακή διαμόρφωση των πολυμερικών αλυσίδων μέσα στα υμένια. Συνεπώς, είναι απαραίτητη η εγκαθίδρυση μιας ξεκάθαρης σύνδεσης δομής και ιδιοτήτων προκειμένου να αξιοποιήσουμε στο μέγιστο τη δυναμική των οργανικών φωτοβολταϊκών, ως μια αειφόρο και αποδοτική ανανεώσιμη πηγή ενέργειας.

Ξεκινώντας από ένα θεμελιώδες επίπεδο, η παρούσα εργασία διερευνά συστηματικά το αντίκτυπο παραμέτρων που σχετίζονται με την επεξεργασία, στην μοριακή διαμόρφωση των οργανικών ημιαγωγών, αναζητάει τρόπους με τους οποίους μπορούμε να ελέγξουμε τη διαμόρφωση αυτή σε τοπικό επίπεδο και σχολιάζει την πιθανή συσχέτισή τους με τις μακροσκοπικές ιδιότητες. Η πολυθειοφίνη ή P3HT, χρησιμοποιείται σαν υλικό αναφοράς και συγκρίνεται με δυο από τα πλέον πολικά παράγωγά της το P3HT-b-PEO και το P3BEOT, προκειμένου να διευκρινιστεί η επίδραση της χημικής υποκατάστασης με πλευρικές αλυσίδες στην διαμόρφωση της κύριας αλυσίδας. Η φασματοσκοπία Raman συντονισμού επιλέχθηκε ως ένας ευαίσθητος δομικός δείκτης και αποκάλυψε ότι η διαφορά πολικότητας μεταξύ κύριας και πλευρικών αλυσίδων μπορεί να διαταράξει σημαντικά την επιπεδότητα της κύριας. Ωστόσο, η ανάμειξη των δειγμάτων αυτών με μονωτικά πλαστικά όπως το PEO αποδείχθηκε μια αξιόπιστη προσέγγιση στο να ελαχιστοποιηθεί αυτή η επίδραση και να διατηρηθεί η επιπεδότητα της κύριας αλυσίδας, καθώς φάνηκε ότι η συμβατότητα συγκεκριμένων συστατικών του μείγματος εξαρτάται από την πολικότητά τους. Ολοκληρώνοντας αυτή τη μελέτη, εξετάστηκε η έκθεση των δειγμάτων σε πολικό περιβάλλον, όπως οι υδρατμοί και αυτό φάνηκε να διευκολύνει την ανακατάταξη της αλυσίδας προς συγκεκριμένες διαμορφώσεις.

Εξελίσσοντας την θεμελιώδη μελέτη των οργανικών ημιαγωγών ώστε να προσεγγίσει την τελική τους εφαρμογή στα οργανικά φωτοβολταϊκά, είναι σημαντικό να διερευνηθεί η διαμόρφωση των πολυμερών –που δρουν ως δότες ηλεκτρονίων- σε συνδυασμό με δέκτες

φουλερενίων, τη δομή δηλαδή του συνόλου του φωτοενεργού στρώματος των συσκευών αυτών. Εστιάζοντας λοιπόν σε μείγματα P3HT:PCBM, εξερευνούμε την επίδραση δυο διαφορετικών τύπων δομικών πολύμορφων του P3HT: των πυκνά και αραιά στοιβαγμένων. Τα φασματοσκοπικά δεδομένα δείχνουν ότι η ενεργειακή διαταραχή στα μείγματα P3HT:PCBM είναι μεγαλύτερη απουσία των πυκνά στοιβαγμένων πολύμορφων και η πιθανή επίπτωση αυτού στην απόδοση των οργανικών φωτοβολταϊκών συσκευών σχολιάζεται λαμβάνοντας υπόψιν δεδομένα από μετρήσεις χρονοεξαρτημένης απορρόφησης (TA) και μετρήσεις πεδίου συλλογής χρονικής υστέρησης (TDCF). Ημι-ολοκληρωμένες οργανικές φωτοβολταϊκές συσκευές χρησιμοποιούνται τέλος, για τη διερεύνηση της δομής στη διεπαφή ενός μεταλλικού ηλεκτροδίου (αργύρου) και μειγμάτων P3HT:PCBM. Η «θαμμένη» διεπαφή οργανικού στρώματος και μετάλλου είναι πειραματικά προσβάσιμη μέσω της φασματοσκοπίας Raman επιφανειακής ενίσχυσης και αποκαλύπτει μια ξεκάθαρη διατάραξη της διαμόρφωσης των πολυμερικών αλυσίδων στην διεπαφή με τον άργυρο. Ωστόσο, το φαινόμενο αυτό μπορεί να αποτραπεί με την παρουσία συγκεκριμένων προσμείξεων στο μείγμα P3HT:PCBM. Τα μικρά μόρια που επιλέχθηκαν είναι το HEG-DT και το BDMT, λόγο των τερματικών ομάδων θειόλης οι οποίες έλκονται από τον άργυρο σχηματίζοντας ένα ενδιάμεσο στρώμα μεταξύ πολυμερούς και ηλεκτροδίου.

Τέλος, καθώς η έρευνα στα οργανικά φωτοβολταϊκά προσανατολίζεται προς τη σχεδίαση συσκευών με μη-φουλερενικούς δέκτες, μελετώνται συμβατά υλικά με αυτή τη νέα γενιά συσκευών προκειμένου να διατηρήσουν ή και να ξεπεράσουν τα ρεκόρ απόδοσης που προσφέρει η επιλογή των φουλερενίων. Μια υποσχόμενη επιλογή προς αυτή την κατεύθυνση είναι το υλικό δότη-δέκτη PCE11 που εκτός από τη συμβατότητα του με μη-φουλερενικούς δέκτες, οι ιδιότητες του παρουσιάζουν μεγάλη ευαισθησία στις συνθήκες επεξεργασίας. Η φασματοσκοπία Raman συντονισμού προσέφερε χρήσιμα στοιχεία σχετικά με την επίδραση του μοριακού βάρους και των συνθηκών επεξεργασίας στην μοριακή του διαμόρφωση. Μεταξύ των δειγμάτων που μελετήθηκαν, εκείνα με το μεγαλύτερο μοριακό βάρος παρουσίασαν συστηματικά βελτιωμένη μικρομοριακή δομή –όπως επιβεβαιώθηκε από θεωρητικούς υπολογισμούς DFT- και διερευνήθηκαν περαιτέρω με φασματοσκοπία συντονισμού Raman θερμοκρασιακής εξάρτησης. Τα δεδομένα αυτής της μεθόδου, συνδυάστηκαν με δεδομένα θερμοεξαρτόμενης απορρόφησης μέσω ενός θεωρητικού εργαλείου που ονομάζεται ανάλυση εντάσεων Raman συντονισμού (RRIA). Αυτό μας έδωσε πρόσβαση σε μια ποσοτική εικόνα της γεωμετρίας στη διεγερμένη κατάσταση και μας επέτρεψε να διακρίνομε τη σχετική συνεισφορά κάθε τρόπου δόνησης στις γεωμετρικές αλλαγές που παρατηρήθηκαν και να εξάγουμε με ακρίβεια τιμές για την ενέργεια αναδιοργάνωσης.

Table of contents

Index of Figures

CHAPTER 2 Organic semiconductors and their role in an OPV

CHAPTER 3 Introduction to Raman spectroscopy

CHAPTER 4 Experimental and computational methods

CHAPTER 5 Controlling local ordering *via* polarity contrast

CHAPTER 6 Photoactive layer morphology and organic metal interface

CHAPTER 7 Spectroscopic and computational study of the donor-acceptor polymer PCE11

Index of Tables

CHAPTER 2 Organic semiconductors and their role in an OPV

CHAPTER 5 Controlling local ordering *via* polarity contrast

CHAPTER 6 Photoactive layer morphology and organic metal interface

CHAPTER 7 Spectroscopic and computational study of the donor-acceptor polymer PCE11

Index of abbreviations and symbols

A	Acceptor
Ag	Silver
Al	Aluminum
BHJ	Bulk heterojunction
BT	2,1,3-Benzodiathiazole
CE	Chemical enhancement
CT	Charge transfer state
D	Donor
D-A	Donor-acceptor
2D-PTs	Two-dimensional conjugated polythiophenes
DFT	Density Functional Theory
DPP	Pyrrolo[3,4-c]pyrrole-1,4-dione
Eg	Energy gap
E_F	Fermi level
EM	Electromagnetic enhancement
FET	Field effect transistor
FF	Fill factor
g	Multiplicity
HH	Head-to-head (coupling)
HOMO	Highest Occupied Molecular Orbital
HT	Head-to-tail (coupling)
Jsc	Short circuit voltage
J_0	Excitonic coupling
ITO	Indium tin oxide
ICMA	Indene-fullerene monoadduct
ICBA	Indene-fullerene bisadduct
MEH-PPV	Poly[2-methoxy-5-(2- ethylhexyl-oxy)-1,4-phenylene-vinylene]
LSPR	Localized surface plasmon resonance (LSPR)
LUMO	Lowest Unoccupied Molecular Orbital
NPs	Nanoparticles
REP	Raman excitation profile
RR	Resonance Raman
RRIA	Resonance Raman Intensity Analysis
OLEDs	Organic light-emitting diodes
OFETs	Organic field effect transistors
OPVs	Organic photovoltaics
OSC	Organic solar cell
P_{max}	Maximum electrical power
PCBM	Fullerene [6,6]-Phenyl-C61-butyric acid methyl ester
PCE	Power conservation efficiency
P_{in}	Incident power
P3AT	Poly(3-alkylthiophene)s
P3HT	Poly-(3-hexylthiophene)

$PC_{60}BM$	[6,6]-phenyl-C61-butyric acid methyl ester
PV	Photovoltaic
s	Spin
SPR	Surface plasmon resonance
SERS	Surface-Enhanced Raman scattering (SERS)
SPR	Surface plasmon resonance (SPR)
SPPs	Surface plasmon polaritons (SPPs)
TT	Tail-to-tail (coupling)
Tg	Glass transition temperature
UPS	Ultra-violet photoelectron spectroscopy
UV-vis	Ultraviolet Visible
V_{oc}	Open circuit voltage
XPS	X-ray photoemission
α	Polarizability
Γ	Homogeneous broadening
Δ	Displacement of the excited state potential well from the equilibrium position
ε	Extinction coefficient
Θ	Inhomogeneous broadening
λ	Wavelength
ν_0	Incident frequency of light
ν_1	BT bending mode
ν_2	BT N-S-N vibration
ν_3	BT C=C stretch
ν_4	Thiophene's C=C stretch
ν_5	BT C=C stretch
ρ	Depolarization ratio
σ_R	Raman cross section
ω_e	Excited-state harmonic frequency
ω_g	Ground-state harmonic frequency
1D	One dimensional
2D	Two dimensional
3D	Three dimensional

CHAPTER 1

Introduction

As global population is rising, so does the energy need for electricity and transportation. Since the 20th century, primary source of energy have been fossil fuels, which although are continually being formed via natural processes, they are being depleted much faster than new ones are being made, thus are not sustainable. Additionally, the burning process of fossil fuels emit gases -mainly CO_2- contributing to global warming and raising serious environmental concerns. It is becoming a broad consensus among scientists and politicians that renewable energy is the only way to effectively address this continuous expansion of the global energy demand. To date, in some countries such as Norway and Iceland an important energy sector, electricity generation relies nearly 100% on renewable energy[1] and hopefully many countries will follow their example in the near future. Among the natural resources such as wind, waves, geothermal heat etc., sunlight is an abundant and inexhaustible fuel source and photovoltaic devices (PVs) are a feasible example of sustainable energy technology which operates by directly converting sunlight to electrical power.

The creation of current in materials upon light exposure –the so called photovoltaic effect- was first reported by Becquerel in 1839.[2] Since then, 3 generations of solar cell (SC) technologies have been developed: 1) SCs based on crystalline Si, 2) SCs based on thin film technology and 3) SCs based on organic and hybrid semiconductors.[3] Organic photovoltaics (OPVs) are part of the technological field of organic electronics that broadly attracts the attention of academic and industrial research. The increasing interest is stimulated by the potential of a more cost and energy effective alternative to inorganic materials. Organic electronics rely on the use of semiconducting organic molecules, which can be synthesised from cheap precursors, offering the potential to tune their optoelectronic properties through alteration of their chemical structure, enabling large scale compatibility by solution-processed manufacturing methods such as ink-jet and roll-to-roll printing.[4] Especially for OPV applications, organic compounds enable high optical absorption coefficient in the visible range of the spectrum such that the light-absorbing layer can be very thin, permitting the fabrication of transparent, lightweight and flexible devices. However, the state-of-the-art

polymer based solar cells suffer from poor long-term stability and despite the promising current reported record power conversion efficiency (PCE) (over 17% for tandem devices)[5] their commercialisation is hampered. Those problems can be addressed by careful design of the devices and synthesis of novel organic materials that can lead to new record PCE. Organic polymers or small molecules act as electron donating materials and together with the electron acceptors -usually fullerene derivatives- constitute the photoactive layer of OPV devices, where light absorption and charge extraction is taking place.

Understanding charge transport at a fundamental level is key to improving charge carrier mobility of OPV materials which is a critical objective of molecular design to optimise device performance. Molecular conformation strongly affects charge transport in organic semiconductors in a complex way and unravelling the structure-property relation of these materials remains a major challenge for scientific research. The overarching goal of this doctoral dissertation is to establish a fundamental understanding on how molecular conformation affects optoelectronic properties with the aim to tune them. Factors that determine molecular conformation, such as interactions between monomers on the polymeric chains or interactions with the surrounding environment, which can be tuned by means of processing, are investigated to evaluate their impact on the macroscopic properties. A deep understanding of the behaviour of organic semiconductors is not only important from a physical chemistry point of view but also from an industrial point of view because it can provide indications of what is actually limiting device efficiency.

The originality of this doctoral dissertation rests in the attempt to answer fundamental questions regarding the impact of synthesis and processing on molecular conformation of organic semiconductors with Raman spectroscopy as a main tool. For this purpose, the combination of two approaches –chemical modification and blending- is utilised to systematically study for the first time how polarity of side chains and the environment affect molecular order, aiming to provide a platform for future materials selection and processing criteria. Moreover, the effect of additives on the structure of organic/metal interfaces in OPV devices is systematically investigated to explore ways of more efficient charge transport between the electrodes and the organic layer. Last but not least, Resonance Raman Intensity Analysis is used to analyse computationally the experimental optical and structural response of a novel donor-acceptor polymer PCE11 to directly monitor its ground as well as the excited state structural evolution.

This doctoral dissertation consists of 8 chapters that discuss the importance of molecular conformation on macroscopic properties of organic semiconductors and is divided in a theoretical and an experimental part.

Chapter 2 provides a broad and comprehensive introduction to the field of organic semiconductors. The basics of organic semiconductors are reviewed based on the current knowledge regarding structure and properties. Then the operating principles of organic solar cells are described to understand and highlight the tight connection between molecular structure and device performance.

Chapter 3 focuses on the theory of Raman scattering and describes the two main spectroscopic techniques used throughout this work: a) Resonance Raman (RR) and b) Surface Enhanced Raman Spectroscopy (SERS). A brief description of the time-dependent formalism of Raman spectroscopy is also included and together with *Chapter 2*, constitute the theoretical background that the experimental part is based on.

Details on the studied materials and the experimental methods employed are provided in *Chapter 4*. Emphasis is given on the set up employed for the RR and SERS experiments as well as the experimental conditions and the theoretical basis for the Resonance Raman Intensity Analysis.

The initial study of P3HT and its polar and non-polar derivatives is discussed in *Chapter 5*. The scope of this chapter is to explore the effect of polarity contrast between backbone and its environment as a possible strategy to effectively manipulate molecular order.

The P3HT:PCBM microstructure of blends and the structure at an organic/metal interface are the subjects of *Chapter 6* which is oriented towards the investigation of the structural properties of a semi-complete OPV device with P3HT and PCBM constituting the active layer.

Supposing that in the future OPV devices will be mostly designed with non-fullerene acceptors, a fundamental study of PCE11 as a promising and suitable material for this kind of technology[6] is presented in *Chapter 7*, where its molecular weight, processing and temperature dependence are reported and discussed in detail.

Two independent chapters are dedicated to the conclusions of this doctoral dissertation (*Chapter 8*) and the future perspectives of the work performed (*Chapter 9*) suggesting potential future research on issues that are still open.

References

(1) Kroposki, B.; Johnson, B.; Zhang, Y.; Gevorgian, V.; Denholm, P.; Hodge, B. M.; Hannegan, B. Achieving a 100% Renewable Grid: Operating Electric Power Systems with Extremely High Levels of Variable Renewable Energy. *IEEE Power Energy Mag.* **2017**, *15* (2), 61–73. https://doi.org/10.1109/MPE.2016.2637122.

(2) E.A., B. Mémoire Sur Les Effets Électriques Produits Sous L'influence Des Rayons Solaires. *Comptes Rendus l'Academie des Sci.* **1839**, *9*, 561–567.

(3) Yan, J.; Saunders, B. R. Third-Generation Solar Cells: A Review and Comparison of Polymer:fullerene, Hybrid Polymer and Perovskite Solar Cells. *RSC Adv.* **2014**, *4* (82), 43286–43314. https://doi.org/10.1039/c4ra07064j.

(4) Guo, X.; Baumgarten, M.; Müllen, K. Designing π-Conjugated Polymers for Organic Electronics. *Prog. Polym. Sci.* **2013**, *38* (12), 1832–1908. https://doi.org/10.1016/j.progpolymsci.2013.09.005.

(5) Meng, L.; Zhang, Y.; Wan, X.; Li, C.; Zhang, X.; Wang, Y.; Ke, X.; Xiao, Z.; Ding, L.; Xia, R.; et al. Organic and Solution-Processed Tandem Solar Cells with 17.3% Efficiency. *Science (80-.).* **2018**, *361* (6407), 1094–1098. https://doi.org/10.1126/science.aat2612.

(6) Cha, H.; Wu, J.; Wadsworth, A.; Nagitta, J.; Limbu, S.; Pont, S.; Li, Z.; Searle, J.; Wyatt, M. F.; Baran, D.; et al. An Efficient, "Burn In" Free Organic Solar Cell Employing a Nonfullerene Electron Acceptor. *Adv. Mater.* **2017**, *29* (33), 1–8. https://doi.org/10.1002/adma.201701156.

CHAPTER 2

Background: Organic semiconductors and their role in an OPV

The scientific field of organic electronics has emerged after the discovery that electrochemical doping can dramatically increase the electrical conductivity of conjugated systems back in 1977. The ground-breaking work performed by Heeger, Mac Diarmid and Shiraka was rewarded with the Nobel Prize in Chemistry in 2000.[1] The state of the art research in organic electronics aims to complement rather than replace inorganic-based devices (such as the field effect transistors (FET), light emitting diodes (LED) and photovoltaics (PVs)) by significantly reducing fabrication cost and enabling functionalities such as optical transparency and mechanical flexibility[2]. This study, by focusing on the structure-processing and structure-property relation of organic semiconductors has a rather general character that potentially can be of interest for the design of any technological device. However, emphasis will be given to organic photovoltaic (OPV) applications, not only because the studied materials show promise for this field, but also because a significant part of the experiments were carried out to monitor photophysical processes that are directly relevant to the operating principles of OPV devices. This chapter provides sufficient background for the understanding of the experimental part by introducing organic semiconductors and discussing their role in OPV devices. A broad outline of an OPV device's operating principles, photo-physics and selected materials is provided in order to emphasise the critical role of the microstructure of the organic layer in the device performance.

2.1 Organic semiconductors

Organic semiconductors are solid materials, essentially hydrocarbons, consisting sometimes of heteroatoms such as oxygen, sulphur and nitrogen. Organic materials are generally known as insulators, but with special treatment such as doping, their electrical conductivity can be increased and they can absorb or emit light.[3] Organic semiconductors are a family of materials classified into 3 categories:

- Amorphous molecular films: Amorphous materials that are formed by depositing small organic molecules through evaporation or spin-coating to substrates of interest.

- Molecular crystals: These crystals have highly ordered crystal lattices and show high charge carrier motilities, making them ideal candidate material, for organic field effect transistor (OFETs) applications.

- Polymer films: Polymer films are made from organic macromolecules that consist of covalent bonded chains of repeated monomers and attract increasing technological interest due to the wide range of potential applications and the simple and low-cost fabrication methods.

Throughout this study we will focus on the last category, namely π-conjugated polymers, as semiconducting character is determined from the energy levels of the prevailing π-electrons.

2.1.1 Conjugated polymers

Organic macromolecules can become semiconductors if molecules have conjugated bonds- at least one alternating double and single bond- that results in delocalization of the electron gas around them. The conductivity of a material can be classified according to its band gap, which defines the energy level between the π orbital or Highest Occupied Molecular Orbital (HOMO) and π* orbital or Lowest Unoccupied Molecular Orbital (LUMO). This energy level structure is analogous to the conduction and valence band respectively in the inorganic semiconductors. The higher band gap a material possesses, the less conductive it is. For example, metals have no energy gap between HOMO and LUMO while insulators have relatively high band gap. A semiconducting polymer can be excited either optically, or by electrical field, or by chemical doping only when the excitation energy is equal or higher than the energy between HOMO and LUMO.

2.1.2 Band structure

Let's now focus on the simplest example of a conjugated polymer, polyacetylene, which consists only of a 1D single chain of alternating single- and double- bonds (**Fig. 2.1**) in order to understand its semiconducting character.

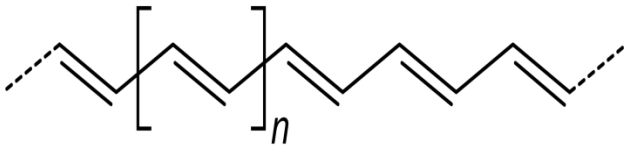

Figure 2.1: *Chemical structure of trans-polyacetylene*

Carbon atoms with sp^2 hybridised orbitals, form σ-bonds and π-bonds, the latter of which are derived from the overlap of the non-hybridised p_z-orbitals. Thus, every carbon atom in the polyacetylene chain has a delocalized π electron perpendicular to the backbone of the polymer chain. The electrons of the π – bonds, which are located in the HOMO, can be transferred to a π* excited state in the LUMO, if a photon with certain energy interacts with a polyacetylene molecule (**Fig. 2.2**).

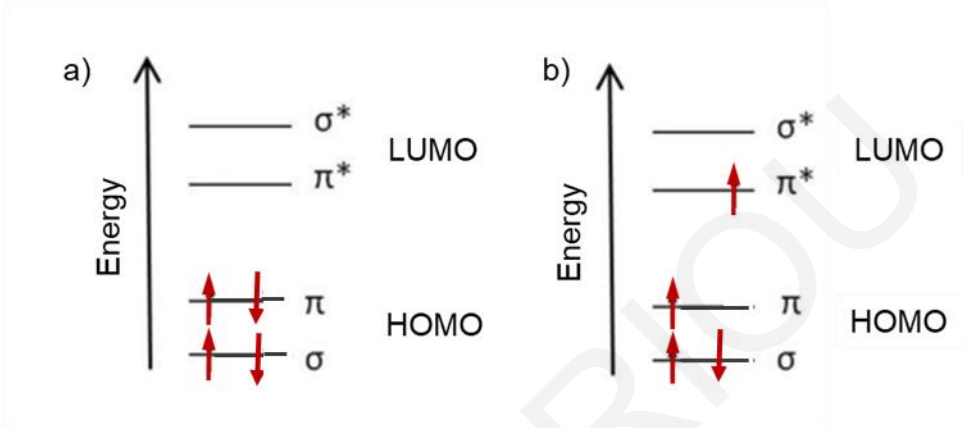

Figure 2.2: *A molecular orbital diagram of an alkene depicting: a) the ground state. b) the excited state, where an electron is excited from the π orbital to the π* orbital.*

For a conjugated polymer the delocalization of double bonds varies, which means that there will be periodic bond alternation and variation in charge density within the polymer chain, known as the Peierls effect. Peierls theory predicts that a spontaneous perturbation of the electron density results in symmetry distortion, meaning that the length of the alternating bonds is no longer equivalent (single bond longer than the double).[18] The practical result is the formation of an energy gap (E_g) at the Fermi level (E_F)[1] since the energy of the occupied states becomes lower in order to restore the perturbation, causing a separation of the π-bonding orbitals from the (unoccupied) anti-bonding π* orbitals. The interaction of the p_z orbitals with each other along the chain leads to further splitting of the energy levels (**Fig. 2.3**), reducing the HOMO-LUMO distance. An electron within this system behaves as a particle in a box,[4] where the larger the box size (degree of conjugation), the less energy is required for electron movement along the chain.

From the above it's clear that the size of the energy gap (E_g) depends on the length of the conjugation of the polymer and it is inversely proportional to it. The necessary energy for the alternation of the bonds in polyacetylene (E_g) is ~1.5 eV. Typically, the E_g range for

[1] Fermi level is a pseudo-energy state that corresponds to the HOMO of the valence band at 0 K.

conjugated molecules is between 1.5 and 3 eV which falls within the visible part of the spectrum, making them particularly attractive for absorption/emission applications.

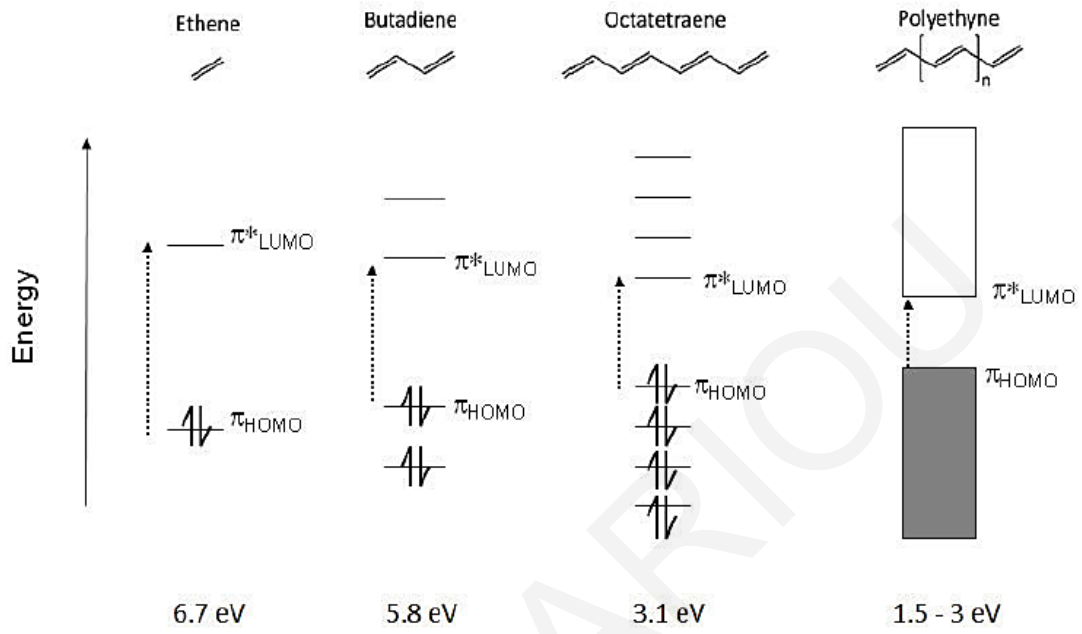

Figure 2.3: *Charge delocalization via conjugation in semi-conductive polymers showing that the greater number of conjugated atoms leads to increasingly band-like π-π* orbitals.* [5]

2.1.3 Doping

The presence of a high degree of conjugation in polymers does not necessarily imply electrical conductivity, as the thermal excitation of the electrons to the empty orbital becomes impossible for energy gap above 2 eV. Similarly to inorganic semiconductors, their conductivity can be increased with doping i.e. inserting charge carriers. This can be achieved in a controlled fashion by means of oxidation/reduction reactions. Doping can be either p-type, which is referred to the creation of positive charges by electron-accepting dopants such as halogens, or n-type, which is achieved by increasing the number of negative charges through electron-donating species such as alkali metals. Conductivity can be increased up to 11 orders of magnitude, allowing the fast three dimensional (3D) charge transport (along each polymer chain and between different chains).[6]

2.2 Excited states

2.2.1 Confined states in π- conjugated systems

For a relatively low doping level, the generated carriers interact electrostatically with each other and with the lattice (phonons[2]) resulting excitations summarized below: [7–10]

Solitons: These are excitations that can be visualized as "interruptions" (lattice distortions) in the conjugated backbone caused by the chemical reaction and they can be electrically neutral, positively or negatively charged depending on the type of doping. They are often called non-dispersive waves as they are able to move at a constant speed along the medium. The conductivity increment is caused by the formation of a new state in the middle of the energy gap that facilitates electrons to cross the gap.[7,11]

Polarons: A pair of coupled solitons, usually a neutral (free radical) and a positive (other types exist though they are less stable). Their role is analogous to solitons as they each generate two new energy states within the forbidden band –positioned symmetrically with respect to the Fermi level- again resulting in increased polymer conductivity. However, the fact that polarons are accompanied with lattice distortion increases their kinetic energy compared to single electrons moving at the same speed, causing the low charge carrier mobilities observed in organic semiconductors.

Bipolarons: Two neighboring polarons can combine to form bipolarons of lower energy. The attractive force that can overcome Coulomb repulsion is the strong lattice deformation. In the case of trans-polyaketylene though, bipolarons are not stable resulting in positive or negative pairs of solitons.

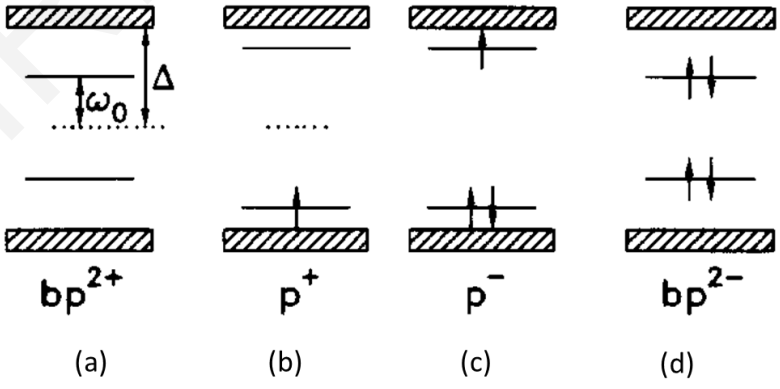

Figure 2.4: *Schematic representation of the intermediate generated energy levels to the 2Δ band gap generated by: hole (a) and electron bipolaron (d), and hole (b) and electron polaron (c)*[12]

[2] Phonon is an energy quantum referring to a collective oscillation of atoms within a crystal at a single frequency.

At this point, it's worth making a distinction between trans-polyacetylene and aromatic polymers such as polythiophene and poly(phenylene-vinylene). Trans-polyacetylene is a degenerate polymer meaning that in its ground state two isoenergetic resonance structures exist, while in aromatic polymers, two energetically inequivalent ground state configurations co-exist: a low energy benzenoid segment and a high energy quinoid segment (see **Figure 2.5**). The quinoid configuration in the latter case, is adopted after the interaction with the doping agents. The distinction lies in the fact that the energy gap is not defined exclusively by the Peierls effect (as assumed for the trans-polyacetylene) but also from intermolecular and electron-electron interactions. This results in different behavior of solitons, where in the case of degenerate polymers charge transport is allowed only along each chain, while in non-degenerate polymers the formation of more localized soliton pairs (polarons, bi-polarons) enables 3D charge transport.

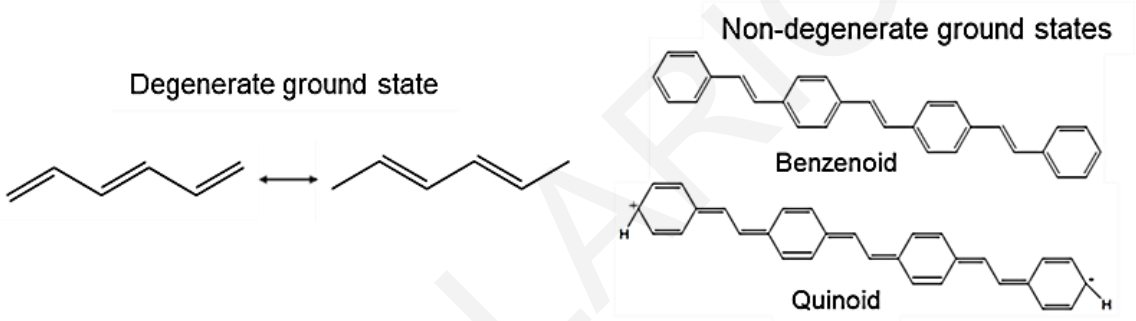

Figure 2.5*: Two isoenergetic fragments of the ground state configuration of trans-polyacetylene (left) and two energetically inequivalent ground state configurations of phenylene-vinylene polymer (PPV).* [18]

2.2.2 Excitons

Polymer excitation, regardless if it is achieved by doping, electrically (through charge injection) or optically (through interaction with light), causes electrons to move from HOMO to LUMO leaving behind positively charged holes. The formation of negatively and positively charged polarons in the lattice which consequently relaxes in a lower energy state, results in Coulomb attraction between pairs of opposite charges that bind together into a quasi-particle called exciton.[13–16] The magnitude of the Coulomb interaction V is given by the expression:

$$V \sim \frac{e^2}{4\pi\varepsilon_r\varepsilon_0 R} \qquad (2.1)$$

Where e is the electron charge, ε_r is the dielectric contact of the medium, ε_0 is the free space permittivity and R is the distance between the electron and the hole (exciton radius). The

Coulomb potential increases the energy of the HOMO and decreases the energy of the LUMO, reducing the bandgap at the excited state which is now referred to as optical bandgap.[17] This change is what mainly defines the exciton binding energy (E_B), which is the energy difference between the initial (fundamental) energy gap (Eg) and the optical bandgap.

2.2.3 Types of excitons

Excitons are categorised according to the magnitude of E_B, which reflects how easily the bound charges can escape from each other. The different types are briefly described below:[18]

Wannier-Mott Excitons[19]

This exciton type is characterised by a large exciton radius (~ 100 nm), encouraging delocalisation over several unit cells of the crystal lattice (3D wavefunction extension). It is a loosely-bound type of exciton common for inorganic materials with strong intermolecular interactions such as silicon, because the large charge carrier distance together with their large dielectric constant (silicon $\varepsilon_r = 12$) results in weak Coulomb attraction and E_B around 10 meV.

Frenkel Excitons[20]

Contrary to inorganic materials, organics have a smaller dielectric constant ($\varepsilon_r \sim 2\text{-}4$)[21] and a one dimensional localised nature of the electronic wavefunctions involved (~10 nm), resulting in tightly-bound excitons namely Frenkel excitons.[22] Typical E_B values for Frenkel excitons range between 100 meV and 1 eV,[23,24] which means that room temperature thermal energy (25 meV)[25] is not sufficient by itself to cause ionisation.

Charge Transfer Excitons

An intermediate exciton model between Wannier-Mott and Frenkel excitons exists and describes two charges that are localised between two separate neighbouring molecules.
All different types are depicted in **Fig. 2.6**.

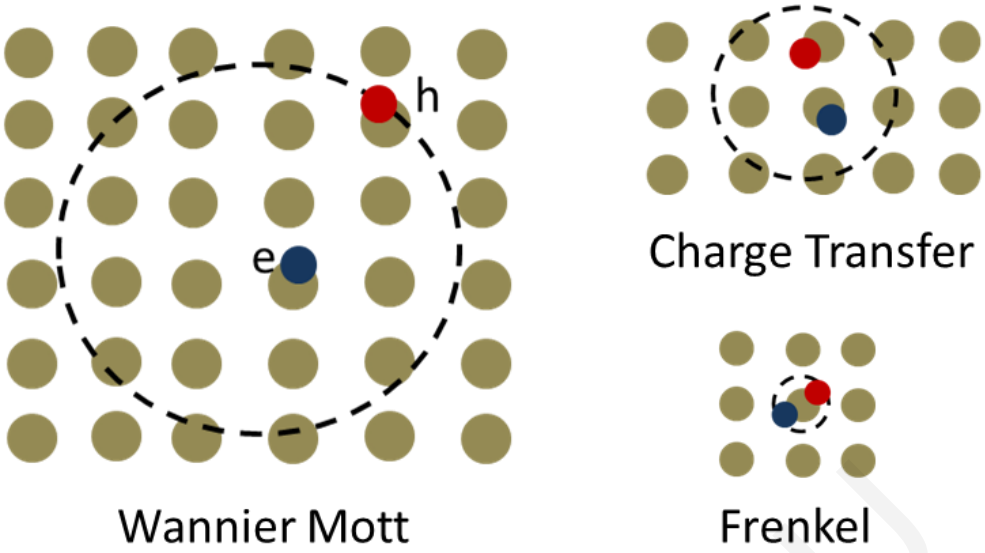

Figure 2.6: *Qualitative schematic representation of Wannier-Mott excitons that exhibit the largest radius, Charge Transfer excitons where electron is located at a neighbouring molecular site with respect to the hole and Frenkel excitons in which the electron-hole pairs have the smallest distance between each other.*

2.3 Introduction to photophysical processes

2.3.1 Singlet and triplet states

Before diving into the details of photophysical processes and optical transitions, it is necessary to introduce a categorisation of the energy levels according to their multiplicity g = 2s +1, where s is the spin of the electron which has two possible directions: up (s=1/2) and down (s= -1/2). Energy levels in which the two electrons have anti-parallel spin vectors leading to an overall spin s=0 and multiplicity of 1, are known as singlet states. Examples of singlet energy states are the ground state S_0 and excited states symbolised S_1, S_2 (see **Fig. 2.7**), …S_n. Respectively, electrons with parallel spin directions (s=1) and multiplicity of 3 are called triplet states. Triplet states are all excited states (symbolised with T_1, T_2,..T_n), however, they have lower energies than singlet states. The higher energy of the singlet states is explained by quantum mechanics together with the Pauli exclusion principle which allows a larger wave-function overlap of electrons with anti-parallel spin in two different orbitals. Thus, singlet electrons are closer together and this increases the Coulomb repulsive energy.[26]

2.3.2 Jablonski diagram

Light interacts with matter through scattering (which is the focus on the next chapter) and absorption. Light is absorbed by molecules in the form of photons[3] and if this energy is equal or greater than the Eg, electrons from the HOMO level are promoted to a higher electronic energy level where various photophysical processes can follow. Those photophysical processes involve electronic transitions through different energy levels and can be visualised employing a Jablonski diagram (See **Fig 2.7**). An overview of the key components and transitions is provided bellow. [24]

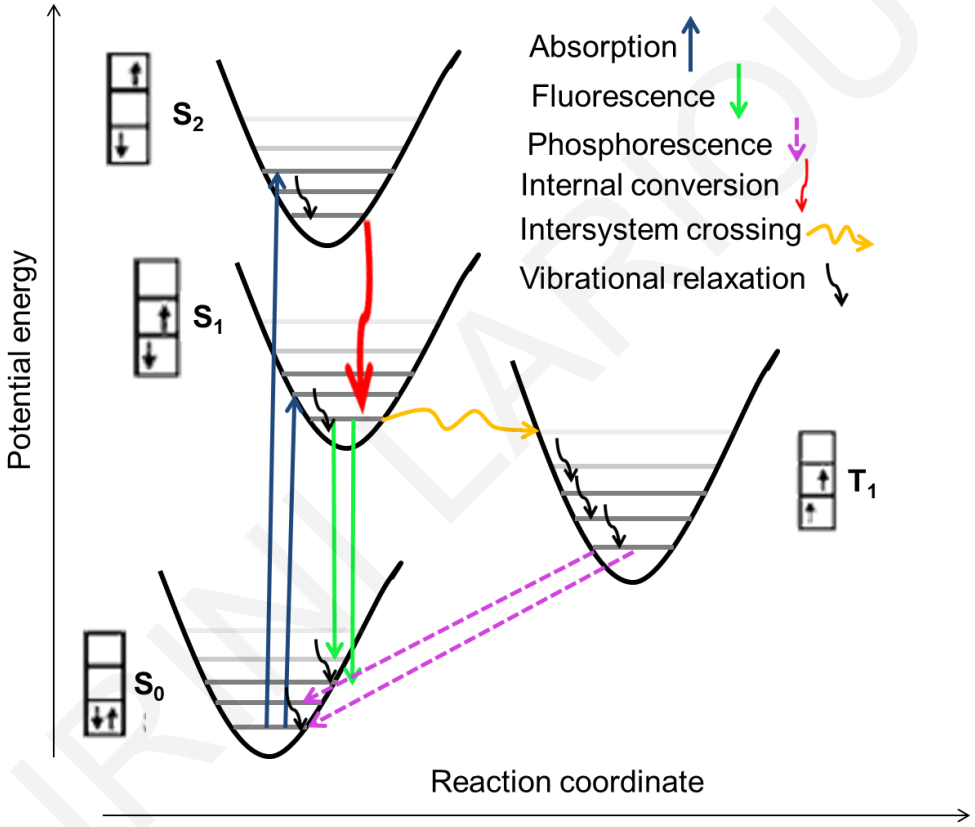

Figure 2.7: *Simplified Jablonski diagram depicting possible optical transitions of an organic molecule as described in the text. Singlet and triplet electronic states are shown as parabolas and vibrational levels are depicted as straight lines. Straight arrows symbolise radiative processes (involving photons) and wavy arrows symbolise non-radiative. (Inspired and redrawn)*[27]

The first photophysical process depicted in a Jablonski diagram is the **absorption** of photons and depending on their energy, electrons are excited from the lowest vibrational level (ν_0) of the ground state S_0 to a vibrational level (ν_n) of a singlet excited state (S_1, S_2,.. S_n) based on Boltzmann distribution. The excited species through phonon interactions (lattice vibrations) quickly relax to LUMO through vibrational relaxation or internal conversion, giving rise to

[3] Energy quanta with E=hν, where h is the Plank's constant and ν is the frequency of light.

the formation of excitons. **Vibrational relaxation** is a transition to a lower energy vibrational level of the same electronic state while **internal conversion** occurs between two different electronic states of the same spin multiplicity. They are both non-radiative processes, releasing the excess energy in the form of heat. Relaxation to S_0 vibrational levels can occur through photon emission from the lowest vibrational level of the S_1 according to Kasha's rule.[28] This process known as **fluorescence** is described by transitions to different vibrational levels of the S_0, giving rise to "multiple colour" photon emission. Competitive to fluorescence can be processes such as quenching or charge trapping.

An alternative, indirect path of the relaxing electrons is called **intersystem crossing** and reflects a non-radiative transition between two isoenergetic vibrational levels belonging to singlet and triplet electronic states. Intersystem crossing is considered a forbidden transition but is weakly allowed provided that there is strong spin-orbit coupling. Thus it can be observed for example in molecules with heavy atoms such as Iridium (Ir). If an electron reaches the first triplet excited state T_1, three possible paths can be followed. The first is to relax to the ground state S_0 through photon emission together with spin change known as **phosphorescence**. The second scenario is the photon absorption which will further excite the electron to a higher triplet state, and the third is to return to the S_1 singlet excited state through reverse intersystem crossing. In this case, the relaxation to the S_0 accompanied by the photon emission that follows this intermediate step is known as delayed fluorescence and is not included in the above Jablonski diagram (**Fig. 2.7**). Its name stands for the longer lifetimes of this process compared to fluorescence, although the emission occurs again from the lowest vibrational level of the S_1. The timescales of the described photophysical processes are shown in **Table 2.1**. [29]

Table 2.1: *Optical transition lifetimes*

Transition	Lifetime (s)
Absorption	10^{-15}
Fluorescence	10^{-10} –10^{-7}
Phosphorescence	10^{-6} – 10
Internal conversion	10^{-11} – 10^{-9}
Intersystem crossing	10^{-10} – 10^{-8}
Vibrational relaxation	10^{-12} – 10^{-10}

Due to the low dielectric constant of organic molecules, these allow interactions between electrons and their surroundings causing strong electronic and vibrational coupling. The energy levels and the corresponding transitions in this case are referred as vibronic.

2.3.3 Selection rules

Electronic transitions are the result of interaction between an electromagnetic field and an electric dipole. This can be expressed quantum mechanically as the transition dipole moment $\vec{M}_{f\leftarrow i}$:

$$\vec{M}_{f\leftarrow i} = \langle \Psi_f^T | \hat{M} | \Psi_i^T \rangle \qquad (2.2.)$$

$\vec{M}$ is the dipole moment operator for a transition of an electron from the initial eigenstate Ψ_i^T to the final eigenstate Ψ_f^T. T stands for the total wavefunction (electronic + vibrational energy) of a molecular electronic state. Every electronic transition between two energy states is characterised by a probability equal to the squared magnitude of the transition dipole moment:

$$\left|\vec{M}_{f\leftarrow i}\right|^2 \qquad (2.3)$$

Transitions with high probability of happening are known as allowed transitions while the ones that are less likely to occur are known as forbidden. Electronic and vibrational selection rules basically arise from the fundamental laws of energy and momentum conservation. The two rules that govern the electronic transitions are:

a) the conservation of spin ($\Delta s = 0$)

b) The orbital rule $\Delta l = 0, \pm 1$ (Laporte)

Forbidden transitions can take place under specific circumstances such as strong spin-orbit coupling (as the example of the intersystem crossing above), where the law of momentum conservation is applied for the overall momentum (spin + orbit).

With regards to vibrational transitions, they are dictated by the Franck-Condon principle, which determines the intensity of vibronic transitions.[18] According to this principle the nuclei are considered "fixed" during electronic transitions because electronic transitions are fast compared to the nuclei response, thus they can be considered vertical transitions on electronic potential energy curves. The probability of a transition to a given vibrational energy level is determined by the overlap integral of the vibrational wavefunctions that gives the overlap of the vibrational wave function in the ground and excited state (nuclear movement $\Delta q \sim 0$).

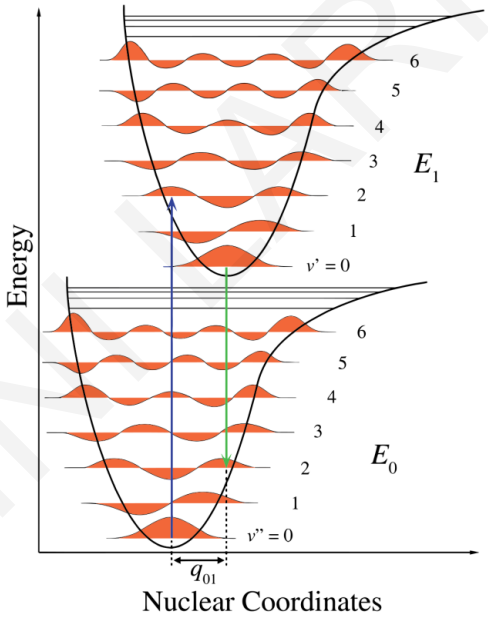

Figure 2.8: *Schematic representation of the Frank-Condon principle showing that upon absorption the vertical transition (same nuclear coordinates q_x) from the v0 vibrational level of the ground state to the v2 vibrational level of the first excited state is favourable. q_{01} is the change in the nuclear coordinates.*[30]

2.4 Introduction to OPV

2.4.1 OPV basic principles and architecture

After this short introduction to photophysical processes, it is useful to understand how an OPV functions. An organic solar cell (OSC) is a type of photovoltaic cell that uses organic conductive polymers or small organic molecules in order to absorb light and cause charge flow that produces electricity from sunlight. In the early 90´s, Yu et al.[31] and Halls et al.[32] suggested the so called ‘‘bulk heterojunction’’(BHJ) structure, which is the most popular OPV device architecture so far. It consists of the photoactive blend layer composed of a conjugated polymer, acting as electron donating material (donor) and an electron accepting material (acceptor), which can be a small molecule or a polymer, sandwiched between two electrodes. Usually the anode is a transparent material such as indium tin oxide (ITO) and the metal cathode is commonly aluminum (Al) (See **Fig 2.10**). The polymer donor (D) serves as light absorber and as the hole transporting phase, whereas the acceptor (A) is the carrier (electrons) transporter.[33] The role of the electrodes is primarily to collect the generated charges and secondly to generate an electric field from the difference in their work function, encouraging the charges to separate and reach their respective electrode. The architecture can become more complex, for example by inserting more interfacial layers, to provide an alignment of the energy levels between the electrodes and the active layer and facilitate charge collection or to enhance light absorption.

An OSC converts solar energy (photons) into electrical energy (charge flow) by the photovoltaic effect. The figure of merit of this process is the so called power conversion efficiency (PCE) which is given by the expression:

$$PCE = \frac{P_{max}}{P_{in}} = \frac{J_{SC} * V_{OC} * FF}{P_{in}} \qquad (2.4)$$

P_{max} is the maximum electrical power and P_{in} is the incident power of illumination. P_{max} is defined by J_{sc}, V_{oc} and FF which are important characteristics, marked in the photocurrent-voltage curve (J/V curve) depicted in **Figure 2.9** .

- J_{SC} is the short circuit current (current measured when the electrodes are connected without any resistor)

- V_{OC} is the open circuit voltage (voltage between the two electrodes when there is no current flow). Together with the J_{SC} represent the theoretical power of the cell.
- FF is the fill factor, defined as the ratio between the maximum power and the theoretical power (depicted from the dotted square). (See **Fig 2.9**)

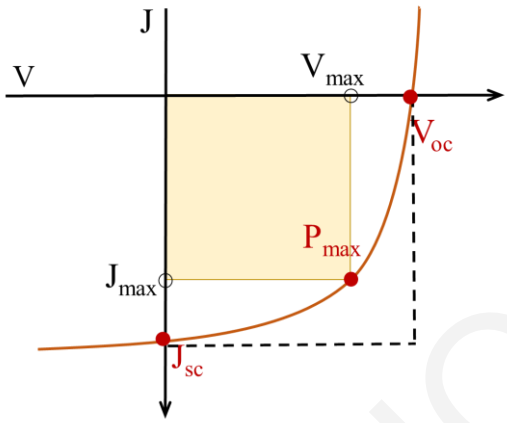

Figure 2.9: *J-V curve for a fictitious solar cell, depicting the key performance parameters analysed above: P_{max}, V_{oc} and J_{sc}. The FF is given by the area ratio: $\frac{J_{max}V_{max}}{J_{sc}J_{oc}}$.*

In order to maximise the PCE of a given OPV, attention should be given to each step of the cells operation (discussed in 2.4.2) to obtain the highest possible values of J_{SC}, V_{OC} and FF and minimise loses. OPVs performance optimization is a widely explored research field and 2018's reported record PCE for single junction cells is over 14%[34] while for small-area tandem OCSs is of 17.3%, which are both considered promising for future industrial applications.[35]

2.4.2 Steps towards photocurrent generation

Upon illumination of OSCs, several physical processes occur from light absorption to photocurrent generation, outlined and discussed below (see **Fig. 2.10**).

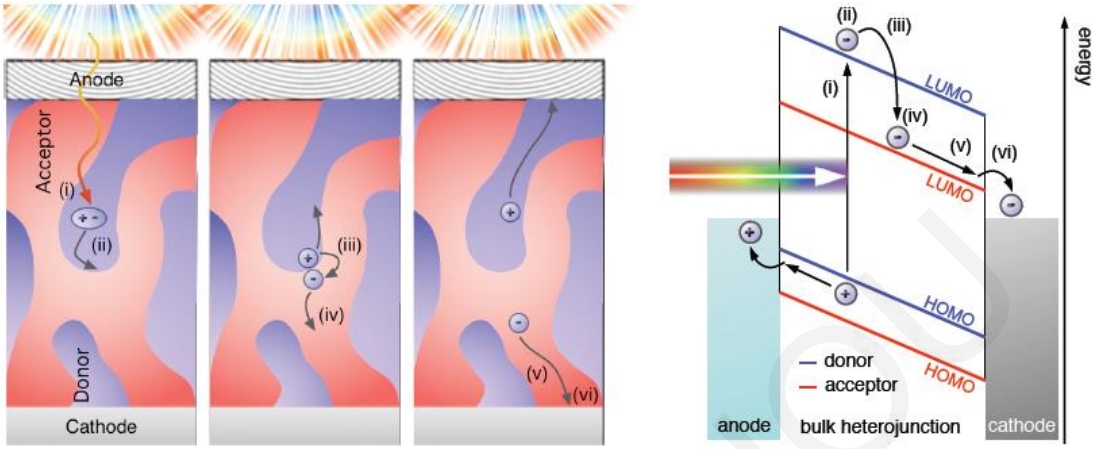

Figure 2.10: *The 6 steps towards photocurrent generation in an OSC: i) light absorption and exciton formation, ii) exciton diffusion towards the D-A interface, iii) exciton dissociation at the D-A interface, iv) CT state – polaron pair, v) charge transport towards the electrodes, vi) charge extraction. Left: Schematic representation of the steps through a BHJ OSC. Right: Photophysical steps from an energy diagram point of view.*[36]

The sequence of the photophysical processes taking place at an OSC begins with the **photon absorption** in the photoactive layer that excites electrons from the HOMO to the LUMO (provided that $E_{photon} > E_g$). The excitation in organic semiconductors **forms Frenkel excitons** (discussed in section 2.2.3) and then, **exciton diffusion** towards the D-A interface is for short distance (a few nm) and occurs via hopping between molecules (the analogous for the inorganic semiconductors is band transport). A critical yet challenging step in the operation of OSCs is the **dissociation of the strongly bound Frenkel excitons** into free charges. For organic semiconductors, room temperature thermal energy (See section 2.2.3) is not sufficient to overcome their high binding energy. The dissociation driving force is provided by the electronegativity of the A (ex. fullerenes) at the D-A interface. The energetically lower LUMO level of the A favors the electron transfer from the (energetically higher) LUMO of the D. It has been observed that electron transfer between donor and acceptor is a very quick process, estimated to take place on the fs timescale,[37,38] quicker than any other relaxation process. Although there is an active debate on the exact mechanism of charge separation,[39–42] there is evidence[41,43–45] that an additional step –after exciton dissociation at the D-A interface– needs to be overcome for the generation of free charges.

The reason is that there is still some attraction between the electron and hole (which is still larger than the thermal energy at room temperature, approximately 0.1-0.5 eV). This configuration which is no longer considered a usual exciton but rather a bound polaron pair that disrupts the surrounding environment is known as **charge transfer state (CT)**. An existing model that explains the final dissociation of polaron pairs as well as excitons is the Onsager-Braun model[4] which gives the probability of dissociation through the expression bellow:[3]

$$P(E) = \frac{k_d(E)}{k_d(E)+k_f} \quad (2.5)$$

where E is the electric field, $k_d(E)$ the diffusion rate of the free charges and k_f is the geminate recombination (see section below) rate.

Once charge separation is achieved, the electrons move through the A towards the cathode and the holes through the D towards the anode where the final step of **charge extraction** occurs and they leave the cell as electrical current.

2.4.3 Potential loss pathways

The above description refers to the ideal scenario that excitons will effectively diffuse at the D-A interface and dissociate into free charges that will generate the photocurrent. In reality, a small fraction of the excitons make it to the electrodes and the rest recombine sooner or later during this process. The excitons formed right after absorption, have a limited lifetime (ns timescale) that corresponds to a certain small distance over which the charge diffuses (diffusion length) before recombination occurs. If the excitons fail to reach the interface their energy is lost and this kind of loss mechanism is known as **geminate recombination** (0.3-0.6 ns) (see **Figure 2.11**).[46] The BHJ structure aims to address this problem by controlling the phase separation of the D-A, which has to be approximately equal to the exciton diffusion length (around 10 nm). Moreover, in this way the D-A interfacial area is increased, increasing the chances of charge dissociation. Once the excitons reach the D-A interface, they can undergo various possible transitions. They can recombine before dissociating (geminate recombination), **decay non-radiatively**, or the electrons can be transferred to the A. At this stage, they can still undergo geminate recombination by the return of the electrons to the D. If charges dissociate further, the BHJ structure comes at a cost as any free electron

[4] Onsager-Braun model is a modified version of the already existing Onsager model which allows a long enough lifetime of the electron-hole pair, to make several attempts towards dissociation.

moving through the A will be in close distance to the free holes that move through the D increasing the chance of recombination. The recombination in this case is called non-geminate or **bimolecular recombination**, it occurs at longer timescales (ns to ms) and it involves free charges that do not originate from the same exciton (**Fig 2.11**). Another obstacle towards charge extraction is **charge trapping** coming from either lattice defects or doping molecules. Trapping sites can act as quenching sites in both D and A materials, triggering non-radiative decay or recombination (both geminate and bimolecular). Moreover, traps limit the already **low mobility** of the charge carries (due to the slower nature of the transport via hopping), increasing the time spent within the active layer, resulting again in high recombination probability.[47]

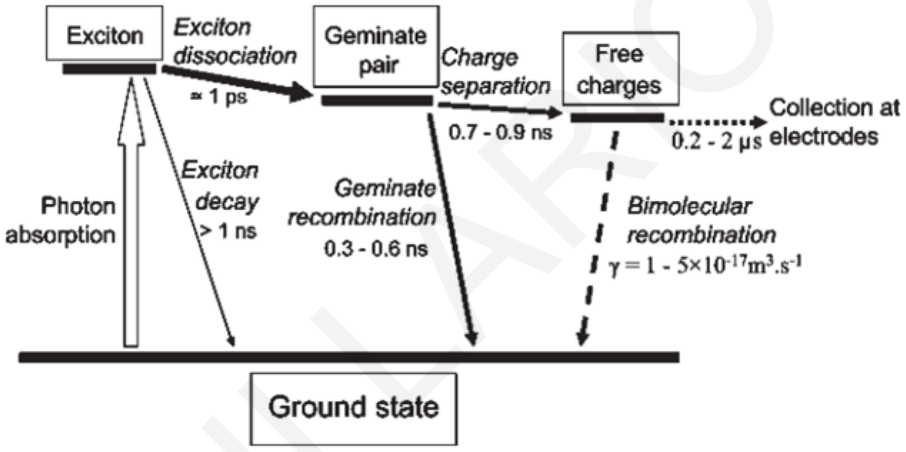

Figure 2.11: *Schematic representation of the various possible charge lifetimes from the creation to recombination/non-radiative decay.*[46]

From the above, it becomes clear that the control of morphology is a crucial factor to minimise system losses and obtain a good compromise between recombination and charge extraction.

2.5 Materials

Bellow the most common types of conjugated polymers used for OPVs are briefly discussed with respect to their performance. Desired properties such as strong and broad absorption, high charge carrier motilities and small band gap are tightly connected to the chemical structure.

2.5.1 Donors

The donor, is the light-absorbing material. This material is electron rich; it is desirable to have a low band gap. Moreover, it should absorb light strongly at a broad region of the solar light spectrum, have high hole mobility to facilitate hole transport and have well aligned energy levels with those of the acceptor material. In considering the electronic energy levels of donor-acceptor materials, the HOMO and LUMO of the donor material should be 0.2–0.3 eV higher than those of the acceptor material, and also the energy gap should be large enough to exceed the exciton binding energy.[48]

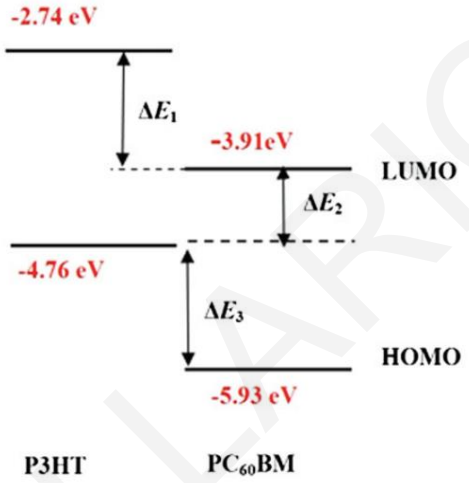

Figure 2.12: *Example of the electronic energy levels between the common donor material (P3HT) and acceptor $PC_{60}BM$.* [49]

Bellow several examples of frequently used donor materials are described.

2.5.1.1 Polythiophene and derivatives

Poly(3-alkylthiophene)s (P3AT) have been widely used as the active material for photovoltaic cells. P3ATs, are polymer donors that combine many desirable properties such as excellent thermal and chemical stability, good light-harvesting ability and high carrier mobility. The length of the alkyl group in P3ATs is important in determining the solubility, crystallinity and morphology with Poly-(3-hexylthiophene) (P3HT), giving the best device performance in the P3AT family. P3ATs can be synthesized easily through various methods. The repeating units of P3ATs are asymmetric, so three relative orientations are available when two thiophene rings are coupled between the 2- (also called head) and 5- (known as tail) positions. So, the first of these is head-to-tail (HT) coupling, the second is head-to-head (HH) coupling, and the third is tail-to-tail (TT) coupling (see **Figure 2.13**).

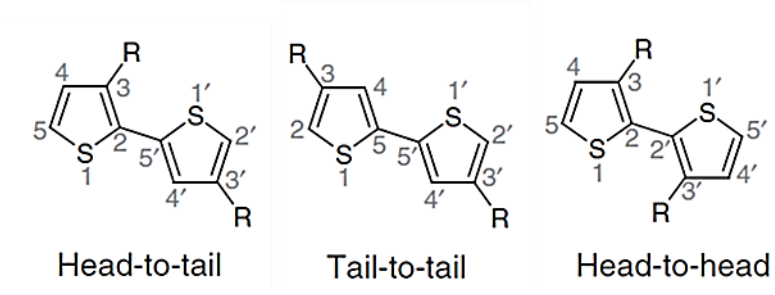

Figure 2.13: *The three possible relative orientations of the connecting thiophene rings. In grey is shown the numbering of the atoms.*[3]

A mixture of four chemically distinct triad regioisomers can be obtained when 3-substituted (or asymmetric) thiophene monomers are employed. The HT–HT structure of polythiophenes is denoted as regioregular, the other three structures are denoted as regiorandom, and the HT–HT isomer proportion in polymers is named as regioregularity. Regioregularity is an important factor in characterization of poly(3-substituted thiophene). Regioregular poly(3-substituted thiophene) is likely to access a low energy planar conformation, leading to highly conjugated polymers. An increase of the torsion angles between thiophene rings leads to higher band gaps, with consequent destruction of high conductivity and other desirable properties.[50] Currently, the influence of regioregularity on photovoltaic properties of other polymer systems has not been well studied, but this parameter would be critical to further improve molecular structures. Although P3HT exhibited promising photovoltaic properties, the absorption band (from 500 to 650 nm) of this polymer is still not broad enough to harvest sunlight well. Two-dimensional conjugated polythiophenes (2D-PTs) provided a feasible way to broaden the absorption band. A representative absorption band of 2D-PT consists of two parts. One part located in the short wavelength region stems from the conjugated side chain; and another located in the long wavelength region originates from the conjugated backbone chain.[49] By adjusting the conjugated length of the side chain, the absorption peak position at higher energies can be tuned. Another effective way to reduce the band gap of polythiophenes that has been reported is to replace the alkyl side groups of P3ATs by alkoxy groups.[51] Finally, a strategy to lower the band gap of rr-P3HT was the synthesis of regioregular poly(3-hexylselenophene) (rr-P3HS).[52]

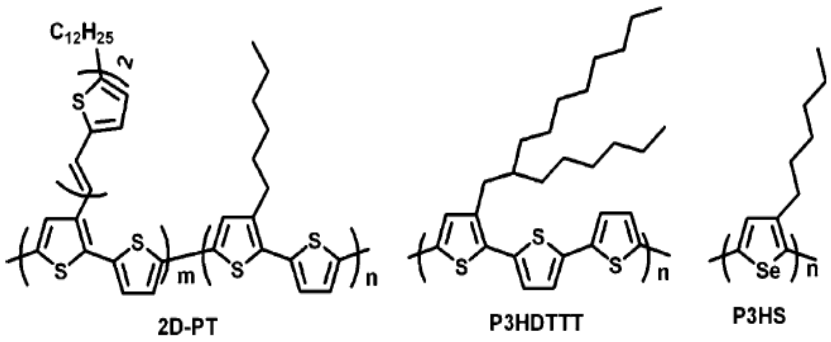

Figure 2.14: *Characteristic polytheophene derivatives.*[53]

2.5.1.2 Benzothiadiazole-based polymers

2,1,3-Benzothiadiazole (BT) has been widely used as an electron deficient building block in conjugated polymers with donor-acceptor (D/A) structure, showing outstanding photovoltaic performances. D/A structures achieve lower band gaps suitable for absorption closer to the near-IR region. Thiophene is a typical electron-rich unit with weak aromatic property and hence thiophene derivatives are broadly used as electron donors in D/A conjugated polymers. In **Fig. 2.15** are shown several copolymers, based on derivatives of dithiophene and BT. We can observe that the dithiophene derivatives possess quite planar structures, which are connected by bridge atoms, like N, C, or Si, or by a planar conjugated unit. Poly[N-1-octylnonyl-2,7-carbazolealt- 5,5-(4,7-di-2-thienyl-2,1´,3´-benzothiadiazole)] (PCPDTBT) is the first low band gap polymer which was successfully used in PSCs.[54] PCPDTBT has a strong and broad absorption band extending to the near-infrared region, corresponding to a band gap of 1.50 eV. Poly(4,4-dioctyldithieno(3,2-b:2',3'-d)silole)-2,6-diyl-alt-(2,1,3-benzothiadiazole)-4,7-diyl) (PSBTBT), shows similar molecular structure as PCPDTBT and also exhibited excellent photovoltaic properties with band gap and HOMO level 1. 55 eV and - 5.1 eV respectively.[51]

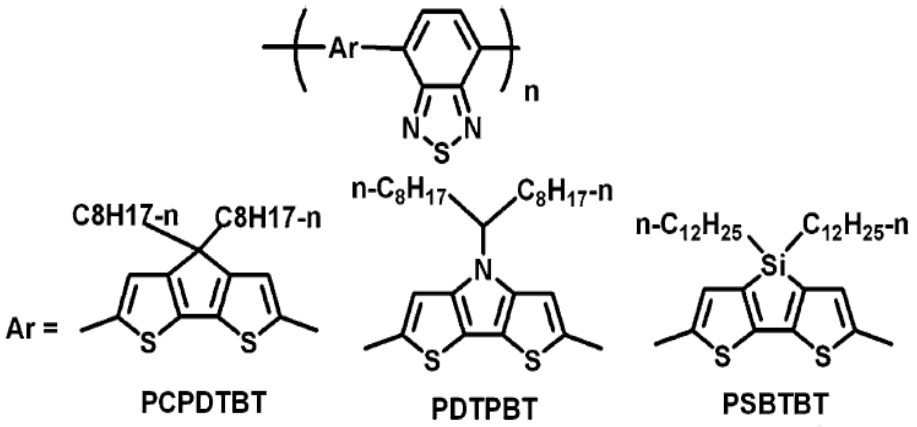

Figure 2.15: *Several characteristic BT-based polymers with D/A structure.*[53]

2.5.1.3 Pyrrolo[3,4-c]pyrrole-1,4-dione (DPP) Derivatives

DPP and its derivatives, have characteristic strong absorption bands in the visible range. Thiophene-based DPP derivatives have well-confined conjugated structures, can be easily synthesized and exhibit good charge-carrier mobilities for both holes and electrons. A large number of low band gap polymers have been synthesized since 2008. Some characteristic ones are shown in **Fig. 2.16**.

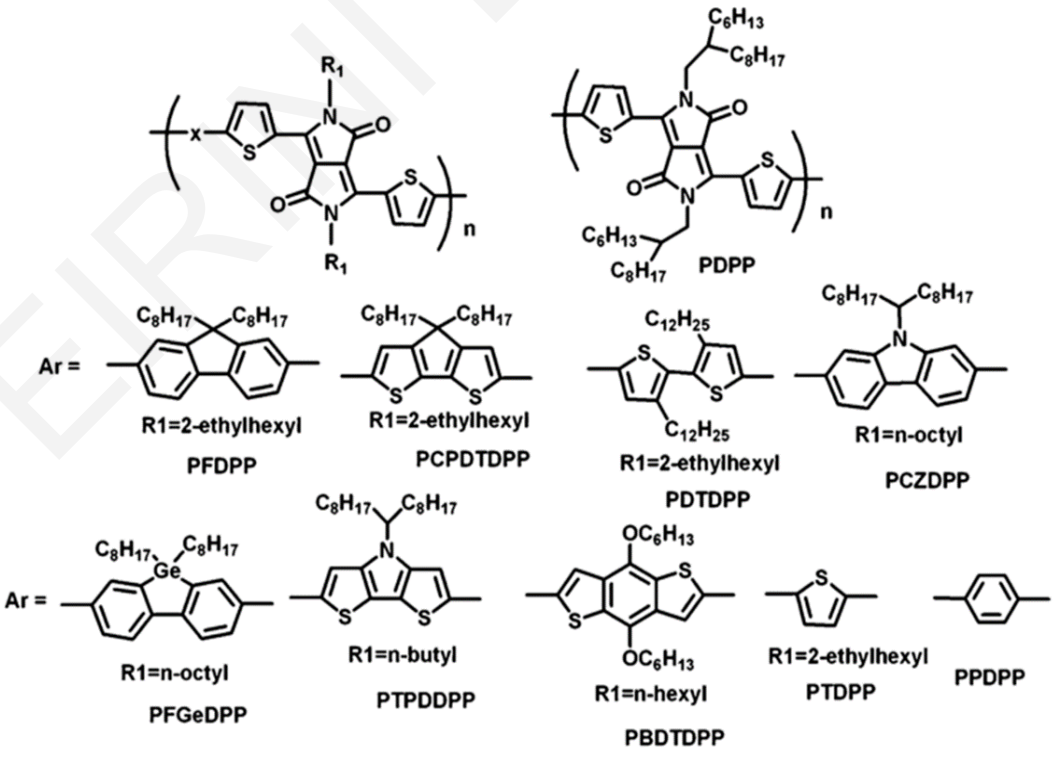

Figure 2.16: *Chemical structures of some DPP-based polymers.*[53]

2.5.2 Acceptors

Acceptors, are the molecules or polymers that receive the electrons from the donors. They are electron-poor materials with high electron mobilities. For both donors and acceptors an ordered structure that enhances charge carrier mobility is highly desirable. Many organic compounds have been investigated as electron acceptor materials, but due to the lack of processability only a few can be employed in highly efficient OPV devices. Fullerene and its derivatives are the most successful electron acceptor materials so far.

2.5.2.1 PCBM and derivatives

Fullerene C_{60} has very symmetric structure and exhibits good electron mobility. As known, one molecule of C_{60} can receive up to four electrons, therefore, C_{60} and its derivatives are suitable as electron acceptor materials. An important disadvantage of C_{60} is that it exhibits very limited solubility in most of the commonly used organic solvents (except CB and DCB). In order to improve its solubility and also to avoid severe phase separation of D/A blend, [6,6]-phenyl-C_{61}-butyric acid methyl ester ($PC_{60}BM$) was used in OPVs. In the past decade, $PC_{60}BM$ and its corresponding C_{70} derivative ($PC_{70}BM$) have been widely used as acceptors in OPVs. $PC_{70}BM$ attracted much interest recently because in comparison with $PC_{60}BM$, it possesses stronger absorption in the visible range. However, C_{70} is much more expensive than C_{60}, so its applications are limited. The molecular structures of $PC_{60}BM$ and $PC_{70}BM$ are shown in Fig. 2.15. $PC_{60}BM$ is a crystalline dark-brown powder, that is highly soluble in common organic solvents such as chloroform, toluene, and o-dichlorobenzene.

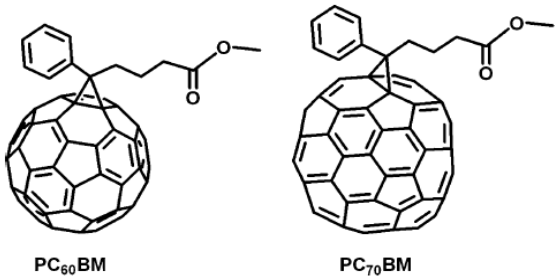

Figure 2.17: *Molecular structure of $PC_{60}BM$ and $PC_{70}BM$.* [53]

Indene-fullerene adducts have been also used as electron acceptor materials in OPVs showing good performances.[55] This kind of compounds can be synthesized easily by a one-pot reaction. Their molecular structure can be found below:

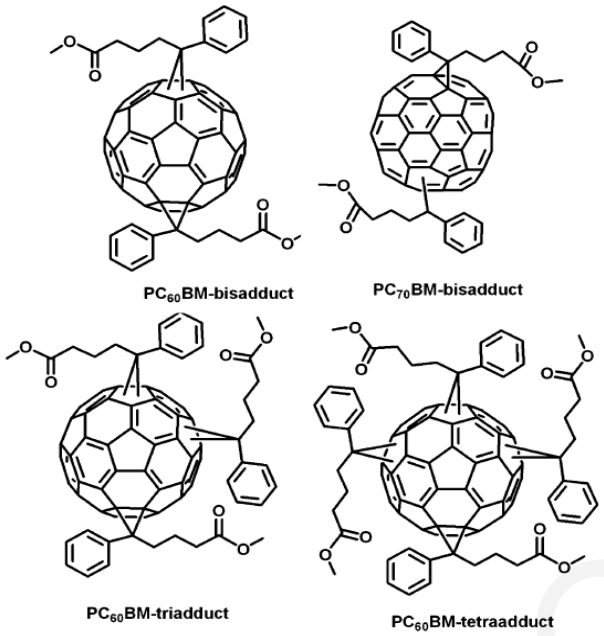

Figure 2.18: *Molecular structure of fullerene multiadduct derivatives.*[53]

2.6 Morphology

2.6.1 The importance of molecular packing and backbone planarity

In sections 2.4.2 and 2.4.3 it became clear that charge transport, charge carrier mobility and potential loss pathways in an OSC are strongly dependent on the molecular conformation of the photoactive layer. Conjugated polymers however, can result in extremely complex microstructures due to the many degrees of conformational freedom and the weak interactions between the chains. To begin with, the basic origin of electronic properties of these materials is the delocalization of π-electrons within and between the molecular chains. The formation of various types of molecular order, from completely amorphous to crystalline, can be categorised according to the potential pathways of the electrons. Molecular order is a broad term, that includes morphological aspects such as **crystallinity** and **backbone planarity**. In the experimental part of this thesis, planarity of the conjugated backbone will be studied extensively and refers to the rotational degrees of freedom of the polymer chain which is directly related to the conjugation length. The higher planarity of a chain leads to higher conjugation length, encouraging fast intra but also inter-molecular charge transport (see **Fig.2.19**) by minimising the distance in the π-π stacking direction.

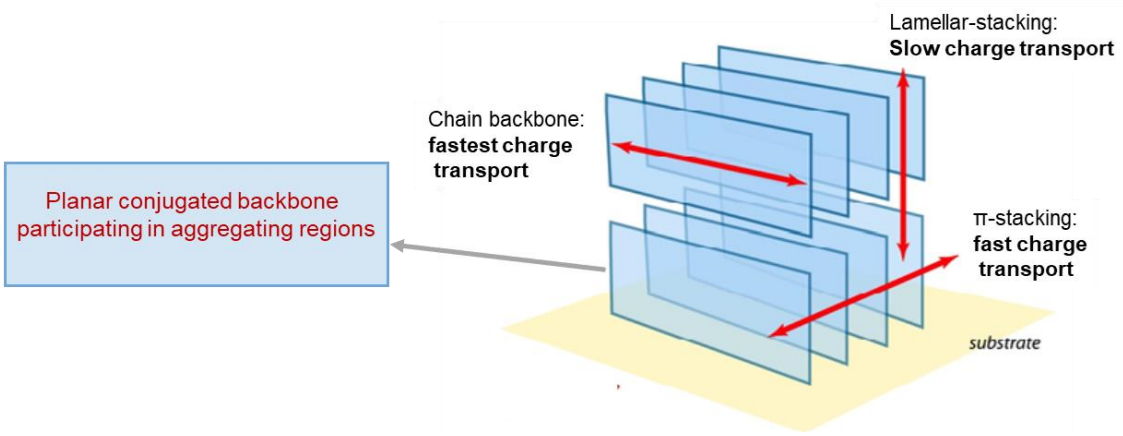

Figure 2.19: *Schematic representation of spatial arrangements of conjugated polymers namely lamellar-stacking and π-π stacking, highlighting (in red arrows) the three main charge transport directions.*[56]

Crystallinity describes the degree of molecular order in terms of spatial arrangement and can be long-range such as π-π stacking (strong noncovalent bonding between the chains) and lamellar stacking (noncovalent interactions between side chains) (see **Fig. 2.19**) or short-range of a few molecular unit aggregates.[56] When neighbouring molecules assemble in the solid state, depending on the relative alignment of their transition dipole moment, they form aggregates which affect the excited state energies and can be recognised by specific signatures in the absorption and emission spectra.[57,58] A head to tail arrangement of neighbouring molecules results in a negative sign of the nearest-neighbour coupling term (excitonic coupling), J_0, and a spectral shift to lower energies (red-shift) characteristic of J-type aggregation, while side-by-side oriented molecules lead to $J_0>0$, shift of the spectrum to higher energies (blue-shift) and this type of aggregation is known as H-type. A second signature of the type of aggregation[58] is the ratio of the oscillator strengths of the first two vibronic peaks $A_{0\text{-}0}/A_{0\text{-}1}$ in the absorption spectrum according to the following expression:

$$R_{abs} = \frac{A_{0-0}}{A_{0-1}} = \left(\frac{1-0.96J_0/w_0}{1+0.92J_0/w_0}\right) \qquad (2.6)$$

where J_0 and w_0 are the nearest-neighbour exciton coupling and frequency of nuclear potentials equivalent to shifted harmonic wells, respectively. Then, the value for the R_{abs} is >1 for J-type aggregation and R_{abs}< 1 for H-type.

The complexity however, arises from the fact that polymer semiconductors are usually polycrystalline, where ordered and amorphous phases co-exist (see **Fig. 2.20**). When such heterogeneity is present, ordered phases are largely responsible for charge transport and it has been shown[59] that if the molecular weight of the polymer is sufficiently high, a minimal amount of aggregation is enough to allow intermolecular transport.

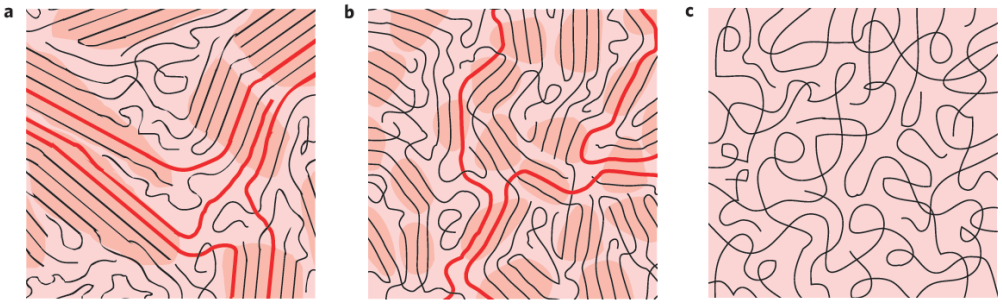

Figure 2.20: *Schematic representation of possible microstructures in semiconducting polymers, depicting a semi-crystalline (a), a weakly ordered (b) and an amorphous (c) polymer film. The red lines highlight fast charge transport pathways.*[59]

2.6.2 Blend films

When it comes to blending films of D and A materials, an additional morphological factor is crucially important for efficient charge transport and exciton dissociation. This is the extent of phase separation between the two materials.[60] In order to fulfil the demands of a large D/A interface (to aid exciton dissociation) and percolated networks of relatively pure domains (to facilitate charge transport), various studies[61–64] have concluded that the active layer should consist of a three-phase morphology: a) an intermixed amorphous phase, b) a pure electron-transporting phase and c) a pure hole-transporting phase (see **Fig. 2.21**).

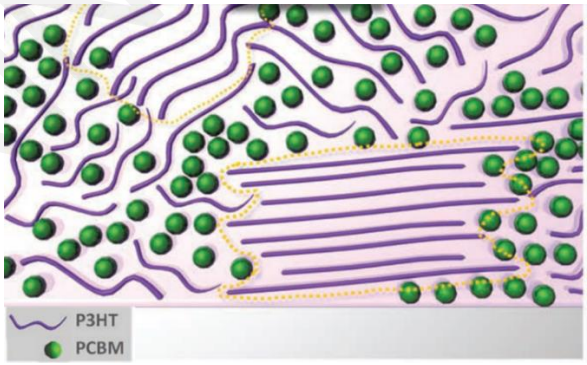

Figure 2.21: *Microstructure of a polymer-fullerene film (polymer is depicted as purple line and fullerene as green ball) comprised of the three-phase morphology: a) pure polymer domains, b) pure fullerene domains and c) mixed polymer-fullerene domains.*[64]

2.6.3 Morphology degradation

Given the complex and multilayer character of polymer solar cells, many factors can contribute to their degradation such as photo-generated radical oxidation, photo-oxidation of fullerene moieties and morphological changes in the device. Although the morphology of the active layer has a key role in device performance, this cannot be retained over time because organic semiconductors are prone to degradation. The blend morphology is often obtained by spin-coating, where a precursor solution is deposited on a substrate and the film is formed by solvent evaporation. This approach results in a thermodynamically unstable microstructure that is highly dependent on temperature. High temperatures cause an evolution of film morphology towards thermodynamic stability that often has a negative effect in device performance.[65] For example, it has been shown that at elevated temperatures the PCBM molecules can diffuse and form large crystals, increasing the extent of phase segregation.[66] However, this phenomenon has been observed below the glass transition temperature (T_g)[5] and it is expected that high T_g polymers or post-treatment such as annealing above the T_g[67] would benefit the stability of the active layer morphology. Together with temperature, other parameters that have been tested for accelerating morphological degradation are humidity, radiation, mechanical pressure and power cycling.[65] Although various strategies have been established to eliminate morphology degradation, the creation of an active layer microstructure that is stable in time and with temperature remains a key challenge that must be overcome before commercialisation of polymer photovoltaics.

2.6.4 Towards morphology control

Despite the complex nature of the active layer microstructure, various strategies have been established over the years of research from the stage of synthesis to post-deposition treatment to control the resulting morphology.[68] For example, molecular weight is an important parameter which can directly affect charge transport as well as chain packing. Long polymer chains are easily organized in ordered domains and they can provide interconnections between amorphous regions.[69] However, this section refers mostly to the importance of film processing which, despite being a broad term that includes various parameters, is a straightforward way to control device characteristics. The first crucial step when it comes to processing, is the **solvent selection**. The aggregation process can be controlled from the type, the polarity and the ratio of the solvent in a polymeric matrix.[70–72] Polymer concentration in

[5] T_g is a reversible transition that the amorhous regions of semi-crystalline materials undergo from a relatively brittle "glassy" state into a rubbery state with increasing temperature

a solvent is also important as molecular interactions favour certain conformations of the polymer in the solution and its highly likely that those characteristics will be present also in the solid phase.[69] The use of **additives** is another common approach to control blend morphology.[73,74] There is no general rule however on their effect. This can be increasing the crystallinity of the donor material, giving rise to a decrease in domain size, diminishing large-scale phase separation, etc., depending on the additive chosen. **D:A ratio** is another factor that can directly impact device performance as it affects molecular conformation and phase separation of thin films.[75] The desired morphology consists of bicontinuous percolation pathways with maximum possible interfacial area and there is no standard optimum D:A ratio, but it depends strongly on the choice of materials and can range from 7:3 to 1:4.[76,77,78] Another important step, especially when it comes to phase separation, is the **film deposition**. Film deposition can be performed with various deposition techniques such as spin coating, wire-bar coating, doctor-blading etc., at various speed rates and deposition temperatures. A general observation regarding the speed, is that slower deposition rates allow the D-A materials more time to separate and form purer domains with better phase separation. Finally, a final post-deposition step that has been observed to have a positive impact on the final device characteristics is the application of heat known as **thermal annealing**. [67,79–81] Thermal annealing refers to the heating of the film above a certain temperature which is the T_g of the selected materials. This allows a re-arrangement of the polymeric chains towards an equilibrium conformation, more ordered and with higher phase separation. It was reported that thermal annealing enhances the crystallization in the case of P3HT and allows PCBM molecules embedded in the disordered P3HT region to diffuse and form larger aggregates.[67,78] The influence of processing on backbone planarity of specific conjugated systems will be extensively studied throughout the experimental part of this doctoral dissertation, contributing to the state of the art research in this field.

References

(1) Heeger, Alan J. ; MacDiarmid, Alan G. ; Shirakawa, H. Advanced Information - The Nobel Prize in Chemistry 2000. *Nobel Media AB 2019* **1974**, 1–16. https://doi.org/10.1007/978-1-84996-290-2.

(2) Facchetti, A. π-Conjugated Polymers for Organic Electronics and Photovoltaic Cell Applications. *Chem. Mater.* **2011**, *23* (3), 733–758. https://doi.org/10.1021/cm102419z.

(3) Köhler, A.; Bässler, H. *Electronic Processes in Organic Semiconductors*; 2015.

(4) Kuhn, H. A Quantum-Mechanical Theory of Light Absorption of Organic Dyes and Similar Compounds. *J. Chem. Phys.* **1949**, *17* (12), 1198–1212. https://doi.org/10.1063/1.1747143.

(5) http://photonicswiki.org/index.php?title=File:Polyene_series.PNG.

(6) Li, Y. Conducting Polymers. In *Organic Optoelectronic Materials*; Springer, 2015; Vol. 91, pp 23–50. https://doi.org/10.1007/978-3-319-16862-3.

(7) Su, W. .; Schrieffer, J. .; and Heeger A.J. Solitons in Polyaeetylene. *Phys. Rev. Lett.* **1979**, *42* (25), 1698–1701.

(8) Chance, R. R.; Brédas, J. L.; Silbey, R. Bipolaron Transport in Doped Conjugated Polymers. *Phys. Rev. B* **1984**, *29* (8), 4491–4495. https://doi.org/10.1103/PhysRevB.29.4491.

(9) Sich, M.; Skryabin, D. V.; Krizhanovskii, D. N. Soliton Physics with Semiconductor Exciton–polaritons in Confined Systems. *Comptes Rendus Phys.* **2016**, *17* (8), 908–919. https://doi.org/10.1016/j.crhy.2016.05.002.

(10) Bredas, J. L.; Street, G. B. Polarons, Bipolarons, and Solitons in Conducting Polymers. *Acc. Chem. Res.* **1985**, *18* (10), 309–315. https://doi.org/10.1021/ar00118a005.

(11) A.J.Heeger, S.Kivelson, J.R.SChrieffer, J. R. S. Solitons in Conducting Polymers. *Rev. Mod. Phys.* **1988**, *60*, 781–850.

(12) Faria, R. M.; Oliveira, O. N. Exploiting the Electrical Properties of Thin Films of Semiconducting Polymers. *Brazilian J. Phys.* **1999**, *29* (2), 360–370. https://doi.org/10.1590/S0103-97331999000200016.

(13) Bulovic, V. Lecture 7: Excitons - Types , Energy Transfer. *6.973 Org. Optoelectron. Spring 2003. (MIT OpenCourseWare Massachusetts Inst. Technol.* **2003**, *5321* (1998), 1–24.

(14) Reid, O. G.; Pensack, R. D.; Song, Y.; Scholes, G. D.; Rumbles, G. Charge Photogeneration in Neat Conjugated Polymers. *Chem. Mater.* **2014**, *26* (1), 561–575. https://doi.org/10.1021/cm4027144.

(15) Scholes, G. D.; Rumbles, G. Excitons in Nanoscale Systems: Fundamentals and Applications. **2008**, *5* (September), 103–157. https://doi.org/10.1142/9789812790248_0003.

(16) Barford, W. Excitons in Conjugated Polymers: A Tale of Two Particles. *J. Phys. Chem. A* **2013**, *117* (13), 2665–2671. https://doi.org/10.1021/jp310110r.

(17) Bredas, J.-L. Mind the Gap! *Mater. Horizons* **2014**, *1*, 17–19. https://doi.org/10.1039/c3mh00098b.

(18) Pope, M.; Swenberg, C. E. *Electronic Processes in Organic Crystals and Polymers*; Oxford Science Publications, 1999.

(19) Wannier, G. H. The Structure of Electronic Excitation Levels in Insulating Crystals. *Phys. Rev.* **1937**, *52* (x), 191–197.

(20) Frenkel, J. On the Transformation of Light into Heat in Solids. I. *Phys. Rev.* **1931**, *37* (1), 17–44. https://doi.org/10.1103/PhysRev.37.17.

(21) Tracey M. Clarke, J. R. D. Charge Photogeneration in Organic Solar Cells. *Chem. Rev.* **2010**, *2* (1), 6736–6767. https://doi.org/10.1117/1.jpe.2.021001.

(22) Arkhipov, V. I.; Heremans, P.; Bässler, H. Why Is Exciton Dissociation so Efficient at the Interface between a Conjugated Polymer and an Electron Acceptor? *Appl.*

Phys. Lett. **2003**, *82* (25), 4605–4607. https://doi.org/10.1063/1.1586456.

(23) Knupfer, M.; Pichler, T.; Golden, M. S.; Fink, J.; Murgia, M.; Michel, R. H.; Zamboni, R.; Taliani, C. Size of Electron-Hole Pairs in π-Conjugated Systems. *Phys. Rev. Lett.* **1999**, *83* (7), 1443–1446. https://doi.org/10.1103/PhysRevLett.83.1443.

(24) Scheblykin, I. G.; Yartsev, A.; Pullerits, T.; Gulbinas, V.; Sundström, V. Excited State and Charge Photogeneration Dynamics in Conjugated Polymers. *J. Phys. Chem. B* **2007**, *111* (23), 6303–6321. https://doi.org/10.1021/jp068864f.

(25) Clarke, T. M.; Durrant, J. R. Charge Photogeneration in Organic Solar Cells. *Chem. Rev.* **2010**, *110* (11), 6736–6767.

(26) Jianhui Hou and Xia Guo. Active Layer Materials for Organic Solar Cells. In *Organic Solar Cells: Materials and Device Physics*; Grosso, R. F. and G., Ed.; Springer, 2013.

(27) Jeff W.Lichtman, J.-A. C. Fluorescence Microscopy. *Nat. Methods* **2005**, *2* (December), 910–919. https://doi.org/10.1002/9783527687732.ch3.

(28) Michael, K. Characterization of Electronic Transitions in Complex Molecules. *Discuss. Faraday Soc.* **1950**, No. c, 14.

(29) Lakowicz, J. R. Fluorescence Lifetimes and Quantum Yields. In *Principles of Fluorescence Spectroscopy*; Springer, 2006. https://doi.org/10.3390/rs10020308.

(30) https://en.wikipedia.org/wiki/Franck%E2%80%93Condon_principle.

(31) Yu, G.; Gao, J.; Hummelen, J. C.; Wudl, F.; Heeger, A. J. Polymer Photovoltaic Cells: Enhanced Efficiencies via a Network of Internal Donor-Acceptor Heterojunctions. *Science (80-.).* **1995**, *270* (5243), 1789. https://doi.org/10.1126/science.270.5243.1789.

(32) Halls, J. J. M.; Walsh, C. A.; Greenham, N. C.; Marseglia, E. A.; Friend, R. H.; Moratti, S. C.; Holmes, A. B. Efficient Photodiodes from Interpenetrating Polymer Networks. *Nature* **1995**, *376* (6540), 498–500. https://doi.org/10.1038/376498a0.

(33) Facchetti, A. Polymer Donor-Polymer Acceptor (All-Polymer) Solar Cells. *Mater. Today* **2013**, *16* (4), 123–132. https://doi.org/10.1016/j.mattod.2013.04.005.

(34) Zhang, H.; Yao, H.; Hou, J.; Zhu, J.; Zhang, J.; Li, W.; Yu, R.; Gao, B.; Zhang, S.; Hou, J. Over 14% Efficiency in Organic Solar Cells Enabled by Chlorinated Nonfullerene Small-Molecule Acceptors. *Adv. Mater.* **2018**, *30* (28), 1–7. https://doi.org/10.1002/adma.201800613.

(35) Meng, L.; Zhang, Y.; Wan, X.; Li, C.; Zhang, X.; Wang, Y.; Ke, X.; Xiao, Z.; Ding, L.; Xia, R.; et al. Organic and Solution-Processed Tandem Solar Cells with 17.3% Efficiency. *Science (80-.).* **2018**, *361* (6407), 1094–1098. https://doi.org/10.1126/science.aat2612.

(36) Deibel, C.; Dyakonov, V. Polymer-Fullerene Bulk Heterojunction Solar Cells. *Reports Prog. Phys.* **2010**, *73* (9), 96401.

(37) N. S. Sariciftci, L. Smilowitz, A. J. Heeger, F. W. Photoinduced Electron Transfer from a Conducting Polymer to Buckminsterfullerene N. *Science (80-.).* **1992**, *258*, 1474–1476. https://doi.org/10.1126/science.258.5087.1474.

(38) Lloyd, M. T.; Lim, Y. F.; Malliaras, G. G. Two-Step Exciton Dissociation in poly(3-

Hexylthiophene)/fullerene Heterojunctions. *Appl. Phys. Lett.* **2008**, *92* (14), 2006–2009. https://doi.org/10.1063/1.2908165.

(39) Dimitrov, S. D.; Durrant, J. R. Materials Design Considerations for Charge Generation in Organic Solar Cells. *Chem. Mater.* **2014**, *26* (1), 616–630. https://doi.org/10.1021/cm402403z.

(40) Zhang, W.; Huang, Y.; Xing, Y.-D.; Jing, Y.; Ye, L.; Fu, L.-M.; Ai, X.-C.; Hou, J.-H.; Zhang, J.-P. Subnanosecond Charge Photogeneration and Recombination in Polyfluorene Copolymer-Fullerene Solar Cell: Effects of Electric Field. *Opt. Express* **2013**, *21* (S2), A241. https://doi.org/10.1364/oe.21.00a241.

(41) Jean-Luc Bredas, Joseph E. Norton, J. C. A. V. C. Molecular Understanding of Organic Solar Cells: The Challenges. *Acc. Chem. Res.* **2009**, *42* (11), 1691–1699. https://doi.org/10.1021/ar900099h.

(42) Clarke, T. M.; Durrant, J. R. Charge Photogeneration in Organic Solar Cells. *Chem. Rev.* **2010**, *110* (11), 6736–6767. https://doi.org/10.1021/cr900271s.

(43) Peumans, P.; Forrest, S. R. Separation of Geminate Charge-Pairs at Donor-Acceptor Interfaces in Disordered Solids. *Chem. Phys. Lett.* **2004**, *398* (1–3), 27–31. https://doi.org/10.1016/j.cplett.2004.09.030.

(44) Artem A. Bakulin, Akshay Rao, Vlad G. Pavelyev, Paul H. M. van Loosdrecht, Maxim S. Pshenichnikov, Dorota Niedzialek, Jérôme Cornil, David Beljonne, R. H. F. The Role of Driving Energy and Delocalized States for Charge Separation in Organic Semiconductors. *Science (80-.).* **2012**, *335* (March), 1340–1344.

(45) Veldman, D.; Meskers, S. C. J.; Janssen, R. A. J. The Energy of Charge-Transfer States in Electron Donor-Acceptor Blends: Insight into the Energy Losses in Organic Solar Cells. *Adv. Funct. Mater.* **2009**, *19* (12), 1939–1948. https://doi.org/10.1002/adfm.200900090.

(46) Massip, S.; Oberhumer, P. M.; Tu, G.; Albert-Seifried, S.; Huck, W. T. S.; Friend, R. H.; Greenham, N. C. Influence of Side Chains on Geminate and Bimolecular Recombination in Organic Solar Cells. *J. Phys. Chem. C* **2011**, *115* (50), 25046–25055. https://doi.org/10.1021/jp2070584.

(47) Liu, C. Y.; Chen, S. A. Charge Mobility and Charge Traps in Conjugated Polymers. *Macromol. Rapid Commun.* **2007**, *28* (17), 1743–1760. https://doi.org/10.1002/marc.200700327.

(48) Zhan, X.; Zhu, D. Conjugated Polymers for High-Efficiency Organic Photovoltaics. *Polym. Chem.* **2010**, *1* (4), 409. https://doi.org/10.1039/b9py00325h.

(49) Hou, J.; Tan, Z.; Yan, Y.; He, Y.; Yang, C.; Li, Y. Synthesis and Photovoltaic Properties of Two-Dimensional Conjugated Polythiophenes with Bi(thienylenevinylene) Side Chains. *J. Am. Chem. Soc.* **2006**, *128* (14), 4911–4916. https://doi.org/10.1021/ja060141m.

(50) Choy, W. C. H. *Organic Solar Cells Materials and Device Physics*; Springer, 2013.

(51) Hou, J.; Chen, T. L.; Zhang, S.; Huo, L.; Sista, S.; Yang, Y. An Easy and Effective Method to Modulate Molecular Energy Level of poly(3-Alkylthiophene) for High-VocPolymer Solar Cells. *Macromolecules* **2009**, *42* (23), 9217–9219. https://doi.org/10.1021/ma902197a.

(52) Ballantyne, A. M.; Chen, L.; Nelson, J.; Bradley, D. D. C.; Astuti, Y.; Maurano, A.;

Shuttle, C. G.; Durrant, J. R.; Heeney, M.; Duffy, W.; et al. Studies of Highly Regioregular poly(3-Hexylselenophene) for Photovoltaic Applications. *Adv. Mater.* **2007**, *19* (24), 4544–4547. https://doi.org/10.1002/adma.200701265.

(53) Jianhui Hou and Xia Guo. Active Layer Materials for Organic Solar Cells. In *Organic Solar Cells: Materials and Device Physics*; Choy, W. C. H., Ed.; Springer-Verlag London, 2013. https://doi.org/10.1007/978-1-4471-4823-4.

(54) Mühlbacher, D.; Scharber, M.; Morana, M.; Zhu, Z.; Waller, D.; Gaudiana, R.; Brabec, C. High Photovoltaic Performance of a Low-Bandgap Polymer. *Adv. Mater.* **2006**, *18* (21), 2884–2889. https://doi.org/10.1002/adma.200600160.

(55) He, Y.; Zhao, G.; Peng, B.; Li, Y. High-Yield Synthesis and Electrochemical and Photovoltaic Properties of Indene-C 70 Bisadduct. *Adv. Funct. Mater.* **2010**, *20* (19), 3383–3389. https://doi.org/10.1002/adfm.201001122.

(56) Noriega, R.; Rivnay, J.; Vandewal, K.; Koch, F. P. V; Stingelin, N.; Smith, P.; Toney, M. F.; Salleo, A. A General Relationship between Disorder, Aggregation and Charge Transport in Conjugated Polymers. *Nat. Mater.* **2013**, *12* (11), 1038–1044. https://doi.org/10.1038/nmat3722.

(57) Wang, H.; Xu, Y.; Yu, X.; Xing, R.; Liu, J.; Han, Y. *Structure and Morphology Control in Thin Films of Conjugated Polymers for an Improved Charge Transport*; 2013; Vol. 5. https://doi.org/10.3390/polym5041272.

(58) Spano, F. C.; Silva, C. H- and J-Aggregate Behavior in Polymeric Semiconductors. *Annu. Rev. Phys. Chem.* **2014**, *65* (1), 477–500. https://doi.org/10.1146/annurev-physchem-040513-103639.

(59) Himmelberger, S.; Salleo, A. Engineering Semiconducting Polymers for Efficient Charge Transport. *MRS Commun.* **2015**, *5* (3), 383–395. https://doi.org/10.1557/mrc.2015.44.

(60) Vandewal, K.; Himmelberger, S.; Salleo, A. Structural Factors That Affect the Performance of Organic Bulk Heterojunction Solar Cells. *Macromolecules* **2013**, *46* (16), 6379–6387. https://doi.org/10.1021/ma400924b.

(61) Yin, W.; Dadmun, M. A New Model for the Morphology of p3ht/pcbm Organic Photovoltaics from Small-Angle Neutron Scattering: Rivers and Streams. *ACS Nano* **2011**, *5* (6), 4756–4768. https://doi.org/10.1021/nn200744q.

(62) Westacott, P.; Tumbleston, J. R.; Shoaee, S.; Fearn, S.; Bannock, J. H.; Gilchrist, J. B.; Heutz, S.; Demello, J.; Heeney, M.; Ade, H.; et al. On the Role of Intermixed Phases in Organic Photovoltaic Blends. *Energy Environ. Sci.* **2013**, *6* (9), 2756–2764. https://doi.org/10.1039/c3ee41821a.

(63) Treat, N. D.; Varotto, A.; Takacs, C. J.; Batara, N.; Al-Hashimi, M.; Heeney, M. J.; Heeger, A. J.; Wudl, F.; Hawker, C. J.; Chabinyc, M. L. Polymer-Fullerene Miscibility: A Metric for Screening New Materials for High-Performance Organic Solar Cells. *J. Am. Chem. Soc.* **2012**, *134* (38), 15869–15879. https://doi.org/10.1021/ja305875u.

(64) Treat, N. D.; Brady, M. A.; Smith, G.; Toney, M. F.; Kramer, E. J.; Hawker, C. J.; Chabinyc, M. L. Interdiffusion of PCBM and P3HT Reveals Miscibility in a Photovoltaically Active Blend. *Adv. Energy Mater.* **2011**, *1* (1), 82–89. https://doi.org/10.1002/aenm.201000023.

(65) Schuller, S.; Schilinsky, P.; Hauch, J.; Brabec, C. J. Determination of the

Degradation Constant of Bulk Heterojunction Solar Cells by Accelerated Lifetime Measurements. *Appl. Phys. A Mater. Sci. Process.* **2004**, *79* (1), 37–40. https://doi.org/10.1007/s00339-003-2499-4.

(66) Yang, X.; Van Duren, J. K. J.; Janssen, R. A. J.; Michels, M. A. J.; Loos, J. Morphology and Thermal Stability of the Active Layer in Poly(p-Phenylenevinylene)/methanofullerene Plastic Photovoltaic Devices. *Macromolecules* **2004**, *37* (6), 2151–2158. https://doi.org/10.1021/ma035620+.

(67) Padinger, F.; Rittberger, R. S.; Sariciftci, N. S. Effects of Postproduction Treatment on Plastic Solar Cells. *Adv. Funct. Mater.* **2003**, *13* (1), 85–88. https://doi.org/10.1002/adfm.200390011.

(68) Brabec, C. J.; Heeney, M.; McCulloch, I.; Nelson, J. Influence of Blend Microstructure on Bulk Heterojunction Organic Photovoltaic Performance. *Chem. Soc. Rev.* **2011**, *40* (3), 1185–1199. https://doi.org/10.1039/c0cs00045k.

(69) Padinger, F.; Rittberger, R. S.; Sariciftci, N. S. Effects of Postproduction Treatment on Plastic Solar Cells. *Adv. Funct. Mater.* **2003**, *13* (1), 85–88. https://doi.org/10.1021/jp993190c.

(70) Arias, A. C.; MacKenzie, J. D.; Stevenson, R.; Halls, J. J. M.; Inbasekaran, M.; Woo, E. P.; Richards, D.; Friend, R. H. Photovoltaic Performance and Morphology of Polyfluorene Blends: A Combined Microscopic and Photovoltaic Investigation. *Macromolecules* **2001**, *34* (17), 6005–6013. https://doi.org/10.1021/ma010240e.

(71) Cho, N.; Yip, H. L.; Jen, A. K. Y. Morphology Evolution by Controlling Solvent-Solute Interactions Using a Binary Solvent in Bulk Heterojunction Solar Cells. *Appl. Phys. Lett.* **2013**, *102* (23). https://doi.org/10.1063/1.4811173.

(72) Wang, W.; Ruderer, M. A.; Metwalli, E.; Guo, S.; Herzig, E. M.; Perlich, J.; Müller-Buschbaum, P. Effect of Methanol Addition on the Resistivity and Morphology of PEDOT:PSS Layers on Top of Carbon Nanotubes for Use as Flexible Electrodes. *ACS Appl. Mater. Interfaces* **2015**, *7* (16), 8789–8797. https://doi.org/10.1021/acsami.5b01327.

(73) Peet, J.; Soci, C.; Coffin, R. C.; Nguyen, T. Q.; Mikhailovsky, A.; Moses, D.; Bazan, G. C. Method for Increasing the Photoconductive Response in Conjugated Polymer/fullerene Composites. *Appl. Phys. Lett.* **2006**, *89* (25), 5–8. https://doi.org/10.1063/1.2408661.

(74) Peet, J.; Kim, J. Y.; Coates, N. E.; Ma, W. L.; Moses, D.; Heeger, A. J.; Bazan, G. C. Efficiency Enhancement in Low-Bandgap Polymer Solar Cells by Processing with Alkane Dithiols. *Nat. Mater.* **2007**, *6* (7), 497–500. https://doi.org/10.1038/nmat1928.

(75) Razzell-Hollis, J.; Limbu, S.; Kim, J. S. Spectroscopic Investigations of Three-Phase Morphology Evolution in Polymer: Fullerene Solar Cell Blends. *J. Phys. Chem. C* **2016**, *120* (20), 10806–10814. https://doi.org/10.1021/acs.jpcc.6b02898.

(76) Sun, Y.; Welch, G. C.; Leong, W. L.; Takacs, C. J.; Bazan, G. C.; Heeger, A. J. Solution-Processed Small-Molecule Solar Cells with 6.7% Efficiency. *Nat. Mater.* **2012**, *11* (1), 44–48. https://doi.org/10.1038/nmat3160.

(77) Shaheen, S. E.; Brabec, C. J.; Sariciftci, N. S.; Padinger, F.; Fromherz, T.; Hummelen, J. C. 2.5% Efficient Organic Plastic Solar Cells. *Appl. Phys. Lett.* **2001**, *78* (6), 841–843. https://doi.org/10.1063/1.1345834.

(78) Huang, Y.; Kramer, E. J.; Heeger, A. J.; Bazan, G. C. Bulk Heterojunction Solar Cells: Morphology and Performance Relationships. *Chem. Rev.* **2014**, *114* (14), 7006–7043. https://doi.org/10.1021/cr400353v.

(79) Yang, X.; Loos, J.; Veenstra, S. C.; Verhees, W. J. H.; Wienk, M. M.; Kroon, J. M.; Michels, M. A. J.; Janssen, R. A. J. Nanoscale Morphology of High-Performance Polymer Solar Cells. *Nano Lett.* **2005**, *5* (4), 579–583. https://doi.org/10.1021/nl048120i.

(80) Brabec, B. C. J.; Gowrisanker, S.; Halls, J. J. M.; Laird, D.; Jia, S.; Williams, S. P. Polymer – Fullerene Bulk-Heterojunction Solar Cells. **2010**, 3839–3856. https://doi.org/10.1002/adma.200903697.

(81) Erb, T.; Zhokhavets, U.; Gobsch, G.; Raleva, S.; Stühn, B.; Schilinsky, P.; Waldauf, C.; Brabec, C. J. Correlation between Structural and Optical Properties of Composite Polymer/fullerene Films for Organic Solar Cells. *Adv. Funct. Mater.* **2005**, *15* (7), 1193–1196. https://doi.org/10.1002/adfm.200400521.

Chapter 3

Introduction to Raman spectroscopy

Raman spectroscopy is a powerful tool towards our understanding of the structure and properties of a wide variety of materials. It is based on the Raman Effect, named after the Indian scientist C.V. Raman who first observed it, together with K.S. Krishnan in 1928.[1] Photons interact with matter through scattering in three possible ways. Most of them, are elastically scattered and this dominant process is known as Rayleigh scattering. However, a small amount of them (approximately one in 10^7 photons)[2] loses or gains energy. If the scattered photons have lower energy (and frequency) than that of the photons absorbed by a sample, this inelastic scattering is known as Stokes scattering. The opposite case, in which the emitted photons have higher energy than the ones absorbed, is called Anti-Stokes scattering. This energy shift is a result of the interaction between the photons and the vibrational energy levels of the molecules that caused the scattering. Each material scatters light in a unique way and by monitoring this process we can access molecular motion and bond structure. In Raman Spectroscopy, the scattered light is detected and analysed to provide insights on vibrational, rotational, and other low-frequency transitions of the examined system. The main advantages of this technique is that it is non-destructive, requires little or no sample preparation and is suitable for solid, liquid and gas samples. Raman spectroscopy will be the main characterisation technique employed in the experimental part of this study therefore, this chapter sets out the basic principles of Raman scattering and provides the essential background for the understanding of the experimental results.

3.1 Theory of Raman Scattering

3.1.1 Classical approach

In physical terms, the Raman effect can be described as a result of the polarisation induced in a sample by the electrical field of a monochromatic light source (laser). If we consider the laser beam as an oscillating electromagnetic wave with electrical vector $\vec{E}$, upon interaction with a sample an electric dipole moment $\vec{P}$ is induced:

$$\vec{P} = \tilde{a}\vec{E} \quad (3.1)$$

$\tilde{a}$ is the polarisability (per molecule/ per Vol etc), reflecting the ease with which the induced dipole forms, and $\vec{E} = E_0 \sin(\omega_i t)$ is the electrical field of the incident (i) radiation.

In case of elastic scattering (Rayleigh) the emitted radiation from the sample has the same frequency ω_i as the incident radiation. However, since the molecules of a sample can vibrate with a different frequency ω_{01} , this affects the polarizability $\tilde{a}$ of the material through changes in bond lengths and atomic positions (expressed in terms of a vibrational coordinate, Q_0). Then $\tilde{a}$ (that will depend on the Q_0) can be expressed as:

$$\tilde{a} = \tilde{a}_0 + \left(\frac{\partial \tilde{a}}{\partial Q}\right)_{Q=0} Q_0 \sin(\omega_{01} t) + \ldots = \tilde{a}_0 + \tilde{\beta} \sin(\omega_{01} t) + \ldots \quad (3.2)$$

where $\tilde{a}_0$ is the polarizability of the system at the equilibrium state and $\tilde{\beta}$ is the amplitude change of the polarizability due to its normal mode.

If we replace equation (3.2) in (3.1) the electric dipole moment will be:

$$\vec{P} = \tilde{a}_0 + \tilde{\beta} \sin(\omega_{01} t)\, E_0 \sin(\omega_i t) = \tilde{a}_0\, E_0 \sin(\omega_i t) + \tilde{\beta} \sin(\omega_{01} t)\, E_0 \sin(\omega_i t)$$

After mathematical transformations we obtain the equation below:

$$\vec{P} = \tilde{a}_0\, E_0 \sin(\omega_i t) + \frac{\tilde{\beta}}{2} E_0 \cos(\omega_i - \omega_{01})t - \cos(\omega_i + \omega_{01})t \quad (3.3)$$

From this, we conclude that the emitted radiation has three distinct frequency components: Firstly, $P(\omega_i)$ with frequency ω_i (same as the frequency of the incident wave), associated with Rayleigh scattering and secondly, $P(\omega_i \pm \omega_{01})$ with two frequencies $\omega_i \pm \omega_{01}$ that result from the frequency shifting by an amount associated with the frequency of a molecular vibration. These last two terms correspond to Anti-Stokes and Stokes inelastic scattering. **Figure 3.1** presents qualitatively a Raman scattering spectrum. This approach, although it explains well the appearance of side bands, is not sufficient to explain the lower intensity observed for the anti-Stokes vibrational modes (see **Fig. 3.1**), thus a quantum-mechanical approach should also be considered.[3]

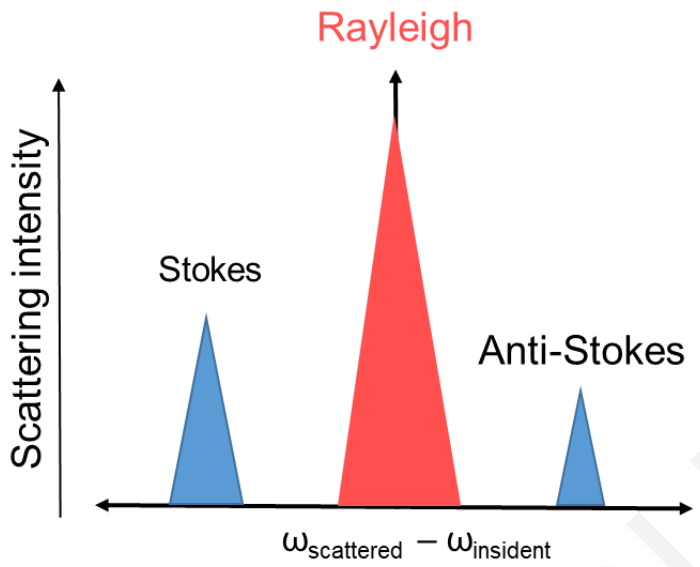

Figure 3.1: *Qualitative schematic representation of a scattering spectrum including the elastic scattering band (Rayleigh) and the Stokes and Anti-Stokes inelastic scattering bands.*

3.1.2 Quantum approach

Through this approach, we consider the laser beam as a sum of photons with energy $E = \hbar\omega_i$, momentum $\overrightarrow{p_i} = \hbar\overrightarrow{k_i}$ and $\omega_i = ck_i$, where c is the speed of light and $\overrightarrow{k_i}$ is the dispersion wave vector with value $k_i = {}^{2\pi}/_{\lambda_i}$. Each phonon of the irradiated material has energy $E_{ph} = \hbar\omega_{ph}$ and momentum $\overrightarrow{p_{ph}} = \hbar\overrightarrow{q_{ph}}$ with the suitable dispersion relation $\omega_{ph} = \omega_{ph}(\vec{q}_{ph})$ of the system. If we think of light as particles (photons) that impinging on a molecule, the system exchanges energy and momentum according to the conservation of energy.

There are two possible paths of this inelastic collision between the photons and phonons. In the first case (Stokes), a photon with wave vector $\vec{k}$ results in a $\overrightarrow{k'}$ photon (from the interaction with the phonon gas) with less energy than the initial and a phonon $\vec{q}$ with energy equal to the energy difference between the two photons. In the second case (Anti-Stokes), the incident photon interacts with a phonon and the resulting photon has energy equal to the sum of the energy of the two particles before their interaction. The resulting conservation of energy relation is:[3]

$$\hbar\omega_k = \hbar\,\omega_{k'} \pm \hbar\omega_q \ ,$$

where (+) is for the Stokes scattering and (-) for the Anti-Stokes. The above processes can be visualised through a Jablonski diagram (see **Fig.3.2**). Photon absorption excites the molecule from an E_0 ground state to a virtual energy state, which lies within the band-gap.

The virtual state relaxes back to E_0 by emitting a scattered photon, which has either equal energy to the incident photon (Rayleigh scattering), or different by a factor equal to the energy of the vibration, $\hbar\omega_{ph}$. If the energy of the scattered photon is increased by $\hbar\omega_{ph}$, the molecule relaxes to a lower vibrational state (anti-Stokes) and accordingly if it is decreased by this factor, the molecule relaxes to a higher vibrational level. The population of the various states of the molecule is what defines the relative intensities of the two processes. Selection rules exist, and the basic idea is that Raman scattering occurs from vibrations which cause a change in polarizability of the electron cloud around the molecule.

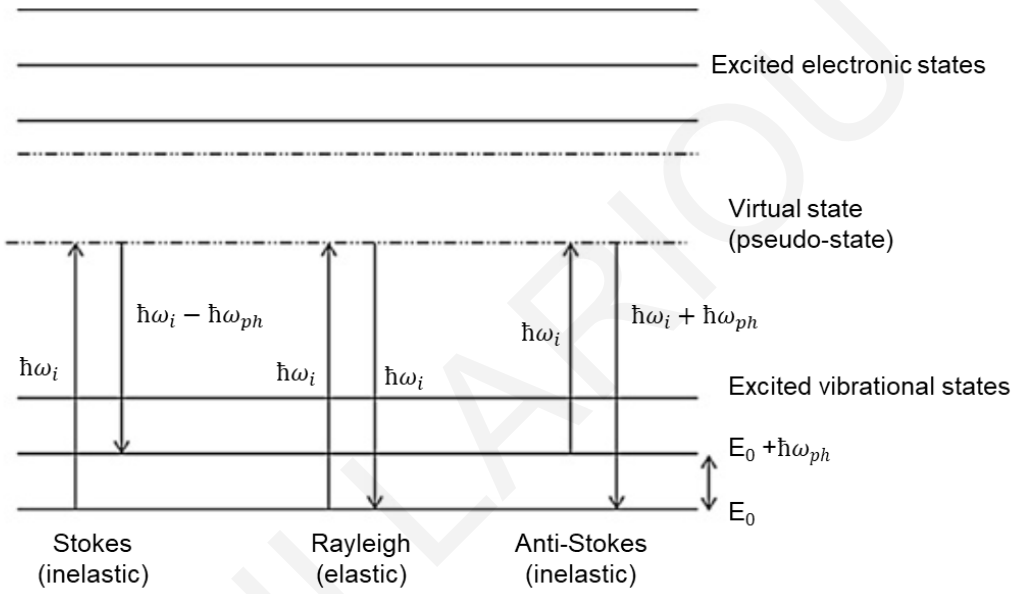

Figure 3.2: *Jablonski Diagram Representing Quantum Energy Transitions for Rayleigh and Raman Scattering (re-sketched from reference).*[4]

Raman spectroscopy is useful in a broad range of scientific fields such as chemistry, biology, physics, archaeology and the medical sector. The evolution of technology improved Raman techniques over the years, and today, the term "Raman spectroscopy" is used to describe a whole family of experimental methods such as Coherent anti-Stokes Raman, Resonance Raman (RR), Surface enhanced-Raman (SERS), Raman Imaging and time-resolved Raman.[2] From these, RR and SERS are the techniques of choice in the experimental part and will be briefly explained in the following sections.

3.2 Resonance Raman Spectroscopy

The resonance condition is achieved when the energy of the incident light matches that of an electronic transition. (see **Fig. 3.3**). The strength of the coupling is determined by the Franck-Condon overlap between the initial and the final vibrational states. The resonance effect can be achieved experimentally when the excitation wavelength is chosen with respect to the absorption band of the scattering molecule. This causes the vibrations of the absorbing species to be selectively enhanced[5,6] by factors up to 10^6 which facilitates the study of compounds present at low concentrations as well as selective probing of specific morphological phases. Resonance Raman (RR) frequencies provide detailed information about electronic structure and geometry of the ground state while RR intensities provide insights on the geometry and dynamics of the resonant electronic state along the particular normal mode as it will be described in detail in section 3.4.[7]

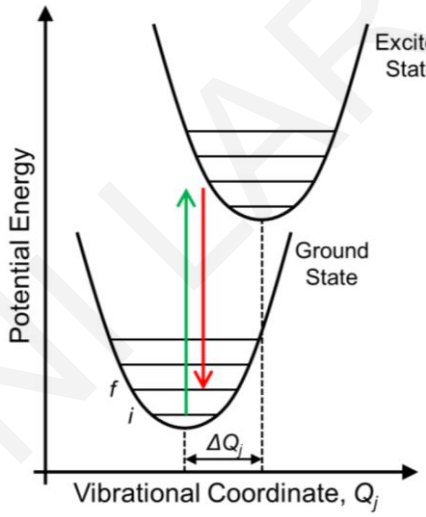

Figure 3.3: *Diagram depicting resonance Raman transition from an initial state i in the ground state to an excited electronic state and return to a final state f in the ground state.*[8]

3.3 Surface Enhanced Raman Spectroscopy

The effect of surface enhancement of Raman scattering (SERS) was first observed in 1974 with the enhanced Raman scattering of pyridine on a silver electrode.[9] This spectroscopic technique, provides Raman signal enhancement which can be up to 10^{11} as previously reported,[10] allowing substance detection at very low concentrations, even single molecule detection.[11] Moreover, since Raman spectroscopy probes mostly the bulk of materials, SERS provides access to the surface enabling surface selectivity. In Chapter 6 we will employ SERS for the selective study of organic-metal (silver) interface in a semi-complete OPV device. Meanwhile, some basic theoretical aspects concerning the origin of SERS are outlined below.

3.3.1 Metallic Nanoparticles

Metallic nanoparticles show interesting properties distinct from those of metals, because quantum effects appear at the nano-scale. Their properties depend on the size, the nature and the structure (5–100 nm is a typical size range).[12] The nanoparticles can be fabricated through various methods such as plasma evaporation, laser ablation, colloidal-type solutions etc. Common nanoparticles employed for SERS studies include silver, platinum, gold and aluminium due to their strong interaction with electro-magnetic radiation.

3.3.2 Plasmons

In nano-scale metallic systems, the percentage of the surface atoms with respect to those in the bulk increases as their size decreases, thus the role of surface atoms becomes important. Such systems can be visualised as positive ions surrounded by an electron cloud (plasma) with overall neutrality at equilibrium. If electromagnetic radiation excites the ion and electron plasma, their interaction stimulates a collective oscillation of the conduction electrons, a state which is known as a plasmon. Specifically, for metallic nanoparticles which can be smaller than the wavelength of the incident light, the surface component of the plasma is so important that the oscillation can be considered as a time varying dipolar mode -instead of multipolar that is observed in a planar surface- known as surface plasmon (See **Fig. 3.4**).[12] Specific wavelengths can be in resonance with the oscillating surface plasmons causing strong absorption and scattering of the incident photons, generating a strong localised electromagnetic field. The resonant frequency of the surface plasmons depends on the shape and size of the nanoparticles.[13]

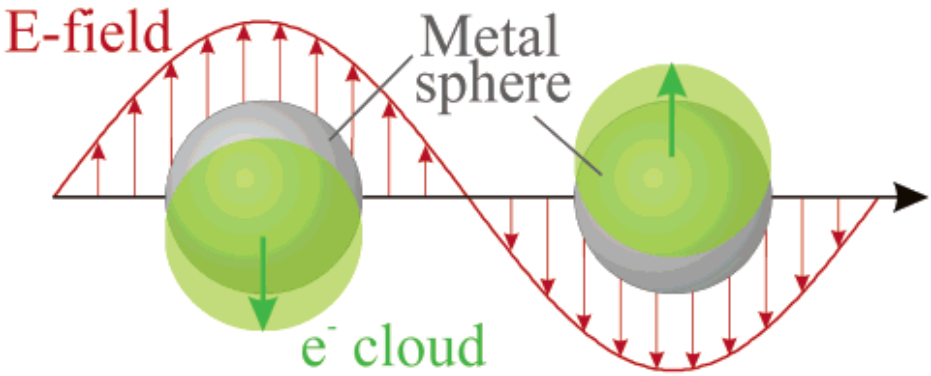

Figure 3.4: *Schematic representation of oscillating metallic spheres illustrating the displacement of the electron cloud relative to the nuclei caused by electromagnetic radiation.*[13]

3.3.3 Origin of surface enhancement

Surface enhancement is caused by two separate contributing factors resulting from the enhancement of either the polarizability $\tilde{\alpha}$ or/and the enhancement of the electric field $\vec{E}$ due to the incident radiation (considering that the intensity of Raman scattering is proportional to the square of the induced dipole moment, $\vec{P} = \tilde{\alpha}\vec{E}$). The enhancement associated with the polarizability, is a weak effect known as chemical enhancement and concerns the charge transfer between the electronic states of the molecule and the Fermi level of the metallic surface. We will not elaborate further on this mechanism, as it can only achieve enhancement of one or two orders of magnitude.[14] The enhancement associated with E is known as electromagnetic enhancement (EM). It is caused by the plasmon resonance and is the dominant enhancement mechanism of the order of 10^8- 10^{14}.[15] The strength of the Raman scattering of a molecule depends on the local electric field (E_{LOC}), thus only those that are in close proximity to the metal surface exhibit enhanced scattering, while the rest experience un-enhanced far-field E_0. In the simplest description, the enhancement factor EF is given by the $|E|^4$aproximation:

$$EF = \frac{I_{SERS}}{I_{RS}} \approx \frac{|E_{LOC}(\omega_0)|^4}{|E_0|^4} \qquad (3.4)$$

where I_{SERS} is the intensity of the Raman scattering by a molecule in the presence of a metal and I_{RS} is the normal Raman scattering intensity in the absence of it.[8] From the above relation, the sensitivity of the enhancement to the local electric field (fourth power dependence) is quite clear, as even a small increase can result in large EF. The electric field on the other hand, strongly depends on the local geometry. Certain positions such as at the corners of triangle structures or in the gap between two nanoparticles can become radiation

nano-antennas, known also as hot spots. In the latter case, a molecule located between two metallic nanoparticles (see **Fig.3.5**) senses two sets of charges arising from polarization of the individual nanoparticles. The combined field of the incident light and the field that results from the vibrating neighbouring nanoparticles induce a dipole that leads to an amplification of the polarization.

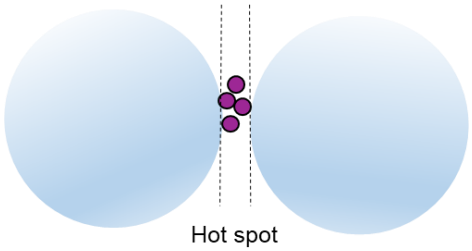

Figure 3.5: *Schematic representation of a hot spot between two nanoparticles where molecules are trapped.*

The spatial localisation of the SERS effect will be exploited in the experimental study of organic semiconductors to selectively probe molecules at a metal-organic interface. Moreover, SERS can be combined with resonance Raman to achieve additional enhancement of up to $x10^2$, an approach known as Surface-Enhanced Resonance Raman Spectroscopy (SERRS).[5]

3.4 Theoretical description of resonance Raman intensities

As mentioned in section 3.2, Resonance Raman is a spectroscopic technique that enables selective enhancement in the Raman scattering of an absorber, providing detailed information about the ground state structure of the examined chromophores[6]. Access to the structure, symmetry and dynamics of the resonant excited electronic state can also be obtained, by having a closer look at the intensities of the Raman lines. The intensity of each resonance Raman band, reflects the projection of the short-lived (femto-second time-scale) excited state geometry change with respect to a specific ground-state normal coordinate. Theoretical tools are able to predict geometry changes accompanying electronic excitations. The relation between RR intensities and excited-state geometry was first reported at 1970 by the early work of Tang and Albrecht.[16] A commonly applied approach to provide resonance Raman intensity analysis (RRIA) was developed by Lee and Heller in 1979 and is based on the time-dependent wavepacket picture of resonance Raman scattering.[17] This

[6] Polymers usually consist of chain segments with different conjugation lengths, each having a characteristic exciton energy (or colour). The term "chromophore" refers to the characteristic energy of each segment.

approach will be employed in the experimental part where both RR and absorption cross sections are modelled simultaneously for the study of the short-lived excited state profile of a donor-acceptor polymer. The essential theoretical background of the calculation is briefly discussed in the section below.

3.4.1 Time dependent formalism

The intensity of a Raman transition from an initial vibrational state $|i\rangle$ to a final vibrational state $|f\rangle$ at incident energy E_L is determined by the Raman cross section $\sigma_{i\to f}$ (in area units) through the relation:

$$P_{i\to f} = I\sigma_{i\to f}(E_L) \qquad (3.5)$$

where $P_{i\to f}$ is the total power of the scattered photon and I is the incident photon flux (photons area^{-1} s^{-1}). The Raman cross section can be derived from second-order perturbation theory:

$$\sigma_{i\to f}(E_L) = \frac{8\pi e^4 {E_s}^3 E_L}{9\hbar^6 c^4}\left|a_{i\to f}(E_L)\right|^2 \qquad (3.6)$$

From the above expression the central quantity is the Raman polarizability tensor $a_{i\to f}(E_L)$, E_L and E_s are the incident and scattered photon energies respectively (in cm^{-1}) and c is the speed of light.

In the time-dependent perspective, the Raman polarizability $a_{i\to f}(E_L)$ can be written as a half Fourier transform of the (time-dependent) overlap between the final state $|f\rangle$ and the initial state $|i\rangle$ propagated under the influence of the excited-state Hamiltonian, $|i(t)\rangle$:

$$a_{i\to f}(E_L) = \frac{iM^2}{\hbar}\int_0^\infty \langle f \mid i_j(t)\rangle exp\left[\frac{i(E_L+\varepsilon_i)}{\hbar}\right] e^{-\Gamma t/\hbar}\mathrm{dt} \qquad (3.7)$$

where M (in Å) is the magnitude of the transition dipole moment evaluated at the equilibrium nuclear geometry, ε_i is the energy of the initial vibrational state and Γ is the homogeneous linewidth. Then the expression for the RR cross section (assuming a single dipole-allowed transition) becomes:

$$\sigma_{i\to f}(E_L) = \frac{8\pi e^4 {E_s}^3 E_L M^4}{9\hbar^6 c^4}\int \partial\, E_{00} H(E_{00})\left|\int_0^\infty \langle f \mid i_j(t)\rangle \exp\left(\frac{i(E_L+\varepsilon_i)t}{\hbar}\right)\mathrm{D(t)}dt\right|^2 \qquad (3.8)$$

In the above equation E_{00} is the energy difference between the ν = 0 vibrational state in the ground and excited electronic state and H(E_{00}) is the contribution of inhomogeneous broadening. The Gaussian function D(t) = $e^{-\frac{\Gamma^2 t^2}{\hbar^2}}$ is the expression from which homogeneous broadening Γ is extracted.

The integrated area under each vibrational peak in an experimental RR spectrum is proportional to the Raman cross section for the corresponding transition between the initial ($|i\rangle$) and final ($|f\rangle$) state. The plot of the cross sections of the possible Raman transitions as a function of excitation frequency is called Raman excitation profile (REP).

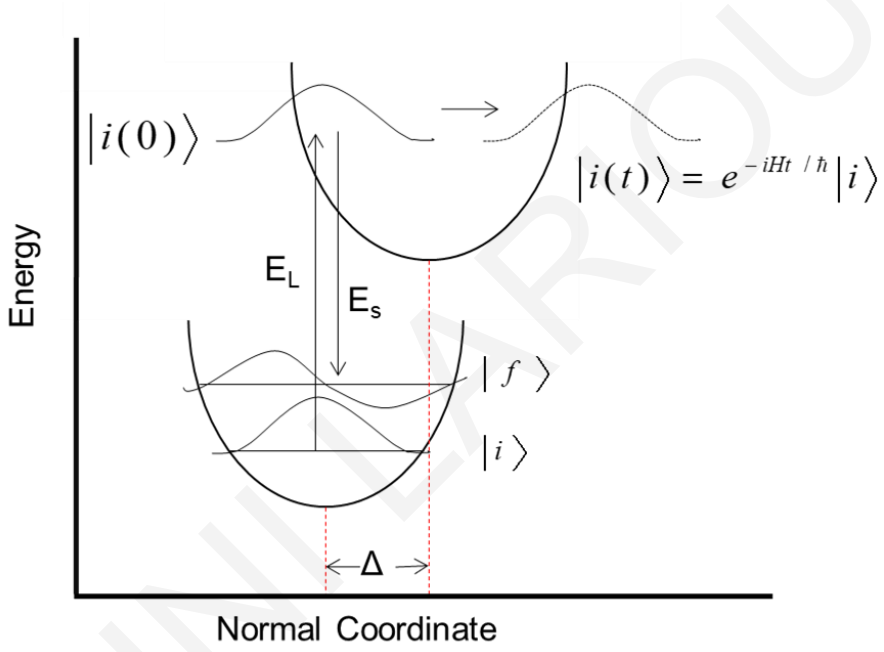

Figure 3.6: *Schematic representation of one-dimentional, time-dependent picture of RR scattering for a bound excited state surface. Δ is the displacement of the excited state potential well from the equilibrium geometry.*

Respectively, a similar time-dependent expression can be obtained for the optical absorption cross section:

$$\sigma_A(E_L) = \frac{4\pi e^2 E_L}{6\hbar^2 cn} \int_{-\infty}^{\infty} dE_{00} H(E_{00}) \times \left[\int_{-\infty}^{\infty} M^2 \langle i | \, i_j(t)\rangle exp \frac{i(E_L + \varepsilon_i)t}{\hbar} \mathrm{D(t)} dt\right] \quad (3.9)$$

where $\langle i|i_j(t)\rangle$ is the time-dependent overlap of the initial ground vibrational state with the same state propagating on the excited state j potential energy surface and "n" is the solvent index of refraction.[18]

The above expressions for the RR and absorption cross sections share the same excited-state parameters. This enables the simultaneous modelling of the experimental absorption

spectrum and Raman excitation profiles of multiple modes to obtain a complete and accurate picture of the potential energy surfaces of the studied material.

3.4.2 Application of RRIA in donor-acceptor systems

The photo-induced charge transfer in conjugated polymer donor/acceptor (D/A) systems occurs on similar timescales as vibrational dynamics (<100fs), indicating the potential of RRIA approaches to unravel excited state geometry changes. In addition, the rate constant of electron-transfer reactions (in the non-adiabatic limit), κ_{et}, can be described in the form of a Fermi Golden Rule expression:

$$\kappa_{et} = (2\pi/\hbar)|V|^2 FC \qquad (3.10)$$

where V is the electronic coupling matrix element and FC is the vibrational term which is the thermally weighted sum of Franck-Condon factors, containing the dependence on the density of states and total nuclear reorganization energy λ.[19,20] Reorganisation energy is the energy cost due to the geometry disruption of the nuclei from the equilibrium position during the charge transfer state, which can be further divided into contributions from individual vibrations, usually referred to as "mode-specific" reorganisation energy λ_j.[21] This important parameter is an indirect indication of the relative time before the wavepacket amplitude is completely damped and it depends directly on the excited state vibrational displacements, Δ_j, through the relation:

$$\lambda_{j=} \left(\frac{\omega_e^2}{\omega_g}\right)\frac{\Delta_j^2}{2} \qquad (3.11)$$

where ω_e and ω_g are the frequencies of the excited and ground state, respectively. As RR spectroscopy provides detailed information on the intra-molecular modes that contribute to the charge transfer it becomes an attractive technique for the study of such processes and has been employed for the study of charge transfer (CT) transitions of organic noncovalent,[19] and covalent[20] donor-acceptor complexes to elucidate the relation between structure and excited state vibrational displacements.

Adam Wise with John Grey have performed RRIA in conjugated polymers, specifically in poly(2-methoxy-5-(3´-7´ -dimethyloctyloxy)-1,4-phenylenevinylene) (MDMO-PPV) and small molecule acceptors (dinitrofluorenone (DNF) and dichloro-dicyano-benzoquinone (DDQ)) blend, to study interfacial excited state structural distortions, and determine vibrational mode-specific displacements of CT transitions.[22] Another recent example, is the study of the prototypical P3HT/PCBM blend to extract vibrational displacements and

dynamics.[23] This study, considered separately P3HT aggregated and amorphous chains, which have their own characteristic optical transitions; and showed that Raman excitation profiles of aggregated forms demonstrates different (larger) RR scattering cross section compared to amorphous forms, implying longer coherence times, consistent with the higher order of these regions.

References

(1) Raman, C. V.; Krishnan, K. S. A New Type of Secondary Radiation. *Nature* **1928**, *121* (3048), 501–502.

(2) Smith, E.; Dent, G. *Modern Raman Spectroscopy - A Practical Approach*; Wiley, 2005. https://doi.org/10.1002/0470011831.

(3) Raptis, Y. *Raman Spectroscopy Lab Notes for the course "Material's Characterisation Methods";* National Technical University of Athens, 2016.

(4) Das, R. S.; Agrawal, Y. K. Raman Spectroscopy: Recent Advancements, Techniques and Applications. *Vib. Spectrosc.* **2011**, *57* (2), 163–176. https://doi.org/10.1016/j.vibspec.2011.08.003.

(5) Ru, E. Le; Etchegoin, P. *Principles of Surface-Enhanced Raman Spectroscopy*; Elsevier B.V., 2009. https://doi.org/10.1192/bjp.112.483.211-a.

(6) Ferraro, J. R.; Nakamoto, K.; Brown, C. W. *Introductory Raman Spectroscopy*, 2nd ed.; Elsevier, 2003. https://doi.org/10.1016/S0304-0208(05)80002-7.

(7) Myers, A. B.; Mathies, R. A. *Biological Applications of Raman Spectroscopy*; John Wiley & Sons, 1987.

(8) Wood, S.; Hollis, J. R.; Kim, J.-S. Raman Spectroscopy as an Advanced Structural Nanoprobe for Conjugated Molecular Semiconductors. *J. Phys. D. Appl. Phys.* **2017**, *50* (7). https://doi.org/https://doi.org/10.1088/1361-6463/50/7/073001.

(9) Fleischmann, M.; Hendra, P. J.; McQuillan, A. J. Raman Spectra of Pyridine Adsorbed at a Silver Electrode. *Chem. Phys. Lett.* **1974**, *26* (2), 163–166. https://doi.org/10.1016/0009-2614(74)85388-1.

(10) Evan J. Blackie, Eric C. Le Ru, and P. G. E. Single-Molecule Surface-Enhanced Raman Spectroscopy of Nonresonant Molecules. *J. Am. Chem. Soc.* **2009**, *131* (40), 14466–14472. https://doi.org/10.1021/ja905319w.

(11) Katrin Kneipp, Yang Wang, Harald Kneipp, Lev T. Perelman, Irving Itzkan, Ramachandra R. Dasari, and M. S. F. Single Molecule Detection Using Surface-Enhanced Raman Scattering (SERS). *Phys. Rev. Lett.* **1997**, *78* (9), 1667–1670.

(12) Moskovits, M. Surface-Enhanced Raman Spectroscopy: A Brief Retrospective. *J. Raman Spectrosc.* **2005**, *36* (6–7), 485–496. https://doi.org/10.1002/jrs.1362.

(13) Kelly, K. L.; Coronado, E.; Zhao, L. L.; Schatz, G. C. The Optical Properties of Metal Nanoparticles: The Influence of Size, Shape, and Dielectric Environment. *J. Phys. Chem. B* **2003**, *107* (3), 668–677. https://doi.org/10.1021/jp026731y.

(14) Janesko, B. G.; Scuseria, G. E. Surface Enhanced Raman Optical Activity of Molecules on Orientationally Averaged Substrates: Theory of Electromagnetic

Effects. *J. Chem. Phys.* **2006**, *125* (12). https://doi.org/10.1063/1.2345368.

(15) Hossain, M. K.; Ozaki, Y. Surface-Enhanced Raman Scattering: Facts and Inline Trends Mohammad. *Curr. Sci.* **2009**, *97* (2), 192–201.

(16) Albrecht, A. C.; Hutley, M. C. On the Dependence of Vibrational Roman Intensity on the Wavelength of Incident Light. *J. Chem. Phys.* **1971**, *55* (9), 4438–4443. https://doi.org/10.1063/1.1676771.

(17) Lee, S. Y.; Heller, E. J. Time-Dependent Theory of Raman Scattering. *J. Chem. Phys.* **1979**, *71* (12), 4777–4788. https://doi.org/10.1063/1.438316.

(18) Vezie, M. S.; Few, S.; Meager, I.; Pieridou, G.; Dörling, B.; Ashraf, R. S.; Goñi, A. R.; Bronstein, H.; McCulloch, I.; Hayes, S. C.; et al. Exploring the Origin of High Optical Absorption in Conjugated Polymers. *Nat. Mater.* **2016**, *15* (7), 746–753. https://doi.org/10.1038/nmat4645.

(19) Market, F.; Myers, A. B.; Ferris, N. S.; Gould, I. R. Mode-Specific Vibrational Reorganization Energies Accompanying Photoinduced Electron Transfer in the Hexamethylbenzene/Tetracyanoethylene Charge-Transfer Complex. *J. Am. Chem. Soc.* **1992**, *114* (15), 6208–6219. https://doi.org/10.1021/ja00041a045.

(20) Lilichenko, M.; Tittelbach-Helmrich, D.; Verhoeven, J. W.; Gould, I. R.; Myers, A. B. Resonance Raman Intensity Analysis of a Dicyanovinyl-Azaadamantane: Mode-Specific Reorganization Energies for Charge-Transfer and Locally-Excited States. *J. Chem. Phys.* **1998**, *109* (24), 10958–10969. https://doi.org/10.1063/1.477792.

(21) Myers, A. B. Resonance Raman Intensities and Charge-Transfer Reorganization Energies. *Chem. Rev.* **1996**, *96* (3), 911–926. https://doi.org/10.1021/cr950249c.

(22) Wise, A. J.; Grey, J. K. Resonance Raman Studies of Excited State Structural Displacements of Conjugated Polymers in Donor/acceptor Charge Transfer Complexes. *Phys. Chem. Chem. Phys.* **2012**, *14* (32), 11273–11276. https://doi.org/10.1039/c2cp41748k.

(23) Gao, J.; Grey, J. K. Resonance Raman Overtones Reveal Vibrational Displacements and Dynamics of Crystalline and Amorphous poly(3-Hexylthiophene) Chains in Fullerene Blends. *J. Chem. Phys.* **2013**, *139* (4). https://doi.org/10.1063/1.4815819.

CHAPTER 4

Experimental and computational methods

This chapter is an introduction to the experimental part of this doctoral dissertation providing details on the experimental and computational methods employed, namely the Raman spectroscopy experiments and resonance Raman intensity analysis (RRIA). Examined materials were received from collaborators within the INFORM network and will be briefly outlined here as well.[1–3]

4.1 Materials

4.1.1 P3HT and derivatives

Regio-regular poly(3-hexylthiophene) (P3HT) was obtained from Dr. James Bannock and Prof. John de Mello at Imperial College London. It was synthesized using a flow-synthesis method[4] that reduces inter-batch variation, and has a weight-averaged molecular weight (M_w) of 100 kg mol^{-1}, dispersity of 1.5, and 99%+ regioregularity. Regioregular poly(3-(2'-ethyl)-hexylthiophene) (P3EHT) was also obtained from Dr. James Bannock and Prof. John de Mello.[1] Poly(ethylene oxide) (M_w = 900 kg mol^{-1}), poly(tetrahydrofuran) (PTHF) (M_w = 3 kg mol^{-1}) and isotactic poly(propylene) (PP) (M_w = 14 kg mol^{-1}) were obtained from Sigma-Aldrich and used as received. Proprietary Low Density Polyethylene (LDPE) with trade name 'Affinity' was obtained from Dow Chemical. P3HT-b-PEO was synthesized by Dr. Harikrishna Erothu and Prof. Paul D. Topham at Aston University. P3BEOT was synthesized by Dr. Olivier Dautel at the Charles Gerhart Institute of Montpellier. It has a M_w of 23 kg mol^{-1}, polydispersity index of 1.4, and 85%+ regioregularity.

Samples were prepared by Dr. Matthew J. Dyson by dissolving polymers (total polymer content 10 mg ml^{-1}) in $CHCl_3$. Solutions were magnetically stirred at 50 ^oC for 3 hours to ensure complete dissolution and homogeneity, before wire-bar coating 15μL of solution onto a 12 mm × 12 mm fused silica substrate. Neat films were processed at room temperature (~23^oC), with solvent allowed to evaporate freely. Blends with PEO were cast at 10^oC (covered with a petri dish to reduce evaporation rate), 15 ^oC, 20 ^oC and 30^oC.

Humidity treatment comprised leaving the sample under a petri dish overnight with a paper tissue soaked in water, resulting in a saturated atmosphere.

4.1.2 P3HT:PCBM[60]

All materials in this study were commercially available and used as purchased without any further purifications. Batches (employed for the polymorph distribution study) of high-M_n P3HT (Mn = 29.6 kDa, RR = 95.7%) batch EE101702) and low-M_n P3HT (Mn = 18.3 kDa, RR = 95.2%) batch EE97802) were purchased from Merck, while PCBM [60] was purchased from Solenne BV.

Samples with different P3HT polymorph distribution were prepared by the group of Prof. P.E. Keivanidis at Cyprus University of Technology.[2] Two types of photoactive layers were prepared based on P3HT:PCBM[60] composites (1:1) with different molecular weight of P3HT. The films were developed by spin-coating of the corresponding P3HT:PCBM[60] solutions, as prepared in chlorobenzene solvent with a concentration of 13 mg/mL with respect to P3HT mass. Thin films of high and low M_n-based P3HT:PCBM[60] were deposited onto solvent cleaned Quartz (Spectrosil 2000, UQG Ltd) or glass/ITO/PEDOT:PSS substrates. Thermal annealing of the films was at 140^{o}C for 15'.

4.1.3 P3HT:PCBM

All materials were commercially available and used as purchased without any further purifications. P3HT employed for the organic-metal interface study (4002-EE, regioregularity 91–94%) was purchased from Rieke Metals; PCBM from Nano-C, Hexa(ethyleneglycol)-dithiol (HEG-DT) M_w = 314.5 g mol^{-1} and 1,4-benzenedimethanethiol (BDMT) M_w = 170.3 g mol^{-1} were purchased from Sigma Aldrich.

Blend samples with additives as well as P3HT:PCBM reference blends, were prepared by Dr. Basel Shamieh at Technion-Israel Institute of Technology.[3] Defined amounts of either HEG-DT or BDMT were dissolved in 1,2-dichlorobenzene (DCB) and added to a P3HT:PCBM (40 : 40 mg ml^{-1}) solution in DCB to obtain a series of P3HT:PCBM (20:20 mg ml^{-1}) solutions with 0 and 2 mg ml^{-1} of each additive. Samples specially prepared for SERRS experiments consist of a 3 nm thick silver patch thermally deposited on a glass substrate and topped with active layers of P3HT (20 mg ml^{-1}), P3HT:PCBM (20 : 20 mg ml^{-1}), P3HT:PCBM: additive (20 : 20 : 5 mg ml^{-1}), or a bilayer of concentrated additive topped with P3HT:PCBM (20 : 20 mg ml^{-1}). All active layers were spun at 1500 rpm for 20 seconds.

4.1.4 PCE11

High (83 kg mol^{-1}, PDI 2.1) and low (55 kg mol^{-1}, PDI 2.14) molecular weight (M_n) PffBT4T-2OD {poly[(5,6-difluoro-2,1,3-benzothiadiazol-4,7-diyl)-alt-(3,3´´´-di(2-octyldodecyl) 2,2´;5´,2´´;5´´, 2´´´-quaterthiophen- 5,5´´´-diyl)]} (PCE11) was purchased from Ossila. Samples were prepared by Dr. Giovanni M. Matrone at Imperial College London. PCE11 solutions were prepared by dissolving each polymer in o-DCB to a concentration of 20 $mg{\cdot}ml^{-1}$ and were magnetically stirred for 30' to ensure complete dissolution and homogeneity. Thin films were fabricated employing the wire-bar coating technique. The deposition temperature was 100^{o}C and the thickness was controlled by the deposition speed from **2** x 2 cm/s (s**2**) to **8** x 2 cm/s (s**8**) resulting in 50 nm and 200 nm thick films respectively.

4.2 Raman spectroscopy

4.2.1 Resonance Raman

Resonance Raman spectroscopy, which greatly enhances the scattering cross-section from resonant chromophores,[5] enables selective enhancement of specific electronic transitions or chromophores by tuning the excitation wavelength to the corresponding absorption. Three different excitation wavelengths were employed throughout this work to achieve these resonance conditions: 473 nm, 532 nm and 633 nm. CW lasers were employed for excitation at 473 nm (Ultralasers, 50 mW OEM DPSS Laser) and at 632.8 nm (HeNe laser, Thorlabs, 12 mW, HRR120).

The 532 nm excitation wavelength was generated from the second harmonic of a Q-switched Nd:YAG laser (PRO-230, 30Hz, Spectra Physics). The experimental setup is depicted in **Figures 4.1** and **4.2**. The Q-switched Nd:YAG laser is equipped with crystals to generate all harmonic frequencies (532, 355 and 266 nm). The laser beam is guided to a 1m stainless steel tube filled with H_2 under pressure of 1.5 bar (Raman shifter) and excites the H_2. The Stokes line ν_0-ν_m that corresponds to the only vibrational mode of the H_2 molecule (ν_m = 4155 cm^{-1}) is strong enough to act as a secondary radiation source exciting the second Stokes line ν_0-$2\nu_m$ and this the third etc. generating stokes and anti-Stokes frequencies. This stimulated Raman scattering allows the flexibility to choose from a wide range of wavelengths between 200 and 740 nm depending on the specific needs.

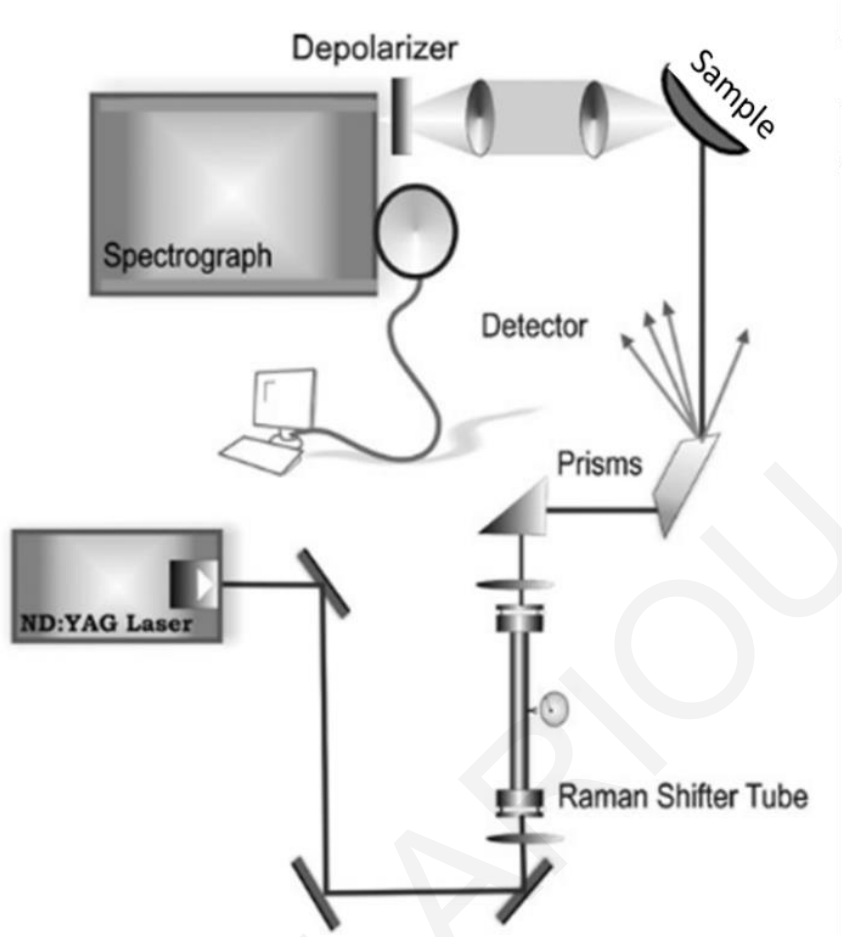

Figure 4.1: *Experimental setup for the 532 nm excitation.*

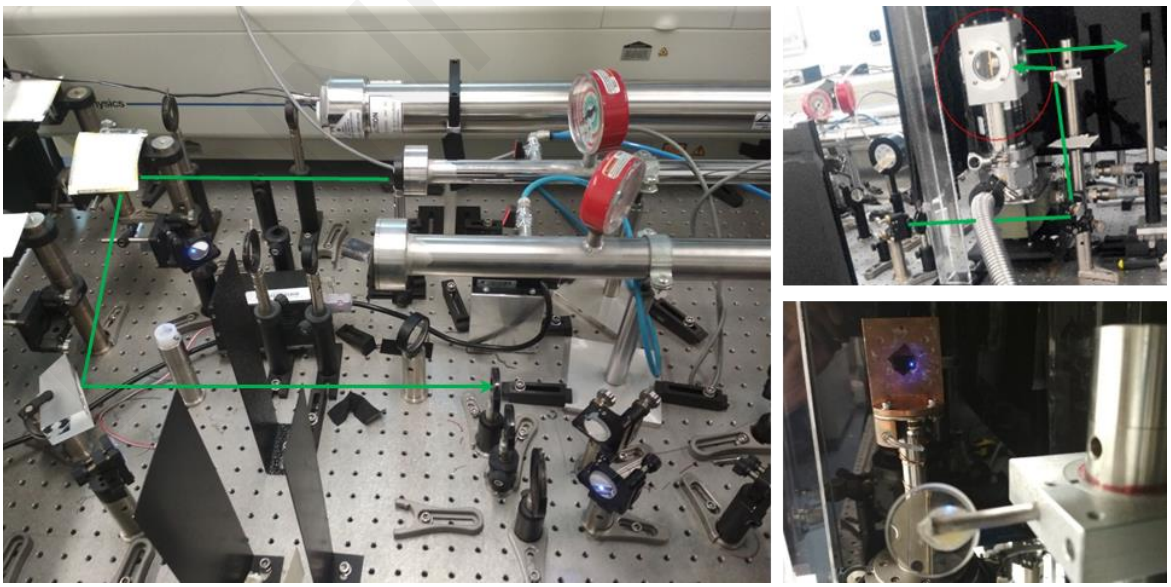

Figure 4.2*: Parts of the actual setup depicting the laser beam exiting the Raman shifter tube, passing through the prism (left) and guided to the sample through mirrors and lenses. (Top right) Sample is kept inside the vacuum chamber (placed on a copper cold finger, bottom right) and the backscattered light is directed towards the spectrograph.*

Then, the light is guided through a prism that separates the generated wavelengths and then, the beam is guided through lenses and mirrors to the sample. The scattered light is collected in a backscattering geometry and delivered to a 0.75 m focal-length Czerny-Turner spectrograph (SpectraPro, SP2760i, Princeton Instruments), equipped with a 1200 grooves mm^{-1} UV-enhanced holographic grating.

All measurements were acquired under vacuum in a cryostat (CCS-150, Janis), employing low excitation powers (0.4 mW for 473 nm, 0.1 mW for 532 nm and 0.8 mW for 632 nm) to minimise sample degradation and avoid photo-oxidation. The cryostat was placed on a translation stage for a periodic translation of the sample so that a fresh part of the sample was exposed to the light. The scattered light was collected in the spectrograph described above. The slit width was set to 100 μm providing ~5 cm^{-1} spectral resolution at 473 and 532 nm, and 2 cm^{-1} spectral resolution at 632 nm. Scattered light was detected by a LN_2-cooled 2048 x 512 pixel, back-illuminated UV-enhanced CCD detector (Spec10:2KBUV/LN, Princeton Instruments). For 633 nm excitation, the scattered light was collected by a LN_2-cooled 1340x100 pixel, back-illuminated deep-depletion CCD detector (Pylon:100BR Excelon, Princeton Instruments) with enhanced sensitivity in the NIR and reduced etaloning effects. Each spectrum presented here is the accumulation of at least 7 × 10 min spectra. Cyclohexane was employed for frequency calibration of the spectra. Resonance Raman spectra where analysed using Matlab and ORIGIN, while IgorPRO 8 Multipeakfit, was employed for fitting part of the data.

4.2.2 Surface enhanced resonance Raman spectroscopy (SERRS)

The samples were excited at 473 nm with a CW diode laser (Ultralasers, 50 mW OEM DPSS Laser) and measured under vacuum, employing low excitation powers (0.8 mW). The films were placed such that the excitation beam light passes first through the substrate, facilitating access to the silver/polymer interface. Resonance Raman spectra were also obtained for comparison by exciting the sample again through the substrate but accessing areas without silver. Raman and SERS measurements were performed under the exact same experimental conditions. The Raman scattered light was collected in a 135º backscattering geometry and delivered to the spectrograph (described above). Cyclohexane was employed for frequency calibration of the spectra.

4.2.3 Temperature-Dependent Resonance Raman Spectroscopy

The samples were excited at two different wavelengths employing the CW laser (described above) for 632.8 nm and the second harmonic of the Nd:YAG laser at 532 nm. All measurements were performed under vacuum, employing low excitation powers (0.4 mW for 473 nm, 0.1 mW for 532 nm and 0.8 mW for 632 nm). Sample cooling (down to 20K) was achieved by a sample-in-vacuum closed-cycle cryostat (CCS-150, JANIS), where the sample was placed on a copper cold finger (see **figure 4.2**). Each spectrum is the accumulation of at least 3 10-min spectra and all temperature steps where performed on the same day. Cyclohexane was employed as a standard solvent for frequency calibration of the spectra and data analysis was performed in Matlab and ORIGIN.

4.3 Resonance Raman Intensity Analysis

Resonance Raman cross sections (σ_R) were determined for the five most intense bands from the RR spectra (at 532 nm excitation) of PCE11 located at 425, 851, 1328, 1441 and 1532 cm^{-1} and for temperatures between 20 and 298 K. In the calculation of the σ_R the 801 cm^{-1} mode of cyclohexane was used as an external standard. The intensities of the Raman bands were corrected for self-absorption according to the equation:[6]

$$\frac{I_{Sample,corrected}}{I_{Reference,corrected}} = \frac{I_s\, c_r(\varepsilon_s+\varepsilon_0)}{I_r c_s(\varepsilon_r+\varepsilon_0)} \qquad (4.1)$$

where c is the concentration of the reference (c_r) or sample (c_s) and ε is the extinction coefficient of the sample at the reference (ε_r), sample peak (ε_s) and laser line wavelength (ε_0). As measurements in this study were performed on films, the definition of the polymer concentration is not possible, thus the calculation will be based on scaled absorption and relative RR cross sections to the 1441 cm^{-1} band of the thiophene. The intensity of the bands was determined from the area under the curve after fitting the bands to Gaussian peaks using Origin.

RR cross sections as a function of excitation wavelength were then determined using the following expression:

$$\sigma_{R(\nu_i)} = \frac{I_{\nu_i} C_{cxn}\left(\frac{1+2\rho}{1+\rho}\right)_{pce11}}{I_{cxn} C_{pce11}\left(\frac{1+2\rho}{1+\rho}\right)_{cxn}} \sigma_{Rcxn} \qquad (4.2)$$

where σ_R is the Raman scattering cross section of mode v_i, ρ is the depolarization ratio, C is the concentration, which again for the PCE11 sample was not defined so determination of relative RR cross sections was possible employing a common scaling factor. I_{vi} and I_{cxn} are the experimentally determined areas for the mode of interest and the external standard, respectively. The absolute Raman cross section and depolarization ratio for the 801 cm^{-1} mode of cyclohexane were previously measured or obtained from an A-term fit to the experimental cross sections (σ_R(532 nm) = 6.68×10^{-13} cm^2, and ρ = 0.09).[7,8] The depolarization ratios for the modes of PCE11 were taken as 1/3.

Simultaneous modelling of absorption and relative RR cross sections was performed according to Resonance Raman Intensity Analysis (RRIA), a theoretical tool based on the time-dependent formalism for absorption and RR scattering. [9–11]

The expression (derived from second order perturbation theory) employed for the calculation of the RR cross section is the following assuming a single dipole-allowed transition:

$$\sigma_{i\to f}(\mathrm{EL}) = \frac{8\pi e^4 {E_s}^3 E_L M^4}{9\hbar^6 c^4} \int \partial\, E_{00} H(E_{00}) \left| \int_0^\infty \langle f | i_j(t) \rangle \exp\left(\frac{i(E_L + \varepsilon_i)t}{\hbar}\right) \mathrm{D(t)} dt \right|^2 \quad (4.3)$$

In the above equation E_s and E_L are the energies of scattered and incident photon, respectively, M is the magnitude of the transition dipole moment for the electronic transition. E_{00} is the energy difference between the v = 0 vibrational states in the ground and excited electronic state and H(E_{00}) is the contribution of inhomogeneous broadening. The Gaussian function D(t) = $e^{-\frac{\Gamma^2 t^2}{\hbar^2}}$ is the expression from which homogeneous broadening Γ is extracted. The expression $\langle f|i_j(t)\rangle$ represents the time-dependent overlap of the final state in the scattering process with the initial state propagating under the influence of the excited state Hamiltonian in state j.

Respectively, the expression for the absorption cross section is:

$$\sigma_A(E_L) = \frac{4\pi e^2 E_L}{6\hbar^2 cn} \int_{-\infty}^{\infty} dE_{00} H(E_{00}) \times \left[\int_{-\infty}^{\infty} M^2 \langle i \mid i_j(t) \rangle \exp\left[\frac{i(E_L + \varepsilon_i)t}{\hbar}\right] \mathrm{D(t)} dt \right] \quad (4.4)$$

where $\langle i|i_j(t)\rangle$ is the time-dependent overlap of the initial ground vibrational state with the same state propagating on the excited state j potential energy surface. "n" is the solvent index of refraction (incorporated in the scaling factor, as this number cannot be extracted for films). [9,11] The initial values for the displacements Δ_i of the i normal coordinates were obtained by

the integrated area A under the corresponding RR band relative to that of the thiophene's C=C stretch at 1441 cm^{-1} (through the relation $\frac{I_i}{I_{1441}} = \frac{\Delta_i^2}{\Delta_{1441}^2}$) and then were iteratively optimized during fitting procedure. The modelling was performed employing Matlab.

4.4 DFT Calculations

Electronic structure and molecular conformations of polymer chains ranging in size from the monomer to the hexamer have been modelled at the density functional theory (DFT) level using the B3LYP/6-31(d, p) functional/basis set. To support experimental Raman spectra, Raman frequency calculation have been modelled at the same level of theory. Raman calculation depending on the torsion angles were performed at DFT level, in which all torsion angles were increased simultaneously from 0° to 25° by step 5° and they are frozen during the calculations.

4.5 Absorption

Absorption spectra were acquired at room temperature using a Shimadzu UV-2600 spectrometer, equipped with an integrating sphere. Transmission *T* and reflection *R* spectra include scattering from the rough, inhomogeneous, phase-separated blend films. Presented absorption spectra are *100-T-R*, giving absorption as a percentage; this distinguishes the intrinsic absorption from losses due to reflection and scattering.

4.6 Photoluminescence (PL)

Photoluminescence (PL) spectra were acquired using a helium filled gas cooled closed-cycle cryostat, with emitted light collected perpendicular to excitation (with a monochromated Fianium supercontinuum laser) and focused into a 100 μm diameter optical fibre after passing through a long-pass filter to attenuate incident beam reflections. An Andor SR-163 spectrometer was then used to disperse emitted light onto a CCD (Andor i-Dus). Spectra had a constant background subtracted, before correcting with a calibration file derived from a known light source (Ocean Optics Halogen Light Source HL-2000) to account for detector response. Site-selective PL spectra (Figure S3) were acquired at 10 K in 10 nm increments of λex, with low pass filters at 550, 600 and 650 nm used to block scattered excitation light. Total luminescence maps were acquired using the same configuration, with relative intensity corrected for excitation intensity variation measured using a beam splitter and power meter (Thorlabs PM2000).

4.7 Time delayed collection field characterisation

Custom-built TDCF setup uses the second harmonic (532 nm) of an actively Q-switched sub-ns Nd:YVO4 laser (INNOLAS picolo AOT) operating at 5 kHz as excitation. To minimize the RC response time, a small device area of 1 mm² is used. The samples were measured under dynamic vacuum conditions to avoid any degradation. A Keysight S1160A functional generator was used to provide the pre-bias and extraction bias, while a Keysight four channel digital oscilloscope was used to measure the current response of the device.

4.8 Transient absorption

The TA spectra were acquired using a home-built setup comprised of a Coherent Legend Duo regenerative amplifier delivering 100 fs pulses of 4.2 mJ at 3 kHz repetition rate at a central wavelength of 800 nm. The fundamental output from the oscillator was decomposed into two beams and applied to a couple of TOPAS prime, an optical parametric amplifier, in order to generate the broad spectral tunability. TOPAS 1 served as the excitation pulse beam and was routed through a retroreflector mounted on a mechanical delay stage, passing twice to obtain a delay line of approximately 10 ns and was focused onto the sample. In parallel to this, a white light continuum was generated by pumping a sapphire crystal with 1300 nm from the second TOPAS. The delayed white light acted as probe beam and was focused on the sample so a spatial overlap between the pump and probe beam was obtained. The transmitted light through the sample was collected, collimated and focused onto a detector, and consequently further processed on a computer to record the acquired transient spectra and the associated charge carrier dynamics. Long delay measurements, in the μs time range were also performed, by employing the electronic delay provided by a delay generator (Stanford Research Systems DG535) to cover a range of 300 μs and by using a Q-switched Nd:YVO4 Innolas picolo AOT sub nano second amplifier, frequency doubled, with an output of 532 nm. The actual excitation was executed at 532 nm for both the long and short delay. Furthermore, the pump fluence was varied from 1.3, 3, 6, 9 and 19 μJ/cm^2 for the short delay measurements. For the latter the laser fluence varied between 0.8 – 12 μJ/cm^2 in order to discriminate geminate and non-geminate charge recombination processes. All measurements were performed at room temperature and the samples were kept under dynamic vacuum with pressure lower than 10^{-4} mbar.

References

(1) Dyson, M. J.; Lariou, E.; Martin, J.; Li, R.; Erothu, H.; Wantz, G.; Topham, P. D.; Dautel, O. J.; Hayes, S. C.; Stavrinou, P. N.; et al. Managing Local Order in Conjugated Polymer Blends via Polarity Contrast. *Chem. Mater.* **2019**, *31* (17), 6540–6547. https://doi.org/10.1021/acs.chemmater.8b05259.

(2) Keivanidis, P. E.; Khan, J. I.; Katzenmeier, L.; Kan, Z.; Limbu, S.; Constantinou, M.; Lariou, E.; Constantinides, G.; Hayes, S. C.; Kim, J. S.; et al. Impact of Structural Polymorphs on Charge Collection and Nongeminate Recombination in Organic Photovoltaic Devices. *J. Phys. Chem. C* **2018**, *122* (51), 29141–29149. https://doi.org/10.1021/acs.jpcc.8b09825.

(3) Shamieh, B.; Anselmo, A. S.; Vogel, U.; Lariou, E.; Hayes, S. C.; Koch, N.; Frey, G. L. Correlating the Effective Work Function at Buried Organic/metal Interfaces with Organic Solar Cell Characteristics. *J. Mater. Chem. C* **2018**, *6* (30), 8060–8068. https://doi.org/10.1039/c8tc02381f.

(4) Bannock, J. H.; Krishnadasan, S. H.; Nightingale, A. M.; Yau, C. P.; Khaw, K.; Burkitt, D.; Halls, J. J. M.; Heeney, M.; De Mello, J. C. Continuous Synthesis of Device-Grade Semiconducting Polymers in Droplet-Based Microreactors. *Adv. Funct. Mater.* **2013**, *23* (17), 2123–2129. https://doi.org/10.1002/adfm.201203014.

(5) Wise, A. J.; Precit, M. R.; Papp, A. M.; Grey, J. K. Effect of Fullerene Intercalation on the Conformation and Packing of Poly-(2-Methoxy-5-(3′-7′-Dimethyloctyloxy)-1,4-Phenylenevinylene). *ACS Appl. Mater. Interfaces* **2011**, *3* (8), 3011–3019. https://doi.org/10.1021/am200508n.

(6) Bailey, S. E.; Cohan, J. S.; Zink, J. I. Interference Effects of Multiple Excited States in the Resonance Raman Spectroscopy of CpCoCOD. *J. Phys. Chem. B* **2000**, *104* (46), 10743–10749.

(7) Trulson, M. O.; Mathies, R. A. Raman Cross Section Measurements in the Visible and Ultraviolet Using an Integrating Cavity: Application to Benzene, Cyclohexane, and Cacodylate. *J. Chem. Phys.* **1986**, *84* (4), 2068–2074. https://doi.org/10.1063/1.450415.

(8) Foster, C. E., Barham, B. P. & Reid, P. J. Resonance Raman Intensity Analysis of Chlorine Dioxide Dissolved in Chloroform : The Role of Nonpolar Solvationo Title. *J.Chem.Phys.* **2001**, No. 114, 8492–8504.

(9) Vezie, M. S.; Few, S.; Meager, I.; Pieridou, G.; Dörling, B.; Ashraf, R. S.; Goñi, A. R.; Bronstein, H.; McCulloch, I.; Hayes, S. C.; et al. Exploring the Origin of High Optical Absorption in Conjugated Polymers. *Nat. Mater.* **2016**, *15* (7), 746–753. https://doi.org/10.1038/nmat4645.

(10) Myers, A. B.; Mathies, R. A. Resonance Raman Intensities: A Probe of Excited-State Structure and Dynamics. *Biological Applications of Raman Spectroscopy*. 1987, pp 1–58.

(11) Hayes, S. C.; Silva, C. Analysis of the Excited-State Absorption Spectral Bandshape of Oligofluorenes. *J. Chem. Phys.* **2010**, *132* (21). https://doi.org/10.1063/1.3432602.

CHAPTER 5

Controlling local ordering *via* polarity contrast

The impact of processing parameters on molecular conformation of organic semiconductors is a major subject of this doctoral dissertation and will be discussed extensively throughout the experimental part as an easy and cost effective strategy to achieve control of the local-ordering and potentially having a substantial effect on macroscopic properties. This chapter focuses on P3HT as a model system for understanding microscopic characteristics such as molecular ordering. P3HT is employed as a reference to explore some of its polar and non-polar derivatives. At the beginning we build on previous knowledge[1] investigating and quantifying the effect of commonly employed approaches on controlling local features, such as blending with additives and we will show that the molecular weight of both active material and additive as well as the casting conditions are key factors that should be judiciously considered. Later, in order to explore the effect of polarity contrast between the backbone and its environment, the synthesis of polar P3HT derivatives, (namely the diblock copolymer poly(3-hexylthiophene)-block-poly(ethylene oxide) (P3HT-b-PEO)[2] and the graft polymer poly[3-but(ethylene oxide)thiophene] (P3BEOT)), and non-polar (namely poly[3-(2'-ethyl)-hexylthiophene] (P3EHT)) was required (P3HT-b-PEO was synthesized by Dr.Harikrishna Erothu and Prof. Paul D. Topham at Aston University and P3BEOT was synthesized by Dr. Olivier Dautel at the Charles Gerhart Institute of Montpellier). The polarity-dependent compatibility between specific moieties is explored by combining these two previously distinct approaches –blending and chemical modification- to control the active material's chain conformation, packing and thus functionality. The question we strive to answer - utilizing the sensitivity of structural and optical properties of polythiophenes and their derivatives to backbone configuration[3,4]- is whether desirable macromolecular arrangements of polymeric semiconductors can be targeted by careful consideration of specific polarity-driven interactions between the semiconductor and the polymer 'additive'. Work presented on this chapter was a result of collaboration with the group of Prof. Natalie Stingelin from the Department of Materials, Imperial College London.[5]

5.1 Background

Nowadays a frequently used strategy to manipulate the local macromolecular arrangement and packing in organic semiconductors, is chemical substitution with side chains.[6–9] This can have a strong effect on contingent optoelectronic properties, such as charge-carrier transport[10] or absorption/emission features.[11,12] Originally, alkyl side chains were introduced to assist solubility and, processability in general,[13] while more recently polar side chains, have attracted interest due to their ability to render the base material more compatible with "green"[14] solvents such as water and simple alcohols.[15,16] The potential applications of polymer semiconductors substituted with polar side chains are not limited to OPVs and can be of interest for bioelectronics, where high biocompatibility is needed, for instance in the case of bio-integrated electronics and wearable devices,[17–19] or where mixed electron/ion conduction is required (*e.g.*, in electrochemical transistors used for biomimetic signal transduction, ion pumps, bioactive sensing elements). However, the steric bulk of non-conjugated side chains can inhibit backbone packing and aggregation, introducing undesirable torsional backbone disorder. Hence, alternative approaches to control structural features of polymer semiconductors have been investigated, including blending with a second component, such as a commodity plastic.[1,20,21] This has been shown to provide an elegant pathway to expand the functionality of the semiconductor, perhaps best exemplified by blends of prototypical poly(3-hexyl thiophene) (P3HT) with bulk insulating plastics such as poly(ethylene oxide) (PEO) that can be manipulated to display drastically different absorption behavior compared to the neat semiconductor. This difference was tentatively attributed to a change in the torsional backbone order of P3HT,[1] but the cause of this change was not further investigated. In contrast, blending P3HT with the insulating commodity polymer high-density polyethylene (HDPE) was found to affect notably neither the semiconductor's optical characteristics nor its charge transport features.[20] It led however to desirable improvements in the mechanical properties of organic devices, producing in certain scenarios stable architectures.[22] Other benefits of blending with electrically inert components are the reduction in the proportion of expensive active material while retaining functionality as well as providing a degree of self-encapsulation.[17,4] The discrepancy however, between the PEO vs. HDPE blends with P3HT, has so far remained elusive and this issue –together with the potential manipulation of the various interactions between them and other relevant systems- is going to be addressed within this chapter.

5.2 P3HT Absorption and Raman Spectral Interpretation

The absorption spectrum of a neat P3HT film is shown in **Fig.5.1** providing a first indication regarding the ordering of the molecule. The absorption band is broad, extending between ~400 nm and ~640 nm and it depicts the π to π* transition of the P3HT backbone. The absorption maximum is located around ~510 nm, exhibiting two weak shoulders around ~560 nm and ~610 nm associated with the 0-1 and 0-0 transitions, respectively. The relative intensity of these absorption shoulders can be described by the Spano model for aggregation,[4,23,24] suggesting a weakly-interacting H-like aggregate where the 0-0 optical transition is suppressed by the inter-chain coupling between π-π stacked chains. The 0-0/0-1 ratio is often employed as a measure of long-range organisation in P3HT[25] as it can vary from H to J-like aggregation depending on the magnitude of intra versus inter-chain excitonic coupling.

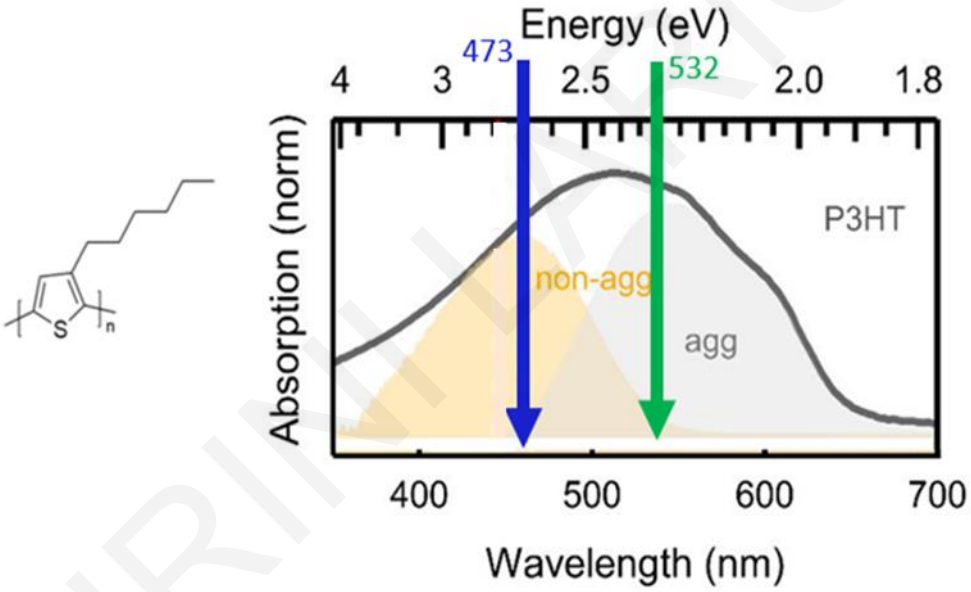

Figure 5.1: *Absorption spectrum of neat P3HT. A P3HT solution spectrum (beige shading), approximately corresponding to non-aggregated chains, is rescaled to fit the high energy side of the absorption. Subtracting this non-aggregated contribution leads to the aggregated contribution (grey shaded).*

The absorption spectrum constitutes our guide to decide Resonance Raman (RR) excitation wavelengths, because it provides information about the presence of particular chromophores within the absorption band that can selectively be excited. It is obvious from **Fig.5.1** and it has been shown previously[26] that shorter excitation wavelengths with higher energy, excite more strongly populations with larger optical band-gaps such as non-aggregated chromophores of shorter effective conjugation lengths. Respectively, longer excitation wavelengths are more strongly in resonance with chromophores of longer effective conjugation lengths which tend to form aggregates. This is depicted in **Fig.5.1** from the

deconvolution of the absorption band in the contribution of the solution spectrum, approximately corresponding to non-aggregated chains and the aggregated contribution resulting from subtraction of the solution phase.

Two excitation wavelengths were employed in this chapter for the study of P3HT and its derivatives: 473 nm, which is in resonance with the non-aggregated populations and 532 nm for effective probing of aggregated chromophores. The characteristic Raman spectrum of P3HT is shown in **Fig.5.2**, in the region between ~700 and ~1700 cm^{-1} under 473 nm excitation. Each peak corresponds to a vibrational mode of the atomic bonds of the molecule. The strongest modes, at 1445 cm^{-1} and 1381 cm^{-1}, have been assigned to the C=C and C-C symmetric in-plane stretching modes, respectively. These are the most sensitive to electron delocalisation and will be monitored and analysed in the next sections. Other less intense peaks present at 727, 1180 and 1208 cm^{-1}, are assigned to C-S-C deformation, C-C stretch and C-C, C-H bending modes, respectively. Those assignments as well as vibrational modes beyond this frequency range, based on existing literature,[26] are summarised in **Table 5.1**.

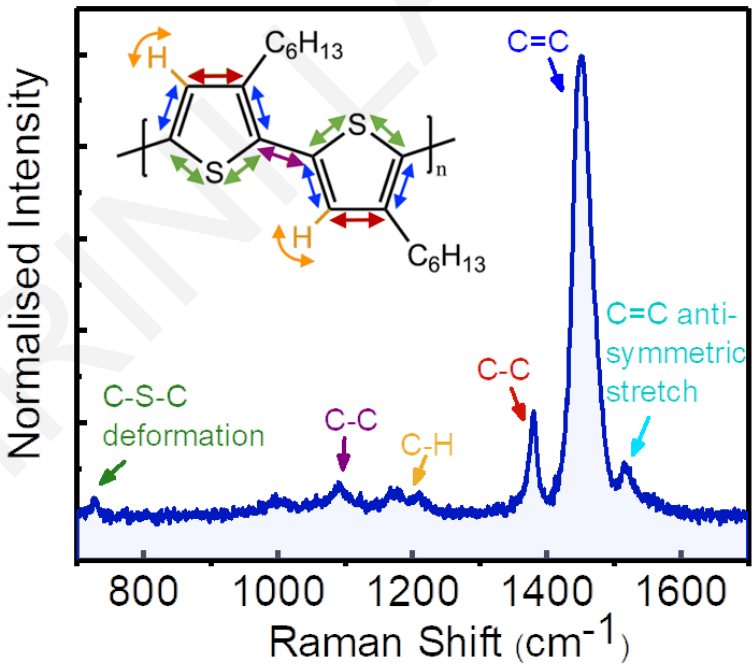

Figure 5.2*: Raman spectrum of neat P3HT film excited at 473 nm. Each peak corresponds to a different vibrational mode of the molecule, described by different colors. Arrows on the chemical structure (inset) depict the movement of the chemical bonds.*

Table 5.1*: Band assignment of P3HT vibrational modes*

Frequency (cm^{-1})	Mode description
727	C-S-C deformation
1095	C-C inter-ring stretch
1208	C-H bending and C-C inter-ring stretch
1380	C –C intra-ring stretch
1450	C = C symmetric stretch
1515	Cα = Cβ antisymmetric stretch
~2900–3000	C-H stretch

Focusing back on the dominant symmetric C=C stretching and the C-C intra-ring stretching modes, the degree of molecular order of the conjugated backbone can be quantified by monitoring variations in C=C peak location and the C-C/C=C peak area ratio as sensitive probes of aggregation and backbone planarity.[26,27] Lower conformational order increases π-electron density on the C=C bonds and this is reflected in Raman scattering by shifts of the C=C vibration to higher frequency. The C=C stretch band in P3HT varies significantly from an ideal Lorentzian line shape due to the broad FWHM, suggesting contributions from more than one species. It has been demonstrated[27] that it can be fitted considering contributions from aggregated chains centered ~1450 $cm^{-1}$and non-aggregated chains with center ~1470 cm^{-1} as depicted in **Fig.5.3.** The ratio $I_{C=C}^{agg}$ / $I_{C=C}^{non\text{-}agg}$ indicates their relative concentrations within a film, extending qualitatively the picture afforded from absorption spectroscopy. The two "extremes" of torsional order in P3HT (illustrated by the aggregated and non-aggregated components) are represented by regioregular (RR) and regiorandom (RRa) P3HT (chemical structures as shown in **Fig.5.3**).[28] Regioregularity refers to the percentage of head-to-tail coupling and has a remarkable influence on the polymer's structure and properties. The difference between RR and RRa-P3HT arise from the alkyl side-chains orientation, where head-to-tail coupling in the case of RR encourages π-π packing of the polymer chains, while tail-to-tail coupling (RRa) induces steric hindrance between the opposite-oriented side chains. However, despite RR and RRa-P3HT being often used as a reference to describe ordered and disordered conformations, it's worth noting that their chains are neither perfectly planar nor completely twisted in the solid state and different proportions of both conformations do exist.

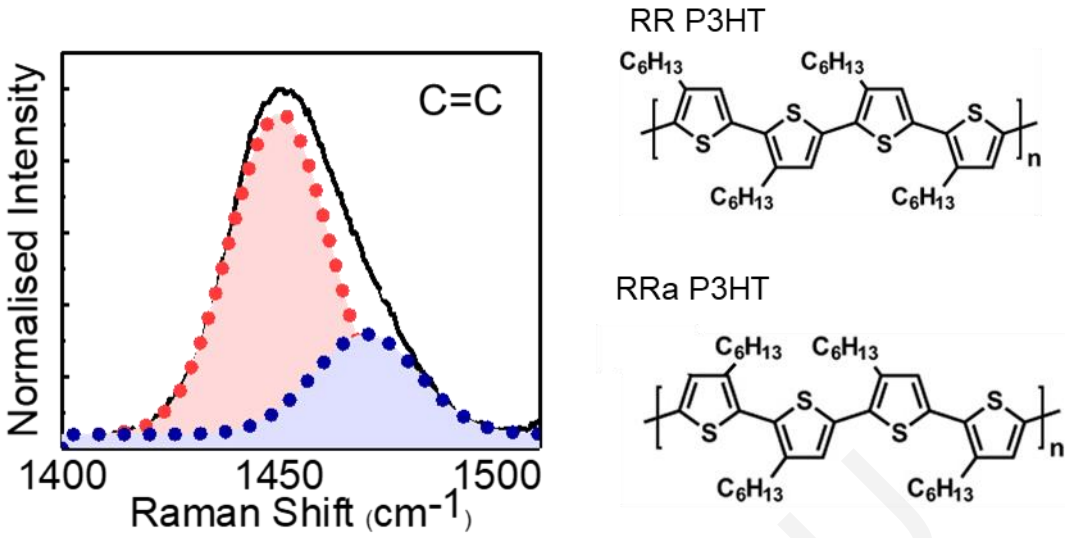

Figure 5.3*: The C=C symmetric stretch mode fitted with two Lorentzian functions showing the relative contributions of aggregated (red) and non-aggregated (blue) components (Left). Chemical structures of RR-P3HT and RRa-P3HT(Right).*

In conclusion, the tight connection between absorption and Resonance Raman can associate short to long-range order (crystallinity) and their combination will be employed throughout this chapter.

5.3 Results and discussion

5.3.1 Investigating Molecular weight dependence of P3HT:PEO

Since neat P3HT has been a widely researched prototypical conjugated polymer, multiple ways to change its aggregation such as solvent, molecular weight, annealing and coating methods are already well-established. In this chapter we will focus on another popular strategy employed to improve processability and mechanical properties, which is blending organic semiconductors with an insulating polymer such as poly(ethylene oxide) (PEO). Thus, we begin our discussion based on the previous knowledge showing that the addition of a polar media to P3HT, specifically PEO, can change optical absorption and emission line shapes, affecting microstructure and aggregation.[1] Moreover, knowing that the molecular weight (M_w) of P3HT in the films strongly affects opto-electronic properties, based on the systematic study of Paquin et al.,[29] we combined these two approaches to elucidate the impact of M_w of PEO in the optical properties of the blend. M_w values of P3HT were judiciously selected considering that there is a certain threshold (M_e) required for entanglement during deposition (lying between 25 and 35 $Kg{\cdot}mol^{-1}$ for P3HT based on literature)[30] and based on the previous knowledge that M_w of 134 $kg{\cdot}mol^{-1}$ exhibits the most pronounced effect when blended with PEO.[1] P3HT is blended with PEO at a weight ratio of

1:1 and films were casted at two different temperatures, 20 and 10 ºC (covered with petri dish to reduce evaporation rate). Details about specific combinations of M_w are reported on **Table.5.2**.

Table 5.2*: Combinations of M_w for P3HT:PEO blends*

Mw		P3HT	
		20 kg mol^{-1}	100 kg mol^{-1}
PEO	3 kg mol^{-1}	L-L	H-L
	900 kg mol^{-1}	L-H	H-H

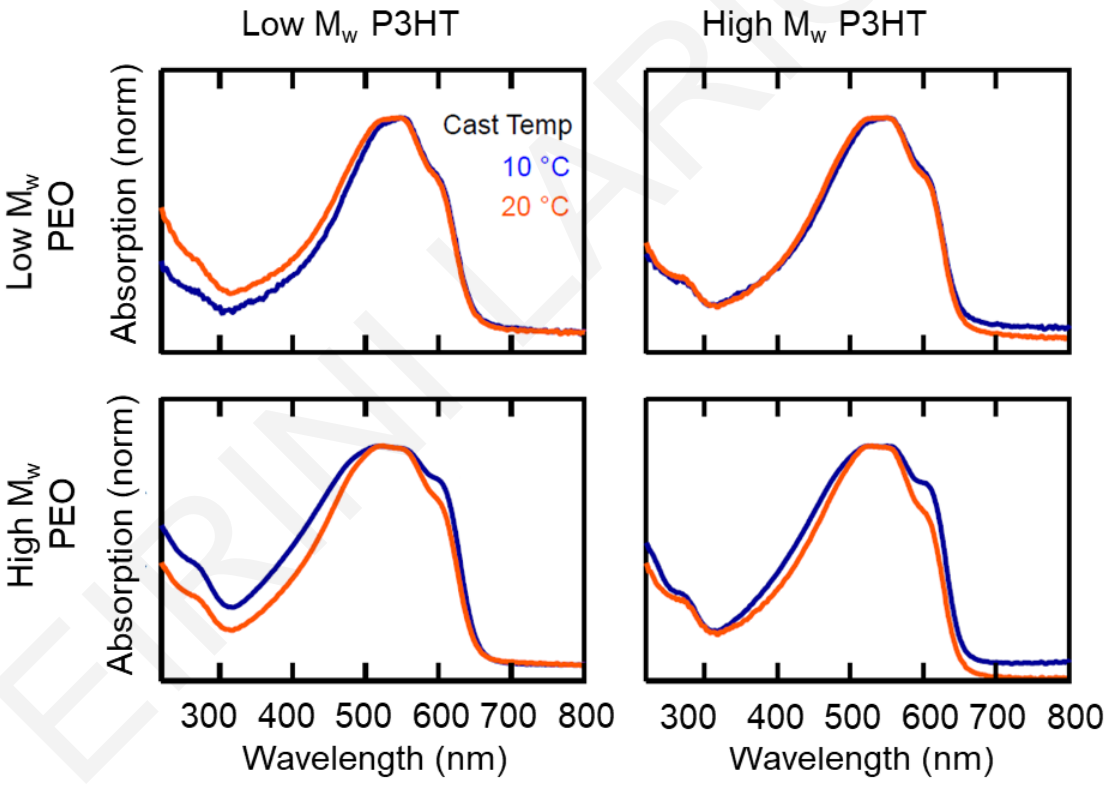

Figure 5.4*: Absorption spectra of the four M_w combinations of P3HT:PEO based on table 5.2. Abs(λ) = 100 – R(λ) – T(λ), peak normalized.*

Figure 5.4 depicts the variation in absorption among the different combinations of M_w of the blends for the two casting temperatures. All samples exhibit similar absorption characteristics with a low energy shoulder at ~600 nm (the 0-0 transition), reaching an absorption maximum at ~580 nm. The most significant observation from this study as shown in **Fig.5.4** is that the M_w of PEO rather than P3HT is the key factor to the changes induced, contradicting previous results from Hellman et al.[1] The above spectra reveal that significant

changes are induced in the case of high molecular weight PEO where increased 0-0 oscillator strength is observed and only for the low casting temperature (10°C), highlighting the role of the environment and indicating possible correlation of solvent evaporation rate to the observed changes. Further elucidation of the effect of casting temperature and evaporation rate will be provided in section 5.2.3.

RR spectroscopy was not as sensitive to additive Mw variations, with the various spectra exhibiting identical features. Only neat P3HT films of high and low Mw showed that despite the predominantly planar conformation of both high and low Mw films (the C=C stretch position is centred at ~1450 cm^{-1}), the relative intensity from the high-frequency component of the C=C stretch at ~1470 cm^{-1}, varied **(Fig. 5.5)**. This variation is reflected in the increased FWHM from 30 cm^{-1} (for the low Mw film) to 33 cm^{-1} for the high Mw, suggesting that the high Mw film has a slightly reduced degree of order.

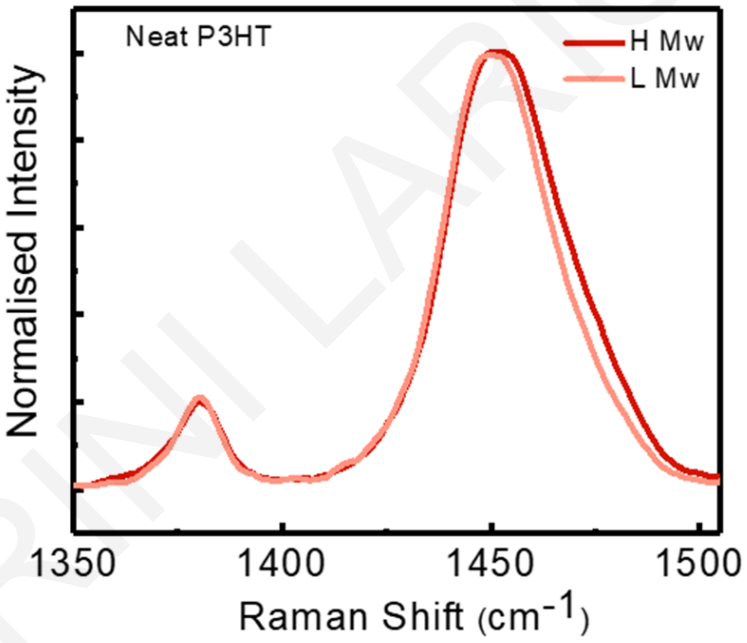

Figure 5.5*: RR spectra of high and low Mw neat P3HT films at 473 nm excitation.*

The relative (to a pristine regio-regular (RR)-P3HT film) degree of molecular order has been quantified in this case employing the relation provided by Tsoi et. al.:

$$C_r = \frac{I_{agg}}{I_{agg} + \frac{I_{non-agg}}{\sigma_{RRa}/\sigma_{RR}}} \quad (5.1)$$

The reference for maximum order is considered the RR-P3HT film and for disordered the regio-random (RRa)-P3HT, Cr is the calculated relative degree of molecular order, I_{agg} and $I_{non\text{-}agg}$ are the intensities of the aggregated and non-aggregated components respectively (quantified by area), and σ_{RRa}/σ_{RR} is the reported equal to ~1.69 Raman scattering cross-

section of RRa-P3HT relative to that of RR-P3HT (calculated for 488 nm excitation).[26] The estimated degree of molecular order is 0.91 for the high Mw film compared to 0.93 for the low Mw sample. The slightly decreased molecular order observed at high Mw is not a surprise considering that 100 kg·mol^{-1} is way above M_e (~30 Kg·mol^{-1}) and thus is possibly less dependent on M_w. However, despite the slightly lower overall degree of order of high Mw films, they are still preferable to low Mw ones concerning device applications, because they can provide transport pathways for long-range interconnectivity.[31]

To sum up, from this study emerged valuable indications that the Mw of PEO is what determines the optical response (i.e. 0-0/0-1 ratio) and from now on, high Mw PEO samples are employed for the experiments presented in this chapter. The second significant observation, was the effect of casting temperature, thus, it will be separately studied in the next section.

5.3.2 Manipulating aggregation with Casting Temperature in P3HT:Insulator Blends

Following the previous discussion, we examine the effect of casting temperature on the optical and structural characteristics of P3HT:PEO. Previous studies have highlighted the importance of temperature when blade coating P3HT films[32,33] as well as the impact of spin coating speed for other donor-acceptor polymers[34] as they both directly affect evaporation rate. However, no studies investigate low deposition temperatures i.e. below room temperature. The phase separation process during solvent evaporation of P3HT:PEO blends has already been reported,[35] showing that P3HT-PEO interactions are unfavorable, forming pure, separate phases. However, this phase behavior is likely dependent on temperature and we examine this effect employing different casting temperatures. To this end, P3HT:PEO blends were deposited onto substrates of different temperatures between 10 and 30ºC. **Figure 5.6** shows the change in absorption *(left)* and RR spectra (*right*) of blend films with respect to the casting temperature. More pronounced changes are observed in absorption spectra, as with decreasing temperature there is a significant increase in the 0-0 intensity, accompanied by a red shift of this transition from ~610 nm at 30ºC to ~630 nm at 10 ºC. The increasing intensity of the 0-0 relative to 0-1 indicates a transition from H-like to J-like character of the aggregates with decreasing temperature, where intra-chain coupling is becoming dominant and the red shift is associated with longer conjugation lengths, likely accompanying this aggregate type.[36] Moreover, the pronounced threshold in absorption characteristics observed around 15ºC, possibly suggests different phase separation behavior.

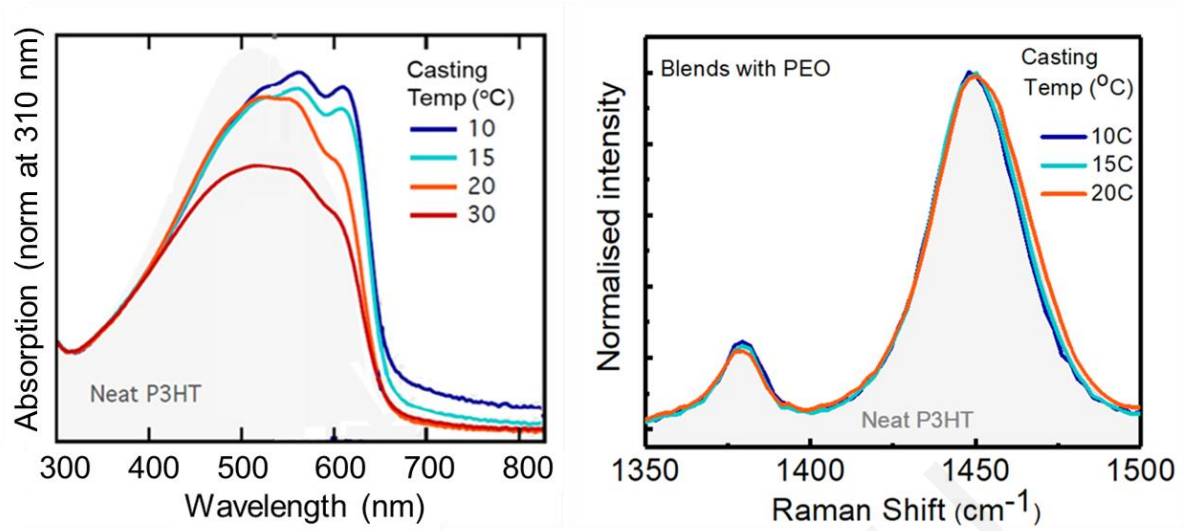

Figure 5.6*: Left: Absorption (100- R -T) spectra of neat P3HT (grey), P3HT:PEO blend films cast at 30°C (red), 20°C (orange), 15°C (light blue) and 10°C (dark blue), measured at room temperature. and normalised at 310 nm. Right: RR spectra of neat P3HT (grey), P3HT:PEO blend films cast at 20°C (orange), 15°C (light blue) and 10°C (dark blue), excited at 473 nm and normalised at C=C stretch.*

The changes in RR spectra with temperature, although marginal, agree with the absorption, complementing our understanding with regards to conformational changes by exhibiting an increasing relative degree of order with lower casting temperature. This increase is obvious both from the increased intensity of the in-plane C-C stretching mode at ~1380 cm^{-1} with respect to the C=C symmetric stretch (reflected in the C-C/C=C intensity ratio) and the reduced scattering from the non-aggregated component. The increase in the C-C/C=C intensity ratio is linear and is illustrated in **Fig 5.7** while the change in relative degree of order (calculated from expression (5.1)) is marginal from 0.91 at 20°C to 0.92 at 15 and 10°C. Those results, although they probe variations in backbone planarity, are not sensitive enough to probe the H-like versus J-like character of aggregation compared to absorption. A possible explanation is that both aggregation types have relatively high molecular order and similar backbone conformation. Nevertheless, the combination of absorption and RR results confirms the general idea that J-aggregates are associated with greater backbone planarity. [4,36]

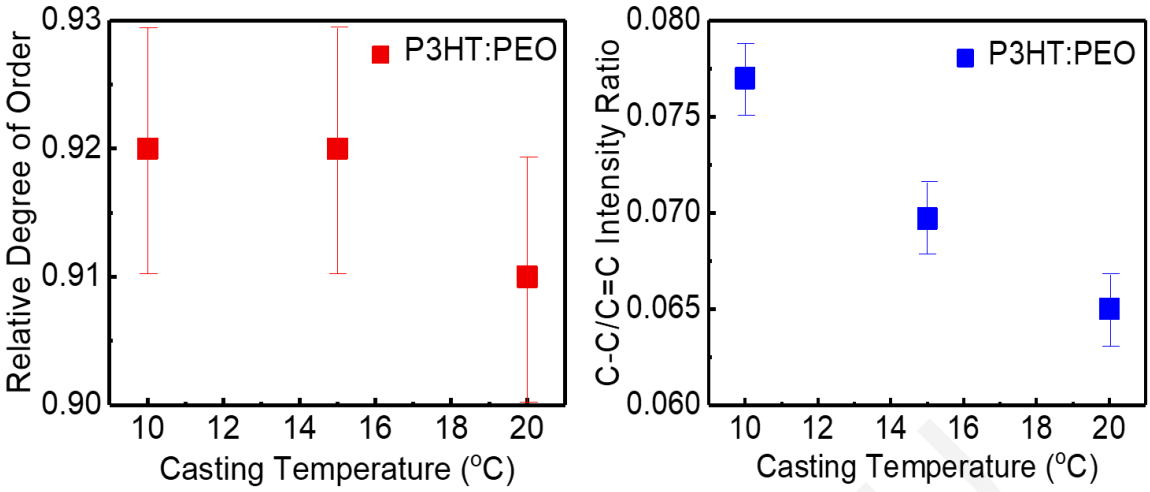

Figure 5.7*: Left: Estimated relative degree of molecular order with respect to casting temperature for P3HT:PEO blend films. Right: C-C/C=C intensity ratio with respect to casting temperature for the same samples.*

The above results indicate that we can achieve controlled manipulation of H vs J-like properties in P3HT:PEO blends by means of processing as both microstructural and optical characteristics vary significantly with casting temperature. It would be interesting to relate those results to temperature dependent phase separation and a previous study by Hellmann et al.[37] can provide insights on this by means of in-situ optical microscopy. Their study on the same material blends concluded that high 0-0 absorption and thus J aggregation type is connected to strong phase separation. From this it is assumed that by lowering temperature, the interactions between P3HT and PEO are discouraged, resulting in phase-pure domains. Although further work is necessary to investigate also the importance of the evaporation rate to the resulting properties, it would be interesting to test this simple processing strategy in more organic semiconductor:insulator systems and explore reproducibility and potential generalisation.

5.3.3 Thiophene derivatives: The effect of chemical modification

After establishing the importance of judicious consideration of the Mw and more specifically, Mw of the additive and elucidating the effect of casting temperatures on the properties of the blend, hence optimizing sample preparation procedures, we performed a systematic study on the local microstructural order and optoelectronic properties by utilising the polarity contrast between backbone, side chains and insulating additives. To this end, we started by a fundamental "mapping" of structural and optical properties of chemically modified thiophene derivatives. The model systems consist of the same conjugated

backbone based on polythiophene chains — the P3HT homopolymer, the diblock copolymer poly(3-heyxlthiophene)-*block*-poly(ethylene oxide) (P3HT-*b*-PEO),[2] and the graft polymer poly[3-but(ethylene oxide)thiophene] (P3BEOT) with the corresponding chemical structures shown in **Fig. 5.8**.

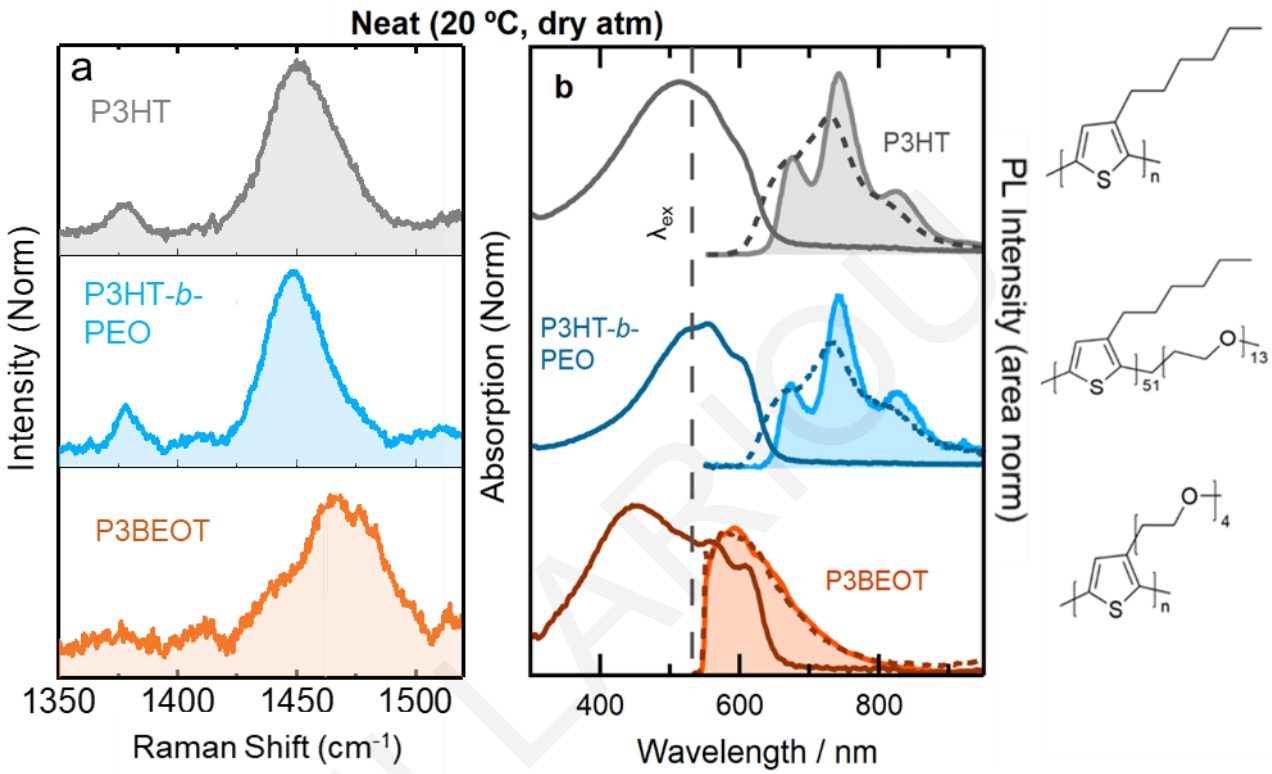

Figure 5.8: *a) Normalised RR spectra of neat P3HT, P3HT-b-PEO and P3BEOT cast from solution at 20 °C, excited at 473 nm b) Normalized absorption and photoluminescence (PL) spectra of same samples. Absorption was determined at room temperature (solid line), PL at RT (dashed) and 10 K (filled) On the right are the corresponding chemical structures.*

The RR excitation wavelength chosen was 473 nm, in resonance with the non-aggregated chromophore absorption of the three neat polymers (wire-bar-coated films from $CHCl_3$ solution) (**Figure 5.8a)**. Immediately apparent is that the PEO-block in P3HT-*b*-PEO has a marginal effect on backbone order of the P3HT moiety. Thiophene's C=C stretch is located around 1453 cm^{-1} for both systems, with a slightly reduced contribution of the non-aggregated component to the FWHM in the case of P3HT-*b*-PEO, while C-C/C=C intensity ratio is around ~0.1 for both, revealing increased planarity between monomer units,[27] as expected for regioregular P3HT.[26] P3BEOT, however, exhibits entirely opposite Raman features with a broad C=C symmetric stretch centered at ~1465 cm^{-1}, shifted by ~12 cm^{-1}, with respect to the P3HT homopolymer and weak in plane C-C stretch, hardly reproduced by a Gaussian function, suggesting a substantially more torsionally disordered backbone conformation, which will be further explored and analyzed in the next section.

Linear absorption and photoluminescence (PL) spectra complement the information obtained by Raman with P3HT-*b*-PEO having similar optical features with those of the homopolymer (see **Fig. 5.8b**). The 0-0/0-1 vibronic peak ratios both in absorption and emission, sensitive indicators of the balance between intra- and inter-chain coupling,[23,36,38] are essentially identical for P3HT and P3HT-*b*-PEO with the latter having a slightly more pronounced vibronic structure and red-shifted absorption maxima located at ~550 nm.

Those findings, considering also the Raman spectra, are attributed to the tendency of P3HT segments in the block copolymer to microphase separate from the PEO segments,[39–41] drastically limiting interactions of the PEO blocks with semiconducting chain segments, leaving the former virtually unaffected by the latter and, thus, maintaining the typical characteristics of P3HT. In stark contrast, the P3BEOT graft copolymer displays significant spectral differences, with a broad absorption band, blue-shifted relative to the homopolymer and with only weak vibronic peaks observed in absorption at ~560 and ~610 nm. The absorption maximum is found at 450 nm, implying that P3BEOT is comprised of a larger fraction of non-aggregated chain segments, in perfect agreement with the RR evidence of a torsionally disordered backbone conformation, similar to regiorandom P3HT.[28] Support for this view is provided by the PL spectra of the graft copolymers, recorded at room temperature and 10 K, where a clear blue shift in spectral maxima is also observed, from 745 nm for the P3HT homopolymer to 595 nm for P3BEOT, accompanied by a clear loss of vibronic structure. Finally, noteworthy is the substantial overlap between absorption and emission spectra in P3BEOT. This, further reinforces the picture that there is a significantly smaller fraction of torsionally ordered aggregates (with a smaller band gap) to which excitons can migrate prior to emission.[42]

Overall, although microphase separation as found in block copolymers, has been shown to have little effect on local molecular ordering, considerable structural changes are induced in graft polymers. A reasonable explanation of the observed changes would be the contrasting polarity between the semiconductor backbone and its side chains, causing the former to twist. This assertion, will be investigated further in the next sections below as well as the possibility to manipulate this backbone order, employing insulating polymer additives.

5.3.4 Thiophene derivatives: The effect of blending with the polar insulating additive PEO

After obtaining a clear picture on the effect of chemical modification on the thiophene's conformation and optical properties, we blend the three polymers with the polar additive PEO (high molecular weight), following procedures described in *Chapter 4*,[43] in an endeavor

to understand the importance of polarity to the resultant interactions with insulating polymer matrices. This time we focus only on the graft polymer P3BEOT which, based on the aforementioned findings, is studied in greater detail and is compared to P3HT and blends of both with PEO. Local ordering and backbone planarity is investigated adopting an additional tool, that of selective probing non-aggregated and aggregated fractions. Selectivity in RR spectroscopy is achieved by exciting either non-aggregated or ordered populations at 473 and 532 nm, respectively.

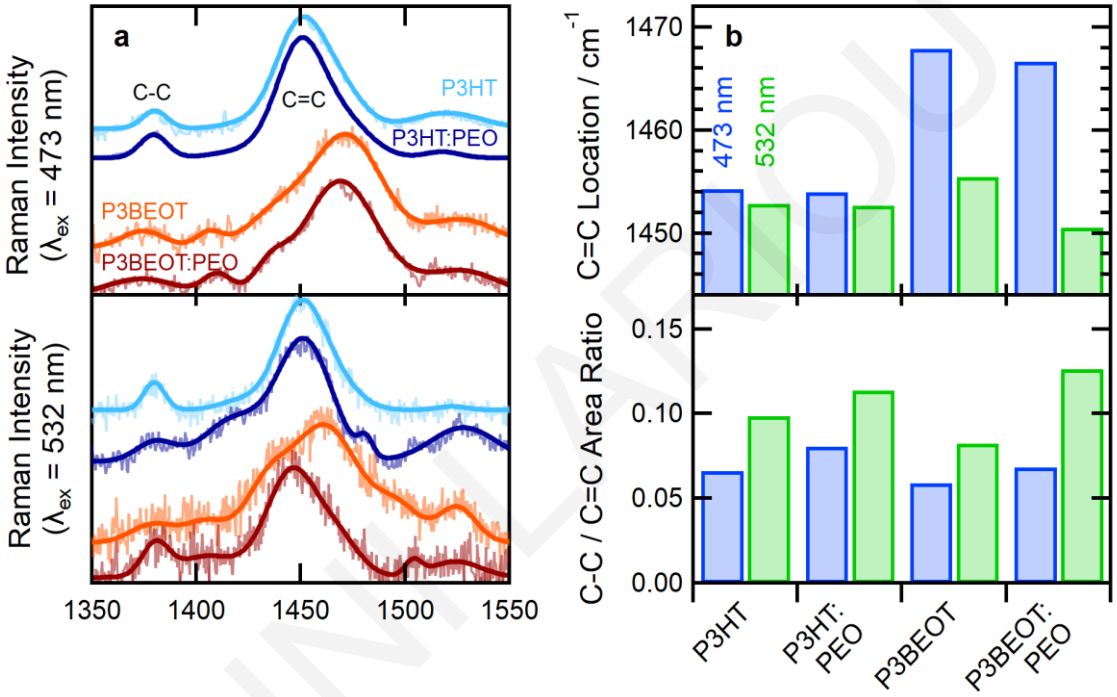

Figure 5.9: *Normalized resonance Raman spectra (a) with λ_{ex} = 473 (top) and 532 nm (bottom) of P3HT, P3HT:PEO, P3BEOT and P3BEOT:PEO, offset vertically for clarity. Original spectra are overlaid with fits (see Figure S1, S2). Extracted parameters (b) are the symmetric C=C stretching mode location (top) (an area weighted average of underlying peaks, higher values indicate increased torsional disorder) and C-C to C=C peak area ratio (bottom) (higher values indicate greater planarity).*

Figure 5.9 shows experimental resonance Raman spectra overlaid with peak fits corresponding to the C-C (~1380 cm^{-1}), symmetric C=C (~1450 to 1470 cm^{-1}) and asymmetric C=C (~1525 cm^{-1}) stretching modes. Again, the frequency of the symmetric C=C band and the C-C/C=C intensity ratio was followed to assess the torsional order of the polythiophene backbones in those systems, expecting C=C stretching vibrations for torsionally disordered chains to be around 1470 cm^{-1} and those for planar chains around 1450 cm^{-1}.[26] Starting with the neat materials (*i.e.* P3BEOT and P3HT), when exciting their non-aggregated regions (λ_{ex} = 473 nm), the symmetric C=C stretching mode (including

contributions from aggregated and amorphous components) appears at ~1465 cm^{-1} and ~1454 cm^{-1} for P3BEOT and P3HT, respectively (see **Figure 5.9b**). While in resonance with more aggregated domains (λ_{ex} = 532 nm), the symmetric C=C stretching mode was observed at ~1456 cm^{-1} for P3BEOT, while in P3HT this mode remains almost unchanged at ~1453 cm^{-1}. Taken together, these observations indicate that the neat graft polymer is substantially more torsionally disordered than P3HT, particularly in the non-aggregated regions, with the aggregated regions comprising a certain fraction of segments of a similar backbone planarity to that found in P3HT. These regions are likely to be responsible for the weak vibronic structure shown in the UV-vis absorption spectrum of P3BEOT (see **Fig.5.8b** in previous section).

Turning the attention to the PEO blends, no significant effect on the symmetric C=C stretching peak location is found when adding PEO to P3HT regardless of the excitation wavelength, *i.e.* independent of whether aggregated or non-aggregated regions are probed. However, the C-C/C=C peak area ratio (see **Figure 5.9b**, bottom panel) increases slightly for the blend compared to neat P3HT, consistent with the addition of PEO slightly increasing P3HT backbone planarity. Interestingly, blending has a striking effect on the P3BEOT:PEO binary blend. Introduction of PEO, leads to a notable decrease in the symmetric C=C stretching mode frequency of ~5 cm^{-1} when probing aggregated regions (**Fig. 5.9b**, top panel), resulting in a peak at ~1451 cm^{-1}. This frequency is slightly (~2 cm^{-1}) lower than what is found for neat P3HT and its blends with PEO, indicating that the addition of PEO to the graft polymer substantially increases the fraction of chain segments with increased backbone planarity, especially in aggregated regions, often beyond that achievable in neat or blended P3HT. This conclusion is supported by the C-C/C=C peak area ratio on probing aggregated regions (λ_{ex} = 532 nm); for P3BEOT:PEO, which is higher than for both P3HT and P3HT:PEO (**Fig. 5.9b**, bottom panel). On the contrary, blending has a far less pronounced effect on the non-aggregated fraction (λ_{ex} = 473 nm), with a comparatively negligible reduction in symmetric C=C location of ~1 cm^{-1}, and a smaller increase in C-C/C=C peak ratio than when exciting the aggregated fraction. Extracted parameters from Fig. 5.9 show that for both P3BEOT and P3HT addition of PEO leads to a lower C=C peak frequency in addition to a higher C-C/C=C peak area ratio, suggesting slightly enhanced backbone planarity These differences are more pronounced in P3BEOT, suggesting that replacing hexyl with BEO side chains possibly increases PEO's influence on the thiophene backbone.

Absorption and PL further reinforce our interpretation of the RR spectra (see **Fig. 5.10**), as adding PEO to the P3HT homopolymer leads to a substantially enhanced 0-0/0-1 peak ratio

in both absorption and emission, consistent with earlier observations[1] and characteristic of a transition from inter- to intra-molecular coupling.[4,29,36]

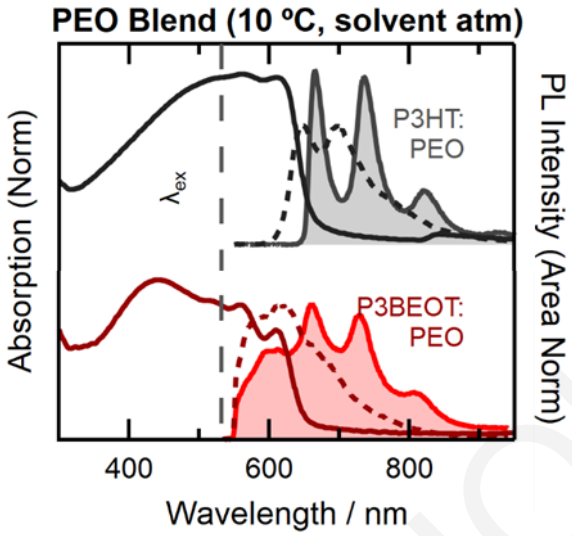

Figure 5.10*: Normalized absorption and photoluminescence (PL) spectra of P3HT and P3BEOT blends with PEO 1:1 (weight%) cast at 10 °C and dried within a solvent rich atmosphere. Absorption was determined at room temperature (solid line), and PL at RT (dashed) and 10 K (filled).*

A similar scenario is observed for the P3BEOT:PEO blend exhibiting the most significant change in optical behavior upon blending — especially in PL. Unlike the spectrum of the neat graft copolymer, the blend exhibits clear vibronic structure at 10 K, although the emission spectrum characteristic of non-aggregated polythiophene segments is still dominant. This implies that the high compatibility between the P3BEOT side chains and PEO leads to the inert component influencing the semiconducting backbone *via* increased interactions due to their mutual polarity, affecting the latter's local assembly and hence its optoelectronic landscape.

From the above, there is strong evidence that the strong affinity between the polar semiconductor side chains and the insulating polymer 'additive' can re-introduce the backbone order in systems with contrasting polarity between backbone and side chains. The increase in the molecular order of P3BEOT:PEO blend can be attributed to favourable interactions between the polar side chains and PEO, reducing steric hindrance between individual chain segments by 'drawing' the side chains away from the semiconducting backbone.

Further support on the view that this process is polarity driven, is provided by the RR and absorption spectra of poly(3-(2'-ethyl)hexylthiophene) (P3EHT), comprising a poly(thiophene) backbone with branched alkyl side chains and blends of this with ultra-low-

density polyethylene (ULDPE), a highly branched version of polyethylene. The idea again, is to match the polarity of the side chains with the additive and in this case both are non-polar. As would be expected from the absence of polarity contrast, thiophene with branched alkyl side chains differ slightly to P3HT, exhibiting a 2 cm^{-1} shift of the C=C stretching to higher frequencies (see **Fig. 511**). The side chain branching of P3EHT is known to increase steric hinderance, reduce aggregation and lower the melting temperature relative to neat P3HT.[44] Although the observed changes are not pronounced, they reveal a slightly icreased backbone disorder thus, are in agreement with this reported description. Selective excitation of aggregated and non-aggregated fractions revealed no sugnificant spectral changes between the two excitation wavelenghts and C=C stretching exhibits a marginal shift of 1 cm^{-1} when excited at 532 nm as shown in **Fig. 5.11d**. The blends with ULDPE have identical Raman and absorption spectra to P3EHT, further supporting that strong affinity between the side chain is not sufficient to affect local order of the semiconductor and that polarity contrast between the backbone and side chains is necessary.

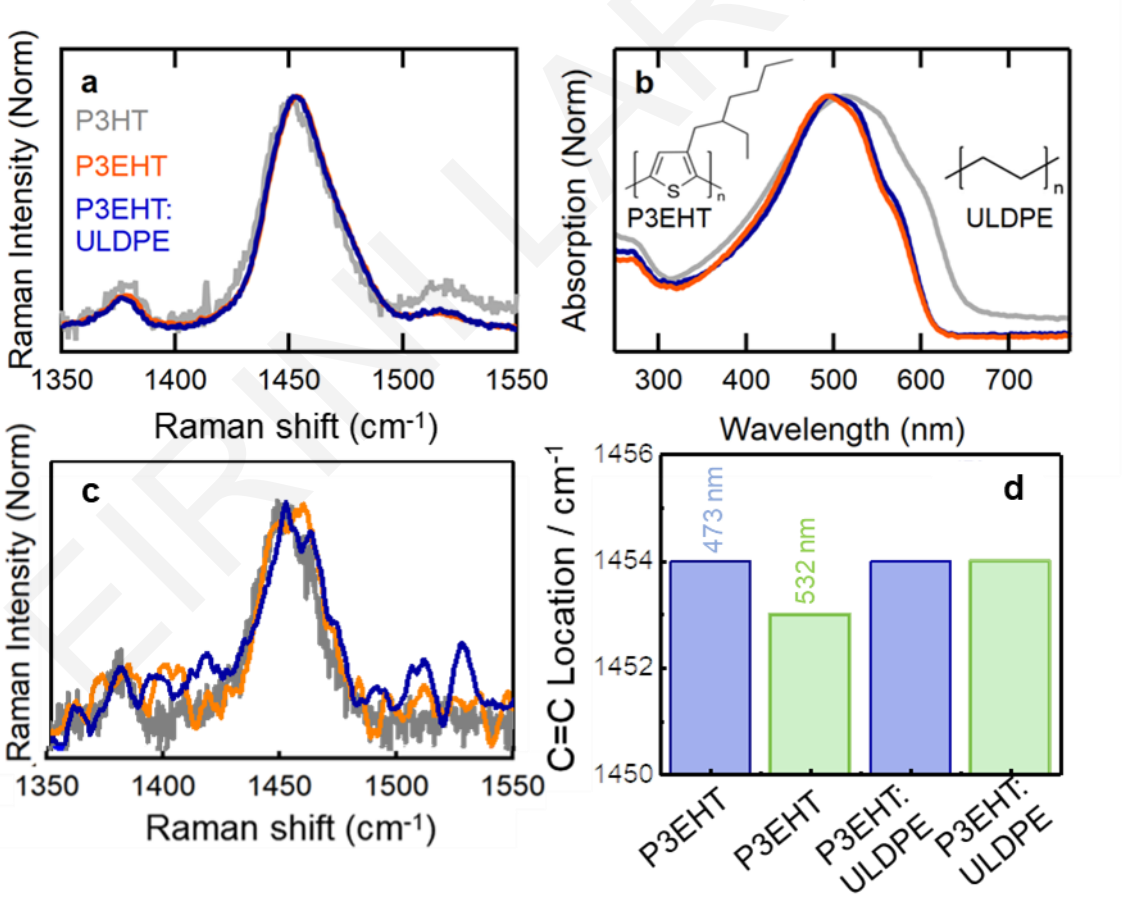

Figure 5.11: *Raman (λ_{ex} = 473 nm) (a) and absorption (b) spectra of poly(3-(2'-ethyl)hexylthiophene) (P3EHT) (inset) and low density poly-ethylene (ULDPE, Dow Affinity) (proprietary structure shown schematically)*

To conclude this section, increased backbone planarity does not necessarily imply increased aggregation and cannot directly be related to long range order, however, it plays an important role in determining the balance between inter- and intra-chain coupling within aggregates. Crystalline ordering and orientation in polymer systems is probed through grazing-incidence wide-angle X-ray scattering (GIWAXS)[45] and suggests the lack of long range order in the case of P3BEOT while blends of P3BEOT and P3HT with PEO show intense lamellar scattering peaks for P3BEOT:PEO. Those data can be found in the published version of the present study,[5] extending our shorter-range ordering interpretation. Overall, blending with insulating polymers can be an efficient tool to manipulate the local, and to a certain extent long-range, arrangement of polymeric semiconductors. Considerable structural changes can be induced in blends with graft polymers as the active component. For this to occur, it appears that two criteria must be satisfied: i) there must be a strong contrast in polarity between the semiconductor backbone and its side chains, and ii) there must be a strong affinity between the semiconductor side chains and the insulating polymer 'additive'. Such

a scenario creates an enthalpic driving force that 'draws' the polar side chains away from the active material's backbone towards the second blend component, reducing the side chain disorder and, possibly, the steric hindrance that normally would lead to torsional disorder and reduced aggregation, especially in materials with relatively bulky side chains.

5.3.5 Extending polarity contrast study to additives of different polarity

To further substantiate the interpretation regarding the dominant contribution of polarity contrast to the interactions between side chains and insulating 'additives', we select structurally similar additives to PEO, but with different Hansen Solubility Parameters (δ) (see **Fig.5.12a**).[46] The solubility of a polymer in a particular solvent depends on the similarity in inter-molecular interactions or simplistically described as 'like attracts like'. To quantify this, Hansen divided these interactions into three types: polar (i.e. permanent dipole) δ_p, dispersion δ_d and hydrogen-bond δ_h. Each solvent and polymer is thus assigned a coordinate in 3D "Hansen Space", with the overall cohesive energy density δ of solvents/polymers comprising dipole (polar), dispersion and hydrogen-bonding components via $\delta^2 = \delta_p^2 + \delta_d^2 + \delta_h^2$ - the closer the co-ordinates, the more similar the interactions, and the greater the solubility. Along with solubility, these parameters indicate the 'compatibility' of polymers or their substituents, as in the case of the polar oligo(ethylene oxide) side chains and insulating additives used in this study.

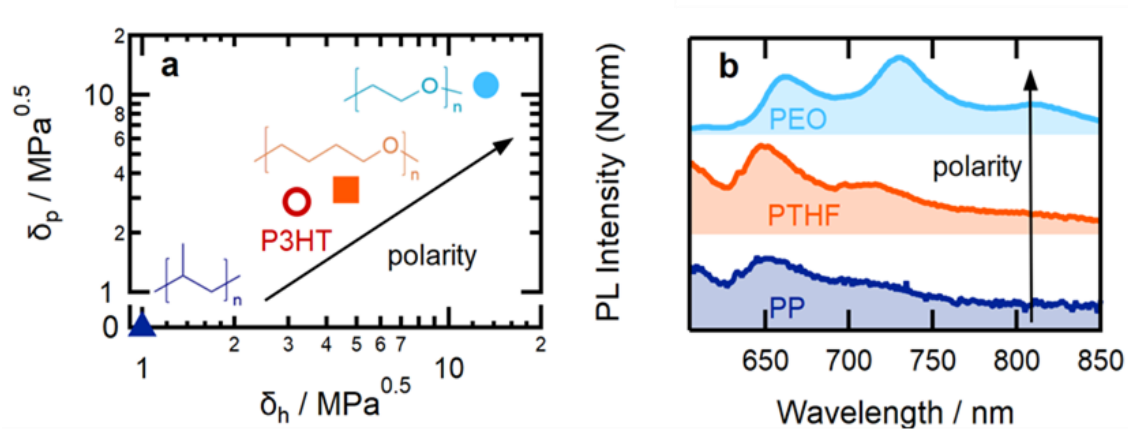

Figure 5.12: *Insulating polymers (a) with different polar δ_p and hydrogen-bonding δ_h Hansen Solubility Parameters, were blended with P3BEOT. 10 K (b) PL of P3BEOT:PEO, P3BEOT:PTHF and P3BEOT:PP (λ_{ex} = 580 nm).*

By employing this solubility parameter approach, we can control the polarity contrast between the side chains and the additives and evaluate the origin and magnitude of the interactions.[46–48] We keep the P3BEOT as a model system from the previous section due to the strong polarity contrast between the backbone and the side chains and explore the effect of blending this with two additional insulators to PEO, namely poly(tetrahydrofuran) (PTHF) and isotactic poly(propylene) (PP) (Chemical structures in **Fig 5.12a** inset). In **Figure 5.12b** we observe the effect of the increasing polymer additive's polarity in the low temperature (10K) PL spectra of the blends with P3BEOT. As PEO, PTHF and PP have different proportions of Oxygen atoms per CH_2 unit, they have a range of Hansen Solubility Parameters (**Fig 5.12a**). Reassuringly, increasing the polarity of the 'additive polymer' leads to more pronounced vibronic structures in the PL (λ_{ex} = 580 nm) of the blends associated with increased interchain interactions.[23] Moving to RR spectra (λ_{ex} = 532 nm) of the blends (see **Fig 5.13a**), we observe that increasing the polarity of the additive causes a reduction in the symmetric C=C stretching frequency and correspondingly an increase in the C-C/C=C intensity ratio (quantified by area) visualized for each sample independently (**Fig. 5.13b**) and as a function of the insulator's polarity (**Fig. 5.13c**). Both these trends indicate reduced torsional disorder with increasing insulator's polarity reinforcing our interpretation that interactions between polar side chains and a similarly polar insulating 'additive' promote planarization of the semiconducting backbone by drawing away side chains and, thus, reducing steric hindrance.

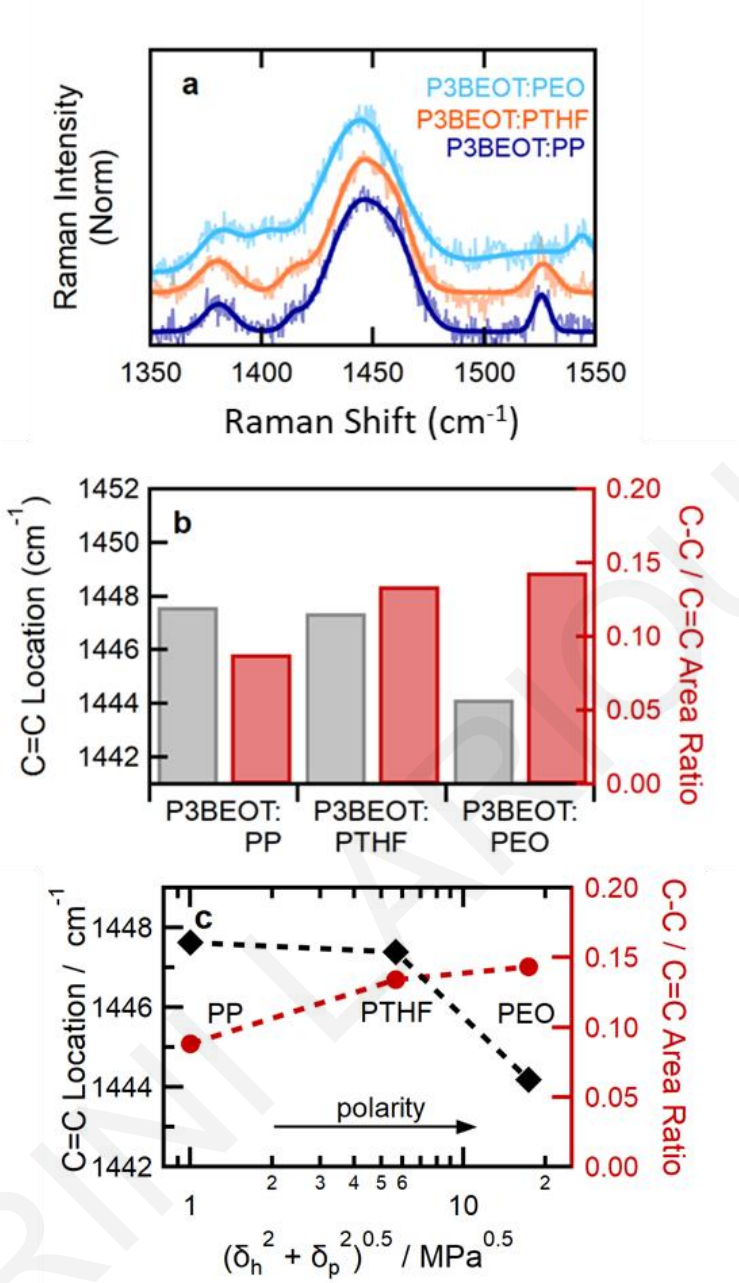

Figure 5.13*: a) Raman spectra at λ_{ex} = 532 nm (a) for P3BEOT:PEO (light blue), P3BEOT:PTHF (orange) and P3BEOT:PP (dark blue) (offset vertically for clarity, fits overlay experimental data). b) Fitting extracted parameters of symmetric C=C position and C-C/C=C area ratio of the same blend samples and c) visualisation of the trends as a fuction of the insulator's PP, PTHF and PEO polarity.*

Polarity contrast is clearly critical and additive polarity rather than just functionality is the key requirement for controlling local microstucture. The addition of insulating polymers with similar structure but different Hansen Solubility Parameters showed that backbone order can be manipulated in a rather straightforward way and the extent of change in local order can be tuned by both selection of the polymer 'additive', and the backbone/side chain polarity difference of the semiconductor.

5.3.6 Evaluating stability: The effect of humidity

One of the main issues conjugated polymers suffer from, is long-term stability. In the present study we address this concern by exploring the effect of controlled exposure to humidity as well as monitoring the aging of samples under environmental conditions (see section **5.2.8**). The local polar environment would be expected to be sensitive to the presence of humidity and this can be exemplified by experiments involving the controlled exposure of neat P3BEOT and its blend with PEO to water vapor. Details on the humidity treatment can be found in chapter 3 where sample preparation is described. Below we follow the evolution of structural and optical behavior of neat and blend samples after the exposure to high humidity. **Figure 5.14** shows the RR spectra of P3BEOT and P3BEOT:PEO before and after the humidity exposure. Following the FWHM and the position of the symmetric C=C stretching mode as most sensitive indicators of backbone changes we observed that the FWHM of neat and blend films follows an opposite trend under the humidity exposure. FWHM of neat films increases suggesting greater inhomogeneity, while FWHM of blend films decreases and accordingly inhomogeneity in this case decreases (**Fig.5. 14c**). However, those changes are not significant, considering also the C=C stretching position (see **Fig. 5.14d**) which remains unchanged for the blends, while shifts by 1 cm^{-1} towards higher frequencies for the neat samples. Greater sensitivity to the effect of humidity compared to RR is observed in the optical behavior of those samples by comparing their absorption in **Fig. 5.15**. Interestingly, P3BEOT:PEO blends exhibit increased vibronic structure with enhanced $A_{0\text{-}0}/A_{0\text{-}1}$ ratio after this treatment revealing increased electronic coupling and possibly relates to an increase in backbone planarity,[23] while this is less prominent for the neat films. A similar increase in $A_{0\text{-}0}/A_{0\text{-}1}$ (consistent with increased intrachain excitonic coupling) has been reported previously by Hellmann et al. within P3HT:PEO blends following water treatment, highlighting the effect of the electronically inert component.[1]

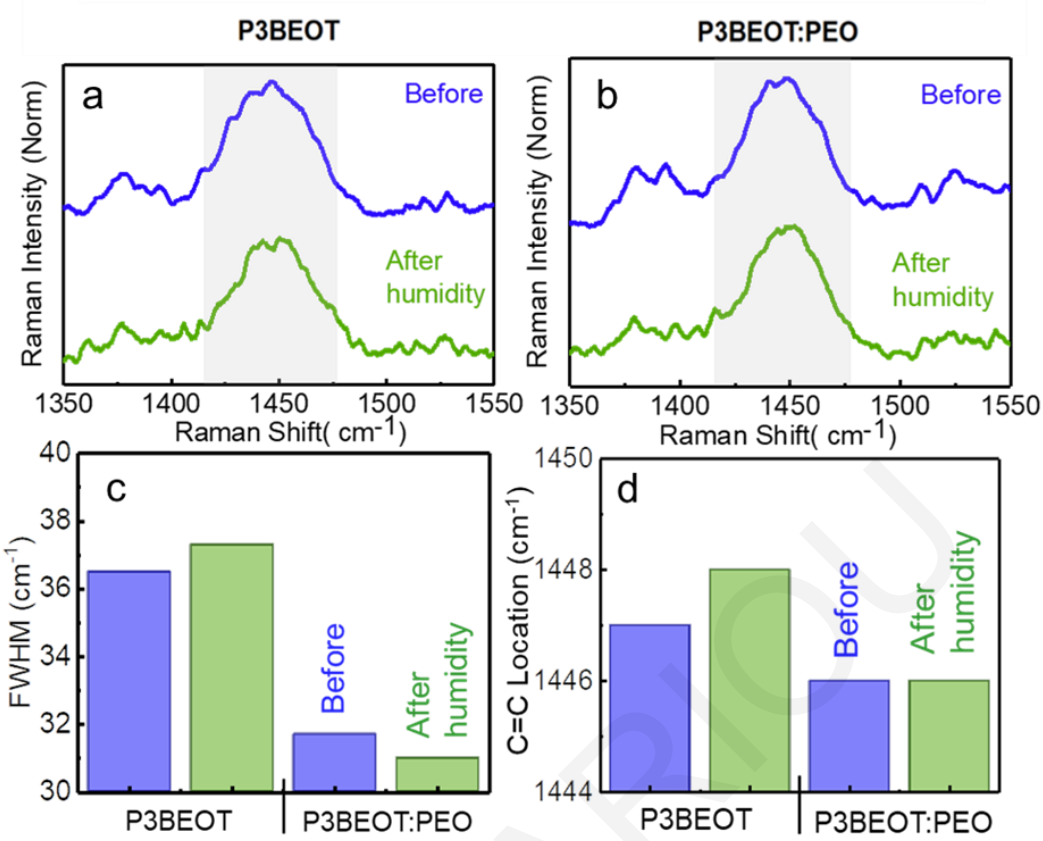

Figure 5.14: *Raman spectra at λ_{ex} = 532 nm of a) Neat P3BEOT flims before (blue) and after (green) humidity treatment and b)Blend P3BEOT:PEO films before (blue) and after (green) humidity treatment. Fitting extracted parameters of c) FWHM of the symmetric C=C stretching and d) symmetric C=C stretching position.*

Two PL excitation wavelengths were employed for probing chain segments of different absorption energies (corresponding to chromophores with different local order). Excitation of primarily non-aggregated species (λ_{ex} = 480 nm) leads to a featureless PL spectrum centred at ~580 nm (Figure 5.15) in P3BEOT both before and after humidity treatment and at ~600 nm for P3BEOT:PEO. When exciting at λ_{ex} 530 nm (thereby more aggregated species), all spectra red-shift as expected and vibronic features appear, more profoundly in P3BEOT:PEO blends but we can hardly correlate these shifts with the moisture treatment.

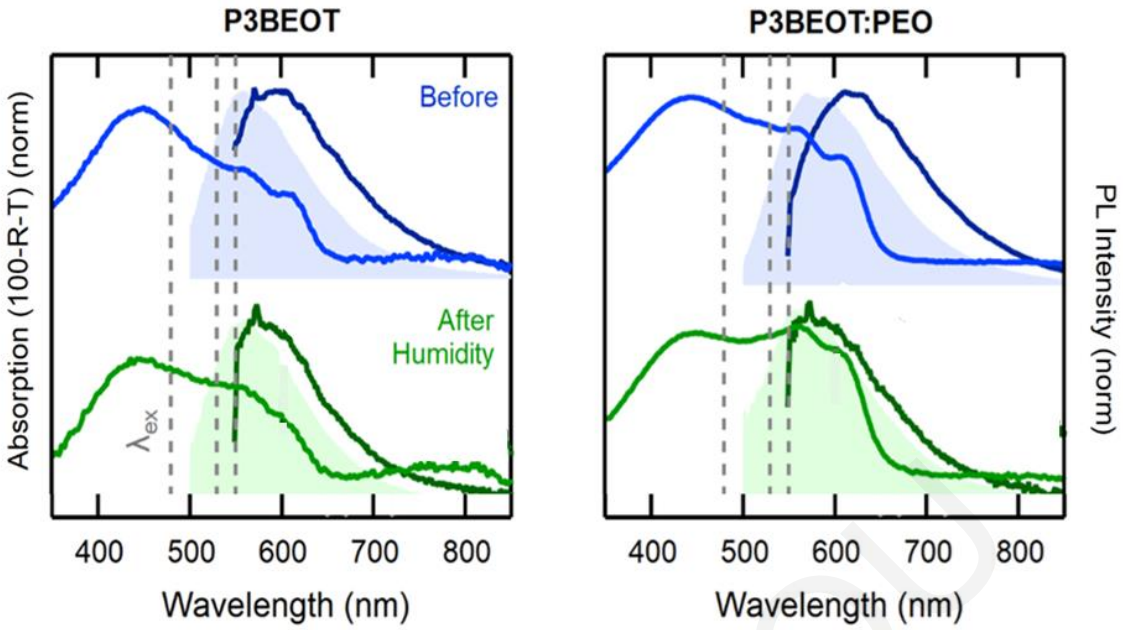

Figure 5.15: *Absorption and PL of P3BEOT and P3BEOT:PEO films just after casting and after humidity treatment. PL spectra were recorded after excitation at 480 nm (filled) and 530 nm, with longer excitation wavelength probing aggregated domains.*

Conclusively, incorporating water into P3BEOT and P3BEOT:PEO blends *via* exposure to water vapor, leads to both systems displaying a more pronounced vibronic structure both in absorption and PL, from which we infer that this treatment leads to higher torsional backbone order, with the effect being notably stronger for the blends. The moisture dependence of P3BEOT and its blends with PEO emphasises the strong correlation between local environment and backbone ordering showing that the hydrophilicity of both PEO and but(ethylene oxide) side chains causes water to be incorporated into the film, attracting and retaining moisture. The polarity contrast between backbone and side chains/PEO is probably enhanced due to the presence of water which acts as a plasticizer.[49,50] This argument is supported by differential scanning calorimetry measurements (DSC) which revealed a lower glass transition temperature (T_g) of both P3BEOT and P3BEOT:PEO.[5] The aging experiments presented in the next section will complement those results contributing to the evaluation of the environmental stability of those systems in general.

5.3.7 Evaluating stability: Aging under ambient conditions

Following the exploration of the environmental stability of the samples via humidity treatment, we monitor the structural evolution of P3BEOT and its blends with PEO after aging over a period of four months in ambient conditions. The initial resonance Raman spectroscopy measurements were performed directly after casting and drying- a process

where humidity is trapped in the resulting thin films — and we repeated after storing in air for four months. As shown in **Figure 5.16**, the neat graft copolymer, when exciting aggregated regions (λ_{ex} = 532 nm), intriguingly, has initially very low (~1447 cm^{-1}) frequency of the symmetric C=C stretching mode, comparable to that of P3BEOT:PEO which is centered at ~1444 cm^{-1} (**Fig. 5.16a**). This implies that, initially, the neat graft copolymer contains a high fraction of planar chain segments. However, this dominant mode shifts over time to higher frequencies until 'saturating' after four months at ~1456 cm^{-1}, accompanied by a noticeable reduction in C-C/C=C peak area ratio (lower values suggest reduced planarity). In stark contrast, the polymer blend is markedly more stable over time with respect to structure. A change in peak frequency in the blend is observed over time, but is drastically smaller than that observed for the neat graft polymer, with aged samples featuring a symmetric C=C stretching mode at ~1450 cm^{-1} accompanied by a slight decrease in C-C/C=C peak ratio (see **Fig. 5.16b**). We attribute the different behavior of P3BEOT and P3BEOT:PEO, with the latter retaining its aggregated character whilst the former does not, leading to the relatively rapid release of water from the P3BEOT system. In contrast, water molecules retained in the P3BEOT:PEO binary blends due to the hydrophilic PEO[51,52] stay trapped, contributing to the polarity contrast and assisting in planarity of the backbone.

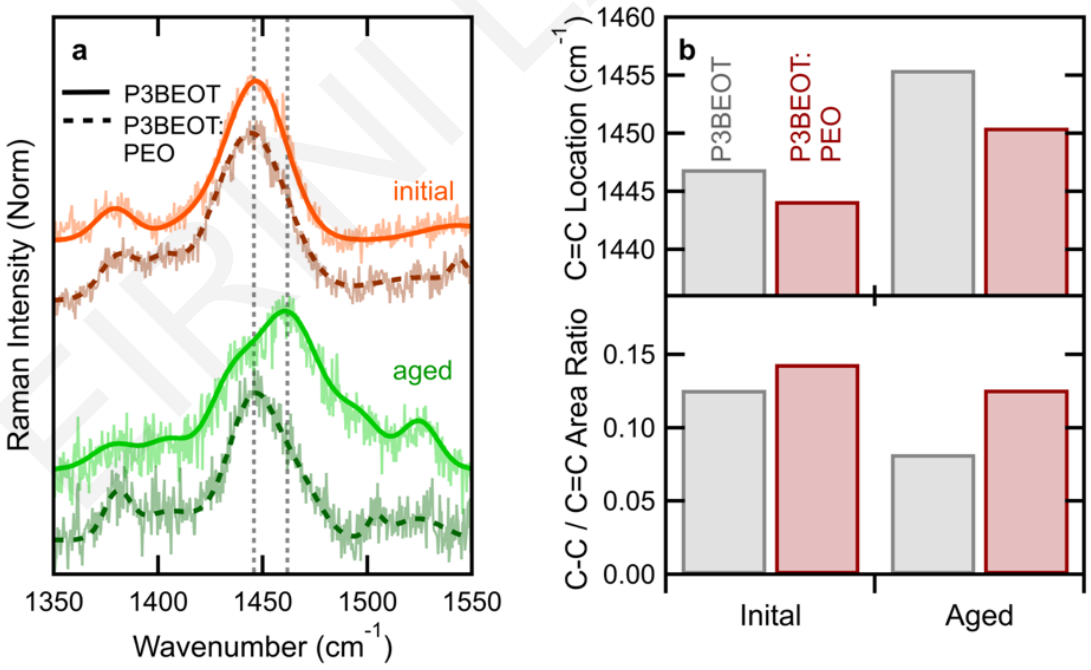

Figure 5.16: *Effect of aging on resonance Raman spectra. Normalized spectra with λ_{ex} = 532 nm for P3BEOT and P3BEOT:PEO, acquired within one week of deposition (orange) and after aging for four months.*

These findings can potentially have wide applicability *via* selection of side chain polarity, polarity of blend component as well as small-molecular additives, such as water, that further affect the polarity contrast between backbone and environment, opening a simple alternative pathway to structural control without the need to realize all functionality exclusively *via* (often complex) chemical design.

References

(1) Hellmann, C.; Paquin, F.; Treat, N. D.; Bruno, A.; Reynolds, L. X.; Haque, S. A.; Stavrinou, P. N.; Silva, C.; Stingelin, N. Controlling the Interaction of Light with Polymer Semiconductors. *Adv. Mater.* **2013**, *25* (35), 4906–4911. https://doi.org/10.1002/adma.201300881.

(2) Erothu, H.; Sohdi, A. A.; Kumar, A. C.; Sutherland, A. J.; Dagron-Lartigau, C.; Allal, A.; Hiorns, R. C.; Topham, P. D. Facile Synthesis of poly(3-Hexylthiophene)-Block-Poly(ethylene Oxide) Copolymers via Steglich Esterification. *Polym. Chem.* **2013**, *4* (13), 3652–3655. https://doi.org/10.1039/c3py00505d.

(3) Grégoire, P.; Vella, E.; Dyson, M.; Bazán, C. M.; Leonelli, R.; Stingelin, N.; Stavrinou, P. N.; Bittner, E. R.; Silva, C. Excitonic Coupling Dominates the Homogeneous Photoluminescence Excitation Linewidth in Semicrystalline Polymeric Semiconductors. *Phys. Rev. B* **2017**, *95* (18). https://doi.org/10.1103/PhysRevB.95.180201.

(4) Niles, E. T.; Roehling, J. D.; Yamagata, H.; Wise, A. J.; Spano, F. C.; Moule, A. J.; Grey, J. K. J-Aggregate Behavior in Poly-3-Hexylthiophene Nanofibers. **2012**, 0–4. https://doi.org/10.1021/jz201509h.

(5) Dyson, M. J.; Lariou, E.; Martin, J.; Li, R.; Erothu, H.; Wantz, G.; Topham, P. D.; Dautel, O. J.; Hayes, S. C.; Stavrinou, P. N.; et al. Managing Local Order in Conjugated Polymer Blends via Polarity Contrast. *Chem. Mater.* **2019**, *31* (17), 6540–6547. https://doi.org/10.1021/acs.chemmater.8b05259.

(6) Kim, J. H.; Wood, S.; Park, J. B.; Wade, J.; Song, M.; Yoon, S. C.; Jung, I. H.; Kim, J. S.; Hwang, D. H. Optimization and Analysis of Conjugated Polymer Side Chains for High-Performance Organic Photovoltaic Cells. *Adv. Funct. Mater.* **2016**, *26* (10), 1517–1525. https://doi.org/10.1002/adfm.201504093.

(7) Himmelberger, S.; Duong, D. T.; Northrup, J. E.; Rivnay, J.; Koch, F. P. V.; Beckingham, B. S.; Stingelin, N.; Segalman, R. A.; Mannsfeld, S. C. B.; Salleo, A. Role of Side-Shain Branching on Thin-Film Structure and Electronic Properties of Polythiophenes. *Adv. Funct. Mater.* **2015**, *25* (17), 2616–2624.

https://doi.org/10.1002/adfm.201500101.

(8) Duan, C.; Willems, R. E. M.; Van Franeker, J. J.; Bruijnaers, B. J.; Wienk, M. M.; Janssen, R. A. J. Effect of Side Chain Length on the Charge Transport, Morphology, and Photovoltaic Performance of Conjugated Polymers in Bulk Heterojunction Solar Cells. *J. Mater. Chem. A* **2016**, *4* (5), 1855–1866. https://doi.org/10.1039/c5ta09483f.

(9) Mei, J.; Bao, Z. Side Chain Engineering in Solution-Processable Conjugated Polymers. *Chem. Mater.* **2014**, *26* (1), 604–615. https://doi.org/10.1021/cm4020805.

(10) Kumar, A.; Baklar, M. A.; Scott, K.; Kreouzis, T.; Stingelin-Stutzmann, N. Efficient, Stable Bulk Charge Transport in Crystalline/crystalline Semiconductor-Insulator Blends. *Adv. Mater.* **2009**, *21* (44), 4447–4451. https://doi.org/10.1002/adma.200900717.

(11) Raithel, D.; Simine, L.; Pickel, S.; Schötz, K.; Panzer, F.; Baderschneider, S.; Schiefer, D.; Lohwasser, R.; Köhler, J.; Thelakkat, M.; et al. Direct Observation of Backbone Planarization via Side-Chain Alignment in Single Bulky-Substituted Polythiophenes. *Proc. Natl. Acad. Sci. U. S. A.* **2018**, *115* (11), 2699–2704. https://doi.org/10.1073/pnas.1719303115.

(12) Delongchamp, D. M.; Kline, R. J.; Fischer, D. A.; Richter, L. J.; Toney, M. F. Molecular Characterization of Organic Electronic Films. *Adv. Mater.* **2011**, *23* (3), 319–337. https://doi.org/10.1002/adma.201001760.

(13) Roncali, J. Conjugated Poly(thiophenes): Synthesis, Functionalization, and Applications. *Chem. Rev.* **1992**, *92* (4), 711–738. https://doi.org/10.1021/cr00012a009.

(14) Capello, C.; Fischer, U.; Hungerbühler, K. What Is a Green Solvent? A Comprehensive Framework for the Environmental Assessment of Solvents. *Green Chem.* **2007**, *9* (9), 927–934. https://doi.org/10.1039/b617536h.

(15) Chen, Z.; Yan, L.; Rech, J. J.; Hu, J.; Zhang, Q.; You, W. Green-Solvent-Processed Conjugated Polymers for Organic Solar Cells: The Impact of Oligoethylene Glycol Side Chains. *ACS Appl. Polym. Mater.* **2019**, *1* (4), 804–814. https://doi.org/10.1021/acsapm.9b00044.

(16) Chen, X.; Zhang, Z.; Ding, Z.; Liu, J.; Wang, L. Diketopyrrolopyrrole-Based Conjugated Polymers Bearing Branched Oligo(Ethylene Glycol) Side Chains for Photovoltaic Devices. *Angew. Chemie - Int. Ed.* **2016**, *55* (35), 10376–10380. https://doi.org/10.1002/anie.201602775.

(17) Giovannitti, A.; Sbircea, D. T.; Inal, S.; Nielsen, C. B.; Bandiello, E.; Hanifi, D. A.;

Sessolo, M.; Malliaras, G. G.; McCulloch, I.; Rivnay, J. Controlling the Mode of Operation of Organic Transistors through Side-Chain Engineering. *Proc. Natl. Acad. Sci. U. S. A.* **2016**, *113* (43), 12017–12022. https://doi.org/10.1073/pnas.1608780113.

(18) Nielsen, C. B.; Giovannitti, A.; Sbircea, D. T.; Bandiello, E.; Niazi, M. R.; Hanifi, D. A.; Sessolo, M.; Amassian, A.; Malliaras, G. G.; Rivnay, J.; et al. Molecular Design of Semiconducting Polymers for High-Performance Organic Electrochemical Transistors. *J. Am. Chem. Soc.* **2016**, *138* (32), 10252–10259. https://doi.org/10.1021/jacs.6b05280.

(19) Pacheco-Moreno, C. M.; Schreck, M.; Scaccabarozzi, A. D.; Bourgun, P.; Wantz, G.; Stevens, M. M.; Dautel, O. J.; Stingelin, N. The Importance of Materials Design to Make Ions Flow: Toward Novel Materials Platforms for Bioelectronics Applications. *Adv. Mater.* **2017**, *29* (4). https://doi.org/10.1002/adma.201604446.

(20) Scaccabarozzi, A. D.; Stingelin, N. Semiconducting:insulating Polymer Blends for Optoelectronic Applications - A Review of Recent Advances. *J. Mater. Chem. A* **2014**, *2* (28), 10818–10824. https://doi.org/10.1039/c4ta01065e.

(21) Jahnke, A. A.; Yu, L.; Coombs, N.; Scaccabarozzi, A. D.; Tilley, A. J.; Dicarmine, P. M.; Amassian, A.; Stingelin, N.; Seferos, D. S. Polytellurophenes Provide Imaging Contrast towards Unravelling the Structure-Property-Function Relationships in Semiconductor: Insulator Polymer Blends. *J. Mater. Chem. C* **2015**, *3* (15), 3767–3773. https://doi.org/10.1039/c5tc00158g.

(22) Babel, A.; Jenekhe, S. A. Morphology and Field-Effect Mobility of Charge Carriers in Binary Blends of poly(3-Hexylthiophene) with poly[2-Methoxy-5-(2-Ethylhexoxy)-1,4- Phenylenevinylene] and Polystyrene. *Macromolecules* **2004**, *37* (26), 9835–9840. https://doi.org/10.1021/ma0482314.

(23) Clark, J.; Silva, C.; Friend, R. H.; Spano, F. C. Role of Intermolecular Coupling in the Photophysics of Disordered Organic Semiconductors: Aggregate Emission in Regioregular Polythiophene. *Phys. Rev. Lett.* **2007**, *98* (20), 1–4. https://doi.org/10.1103/PhysRevLett.98.206406.

(24) Spano, F. C.; Siddiqui, S. Exciton-Vibrational Coupling in Pinwheel Aggregates of π-Conjugated Molecules. *Chem. Phys. Lett.* **1999**, *314* (5–6), 481–487. https://doi.org/10.1016/S0009-2614(99)01078-7.

(25) Gao, Y.; Martin, T. P.; Niles, E. T.; Wise, A. J.; Thomas, A. K.; Grey, J. K. Understanding Morphology-Dependent Polymer Aggregation Properties and Photocurrent Generation in Polythiophene/fullerene Solar Cells of Variable

Compositions. *J. Phys. Chem. C* **2010**, *114* (35), 15121–15128. https://doi.org/10.1021/jp104111h.

(26) Tsoi, W. C.; James, D. T.; Kim, J. S.; Nicholson, P. G.; Murphy, C. E.; Bradley, D. D. C.; Nelson, J.; Kim, J. S. The Nature of in-Plane Skeleton Raman Modes of P3HT and Their Correlation to the Degree of Molecular Order in P3HT:PCBM Blend Thin Films. *J. Am. Chem. Soc.* **2011**, *133* (25), 9834–9843. https://doi.org/10.1021/ja2013104.

(27) Gao, Y.; Grey, J. K. Resonance Chemical Imaging of Polythiophene/fullerene Photovoltaic Thin Films: Mapping Morphology-Dependent Aggregated and Unaggregated C=C Species. *J. Am. Chem. Soc.* **2009**, *131* (28), 9654–9662. https://doi.org/10.1021/ja900636z.

(28) Korovyanko, O. J.; Österbacka, R.; Jiang, X. M.; Vardeny, Z. V. Photoexcitation Dynamics in Regioregular and Regiorandom Polythiophene FIlms.pd. **2001**, *64*, 1–6. https://doi.org/10.1103/PhysRevB.64.235122.

(29) Paquin, F.; Yamagata, H.; Hestand, N. J.; Sakowicz, M.; Bérubé, N.; Côté, M.; Reynolds, L. X.; Haque, S. A.; Stingelin, N.; Spano, F. C.; et al. Two-Dimensional Spatial Coherence of Excitons in Semicrystalline Polymeric Semiconductors: Effect of Molecular Weight. *Phys. Rev. B - Condens. Matter Mater. Phys.* **2013**, *88* (15), 12–14. https://doi.org/10.1103/PhysRevB.88.155202.

(30) Koch, F. P. V.; Rivnay, J.; Foster, S.; Müller, C.; Downing, J. M.; Buchaca-Domingo, E.; Westacott, P.; Yu, L.; Yuan, M.; Baklar, M.; et al. The Impact of Molecular Weight on Microstructure and Charge Transport in Semicrystalline Polymer Semiconductors-poly(3-Hexylthiophene), a Model Study. *Prog. Polym. Sci.* **2013**, *38* (12), 1978–1989. https://doi.org/10.1016/j.progpolymsci.2013.07.009.

(31) Noriega, R.; Rivnay, J.; Vandewal, K.; Koch, F. P. V; Stingelin, N.; Smith, P.; Toney, M. F.; Salleo, A. A General Relationship between Disorder, Aggregation and Charge Transport in Conjugated Polymers. *Nat. Mater.* **2013**, *12* (11), 1038–1044. https://doi.org/10.1038/nmat3722.

(32) Shin, N.; Richter, L. J.; Herzing, A. A.; Kline, R. J.; DeLongchamp, D. M. Effect of Processing Additives on the Solidification of Blade-Coated Polymer/fullerene Blend Films via in-Situ Structure Measurements. *Adv. Energy Mater.* **2013**, *3* (7), 938–948. https://doi.org/10.1002/aenm.201201027.

(33) Abdelsamie, M.; Zhao, K.; Niazi, M. R.; Chou, K. W.; Amassian, A. In Situ UV-Visible Absorption during Spin-Coating of Organic Semiconductors: A New Probe for Organic Electronics and Photovoltaics. *J. Mater. Chem. C* **2014**, *2* (17), 3373–

3381. https://doi.org/10.1039/c3tc32077d.

(34) Liu, Y.; Zhao, J.; Li, Z.; Mu, C.; Ma, W.; Hu, H.; Jiang, K.; Lin, H.; Ade, H.; Yan, H. Aggregation and Morphology Control Enables Multiple Cases of High-Efficiency Polymer Solar Cells. *Nat. Commun.* **2014**, *5* (9), 1–8. https://doi.org/10.1038/ncomms6293.

(35) Hellmann, C.; Treat, N. D.; Scaccabarozzi, A. D.; Hollis, J. R.; Fleischli, F. D.; Bannock, J. H.; De Mello, J.; Michels, J. J.; Kim, J. S.; Stingelin, N. Solution Processing of Polymer semiconductor:Insulator Blends - Tailored Optical Properties through Liquid-Liquid Phase Separation Control. *J. Polym. Sci. Part B Polym. Phys.* **2015**, *53* (4), 304–310. https://doi.org/10.1002/polb.23656.

(36) Spano, F. C.; Silva, C. H- and J-Aggregate Behavior in Polymeric Semiconductors. *Annu. Rev. Phys. Chem.* **2014**, *65*, 477–500. https://doi.org/10.1146/annurev-physchem-040513-103639.

(37) Hellmann, C.; Treat, N. D.; Scaccabarozzi, A. D.; Hollis, J. R.; Fleischli, F. D.; Bannock, J. H.; De Mello, J.; Michels, J. J.; Kim, J. S.; Stingelin, N. Solution Processing of Polymer semiconductor:Insulator Blends - Tailored Optical Properties through Liquid-Liquid Phase Separation Control. *J. Polym. Sci. Part B Polym. Phys.* **2015**, *53* (4), 304–310. https://doi.org/10.1002/polb.23656.

(38) Yamagata, H.; Spano, F. C. Interplay between Intrachain and Interchain Interactions in Semiconducting Polymer Assemblies: The HJ-Aggregate Model. *J. Chem. Phys.* **2012**, *136* (18). https://doi.org/10.1063/1.4705272.

(39) Patel, S. N.; Javier, A. E.; Beers, K. M.; Pople, J. A.; Ho, V.; Segalman, R. A.; Balsara, N. P. Morphology and Thermodynamic Properties of a Copolymer with an Electronically Conducting Block: Poly(3-Ethylhexylthiophene)-Block-Poly(ethylene Oxide). *Nano Lett.* **2012**, *12* (9), 4901–4906. https://doi.org/10.1021/nl302454c.

(40) Erothu, H.; Kolomanska, J.; Johnston, P.; Schumann, S.; Deribew, D.; Toolan, D. T. W.; Gregori, A.; Dagron-Lartigau, C.; Portale, G.; Bras, W.; et al. Synthesis, Thermal Processing, and Thin Film Morphology of poly(3-Hexylthiophene)-Poly(styrenesulfonate) Block Copolymers. *Macromolecules* **2015**, *48* (7), 2107–2117. https://doi.org/10.1021/acs.macromol.5b00213.

(41) Park, S. J.; Kang, S. G.; Fryd, M.; Saven, J. G.; Park, S. J. Highly Tunable Photoluminescent Properties of Amphiphilic Conjugated Block Copolymers. *J. Am. Chem. Soc.* **2010**, *132* (29), 9931–9933. https://doi.org/10.1021/ja1004569.

(42) Hoffmann, S. T.; Bässler, H.; Koenen, J. M.; Forster, M.; Scherf, U.; Scheler, E.;

Strohriegl, P.; Köhler, A. Spectral Diffusion in Poly(para-Phenylene)-Type Polymers with Different Energetic Disorder. *Phys. Rev. B - Condens. Matter Mater. Phys.* **2010**, *81* (11), 1–8. https://doi.org/10.1103/PhysRevB.81.115103.

(43) Zhao, K.; Yu, X.; Li, R.; Amassian, A.; Han, Y. Solvent-Dependent Self-Assembly and Ordering in Slow-Drying Drop-Cast Conjugated Polymer Films. *J. Mater. Chem. C* **2015**, *3* (38), 9842–9848. https://doi.org/10.1039/c5tc02415c.

(44) Boudouris, B. W.; Ho, V.; Jimison, L. H.; Toney, M. F.; Salleo, A.; Segalman, R. A. Real-Time Observation of poly(3-Alkylthiophene) Crystallization and Correlation with Transient Optoelectronic Properties. *Macromolecules* **2011**, *44* (17), 6653–6658. https://doi.org/10.1021/ma201316a.

(45) Rivnay, J.; Mannsfeld, S. C. B.; Miller, C. E.; Salleo, A.; Toney, M. F. Quantitative Determination of Organic Semiconductor Microstructure from the Molecular to Device Scale. *Chem. Rev.* **2012**, *112* (10), 5488–5519. https://doi.org/10.1021/cr3001109.

(46) Hansen, C. M. *Hansen Solubility Parameterss: A User's Handbook*; CRC Press, Boca Raton, FL, USA, 2007.

(47) Barton, A. F. M. Solubility Parameters. *Chem. Rev.* **1982**, *75* (6), 731–751. https://doi.org/10.1177/004051758205200904.

(48) Huang, J. C.; Deanin, R. D. *Multicomponent Solubility Parameters of Poly(vinyl Chloride) and Poly(tetramethylene Glycol)*; 2005; Vol. 227. https://doi.org/10.1016/j.fluid.2004.11.005.

(49) Scharsich, C.; Lohwasser, R. H.; Sommer, M.; Asawapirom, U.; Scherf, U.; Thelakkat, M.; Neher, D.; Köhler, A. Control of Aggregate Formation in poly(3-Hexylthiophene) by Solvent, Molecular Weight, and Synthetic Method. *J. Polym. Sci. Part B Polym. Phys.* **2012**, *50* (6), 442–453. https://doi.org/10.1002/polb.23022.

(50) Levine, H.; Slade, L. *Water as a Plasticizer: Physico-Chemical Aspects of Low-Moisture Polymeric Systems*; 2010. https://doi.org/10.1017/cbo9780511552083.002.

(51) Kjellander, R.; Florin, E. Water Structure and Changes in Thermal Stability of the System Poly(ethylene Oxide)-Water. *J. Chem. Soc. Faraday Trans. 1 Phys. Chem. Condens. Phases* **1981**, *77* (9), 2053–2077. https://doi.org/10.1039/F19817702053.

(52) Carlsson, M.; Hallén, D.; Linse, P. Mixing Enthalpy and Phase Separation in a Poly(propylene Oxide)-Water System. *J. Chem. Soc. Faraday Trans.* **1995**, *91* (14), 2081–2085. https://doi.org/10.1039/FT9959102081.

Chapter 6

Photoactive layer morphology and organic metal interface

Thus far, we have examined inherent properties of P3HT and its derivatives and discussed the conformation of thin films which potentially can be of interest for various technological applications apart from OPVs such as electrochemical transistors and biocompatible sensing elements. To orient this fundamental study towards OPV applications, it is essential to consider the conformation of the photoactive layer which consists of both P3HT (or any other electron donating material) and an electron accepting material, which here is PCBM. To this end, this chapter focuses on the archetypal P3HT:PCBM system and is divided in two separate topics. The first one is the evaluation, by means of resonance Raman (RR) spectroscopy, of the impact of P3HT polymorph distribution ("densely" and "non-densely" packed structural motifs) on the energetic disorder of the blend. For the second topic, semi-complete OPV devices are employed, to explore the interface between a silver electrode and the photoactive layer. The buried organic/metal interface is experimentally accessible through Surface Enhanced Resonance Raman spectroscopy (SERRS) which reveals the polymer structure in close proximity to the metal. We investigate in this case P3HT:PCBM blends as well as neat P3HT films and explore how the structure is affected by the presence of specific additives in the blend, employed to spontaneously generate an interlayer at the organic-metal interface. For both cases, the correlation of structure with organic solar cell (OSC) characteristics is discussed considering experiments performed at collaborating institutions. Investigation of P3HT structural polymorphs is part of collaboration with Prof. Keivanidis,[1] while research on organic-metal interfacial properties was conducted in collaboration with the group of Prof. Gitti Frey from Technion.[2]

*Reproduced in part with permission from "J. Phys. Chem. C **2018**, 122, 29141−29149" published by the American and from "*J. Mater. Chem. C*, **2018**, 6, 8060—8068" published by the Royal Society of Chemistry.

6.1 Background

The bulk heterojunction OPV architecture was introduced back in the 90's,[3,4] aiming to provide an efficient heterojunction for charge separation, facilitating as well charge carrier transport towards the respective electrode.[5] The preparation of OPV photoactive layers where microstructure is critical to the final PCE of the device is a complex task that relies on well-established protocols as well as empirical procedures. Frequently applied approaches towards controlling microstructure and device characteristics include thermal annealing,[6] careful selection of P3HT's molecular weight,[7] controlled plasticization and the use of additives.[8] A less explored factor that can be controlled by means of processing is material polymorphism i.e the presence of multiple structural motifs (crystalline and/or amorphous) in the solid-state phase. Regarding polymorphism in P3HT, experimental and computational fundamental studies exist, attempting to correlate molecular order to charge transport,[9,10] while Panzer et.al. reported evidence for the presence of two distinct P3HT polymorphs in single-component P3HT films by means of temperature dependent fluorescence.[11] However, the presence of P3HT polymorphs in binary blends such as the archetypal P3HT:PCMB OPV system is less explored,[12] let alone the correlation of their presence with OPV's photophysical processes and device characteristics. The two types of polymorphs, which is the focus of the first part of this chapter, can be described in terms of lamellar packing distance (side chain interdigitation) as a) densely-packed and b) non-densely packed for short and larger stacking distance respectively.[13] The distribution of polymorphs can be controlled by varying the number-averaged molecular weight (M_n) of the P3HT polymer matrix. We examine here a bimodal distribution (coexistence of "densely" and "non-densely" packed polymorphs) obtained by low-M_n-P3HT-based blend and a uniform distribution of "non-densely" packed, resulting from high-M_n P3HT-based P3HT:PCMB blend.[13]

A different approach to the study of P3HT:PCBM binary blends is adopted in the second part of this chapter, where we primarily investigate the structure of the polymer/electrode interface, considering also the properties of the bulk and exploring possible composition gradients due to vertical organisation within the blend. The study of OPV's interfacial structure is based on the utilisation of SERRS. SERRS is a relatively novel approach for this purpose and has been mostly considered as a means for increasing the photocurrent of OPVs by the exploitation of surface plasmon resonance (SPR),[14–18] rather than studying interfacial properties, with very few examples in existing literature.[19,20] Here SERRS will be employed for the study of the interface between silver (Ag) and the photoactive layer of semi-complete OPV devices. Silver, is a highly stable metal, however, it is rarely chosen as a cathode

material due to its high work function (Φ = 4.3eV[21]) imposing a significant barrier for electron extraction.[22] This problem is often addressed by the use of interlayers which either enhance charge collection,[23] or modify the work function of the electrode.[23] An efficient and cost-effective way to create interlayers demonstrated by Deckman et al. is their spontaneous generation through additive migration –initially blended into P3HT:PCBM solution- towards the metal interface during deposition. Additives are carefully selected to encourage interactions between their end groups and the deposited metal clusters.[24,25] In this study two thiol-terminated additives; hexa(ethyleneglycol)-dithiol (HEG-DT) and 1,4-benzenedimethanethiol (BDMT), which are known to form interlayers in combination with silver, are employed separately (blended into P3HT:PCBM solution) to study the effect of interlayer formation on the bulk of the photoactive layer and the near-interface molecular conformation. The near-interface structure is compared to that of the typical P3HT:PCBM blend, as well as to the structure in the bulk of the active layer.

6.2 P3HT:PCBM spectroscopic identification

Before presenting the main topics of this chapter, it's necessary to introduce the impact of blending P3HT with PCBM to its spectroscopic signature. **Figure 6.1** shows the normalised resonance Raman (RR) spectrum of neat P3HT film versus that of the blend with PCBM (1:1 weight %). Excitation wavelength is 473 nm and will be employed throughout this chapter due to its sensitivity to probe disordered populations of P3HT. Rather than directly monitoring PCBM's Raman spectrum, we focus on its effect on P3HT's chain conformation and consistently with the previous chapter, we detect vibrational modes of chemical bonds along the conjugated backbone i.e. the C-C and C=C symmetric in-plane stretching modes at 1381 and 1450 cm^{-1}, respectively. Following the interpretation demonstrated by Tsoi et al.,[26] the C=C stretching frequency of neat P3HT at 1451 cm^{-1} reflects a planar polymer chain conformation and the 1 cm^{-1} up-shift of the blend sample, doesn't suggest significant conformational distortion due to the presence of PCBM (**see Fig. 6.1**).

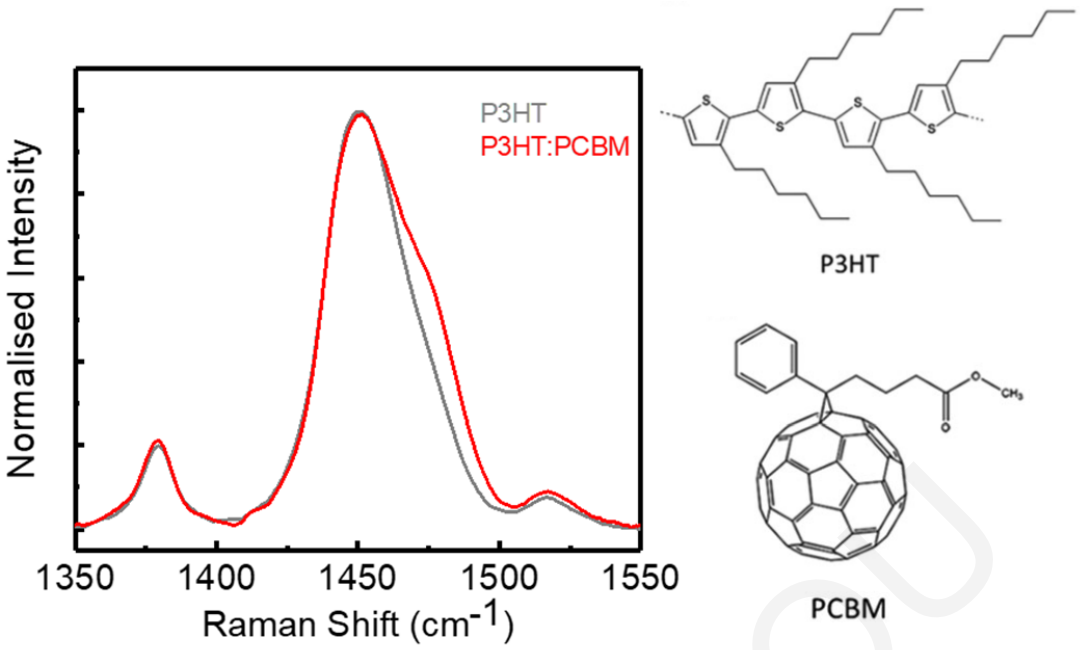

Figure 6.1: *RR spectra of neat P3HT and P3HT:PCBM blend films (chemical structures are shown on the left) excited at 473 nm.*

However, a closer inspection of the C=C stretching shows a shoulder at 1475 cm^{-1}, which results in a significantly increased FWHM of 52.5 versus 34.7 cm^{-1} for the neat film and thus, increased fraction of non-aggregated P3HT chains. Those results are in accordance with existing literature[27,28] providing evidence that PCBM hinders the organisation of P3HT. Although Falke et al. propose that the shoulder at 1475 cm^{-1} is possibly related to the pentagonal-pinch mode Ag of C_{60},[27] we choose to attribute it to the non-aggregated species of P3HT, since 473 nm is not a resonance excitation wavelength for PCBM and thus, the signal of P3HT is expected to dominate the spectrum. Moreover, an existing PCBM concentration- dependent study showed that increasing PCBM concentration above 30% (by weight) has a deleterious effect on molecular order of P3HT in blend films, further supporting the view that PCBM inhibits the planarity of P3HT chains.[28] Those results concern as-spun films and can be related to the spectra in **Fig. 6.1** which are as-spun as well. Of course, some "standard" post-treatments such as thermal annealing can modify the effect of PCBM, stabilising P3HT properties towards a thermodynamic equilibrium morphology regardless of PCBM content.

6.3 Results and discussion

6.3.1 The impact of polymorph distribution to the energetic disorder

We will primarily focus on the bulk properties of a P3HT:PCBM photoactive layer and examine its structure with respect to the bimodal versus uniform distribution of P3HT polymorphs. Bimodal distribution refers to the presence of two different types of P3HT polymorphs; i.e. densely and non-densely packed in the P3HT matrix, while uniform distribution refers to solely non-densely packed structural motif. As mentioned in section 6.1, the distribution of polymorphs results from two different P3HT matrices: a) low-M_n-P3HT-based P3HT:PCMB[60] blend, exhibiting bimodal distribution in spin-coated thin films and b) high-M_n P3HT-based blend resulting in a uniform distribution of non-densely packed polymorphs. RR study performed on as-spun versus annealed films, confirms that thermal treatment greatly enhances the planarity of P3HT backbone minimising energetic disorder.[1] Considering this observation, our study is focused solely on annealed films, deposited on two different substrates: a) glass/ITO/PEDOT:PSS (semi-complete OPV devices) and b) plain quartz. RR spectra of Low-M_n annealed P3HT:PCBM[60] blends are compared to those of high-M_n ones, recorded at room and low temperature (50 K) (see **Fig. 6.2**). At a first glance, it's hard to distinguish spectral changes between the two samples as both samples have probably reached their optimum morphology due to the thermal processing applied. Thus, we performed additionally low temperature measurements (50 K) to detect possible changes in the spectral signature of the two polymorph types bellow the transition temperature (265 K).[29]

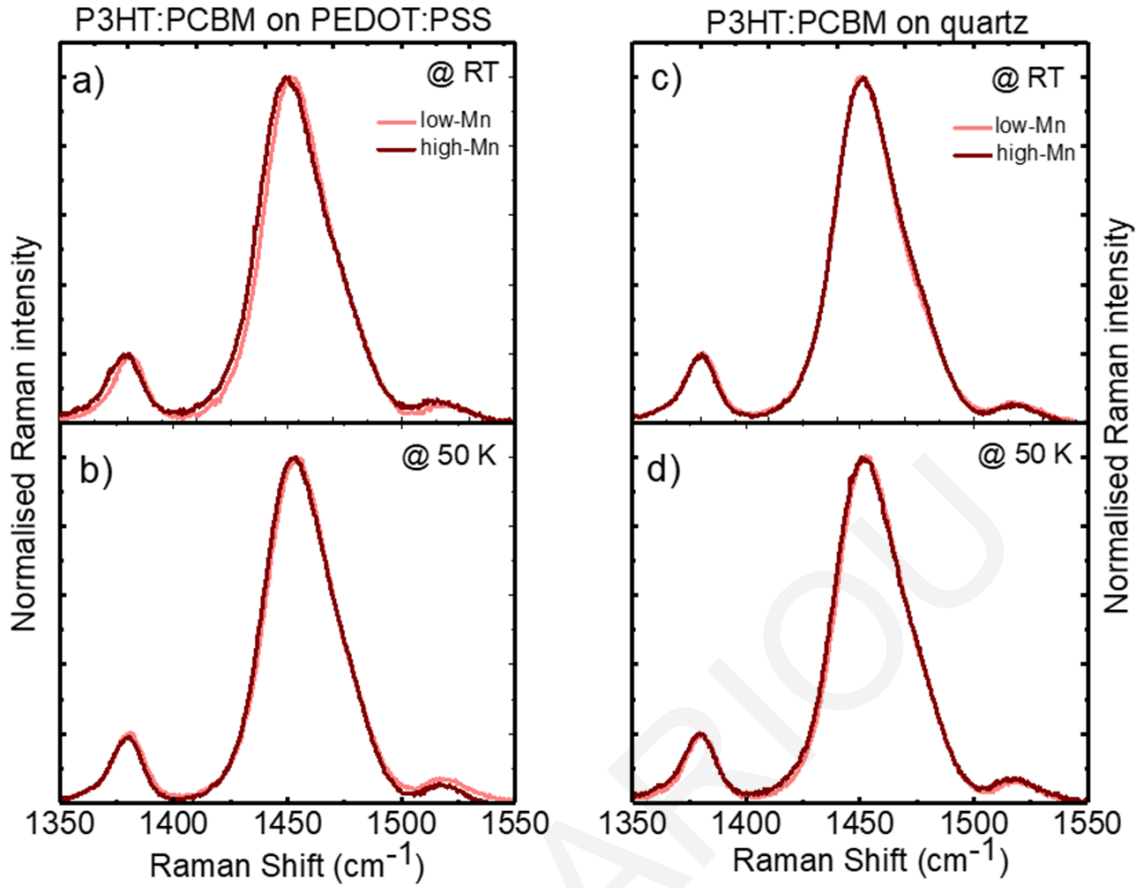

Figure 6.2: *RR spectra of semi-complete P3HT:PCBM[60] devices with thermally annealed P3HT:PCBM[60] photoactive layers developed by low- and high-M_n P3HT and acquired at a) room temperature and b) at 50 K. Resonance Raman spectra of thermally annealed P3HT:PCBM[60] films deposited on plain quartz substrates developed by low- and high-M_n P3HT and acquired at c) room temperature and d) at 50 K. Excitation wavelength is 473 nm.*

Data analysis summarised at **Table. 6.1** (and visualised at **Figure 6.3)** reveals that interestingly, some energetic disorder persists in the absence of densely packed polymorphs (High-M_n-P3HT based blends). This conclusion is drawn due to the larger FWHM of the C=C stretching mode –suggesting the presence of more than one competitive conformations- which is consistently observed at high-M_n blends, regardless of the film substrate and the temperature that the measurement was performed. The location of the C=C stretching mode on the other hand, was not a sensitive indicator of molecular conformation this time, exhibiting minute variations that is hard to safely evaluate.

Table 6.1: *RR spectra's extracted parameters of room and low (50K) temperature obtained for the annealed P3HT:PCBM[60] films*

System (Annealed samples)	Room temperature		50 K	
	C=C centre (± 0.7 cm^{-1})	C=C FWHM (± 1 cm^{-1})	C=C centre (± 0.7 cm^{-1})	C=C FWHM (± 1 cm^{-1})
high-M_n, PEDOT:PSS	1449.5	35	1453.0	36
low-M_n, PEDOT:PSS	1451.7	33	1454.5	34
high-M_n, quartz	1451.4	34	1451.5	37
low-M_n, quartz	1451.0	33	1452.4	36

Another interesting feature is that an overall increase in FWHM is observed at low temperature, having a negative impact on backbone planarity, which could possibly be related to a different arrangement of the side chains upon cooling. Similar behaviour was observed by Martin et. al. in a study of P3HT nanofiber structures with pressure and temperature dependent photoluminescence (PL) measurements.[30] Upon decreasing nanofiber volume (while cooling or increasing the pressure) a change in the arrangement of the alkyl side groups occurs, lowering intra-chain order. Although variations attributed to the two different types of substrates would be expected, because they are known to affect the degree of vertical phase separation of P3HT and PCBM component,[31,32] this dependence was not observed at room temperature measurements. Of course all samples exhibit highly ordered molecular conformation due to the thermal annealing, and changes observed between the two different types of P3HT matrices although are clear, they are not considered significant.

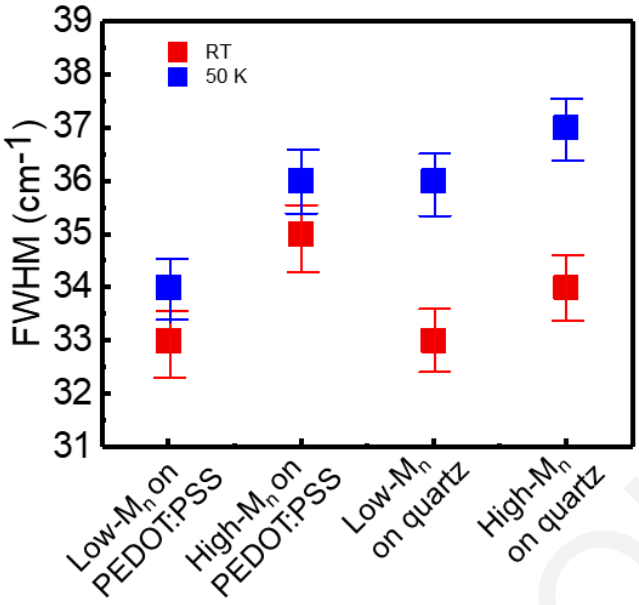

Figure 6.3: *Comparative results for the width (FWHM) of the Raman C=C stretching mode of the thiophene ring in P3HT:PCBM blend films spectra as obtained at room temperature (red) and low temperature (50 K) (blue).*

Conclusively, RR can effectively probe the content of energetic disorder in the studied P3HT:PCBM[60] layers which is correlated to the absence of densely packed P3HT polymorphs in the layers. Adopting a spectroscopic approach for this purpose is straightforward, however direct quantification of the energetic disorder would require electrical device characterization techniques e.g. by monitoring the temperature dependence of charge carrier mobility.

6.3.2 Correlating energetic disorder with power conversion efficiency (PCE)

OPV devices, based on identically processed photoactive layers to those used for the RR experiments can provide a direct link to the device performance of these systems. **Table 6.2** presents a comparison of the figures-of-merit of the two types of OPV devices when the two different M_n P3HT derivatives are used (extracted under simulated solar illumination from current density-voltage (*J-V*) curves). Each figure-of-merit presented, (namely the short-circuit current density (J_{sc}), the open-circuit voltage (V_{oc}), the fill factor (FF) and the power conversion efficiency (PCE)) is a mean value of 4-5 devices from each system, accompanied by the corresponding standard deviation. The maximum PCE of 2.3% is obtained from the low-M_n-P3HT matrix, being an acceptable performance for conventional P3HT:PCBM devices.[33]

Table 6.2*: Figures-of-merit for the two different P3HT:PCBM photoactive layers*

Device type	J_{sc} (mA cm^{-2})	V_{oc} (mV)	FF (%)	PCE (%)
Annealed high-M_n-P3HT	5.16 ± 0.17	564 ±4	30.7 ± 1.1	0.89 ± 0.04
Annealed low-M_n-P3HT	7.00 ± 0.10	545 ± 2	60 ± 0.8	2.3 ± 0.06

Together with the increased PCE of these samples, another interesting feature is the averaged FF parameter that reaches 60%. Those results potentially can be associated to the lower energetic disorder found in low-Mn-P3HT, however they are not sufficient to describe the impact of polymorphism on device performance and explain the high FF parameter. To be able to correlate energetic disorder to power conversion efficiency (PCE) it is essential to additionally consider and evaluate the impact of competing processes such as nongeminate recombination and charge extraction. Insights on photo-physical processes such as charge recombination can be obtained by transient absorption (TA) spectroscopy. Experiments were performed at ultrafast (ps-ns) timescales and data are shown in **Figure 6.4 a** and **b** for the films prepared with the low-M_n and high-M_n P3HT, respectively. The evolution of TA spectra is similar for both systems exhibiting the characteristic ground-state bleach (GSB) of P3HT at 2.0 eV, photo-induced absorption (PA) between 1.2 and 1.4 eV and stimulated emission (SE) of singlet excitons between 1.5 and 1.8 eV. The dynamics of the photogenerated charges can be monitored in the spectral region around 1.2-1.3 eV of the PA band. The SE band can be tracked up to 4 ps, while later on it is masked by the emergence of charge-induced absorption, which coexists with the exciton-induced absorption up to 30 ps after photoexcitation. If we consider previously reported exciton diffusion coefficient of crystalline P3HT to be between 1.8-7.9 x 10^{-3} cm^2 s^{-1},[34] from the lifetime of the SE signal we deduce that P3HT excitons can probe a distance of 2.3-4.8 nm of P3HT domains in the P3HT:PCBM[60] blends. At later times, the remaining PA band is exclusively charges. The extracted TA kinetics of the photogenerated charge carriers, shown in Figure **6.4 c** and **d** reveal differences in the charge carrier dynamics. The decay dynamics accelerate at high photoexcitation fluences for both systems, indicating that at early delay times, higher-order processes such as exciton-charge or exciton-exciton annihilation occur. By using a range of photo-excitation intensities it's clear that TA kinetics are considerably faster when the low-M_n P3HT derivative is used.

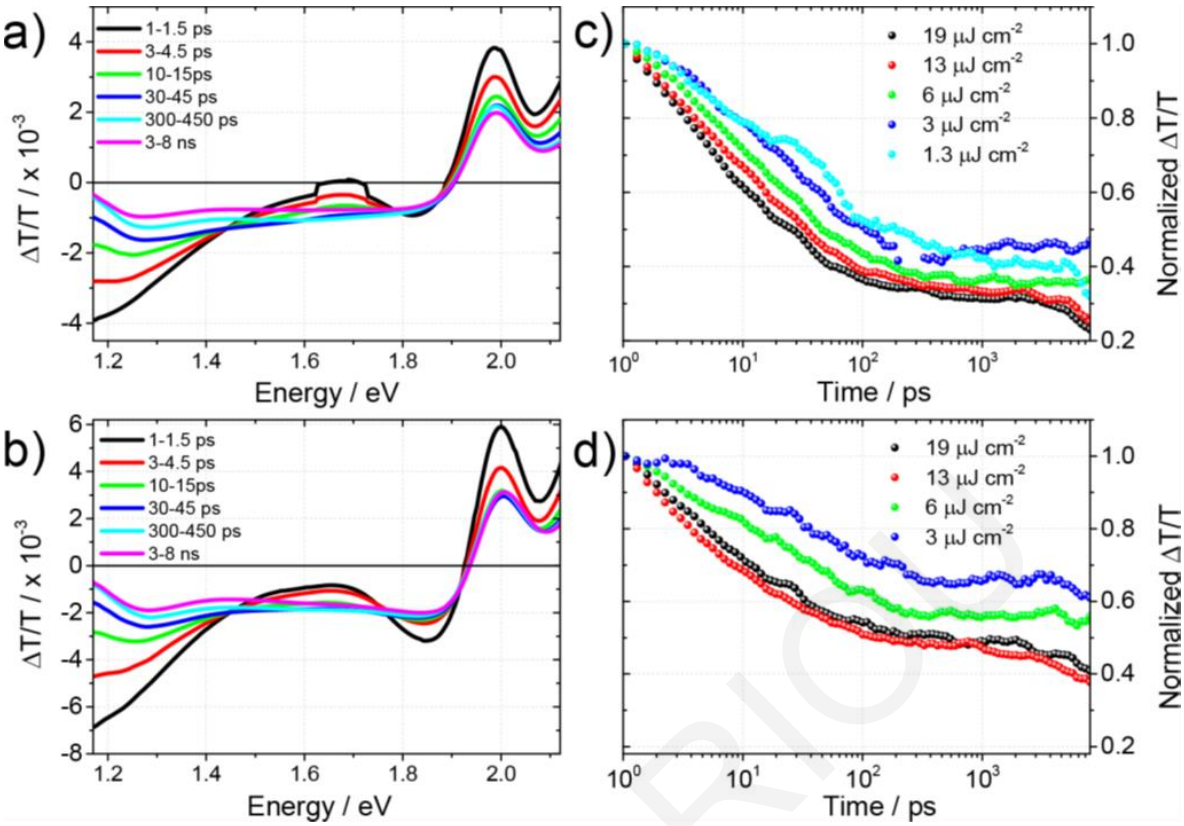

Figure 6.4*: ps−ns transient absorption spectra for annealed P3HT:PCBM[60] blend films developed by (a) a low-Mn P3HT derivative and (b) high-Mn P3HT derivative. Fluence-dependent kinetics extracted at the region of photoinduced absorption in the spectral range of 1.2−1.3 eV for annealed P3HT:PCBM[60] blend films developed by (c) a low-Mn P3HT derivative and (d) high-Mn P3HT derivative. The TA spectra shown in (a) and (b) were registered with a fluence of 19 μJ cm*$^{-2}$*.*[1]

Having qualitative evidence from TA regarding non-geminate recombination rate (which is faster in the case of the low-M_n P3HT-based blend), we can explore whether the antagonistic process of charge carrier extraction is efficient enough, to compensate for the fast non-geminate recombination. Charge carrier collection can be monitored by time-delayed collection field (TDCF) experiments,[35] a powerful tool to study the efficiency of free charge generation and the dynamics of non-geminate recombination. In the TDCF experiment the device is illuminated by a short laser pulse, while being kept at constant pre-bias voltage (V_{pre}). After a variable time delay (t_d), a rectangular bias voltage (V_{coll}) with 1μs pulse length is applied to extract (collect) all remaining free carriers from the device. The measured photocurrent response exhibits two peaks, one following photoexcitation and a second after application of the V_{coll} extraction pulse. Integration of the area below the two curves yields the quantity of charges generated by photoexcitation (Q_{pre}) and extracted before (with an applied V_{pre} bias) and during (Q_{col}) the application of the collection field, respectively (with an applied V_{coll} bias). The sum of Q_{pre} and Q_{col} equals the total number of generated charges Q_{tot}. **Figure 6.5** shows the dependence of photocurrent generation on the laser fluence for

the low and high-M_n P3HT-based devices when photoexcited at 532 nm with a sub-ns pulse. For a constant t_d of 10 ns and a constant prebias voltage (V_{pre}= 0), the laser fluence was varied between 0.1 and 4.4 μJcm^{-2}. The data were fitted linearly based on the power-law function $Q \propto I_{exc}^{a}$ where Q corresponds to the generated charge and I_{exc} to the laser fluence. Prior to the application of the rectangular bias voltage, V_{coll}, the high-M_n-P3HT based device generated more Q_{pre} across the whole range of laser fluences applied while the low-M_n P3HT-based device collects a smaller amount. Evidently from the deviation of the power-law exponent "a" from linearity, this can be attributed to geminate charge recombination losses at short-circuit conditions. The values of the α exponent were found to be very close to unity for both types of photoactive layer; with α=0.93 and α=0.99 for the devices with low-M_n P3HT-based and high-M_n P3HT-based layers, respectively. Interestingly, after applying the rectangular bias voltage (V_{coll}= −4 V) the situation is reversed and the largest amount of total collected charge, Q_{tot}, is delivered by the low-M_n P3HTbased OPV device. The improved charge extraction efficiency of the low-M_n P3HT-based device with respect to the high-M_n P3HT-based device can be understood because of a photogeneration mechanism that is operative in the presence of the static external field created by the bias pulse V_{coll}. The electric field has a typical value of 40x10^6 Vm^{-1}, which, considering the thickness of the photo-active layer, is sufficient for fully dissociating the residual geminate charge pairs in the low-M_n P3HT-based system. However, those results suggest also increased charge recombination losses, obvious from the decreased value of the power-law exponent a= 0.72.

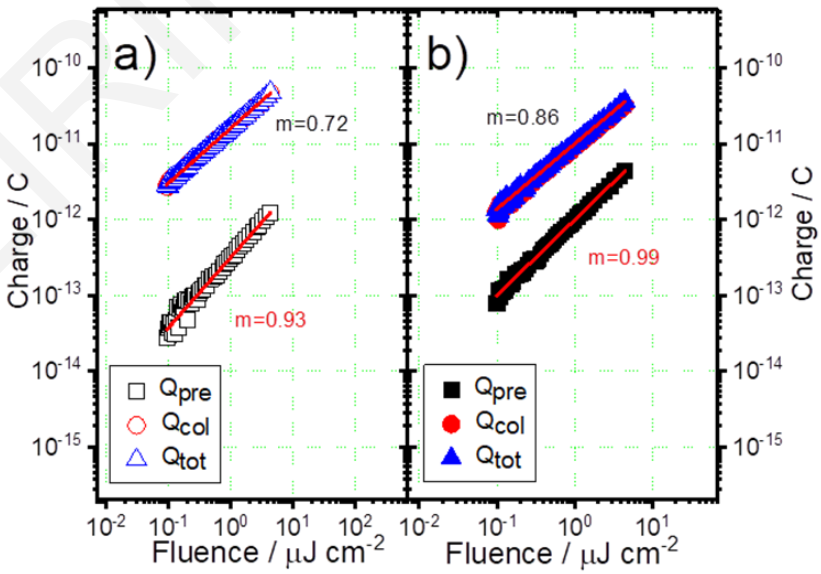

Figure 6.5: *Collected charge as a function of fluence measured with t_d =10 ns and V_{pre}= 0 V (short-circuit conditions) (a) of low-M_n P3HTPCBM device and (b) of high-M_n P3HT:PCBM[60] device. Both device types were based on annealed P3HT:PCBM[60] layers. The solid lines are linear fits to the data (based on the functional form $Q \propto I_{exc}^{\alpha}$)* [1]

This is also supported by modifying this experiment by a gradual increase of the applied pre-bias (V_{pre} between -1 and 0.6 V) while keeping laser fluence constant at 1μJ cm^{-2} and t_d at 10 ns. **Figure 6.6 a** and **b** show that the total number of generated charges is independent of the field created by V_{pre}. Hence, in both systems the fill factor is predominantly determined by non-geminate recombination losses.

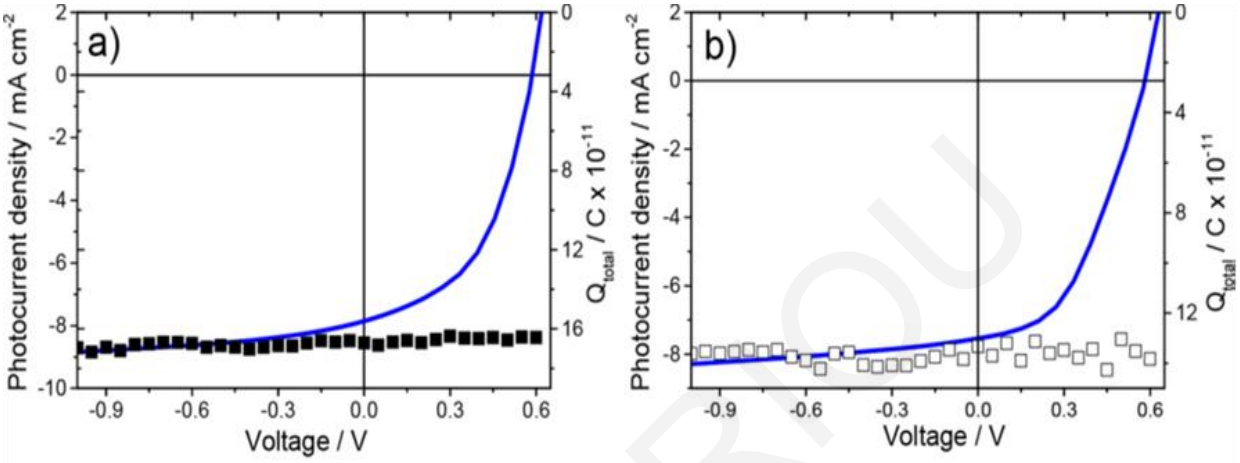

Figure 6.6*: Total amount of charge ($Q_{to}t$) extracted from the device as a function of applied pre-bias and the corresponding J−V curves of devices prepared with annealed photoactive layers of (a) low-M_n P3HT:PCBM[60] and (b) high-M_n P3HT:PCBM[60].*[1]

Considering the results obtained by TDCF, TA and RR we can safely describe the effect of the presence of the densely packed P3HTpolymorph on the device performance. TDCF results suggest that the low-M_n-P3HT-based devices -containing the densely packed P3HT polymorph- have the capacity to facilitate charge carrier collection in the presence of an external electric field and that the charge collection efficiency in this system dominates over the antagonistic process of non-geminate charge recombination which is fast according to the TA data. The charge collection efficiency enables the high FF determined for the low-M_n-based devices and reasonably explains the high PCE compared to the high-M_n-based devices. Finally, the lower energetic disorder in the presence of densely packed P3HT polymorphs –evident from the RR results- supports high charge extraction rates,[36] and is a possible explanation regarding the mechanism that leads to the efficient charge collection.

6.3.3 Exploring molecular conformation at the metal-organic interface

Considering the bulk properties of an OPV's active-layer is usually the primal focus while studying device performance. However, the presence of a top and bottom electrode can drastically affect the organic-metal interfacial properties and inhibit charge transport and collection. For example, a crucial parameter for the efficiency of charge injection and collection in OPVs is the energy level alignment at organic semiconductor/metal interfaces. An effective platform to adjust the energy level alignment is introducing interlayers of organic or inorganic compounds between the organic semiconductor and the metal[37] in order to modify the work function of the metal, resulting in a different alignment of the interfacial energy levels.[23,38] The approach employed in this study to control energy level alignment is based on self-generated interlayers formed by the migration of additives from the bulk of the active layer to the organic/metal interface.[22,24,25] The two additives chosen are hexa(ethyleneglycol)dithiol (HEG-DT) and 1,4-benzenedimethanethiol (BDMT) (**Fig. 6.7** *inset*) due to their thiol end groups which interact with the silver (Ag) electrode facilitating the formation of the interlayer. The effect of interlayer formation on the molecular conformation near the interface is studied *via* surface-enhanced resonance Raman spectroscopy (SERRS). SERR scattering, is a mechanism (described in detail in section 3.3) that offers selective enhancement of the signal from the metal-polymer interface, enabling the study of the polymer's micro-structure. This can be achieved through the enhancement of the electric field "felt" by the polymer due to the metal plasmon resonance that is generated from the excitation laser light, which in turn enhances the Raman signal of any molecule within 10 nm from the metal surface.[20] The excitation wavelength at 473 nm was chosen to both probe effectively the amorphous component of the examined P3HT blend films and encourage plasmon resonance with the Ag electrode. Before exploring the conformation at the interface, it is worth focusing on the bulk first, to see how the presence of the additives affect the blend structure. Molecular conformation at the bulk of the organic layer (as well as at the organic/metal interface) is studied by monitoring the effect of HEG-DT and BDMT on the Raman spectrum of P3HT. Direct fingerprint of HEG-DT or BDMT in the Raman spectra was not possible to be obtained due to the dominance of P3HT scattering (resonant conditions). Features of interest as previously are the ring C-C (1381 cm^{-1}) and C=C (1450 cm^{-1}) symmetric stretches of P3HT. The presence of additives induces conformational changes to P3HT which can be monitored with respect to neat films and P3HT:PCBM blends. The samples studied consist of a glass substrate, a polymer layer (P3HT Neat, or blends: P3HT:PCBM, P3HT:PCBM:HEG-DT, P3HT:PCBM:BDMT), or

HEG-DT and BDMT were deposited as a separate layer (P3HT:PCBM|HEG-DT, P3HT:PCBM|BDMT)) and a thin Ag layer sandwiched between them (see **Fig 6.7**). No further post-treatment (ex. annealing) was applied. Properties of the bulk can be studied by targeting samples away from silver as shown in **Fig. 6.7** (*right*). The presence of additives induces conformational changes to the Raman spectra with respect to neat P3HT and P3HT:PCBM blends at the bulk of the active layer, quantified at the **Table 6.3**.

Table 6.3*: Extracted parameters from RR spectra for the various systems referring to the bulk properties.*

System	Bulk Film		
	C=C centre (± 0.7 cm^{-1})	C=C FWHM (± 1 cm^{-1})	C-C/C=C (± 0.05)
P3HT	1450.6	35	0.19
P3HT:PCBM	1450.9	43	0.20
P3HT:PCBM:HEG-DT	1450.5	33	0.21
P3HT:PCBM:BDMT	1451.2	37	0.22
P3HT:PCBM|HEG-DT	1452.1	42	0.20
P3HT:PCBM|BDMT	1453.1	44	0.21

In more detail, HEG-DT when blended with P3HT and PCBM (P3HT:PCBM:HEG-DT) causes a significant narrowing of the C=C stretching mode by 10 cm^{-1} compared to P3HT:PCBM and by 2 cm^{-1} compared to neat P3HT, minimising the contribution of torsionally disordered chains (high frequency shoulder at 1470 cm^{-1} almost disappears).[26] The effect of BDMT on the structure of the blend is similar but less significant than HEG-DT, causing a 6 cm^{-1} narrowing of the C=C stretch compared to P3HT:PCBM, being broader however by 2 cm^{-1} compared to P3HT neat. The effect of the additives in the conformation of the active layer is different when they are not blended in the organic film but deposited as a separate layer, exhibiting comparable FWHM to the P3HT:PCBM blend and up-shifting the thiophene's C=C stretching position by 2 cm^{-1} and 3 cm^{-1} for HEG-DT and BDMT respectively. Those results indicate that incorporating additives in the P3HT:PCBM photoactive layer, has a positive effect on the microscopic ordering of the chains but only when those additives are blended in the organic layer.

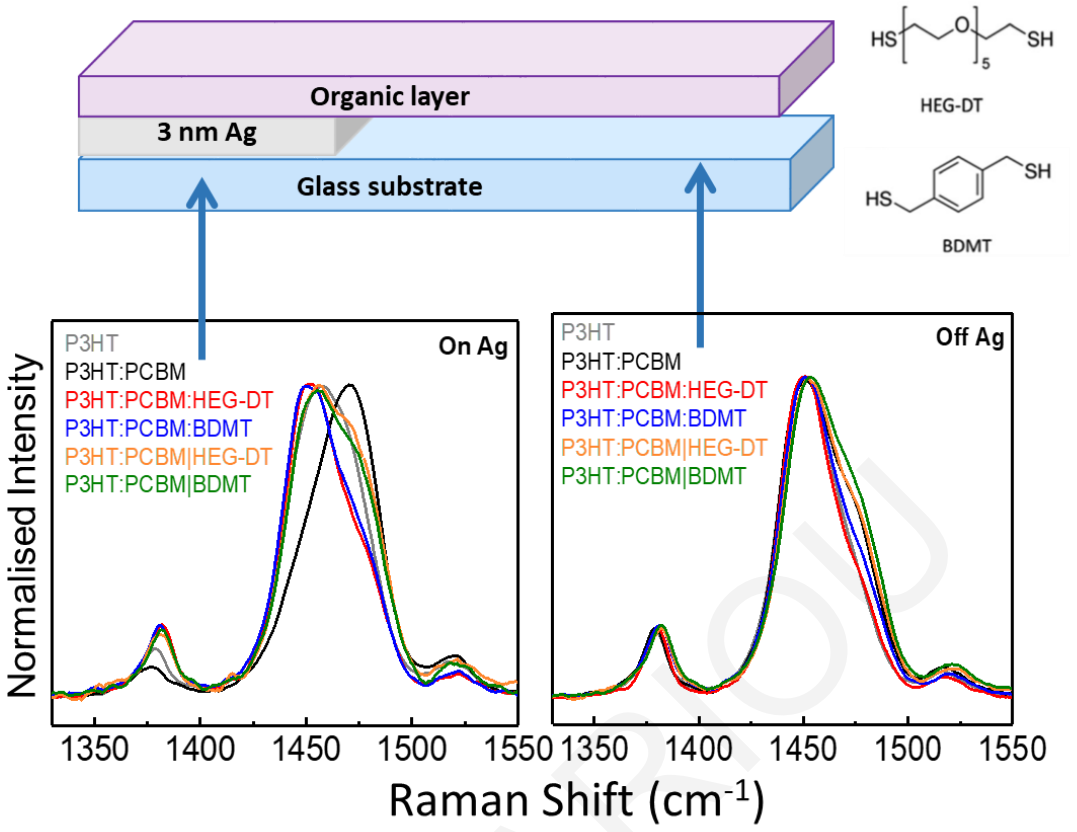

Figure 6.7*: SERR (targeting the silver patch) and RR (probing the organic layer) spectra of P3HT neat and blend thin films with PCBM, PCBM:HEG-DT, PCBM:BDMT. Samples were irradiated from the back as depicted in the scheme, excitation wavelength was 473 nm. Chemical structures of HEG-DT and BDMT are also included.*

An entirely different structural signature is observed for most samples when probed at the organic/metal interface as shown in **Fig. 6.7** *(left)*. Neat P3HT samples, exhibit a 7 cm^{-1} shift of the C=C stretching position to higher frequencies compared to the spectra recorded in the bulk, accompanied by a 7 cm^{-1} broadening of the same mode and a slight reduction of the C-C/C=C stretching modes intensity ratio, clearly suggesting a distortion of P3HT chain planarity at the interface with Ag. This effect is even more pronounced in P3HT:PCBM blends where the thiophene's C=C stretch is up-shifted by 20 cm^{-1} , a characteristic location centre for the regiorandom P3HT, suggesting the dominant presence of the torsionally disordered chains.[26] The distortion of chain planarity in the absence of additives at the interface with a metal electrode has been previously reported and attributed to the proximity with a rough metal surface which is likely to disrupt the order of P3HT chains.[20,39]

Interestingly, when HEG-DT is incorporated in the P3HT:PCBM blend, this effect is prevented, with the conformation minimally disturbed by the presence of Ag, causing a 6 cm^{-1} broadening of the C=C stretch, but not affecting its position and the C-C/C=C intensity ratio. The effect of BDMT on the conformation of the blend at the interface is similar to that of HEG-DT with the only change observed compared to the bulk properties is again a

broadening of the C=C stretch, resulting in a FWHM of 41 cm^{-1}, slightly larger compared to that of P3HT:PCBM:HEG-DT (at the interface). It's worth noticing also that when additives were deposited as a separate layer, the presence of Ag disrupted again the interfacial conformation, but to a lesser extent compared to P3HT:PCBM.

Table 6.4*: RR spectra's extracted parameters for the various systems referring to the organic-metal interfacial properties.*

System	Metal-organic interface		
	C=C centre (± 0.7 cm^{-1})	C=C FWHM (± 1 cm^{-1})	C-C/C=C (± 0.05)
P3HT	1457.7	42	0.15
P3HT:PCBM	1470.7	39	0.08
P3HT:PCBM:HEG-DT	1451.1	39	0.22
P3HT:PCBM:BDMT	1450.9	41	0.21
P3HT:PCBM|HEG-DT	1456.9	46.8	0.19
P3HT:PCBM|BDMT	1456.5	46	0.20

An additional parameter we should consider while studying thin film active layers, is that blends of two or more materials during deposition can exhibit different vertical organisation leading to composition gradients with potential implications for charge extraction.[32] Thus, to evaluate the magnitude of this gradient, spectra were recorded at the bulk of the active layer from the front and back side of the samples. In **Figure 6.8** spectra of P3HT:PCBM blends with the additives are shown. Organic-air interface, effectively probed when irradiating from the front side of samples, exhibits a narrower C=C symmetric stretch at both P3HT:PCBM:HEG-DT (33 cm^{-1}) and P3HT:PCBM:BDMT (33 cm^{-1}) blends compared to the organic-substrate interface, effectively probed from the back side (37 and 41 cm^{-1} respectively). Those results possibly suggest a P3HT-rich organic-air interface (similar conformation to neat P3HT) and a corresponding PCBM-rich organic-substrate interface (features similar to those of P3HT:PCBM films). Safe conclusions regarding the additive's preferential vertical segregation cannot be extracted, since there is no direct fingerprint of it at the Raman spectra of the blends, we can only hypothesize that the additives are attracted by the blend-Ag interface during deposition as reported previously for a similar additive.[40]

This interpretation, considering the low surface energy of P3HT (~27 mJ m^{-2}) preferably attracted to the organic-air interface and respectively the high surface energy of PCBM (~38 mJ m^{-2})[40] attracted to the substrate interface provides valuable indications regarding the direction of vertical phase separation potentially facilitating electron extraction at the cathode.[32,41]

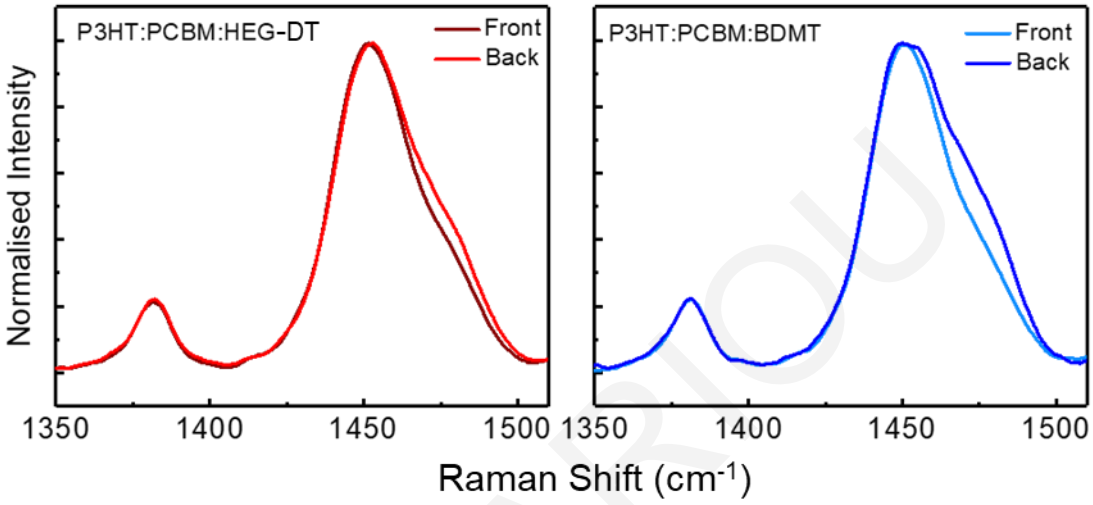

Figure 6.8: *RR spectra of P3HT:PCBM:HEG-DT (left) and P3HT:PCBM:BDMT (right) blend films recorder from the front and back side of samples. Excitation wavelength was 473 nm.*

Conclusively, incorporating HEG-DT and BDMT as additives in P3HT:PCBM blends improve the planarity of P3HT chains regardless of the presence of Ag. Their effect, however, at the organic-metal interface is significant, minimising the distortion of polymer chains caused by the metal. The self-generation of the interlayer (caused by the chemical interaction of thiol end groups with the metal during deposition) rather than its independent deposition is capable to minimise the negative effect of the metal interface, resulting in ordered microscopic arrangement of the chains which can potentially facilitate charge transport in the vicinity of Ag through inter-chain interactions. In the next section we will discuss further whether the significant modification of interfacial morphology caused by the additive migration to the organic/metal interface is sufficient to determine device characteristics.

6.3.4 Correlating interfacial conformation with organic solar cell characteristics

We begin our discussion by considering the average figures-of-merit of OSC devices incorporating HEG-DT and BDMT additives (additive content 2 mg/ml) (self-generating interlayers between the organic layer and the electrode) compared to the absence of interlayer at typical P3HT:PCBM blends presented at **Table 6.5** (extracted from current density-voltage (*J*-*V*) curves). At least 16 devices of each type were measured and the reported values are the average values accompanied by the corresponding standard deviation.

Table 6.5*: Average performance values (figures-of-merit) of OSC devices*

Active layer system	J_{sc} (mA cm^{-2})	V_{oc} (V)	FF	PCE (%)
P3HT:PCBM	6.17 ± 0.36	0.42 ± 0.01	0.42 ± 0.02	1.09 ± 0.12
P3HT:PCBM:HEG-DT	8.27 ± 1.05	0.58 ± 0.01	0.54 ± 0.01	2.57 ± 0.28
P3HT:PCBM:BDMT	6.87 ± 0.68	0.20 ± 0.01	0.32 ± 0.01	0.44 ± 0.07

From **Table 6.5** we observe that the maximum PCE of 2.57 % is obtained from the P3HT:PCBM:HEG-DT system while the lowest PCE of 0.44 % is recorded for the P3HT:PCBM:BDMT. Those results provide a first indication that although both additives have a similar (positive) effect on the interfacial morphology, this is not depicted at device characteristics, implying that charge injection and collection is not determined by the structure. Turning attention to the selected additives, we observe that despite the similar methane-thiol end groups, their cores are significantly different (see **Fig. 6.7**), with an aliphatic backbone in the case of HEG-DT and a benzene ring for BDMT. Therefore, their corresponding interlayers should impose distinctly different chemical environments at the buried organic/metal interface which is likely to determine the interfacial energy level alignment. Access to interfacial energy level alignment can be provided by measuring the sample work function and valence electronic structure prior to the deposition of the active organic layer by means of photoemission spectroscopy.[42,43] However, since it is extremely challenging to investigate the changes occurring at the organic/metal interfaces upon additive migration towards the metal during and after top metal deposition using a surface sensitive method, its more appropriate to refer to the analogue at a buried interface as an "effective work function" (EWF) because work function is only meaningful for surfaces.[44] The way to assess how HEG-DT and BDMT as interlayers impact the EWF at interfaces

between an Ag electrode and the organic active layer is not straightforward and the approach chosen here should yield the best possible approximation to the energetics inside a device. Interfaces between the additives and Ag are formed by step-depositing Ag onto a thin additive layer on a rather inert conductive substrate (indium-tin-oxide (ITO)), and compared to additive layers formed directly on Ag thin films by means of X-ray photoemission (XPS) and ultra-violet photoelectron spectroscopy (UPS). In this way each additive/Ag interface is constructed in two opposing ways, which allows assessing plausible EWF values, provided that the Ag overlayers are not too thick and continuous, which would yield only the work function of a bare Ag surface. XPS and UPS spectra of Ag deposited on a spin-coated layer of HEG-DT (supported by ITO) are shown in **Figure 6.9**. The HEG-DT layer was approximately a monolayer as inferred from the evaluation of all core level spectra. **Figure 6.9** demonstrates in detail the findings for HEG-DT/Ag interface and analogous experiments were carried out to access the BDMT/Ag and P3HT:PCBM/Ag interfaces (most important findings presented at **Figure 6.10**).

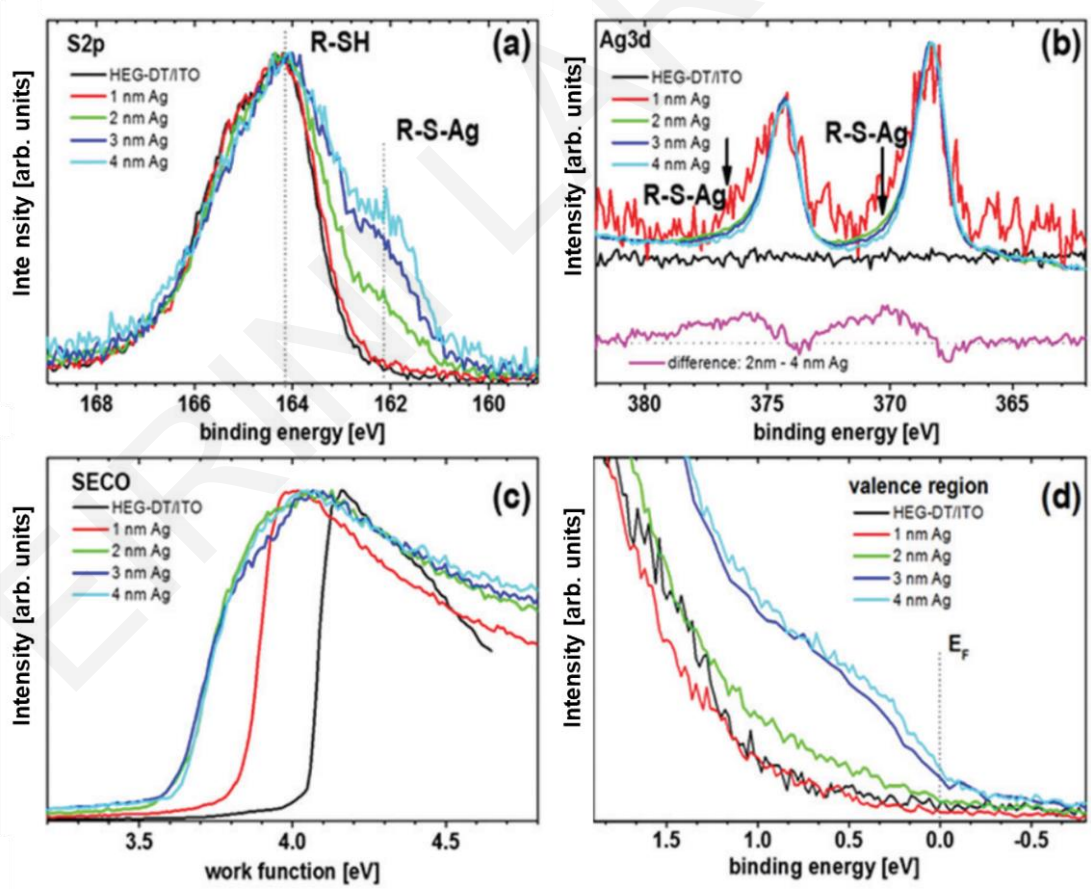

Figure 6.9*: Incremental Ag deposition onto HEG-DT/ITO followed by XPS and UPS spectra of (a) S2p core levels, (b) Ag3d core levels and difference spectrum obtained by subtracting the 4 nm from the 2 nm Ag coverage spectrum (bottom spectrum), (c) sample work function from SECO spectra, and (d) valence region close to the Fermi level (EF).*[2]

Fig. 6.9 a shows that the incremental deposition of Ag from one to four nm leads to an emergence of a low binding energy component at ca. 162.2 eV in the S2p spectra, indicative of additive/silver interactions (formation of Ag-S-R bonds). In **Fig. 6.9 b** the spectra of Ag3d levels indicate that metallic Ag dominates with the spin-orbit split 5/2 and 3/2 doublet peaks at 368.3 eV and 374.3 eV binding energy (eV). At low coverage, we observe a low intensity higher BE emission contribution, corresponding to a doublet centred at ca. 370 eV and 376 eV, as clearly visible in the different spectrum obtained by subtracting the 4 nm from the 2 nm Ag coverage spectrum (bottom in **Fig. 6.9 b**). This higher BE component is from Ag that formed bonds with S, but its comparably small intensity and vanishing at higher coverage shows that metallic island/cluster growth dominates. Notably, the work function of the sample gets reduced upon Ag deposition (**Fig. 6.9 c**) from 4.05 eV (bare HEG-DT/ITO) to 3.7 eV (1nm Ag), saturating quickly at 3.6 eV for higher Ag thickness. This goes in parallel with the formation of metallic Ag signatures in the valence region (**Fig. 6.9 d**), inferred by the emergence of the Fermi edge at 0 eV BE. At this stage we can safely observe the EWF of the Ag/HEG-DT interlayer, as the work function does not vary notably with Ag deposition and the value is far from that of a thick Ag film (4.15 eV and higher).

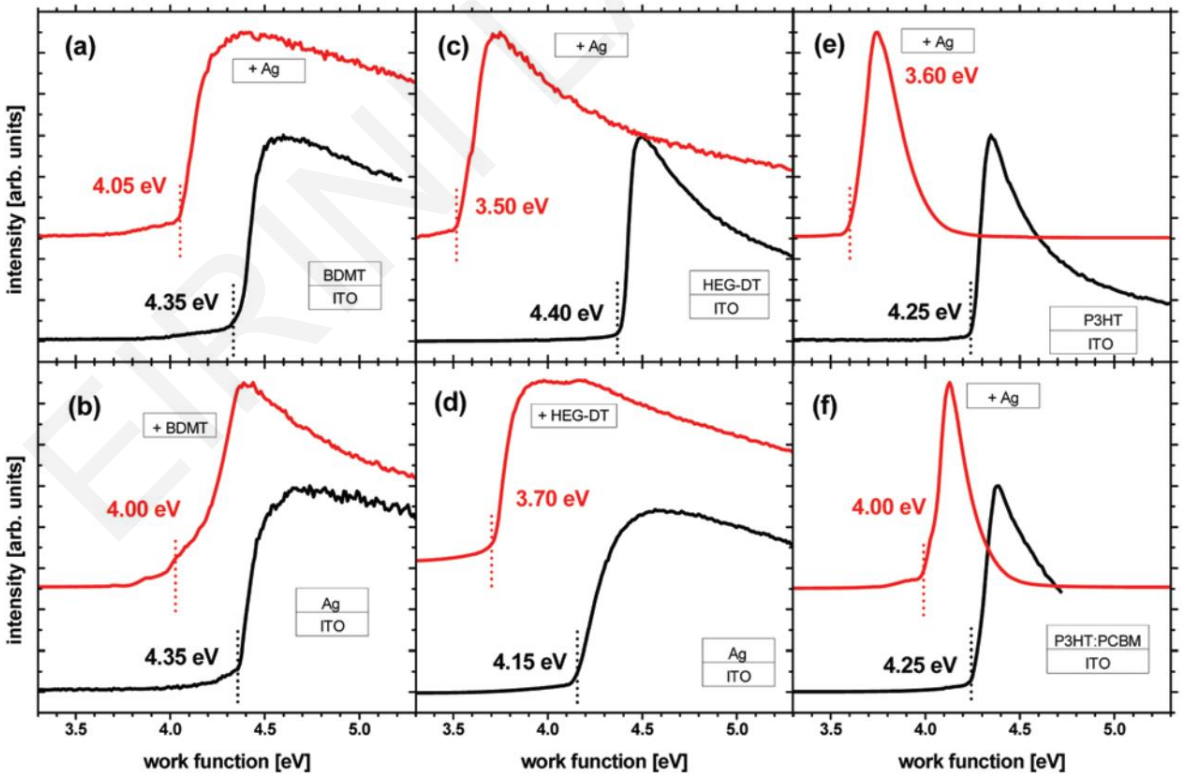

Figure 6.10*: SECO spectra and corresponding work function values of samples before and after the deposition of nominally 3 nm Ag: (a) BDMT on ITO, (c) HEG-DT on ITO, (e) P3HT, and (f) P3HT:PCBM. Before and after the deposition of (b) BDMT and (d) HEG-DT on an Ag surface.*[2]

The sample work function is derived from the secondary electron cut-off (SECO) spectra in **Figure 6.10** which summarise the representative trends upon the deposition of nominal 3 nm Ag on the additives and the opposite (depositing the additives on an Ag surface). A ca. monolayer film of BDMT spin-cast on ITO exhibits a work function of 4.35 eV (**Fig. 6.10 a**) which decreases to 4.05 eV upon the deposition of nominal 3 nm Ag. Similarly, the deposition of BDMT from a solution onto a pristine Ag film decreases the work function from 4.35 eV to 4.0 eV (**Fig. 6.10 b**). In contrast, the same experimental procedures done with HEG-DT instead of BDMT lead to substantially lower work function values, typically in the range between 3.5 eV and 3.7 eV (**Fig. 6.10 c** and **d**). For comparison, the work function of interfacial Ag/P3HT-only and Ag/P3HT:PCBM was included with estimated values between 3.6 eV and 4.0 eV (**Fig. 6.10 e** and **f**). As all work function values are not representative of a pristine Ag surface, they can be regarded as the EWF values relevant at the buried interfaces in OSCs when BDMT and HEG-DT, respectively, form an interlayer between Ag and the P3HT:PCBM layer. The average EWF values (obtained by the average of both ways of constructing the additive/Ag interface) are summarised at **Table 6.6**.

Table 6.6*: Values for average EWF for the various organic/Ag interfaces*

Interface type	Average EWF (eV)
Ag/P3HT:PCBM	3.85 ± 0.25
Ag/P3HT:PCBM:HEG-DT	3.65 ± 0.20
Ag/P3HT:PCBM:BDMT	4.1 ± 0.11

The reason for the difference in the work function obtained for HEG-DT and BDMT in combination with Ag is most likely attributed to a preferential orientation of the polar O–C bonds of HEG-DT at the interface, which lowers the work function.[45,46] Such polar bonds are not present in BDMT, and the bond-dipole formed between thiol and Ag is the same for both molecules.

Considering the above, the highest EWF values where obtained when interfacial BDMT is present, followed by Ag/P3HT:PCBM (or P3HT-only) interfaces and the lowest EWF values were recorded for HEG-DT. This trend is in perfect agreement with the device characteristics presented in **Table 6.5** suggesting that EWF approach provides an accurate estimation of the interfacial energy alignment for electron transfer from PCBM to the electrode. To this end we assume that interfaces with HEG-DT have the optimum energy-level alignment, followed

by interfaces without additives while BDMT/Ag interfaces exhibit the highest energetic misalignment. Finally, considering the RR results which probed the interfacial morphologies, we conclude that the electrochemical potential at the interface rather than morphology is what determines device characteristics in this study.

References

(1) Keivanidis, P. E.; Khan, J. I.; Katzenmeier, L.; Kan, Z.; Limbu, S.; Constantinou, M.; Lariou, E.; Constantinides, G.; Hayes, S. C.; Kim, J. S.; et al. Impact of Structural Polymorphs on Charge Collection and Nongeminate Recombination in Organic Photovoltaic Devices. *J. Phys. Chem. C* **2018**, *122* (51), 29141–29149. https://doi.org/10.1021/acs.jpcc.8b09825.

(2) Shamieh, B.; Anselmo, A. S.; Vogel, U.; Lariou, E.; Hayes, S. C.; Koch, N.; Frey, G. L. Correlating the Effective Work Function at Buried Organic/metal Interfaces with Organic Solar Cell Characteristics. *J. Mater. Chem. C* **2018**, *6* (30), 8060–8068. https://doi.org/10.1039/c8tc02381f.

(3) Yu, G.; Gao, J.; Hummelen, J. C.; Wudl, F.; Heeger, A. J. Polymer Photovoltaic Cells: Enhanced Efficiencies via a Network of Internal Donor-Acceptor Heterojunctions. *Science (80-.).* **1995**, *270* (5243), 1789. https://doi.org/10.1126/science.270.5243.1789.

(4) Halls, J. J. M.; Walsh, C. A.; Greenham, N. C.; Marseglia, E. A.; Friend, R. H.; Moratti, S. C.; Holmes, A. B. Efficient Photodiodes from Interpenetrating Polymer Networks. *Nature* **1995**, *376* (6540), 498–500. https://doi.org/10.1038/376498a0.

(5) Deibel, C.; Dyakonov, V. Polymer-Fullerene Bulk Heterojunction Solar Cells. *Reports Prog. Phys.* **2010**, *73* (9), 96401.

(6) Kim, Y.; Choulis, S. A.; Nelson, J.; Bradley, D. D. C.; Cook, S.; Durrant, J. R. Composition and Annealing Effects in Polythiophene/fullerene Solar Cells. *J. Mater. Sci.* **2005**, *40* (6), 1371–1376. https://doi.org/10.1007/s10853-005-0568-0.

(7) Wadsworth, A.; Hamid, Z.; Bidwell, M.; Ashraf, R. S.; Khan, J. I.; Anjum, D. H.; Cendra, C.; Yan, J.; Rezasoltani, E.; Guilbert, A. A. Y.; et al. Progress in Poly (3-Hexylthiophene) Organic Solar Cells and the Influence of Its Molecular Weight on Device Performance. *Adv. Energy Mater.* **2018**, *8* (28), 1–15. https://doi.org/10.1002/aenm.201801001.

(8) Kniepert, J.; Lange, I.; Heidbrink, J.; Kurpiers, J.; Brenner, T. J. K.; Koster, L. J. A.; Neher, D. Effect of Solvent Additive on Generation, Recombination, and Extraction in PTB7:PCBM Solar Cells: A Conclusive Experimental and Numerical Simulation Study. *J. Phys. Chem. C* **2015**, *119* (15), 8310–8320. https://doi.org/10.1021/jp512721e.

(9) Poelking, C.; Andrienko, D. Effect of Polymorphism, Regioregularity and Paracrystallinity on Charge Transport in poly(3-Hexylthiophene) [P3HT] Nanofibers. *Macromolecules* **2013**, *46* (22), 8941–8956. https://doi.org/10.1021/ma4015966.

(10) Zhugayevych, A.; Mazaleva, O.; Naumov, A.; Tretiak, S. Lowest-Energy Crystalline Polymorphs of P3HT. *J. Phys. Chem. C* **2018**, *122* (16), 9141–9151. https://doi.org/10.1021/acs.jpcc.7b11271.

(11) Panzer, F.; Sommer, M.; Bässler, H.; Thelakkat, M.; Köhler, A. Spectroscopic Signature of Two Distinct H-Aggregate Species in poly(3-Hexylthiophene). *Macromolecules* **2015**, *48* (5), 1543–1553. https://doi.org/10.1021/acs.macromol.5b00129.

(12) Sanyal, M.; Schmidt-Hansberg, B.; Klein, M. F. G.; Munuera, C.; Vorobiev, A.; Colsmann, A.; Scharfer, P.; Lemmer, U.; Schabel, W.; Dosch, H.; et al. Effect of Photovoltaic Polymer/fullerene Blend Composition Ratio on Microstructure Evolution during Film Solidification Investigated in Real Time by X-Ray Diffraction. *Macromolecules* **2011**, *44* (10), 3795–3800. https://doi.org/10.1021/ma2000338.

(13) Kan, Z.; Colella, L.; Canesi, E. V.; Vorobiev, A.; Skrypnychuk, V.; Terraneo, G.; Barbero, D. R.; Bertarelli, C.; MacKenzie, R. C. I.; Keivanidis, P. E. Charge Transport Control via Polymer Polymorph Modulation in Ternary Organic Photovoltaic Composites. *J. Mater. Chem. A* **2015**, *4* (4), 1195–1201. https://doi.org/10.1039/c5ta08120c.

(14) Wang, D. H.; Park, K. H.; Seo, J. H.; Seifter, J.; Jeon, J. H.; Kim, J. K.; Park, J. H.; Park, O. O.; Heeger, A. J. Enhanced Power Conversion Efficiency in PCDTBT/PC 70 BM Bulk Heterojunction Photovoltaic Devices with Embedded Silver Nanoparticle Clusters. *Adv. Energy Mater.* **2011**, *1* (5), 766–770. https://doi.org/10.1002/aenm.201100347.

(15) Atwater, H. A.; Polman, A. <Nmat2629.Pdf>. *Nat. Mater.* **2010**, *9* (3), 205–213. https://doi.org/10.1038/nmat2629.

(16) Wang, D. H.; Kim, J. K.; Lim, G. H.; Park, K. H.; Park, O. O.; Lim, B.; Park, J. H. Enhanced Light Harvesting in Bulk Heterojunction Photovoltaic Devices with Shape-Controlled Ag Nanomaterials: Ag Nanoparticles versus Ag Nanoplates. *RSC Adv.* **2012**, *2* (18), 7268–7272. https://doi.org/10.1039/c2ra20815f.

(17) Wang, C. C. D.; Choy, W. C. H.; Duan, C.; Fung, D. D. S.; Sha, W. E. I.; Xie, F. X.; Huang, F.; Cao, Y. Optical and Electrical Effects of Gold Nanoparticles in the Active Layer of Polymer Solar Cells. *J. Mater. Chem.* **2012**, *22* (3), 1206–1211. https://doi.org/10.1039/c1jm14150c.

(18) Stavytska-Barba, M.; Salvador, M.; Kulkarni, A.; Ginger, D. S.; Kelley, A. M. Plasmonic Enhancement of Raman Scattering from the Organic Solar Cell Material P3HT/PCBM by Triangular Silver Nanoprisms. *J. Phys. Chem. C* **2011**, *115* (42), 20788–20794. https://doi.org/10.1021/jp206853u.

(19) Li, D.; Borys, N. J.; Lupton, J. M. Probing the Electrode-Polymer Interface in Conjugated Polymer Devices with Surface-Enhanced Raman Scattering. *Appl. Phys. Lett.* **2012**, *100* (14). https://doi.org/10.1063/1.3701278.

(20) Razzell-Hollis, J.; Thiburce, Q.; Tsoi, W. C.; Kim, J. S. Interfacial Chemical Composition and Molecular Order in Organic Photovoltaic Blend Thin Films Probed by Surface-Enhanced Raman Spectroscopy. *ACS Appl. Mater. Interfaces* **2016**, *8* (45), 31469–31481. https://doi.org/10.1021/acsami.6b12124.

(21) Michaelson, H. B. The Work Function of the Elements and Its Periodicity. *J. Appl. Phys.* **1977**, *48* (11), 4729–4733. https://doi.org/10.1063/1.323539.

(22) Shamieh, B.; Obuchovsky, S.; Frey, G. L. Spontaneous Generation of Interlayers in OPVs with Silver Cathodes: Enhancing Voc and Lifetime. *J. Mater. Chem. C* **2016**, *4* (9), 1821–1828. https://doi.org/10.1039/c5tc04141d.

(23) Ratcliff, E. L.; Zacher, B.; Armstrong, N. R. Selective Interlayers and Contacts in Organic Photovoltaic Cells. *J. Phys. Chem. Lett.* **2011**, *2* (11), 1337–1350. https://doi.org/10.1021/jz2002259.

(24) Deckman, I.; Obuchovsky, S.; Moshonov, M.; Frey, G. L. Chemical Composition of Additives That Spontaneously Form Cathode Interlayers in OPVs. *Langmuir* **2015**, *31* (24), 6721–6728. https://doi.org/10.1021/acs.langmuir.5b00884.

(25) Vinokur, J.; Shamieh, B.; Deckman, I.; Singhal, A.; Frey, G. L. Mechanisms for Spontaneous Generation of Interlayers in Organic Solar Cells. *Chem. Mater.* **2016**, *28* (24), 8851–8870. https://doi.org/10.1021/acs.chemmater.6b03770.

(26) Tsoi, W. C.; James, D. T.; Kim, J. S.; Nicholson, P. G.; Murphy, C. E.; Bradley, D. D. C.; Nelson, J.; Kim, J. S. The Nature of in-Plane Skeleton Raman Modes of P3HT and Their Correlation to the Degree of Molecular Order in P3HT:PCBM Blend Thin Films. *J. Am. Chem. Soc.* **2011**, *133* (25), 9834–9843. https://doi.org/10.1021/ja2013104.

(27) Falke, S.; Eravuchira, P.; Materny, A.; Lienau, C. Raman Spectroscopic Identification of Fullerene Inclusions in Polymer/fullerene Blends. *J. Raman Spectrosc.* **2011**, *42* (10), 1897–1900. https://doi.org/10.1002/jrs.2966.

(28) Razzell-Hollis, J.; Limbu, S.; Kim, J. S. Spectroscopic Investigations of Three-Phase Morphology Evolution in Polymer: Fullerene Solar Cell Blends. *J. Phys. Chem. C* **2016**, *120* (20), 10806–10814. https://doi.org/10.1021/acs.jpcc.6b02898.

(29) Panzer, F.; Sommer, M.; Bässler, H.; Thelakkat, M.; Köhler, A. Spectroscopic Signature of Two Distinct H-Aggregate Species in poly(3-Hexylthiophene). *Macromolecules* **2015**, *48* (5), 1543–1553. https://doi.org/10.1021/acs.macromol.5b00129.

(30) Martin, T.; Wise, A.; Busby, E.; Gao, J.; Roehling, J. D.; Ford, M. J.; Larsen, D. S.; Moulé, A. J.; Grey, J. K. Packing Dependent Electronic Coupling in Single Poly (3-Hexylthiophene) H-and J-Aggregate Nanofibers. *J. Phys. Chem. B* **2013**, *117* (16), 4478–4487. https://doi.org/10.1021/jp308586k.

(31) Razzell-Hollis, J.; Tsoi, W. C.; Kim, J.-S. Directly Probing the Molecular Order of Conjugated Polymer in OPV Blends Induced by Different Film Thicknesses, Substrates and Additives. *J. Mater. Chem. C* **2013**, *1* (39), 6235. https://doi.org/10.1039/c3tc31245c.

(32) Campoy-Quiles, M.; Ferenczi, T.; Agostinelli, T.; Etchegoin, P. G.; Kim, Y.; Anthopoulos, T. D.; Stavrinou, P. N.; Bradley, D. D. C.; Nelson, J. Morphology Evolution via Self-Organization and Lateral and Vertical Diffusion in Polymer:fullerene Solar Cell Blends. *Nat. Mater.* **2008**, *7* (2), 158–164. https://doi.org/10.1038/nmat2102.

(33) Dang, M. T.; Hirsch, L.; Wantz, G. P3HT:PCBM, Best Seller in Polymer Photovoltaic Research. *Adv. Mater.* **2011**, *23* (31), 3597–3602. https://doi.org/10.1002/adma.201100792.

(34) Tamai, Y.; Ohkita, H.; Benten, H.; Ito, S. Exciton Diffusion in Conjugated Polymers: From Fundamental Understanding to Improvement in Photovoltaic Conversion Efficiency. *J. Phys. Chem. Lett.* **2015**, *6* (17), 3417–3428. https://doi.org/10.1021/acs.jpclett.5b01147.

(35) Kurpiers, J.; Neher, D. Dispersive Non-Geminate Recombination in an Amorphous

Polymer:Fullerene Blend. *Sci. Rep.* **2016**, *6* (February), 1–10. https://doi.org/10.1038/srep26832.

(36) Wright, B.; Nakajima, Y.; Clarke, T. M.; Okuda, K.; Paananen, H.; Mozer, A. J.; Mori, S. Quantifying Recombination Losses during Charge Extraction in Bulk Heterojunction Solar Cells Using a Modified Charge Extraction Technique. *Adv. Energy Mater.* **2017**, *7* (11), 1–9. https://doi.org/10.1002/aenm.201602026.

(37) Lai, T. H.; Tsang, S. W.; Manders, J. R.; Chen, S.; So, F. Properties of Interlayer for Organic Photovoltaics. *Mater. Today* **2013**, *16* (11), 424–432. https://doi.org/10.1016/j.mattod.2013.10.001.

(38) Chen, L. M.; Xu, Z.; Hong, Z.; Yang, Y. Interface Investigation and Engineering - Achieving High Performance Polymer Photovoltaic Devices. *J. Mater. Chem.* **2010**, *20* (13), 2575–2598. https://doi.org/10.1039/b925382c.

(39) Wood, S.; Franklin, J. B.; Stavrinou, P. N.; Mclachlan, M. A.; Kim, J.; Wood, S.; Franklin, J. B.; Stavrinou, P. N.; Mclachlan, M. A. Interfacial Molecular Order of Conjugated Polymer in P3HT : ZnO Bilayer Photovoltaics and Its Impact on Device Performance Interfacial Molecular Order of Conjugated Polymer in P3HT : ZnO Bilayer Photovoltaics and Its Impact on Device Performance. **2014**, *153304* (2013), 0–5. https://doi.org/10.1063/1.4824847.

(40) Dekman, I.; Brener, R.; Frey, G. L. Thermal Metal Deposition Induces Segregation in Polymer Thin Films: A Demonstration on OPVs. *J. Mater. Chem. C* **2013**, *1* (40), 6522–6525. https://doi.org/10.1039/c3tc31430h.

(41) Kim, J. S.; Ho, P. K. H.; Murphy, C. E.; Friend, R. H. Phase Separation in Polyfluorene-Based Conjugated Polymer Blends: Lateral and Vertical Analysis of Blend Spin-Cast Thin Films. *Macromolecules* **2004**, *37* (8), 2861–2871. https://doi.org/10.1021/ma035750i.

(42) Koch, N. Organic Electronic Devices and Their Functional Interfaces. *ChemPhysChem* **2007**, *8* (10), 1438–1455. https://doi.org/10.1002/cphc.200700177.

(43) Kahn, A.; Koch, N.; Gao, W. Electronic Structure and Electrical Properties of Interfaces between Metals and π-Conjugated Molecular Films. *J. Polym. Sci. Part B Polym. Phys.* **2003**, *41* (21), 2529–2548. https://doi.org/10.1002/polb.10642.

(44) Yang, D. S.; Bilby, D.; Chung, K.; Wenderott, J. K.; Jordahl, J.; Kim, B. H.; Lahann, J.; Green, P. F.; Kim, J. Work Function Modification via Combined Charge-Based Through-Space Interaction and Surface Interaction. *Adv. Mater. Interfaces* **2018**, *5* (15), 1–6. https://doi.org/10.1002/admi.201800471.

(45) Zhou, Y.; Fuentes-hernandez, C.; Shim, J.; Meyer, J.; Giordano, A. J.; Li, H.; Winget, P.; Papadopoulos, T.; Cheun, H.; Kim, J.; et al. A Universal Method to Produce Low–Work Function Electrodes for Organic Electronics. **2012**, *873* (April), 327–332. https://doi.org/10.1126/science.1218829.

(46) Yeo, J. S.; Kang, M.; Jung, Y. S.; Kang, R.; Lee, S. H.; Heo, Y. J.; Jin, S. H.; Kim, D. Y.; Na, S. I. In-Depth Considerations for Better Polyelectrolytes as Interfacial Materials in Polymer Solar Cells. *Nano Energy* **2016**, *21*, 26–38. https://doi.org/10.1016/j.nanoen.2016.01.003.

CHAPTER 7

Spectroscopic and computational study of the donor-acceptor polymer PCE11

This chapter focuses on the fundamental study of the new generation donor-acceptor polymer PffBT4T-2OD or PCE11, a name that stands for the record PCE of ~11.0% reported in 2014.[1] PCE11 is a low band-gap (1.65 eV) semiconducting polymer, highly crystalline, having a broad absorption spectrum reaching the near IR region, characteristics that make it a particularly attractive material for OPV applications.[2] Additionally, recent studies reveal its compatibility with non-fullerene acceptors.[3] Although in the last two decades fullerene derivatives have been the dominant choice as electron accepting material due to their superior charge transporting properties, they suffer from several drawbacks such as the limited absorption in the visible region and the high production and purification cost. Considering the rapid growth of non-fullerene systems within the last three years,[4] research on compatible materials for this new generation of OPV devices is necessary, in order to sustain and exceed the efficiencies achieved with fullerenes. This study has a rather fundamental character as we examine neat films before mixing with any acceptor to elucidate the effect of molecular weight and processing conditions on molecular conformation. Then, we perform a temperature dependent study to extract information about ground and excited state structure. For this work we collaborated with Prof. Anna Köhler's group from the University of Bayreuth, who performed the temperature dependent absorption measurements and the group of Prof. David Beljonne from the University of Mons, who performed DFT calculations.

7.1 Background

The morphology of conjugated polymers is determined by several factors as described in section 2.6.4, the most fundamental however are the inherent properties resulting from synthesis such as chemical nature and molecular weight (M_n). PCE11 exhibits processing-controlled aggregation and strong crystallisation, attributed to the branching position and

size of the branched alkyl side chains (2-octyldodecyl (2OD) chains on quaterthiophene).[1] Moreover, several studies[5–7] have highlighted the significant impact of M_n of various donor-acceptor systems on photovoltaic properties and PCE11 is not an exception as M_n affects the aggregation process and morphological characteristics.[1] With this knowledge, we can further explore the effect of various parameters on its molecular conformation, and particularly evaluate the sensitivity of PCE11 structure to M_n and processing. Another fundamental step towards understanding the structure-property relation of PCE11 is to monitor its temperature-dependent behaviour and elucidate temperature effects such as thermochromism, thermal motions and phase transitions on polymer photophysics. An extensive part of this chapter is dedicated to this because such knowledge is valuable to shape industrial standards for OSC devices, both in terms of film processing conditions as well as excluding possible interference with operating temperatures, as they can have crucial impact on the efficiency and potentially limit their lifetime. The temperature dependence of the optical response in organic semiconductors is a subject that has been addressed in the past by several studies by means of temperature-dependent absorption and photoluminescence spectroscopy. Among the studied materials are poly(3-alkylthiophenes),[8,9,10] quasi-isolated (extremely diluted) oligothiophenes,[11] (poly-(2-methoxy-5-(2‘-ethylhexyl)oxy 1,4-phenylene vinylene)) (MEH-PPV)[12,13] and donor-acceptor polymers.[14] It has been consistently documented that conjugated polymers and oligomers exhibit a red shift in their optical spectra upon cooling which is often associated with an increase in the effective conjugation length (ECL) upon backbone planarization. Panzer et al. performed an extensive study on various different compounds in solution to establish a mechanism that describes their aggregation behaviour.[15] The 3-step order-disorder transition for decreasing temperature according to this study involves firstly planarization of the disordered phase, secondly aggregate formation and lastly planarization of the aggregate phase. On the other hand, the optical spectra of conjugated polymers encode the contribution of various structural elements such as the presence of different conjugation lengths and their excitonic coupling -more generally described as inhomogeneity- that can be difficult to determine their origin. The combination of optical spectroscopy with structurally sensitive techniques such as Raman spectroscopy can provide valuable insights on the link between optical properties and molecular conformation. However, Raman spectroscopy is not so commonly employed for temperature-dependent studies, with only a few examples focusing on conjugated polymers.[16,17,18] PCE11 exhibits a pronounced and well-characterised temperature dependent aggregation in solution as reported by Liu et. al. which enables the development of processing protocols towards morphology control in the

solid state i.e. film drying process.[1] In the present study we focused on films rather than solutions as a step closer towards applications and we combined temperature-dependent absorption and Resonant Raman (RR) spectroscopy as an optical and structural probe, respectively, to explore their sensitive interconnection. Moreover, as absorption and RR cross sections share important physical parameters, this enables simultaneous modelling of RR and absorption spectra by a theoretical tool known as resonance Raman intensity analysis (RRIA).[19–21] This method exploits the vibrational coherence that expose the time-dependent wavepacket overlaps on sub-picosecond timescales and enables us to distinguish between the relative contribution from each vibrational mode to the excited state geometry changes, extract values for the mode specific reorganisation energy, and accurately estimate the relative contributions of homogeneous and inhomogeneous broadening.

7.2 Results and discussion

7.2.1 Absorption Spectroscopy

Decision on the excitation wavelengths for the RR experiments is based on the PCE11 absorption spectrum (chemical structure in **Figure 7.1** *inset*). The electronic absorption spectrum of the PCE11 film shown in **Figure 7.1** exhibits two absorption bands: a high energy band with a maximum at ~440 nm and a lower energy band with clear vibronic structure and well resolved features at ~620 and ~680 nm, corresponding to the 0-0 and 0-1 transitions, respectively. Through density functional theory calculations (DFT) we are able to elucidate the nature of each electronic transition. **Figure 7.1** shows the hole and electron density distribution diagrams associated with the two most prominent electronic transitions of PCE11.

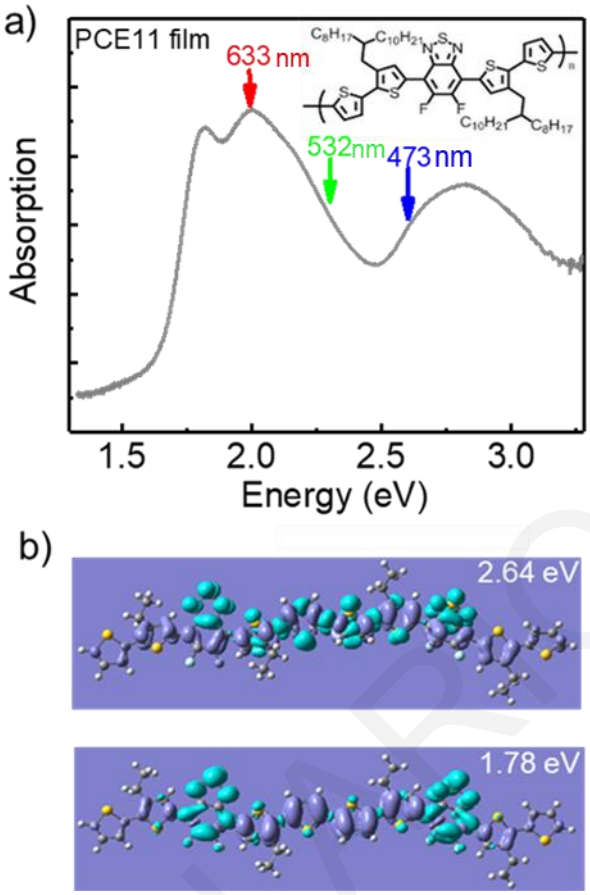

Figure 7.1: *a) Absorption spectrum of PCE11(chemical structure inset). The arrows indicate the selected RR excitation wavelengths employed. b) Electron-hole density distribution diagrams for the lower (1.78 eV) and higher (2.64 eV) energy transitions at a dihedral of 25°.*

We observe that for the lowest energy transition (excitation energy ~1.8 eV) the electron cloud becomes localised on the acceptor unit of the molecule (BT) upon excitation, suggesting that the low energy absorption band corresponds to a charge transfer (CT) transition. At higher excitation energies (~2.6 eV) we observe that the electron cloud is spread along the chain adopting a quinoidal conformation; thus, we can safely attribute the high energy absorption band to the π-π* electronic transition. The presence of the two absorption bands and the vibronic characteristics, such as the 0-0/0-1 peak ratio of the absorption spectrum, are in agreement with previous studies of PCE11 in solution,[1] and the similar PffBT4T-2DT polymer with the same backbone but longer alkyl side chains.[22] The increased intensity of the 0-0 with respect to the 0-1 –indicator of the intramolecular order and intrachain coupling- suggest the presence of J aggregates that promote electron delocalisation along the polymer backbone.[23]

7.2.2 Resonance Raman Spectroscopy - Excitation wavelength dependence

The vibrational frequencies of the RR modes are sensitive probes of conformational characteristics such as the degree of torsional order of the chains, while the intensities reflect the structural distortion in the excited state with respect to the ground state. Selective access to the spectral characteristics of each electronic transition is provided by judicious choice of the excitation energy. Raman excitation wavelengths were chosen according to the absorption spectrum of PCE11 (marked with arrows in **Fig.7.1**) to achieve resonance conditions for each electronic transition.

Figure 7.2 shows the RR spectra of PCE11 at the three excitation wavelengths. DFT computations reveal that the bands observed correspond to modes associated either with the thiophene ring (the donor unit of the molecule) or the BT unit (the acceptor). The band at ~1441 cm^{-1} corresponds to the C=C symmetric stretching mode of thiophene, while the bands at 1328 and 1530 cm^{-1} are due to C=C stretching of the acceptor unit. In the lower frequency region (not displayed here), weaker bands appear at 850 cm^{-1} originating from the N-S-N stretching of the BT and 429 cm^{-1} ascribed to a BT bending mode. Upon excitation at 473 nm, we observe that the 1441 cm^{-1} thiophene mode dominates the spectrum. The strong intensity of this mode is expected while on resonance with a π to π^* transition as it encodes the excited-state geometry change which -based on the hole and electron density distribution plots in **Figure 7.1** - is changing from a benzenoid to a quinoid-like conformation in the excited state. Similar spectra have been obtained in other donor-acceptor polymers involving these two functional groups when on resonance with the π-π^* transition.[24]

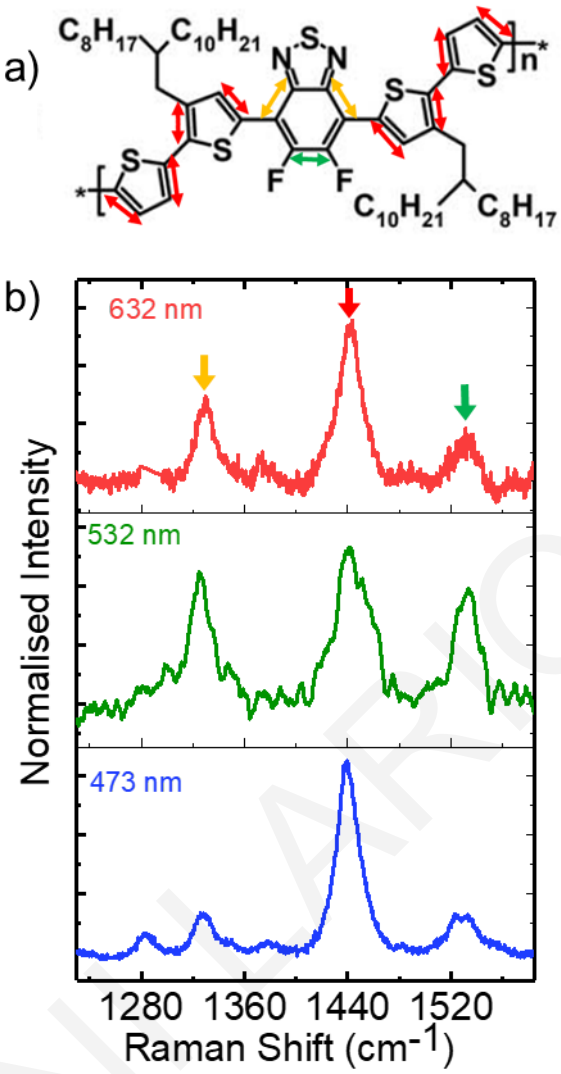

Figure 7.2: a) *The 3 dominant vibrations of the molecule are marked with coloured arrows on the chemical structure of PCE11 (red for the thiophene's C=C stretch, yellow and green for the C=C stretching modes of the BT unit). b) Raman spectra excited at 473nm (blue), 532 nm (green) and 632 nm (red). The coloured arrows link the vibrational modes to the Raman peaks.*

The fact that we observe larger intensity in the acceptor modes (C=C stretching at 1328 and 1530 cm^{-1}) with respect to the thiophene mode, in the RR spectra obtained with 532 and 632 nm excitation, is an indication of the CT nature of this transition (**Fig.7.2 b)**). Analogous spectroscopic signature has been reported before for the similar donor-acceptor system poly[2,6-(4,4bis-(2-ethylhexyl)-4H-cyclopenta[2,1-b;3,4-b0] dithiophene)-alt-4,7(2,1,3-benzothiadiazole)] (PCPDTBT).[25] This can also be explained by the hole and electron density distribution plots for this transition, where the electron density at the excited state is localised on the acceptor unit of the molecule. Considering the above, we can safely confirm that excitation at 473 nm is on resonance with the π-π* transition, while at 532 and 633 nm we access the CT transition. Although at both 532 and 633 nm we are on resonance with a

CT transition, we can still observe differences between these two spectra, such as the 3 cm^{-1} lower frequency of the C=C thiophene stretch at 633 nm and the significantly reduced intensities of the BT modes with respect to the thiophene. Insights on the nature of the changes observed are provided by DFT calculations that reveal the impact of changing all dihedral angles simultaneously from 0° to 25° by step 5°.

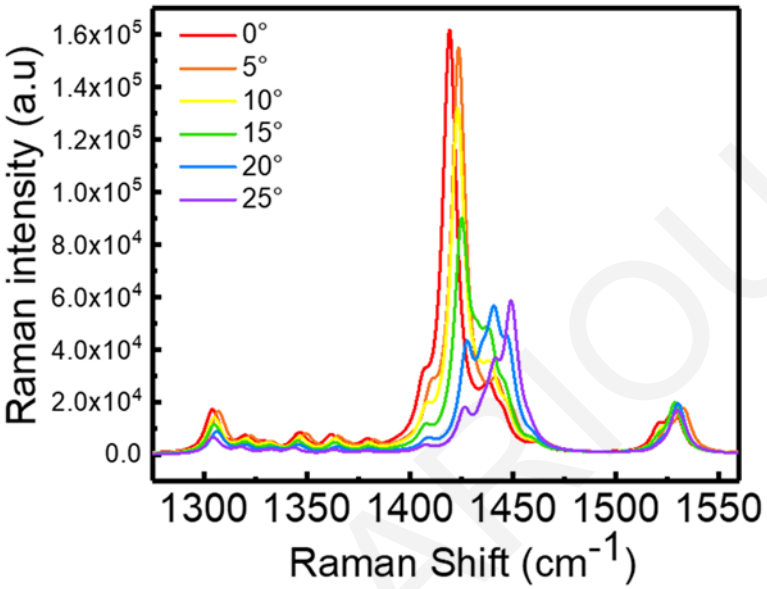

Figure 7.3: *DFT calculation of the thiophene-thiophene unit dihedral angle dependence of the Raman spectra.*

In **Figure 7.3** we can see that larger dihedral angles cause a significant shift of the position of the thiophene mode to higher wavenumbers, as well as a sharp reduction in the intensity of this mode with respect to the C=C stretching modes of the BT. Based on this fact, we can interpret the lower BT/Thiophene intensity ratio accompanied by the low frequency of the thiophene mode observed at 633 nm as a sign of a more planar conformation. Considering that 633 nm is a lower energy excitation compared to 532 nm it is likely that ordered populations of the molecule are effectively probed at this wavelength. The mode assignments of the bands as well as their position (depending on the different dihedral angles) depicted in the Raman spectra are summarised in **Table 7.1**.

Table 7.1: *Band assignment of PCE11 vibrational modes*

Exp. $\bar{\nu}$ (cm^{-1})	Calc. $\bar{\nu}$ (cm^{-1}) 0°	Calc. $\bar{\nu}$ (cm^{-1}) 5°	Calc. $\bar{\nu}$ (cm^{-1}) 10°	Calc. $\bar{\nu}$ (cm^{-1}) 15°	Calc. $\bar{\nu}$ (cm^{-1}) 20°	Calc. $\bar{\nu}$ (cm^{-1}) 25°	Description
429	424	423	424	424	425	425	BT bending mode
850	856	852	850	854	852	855	BT N-S-N vibration
1328	1337	1336	1336	1335	1334	1334	BT C=C stretch y direction
1441	1409	1410	1412	1436	1436	1439	Thiophene's C=C stretch
1530	1517	1516	1517	1518	1518	1519	BT C=C stretch x direction

7.2.3 Impact of molecular weight on backbone planarity

Having identified vibrational modes of PCE11 and after developing a basic understanding on how spectral changes relate to molecular conformation, we can employ RR spectroscopy to further explore the effect of specific parameters on molecular ordering and specifically how they affect backbone planarity. The impact of molecular weight will be firstly discussed, as its connection to solid state microstructure of polymers is well-established.[5–7,26,27] Molecular weight is directly proportional to the (average) length of the individual chains thus determines a polymer's mechanical, structural and thermal properties.[28,29] Concerning OPV applications, high molecular weight is desirable in general and is expected to benefit device performance by providing good interconnections within the active layer and longer conjugation length.[27] However, if molecular weight exceed a certain threshold (M_e), it may cause increased entanglement during deposition with negative impact on long-range molecular order.[30] Here, the importance of molecular weight on the polymer conformation will be evaluated by considering two extreme cases of low (55 $kg{\cdot}mol^{-1}$) and high (83 $kg{\cdot}mol^{-1}$) M_n films. Two sets of samples were studied, thin films (50 nm) and thick ones (200 nm). RR excitation was performed in three different wavelengths accessing the π-π* and CT transitions at 473 and 532, 633 nm respectively.

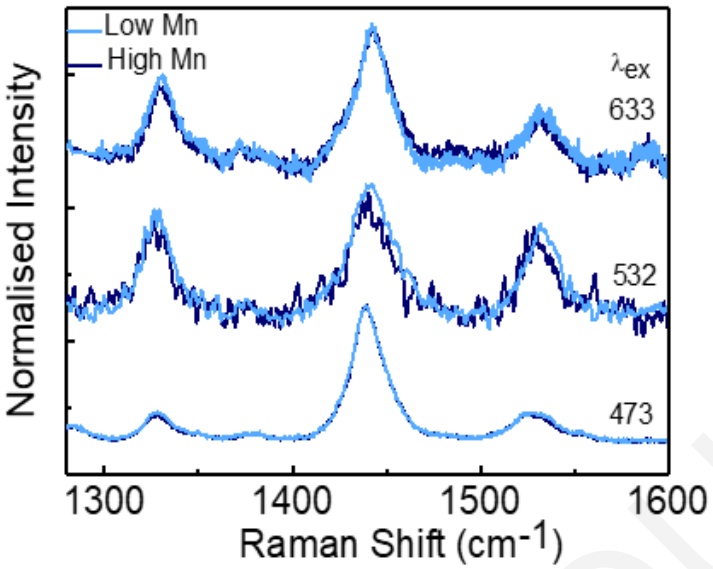

Figure 7.4: *RR spectra of low (light blue) and high (dark blue) M_n PCE11 200 nm thick films for excitation wavelengths at 473, 532 and 633 nm.*

In **figure 7.4** the results for the thick films (200 nm) are presented. Structural information can be extracted by monitoring frequency shifts as well as variations in the relative intensities of the acceptor modes with respect to the thiophene. Although, extended spectra were obtained for all samples, we focus on a rather narrow high frequency region due to the higher sensitivity of the C=C stretching modes to electron delocalisation. Apparently, at 532nm, the thiophene C=C stretch of high M_n samples is located at 1440 cm^{-1}, shifted by 4cm^{-1} towards lower frequencies compared to low molecular weight ones. This is accompanied by a narrower FWHM of 25.6 cm^{-1} and reduced intensity ratio of the BT with respect to the thiophene compared to the FWHM of 35.1 cm^{-1} for the low M_n. Spectral characteristics of high M_n samples suggest a greater degree of chain planarity compared to low Mn and are consistent with the high M_n films of different thickness (thin, 50 nm) shown in **Fig. 7.5** which again exhibit a narrower FWHM (30.2 cm^{-1} vs 34.8 cm^{-1}) and reduced intensity ratio of the BT with respect to the thiophene compared to low M_n (thin) samples. At 473 and 633 nm excitation wavelengths the spectra of high and low M_n samples are identical (see **Fig.7.4**) suggesting that those wavelengths are insensitive to conformational changes.

The above results provide evidence that high M_n PCE11 (83 $kg{\cdot}mol^{-1}$) sustains a planar conformation in films, further supporting and generalising the results reported in existing literature for other donor-acceptor polymers regarding the impact of molecular weight.[5–7]

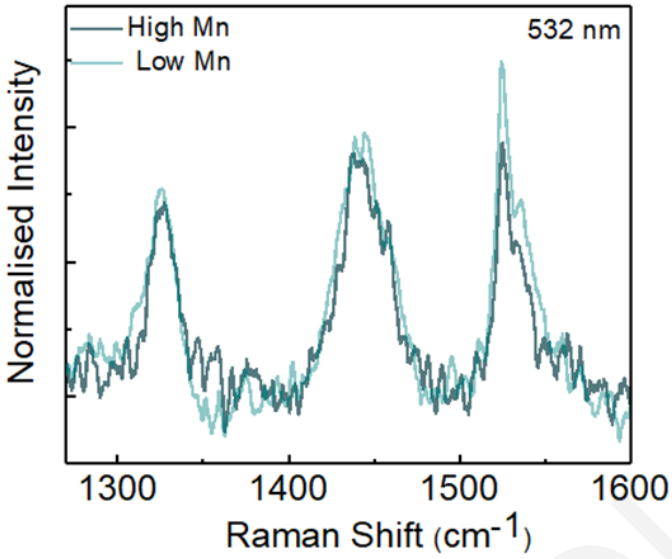

Figure 7.5: *RR spectra of low (light cyan) and high (dark cyan) M_n PCE11 50 nm thick films for 532 nm excitation wavelength.*

7.2.4 The impact of processing

7.2.4.1 The effect of thickness

As discussed in the second chapter (section 2.6.4) processing is a broad term that may involve various parameters such as the choice of solvent, the evaporation rate, thermal treatment etc, which can be easily controlled, with however a significant impact on device characteristics. In previous studies,[31,32] the effect of active layer thickness on the device performance has been addressed and has been shown to affect short circuit current, efficiency and charge recombination losses. Here, at a more fundamental level we examine the effect of film thickness on molecular ordering of neat films. Typical values of film thicknesses are between 80 and 100 nm,[32] however, here we focus again on extreme values, of 50 (thin) and 200 nm (thick) films. As in the previous section the effect of thickness is evaluated considering two sets of samples: high and low M_n ones. Excitation at 532 nm, again proved the most sensitive to probe conformational changes, thus the results presented here focus on this excitation wavelength. In **Figure 7.6** the RR spectra of thin films exhibit consistently (for both high and low M_n sets) characteristics of more torsionaly disordered conformation compared to the thicker ones, considering the higher intensity of the BT's C=C stretching mode, the increased FWHM and the position of the thiophene's C=C stretch located in higher wavenumbers.

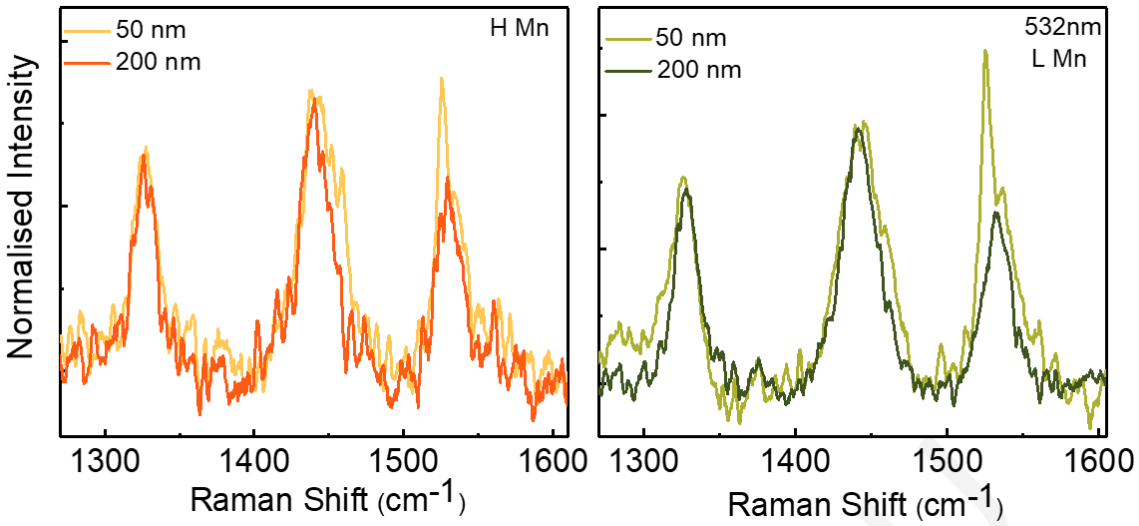

Figure 7.6*: Left: RR spectra of thin (yellow) and thick (orange) high M_n PCE11 films Right: Raman spectra of thin (light green) and thick (green) low M_n PCE11 films. Excitation wavelength is 532 nm.*

Those changes are quantified in **table 7.2** showing that FWHM is significantly narrower at the thick films and this difference is up to ~10 cm^{-1}. Moreover, the frequency of the thiophene C=C stretch is up to 3 cm^{-1} lower and the $BT_{C=C}/T_{C=C}$ intensity ratio (weighted by area) is up to 9% reduced compared to the thin samples.

Table 7.2: *Quantitative RR mode characteristics for each studied sample.*

Sample		Thiophene C=C Stretch		Ratio $BT_{C=C}/T_{C=C}$
		Position (cm^{-1})	FWHM	
Thin	Low M_n	1444	32.1	0.59
	High M_n	1444	26.7	0.54
Thick	Low M_n	1443	24	0.5
	High M_n	1441	22.4	0.52

In conclusion we can say that although few publications to date [29,31] consider film thickness as a way to control device characteristics, and thickness is often chosen based on convenience, the above results indicate that it has a significant impact on backbone conformation and potentially (after combining with appropriate acceptors), can be linked to device performance.

7.2.4.2 The effect of blending with HDPE

The addition of an insulating component in an OPV, although it would be expected to negatively impact electronic properties as discussed also in the 5th chapter, is a widely employed strategy in the attempt to enhance device performance, reduce cost, and enable additional functionalities. Insulating commodity polymers such as high-density polyethylene (HDPE) have been employed in the past as blending additives with the prototype system P3HT:PCBM[33] and poly(3hexyltellurophene) (P3HTe)[34,35] to address the issue of mechanical and photochemical stability providing local encapsulation.[36] Moreover, the optimum active layer thickness of 100 nm, remains a technological challenge for various printing technologies, which require several hundreds of nm of wet-layer thicknesses to achieve structural stability. The inert component can lead to active layers of increased thickness without significant device performance loses.[33]

Here, preliminary RR experiments reveal the impact of blending PCE11 with HDPE on the polymers backbone planarity. PCE11 neat and PCE11:HDPE blends (both low M_n samples of 55 kg·mol^{-1} and of comparable thickness), were compared with 532 nm excitation, again focusing in the spectral region of the C=C stretching modes of the molecule.

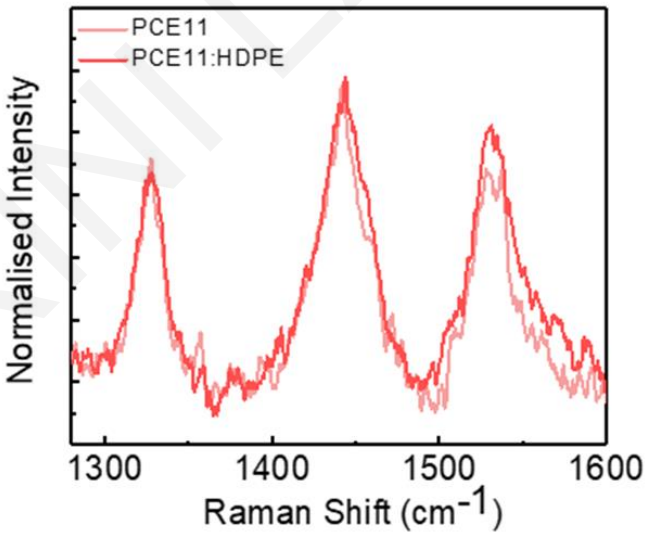

Figure 7.7: *RR spectra of low M_n PCE11 films. Comparison between neat (pink) and blend films with HDPE (red). Excitation wavelength is 532 nm.*

In **figure 7.7** we observe that the position of the thiophene C=C in the blend film is located at 1441 cm^{-1}, upshifted by 2 cm^{-1} compared to the neat film, indication of higher chain planarity. This, is supported by the slightly increased FWHM of the same vibrational mode, 31 cm^{-1} against 30 cm^{-1} in the case of the neat and the increased $BT_{C=C}/T_{C=C}$ intensity ratio

in the blend film. Consistent results were obtained for a second pair of samples where neat films exhibited spectral characteristics of higher degree of order. To expand a bit further this study on the blend films, we address the issue of film thickness as well.

Table 7.3: *Quantitative RR mode characteristics for each studied sample.*

Sample		Thiophene C=C Stretch		Ratio $BT_{C=C}/T_{C=C}$
		Position (cm^{-1})	FWHM	
Thin	PCE11	1441	30	0.52
Thin	PCE11:HDPE	1443	31	0.6
Thick	PCE11:HDPE	1443	29	0.57

As shown in **figure 7.8**, the RR spectra of the thin (100 nm) and thick (320 nm) films are similar, when considering the characteristics of the thiophene C=C stretch, with only minor variations in the $BT_{C=C}/T_{C=C}$ intensity ratio (which is slightly higher in the thin film) in accordance with the trend observed in neat films in the previous section. These results are summarised in **Table 7.3**.

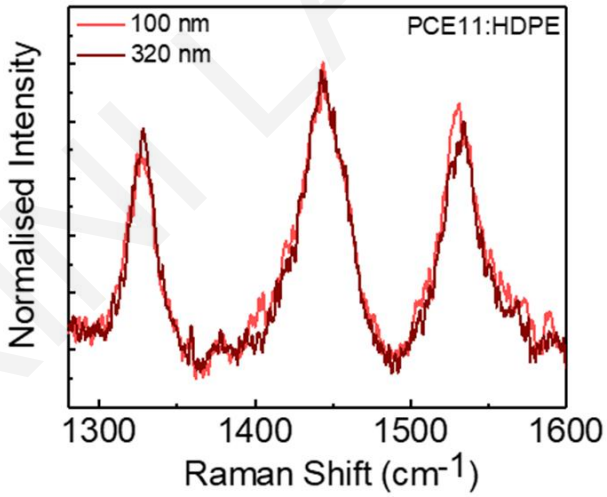

Figure 7.8: *RR spectra of low Mn PCE11:HDPE blend films. Comparison between thin (light red) and thick (red) films. Excitation wavelength is 532nm.*

To conclude, changes observed between neat and blend films as well as between thin and thick PCE11:HDPE blend films provide indications regarding the planarity of the polymer's backbone; however, the effect of those parameters on short-range order is not sufficient to question the impact on longer-scale characteristics. Of course, a systematic study on a large number of samples and considering additional characterisation techniques would provide solid information and a more detailed view of the overall properties.

7.2.5 Temperature dependence

A fundamental step towards understanding in depth the structure-property relation of donor-acceptor polymer systems is to monitor their temperature-dependent behaviour. To this end, we focused on low temperatures and monitored the effects that arise during this process. Following the same gradual cooling procedure down to 20 K for all films measured, RR spectra where recorded with excitation at 532 nm. **Figure 7.9** shows a qualitative example of the spectra obtained for a high M_n thin neat PCE11 film measured at six different temperatures. Shifts of the thiophene C=C stretch as well as changes in FWHM of the same mode as a function of temperature have been quantified and illustrated in **Figure 7.10** for six different samples.

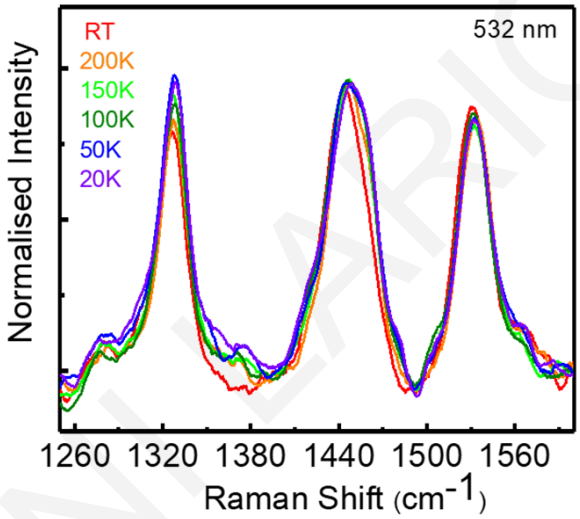

Figure 7.9: *Temperature dependent Raman spectra of high M_n (83 kg·mol^{-1}, 50 nm film thickness) PCE11 in the spectral region 1260 – 1580 cm^{-1}.*

Beginning with the position of the thiophene C=C stretch, although this differs from sample to sample, it exhibits the same trend as a function of temperature. A transition-like shift to higher frequencies is observed in all cases around 200 K. This shift is accompanied by an increase in the intensity of the BT C=C stretch around 1328 cm^{-1} (see **Fig. 7.9**) suggesting reduced torsional order of the chain backbone. FWHM values on the other hand, do not have a consistent behaviour upon cooling, except in one case that shows a gradual increase. In general, the width (FWHM) of the thiophene's C=C stretch (around 36 cm^{-1} for the majority of measurements) is broad enough to suggest inhomogeneity in the sample, i.e. competition between ordered and amorphous phases.

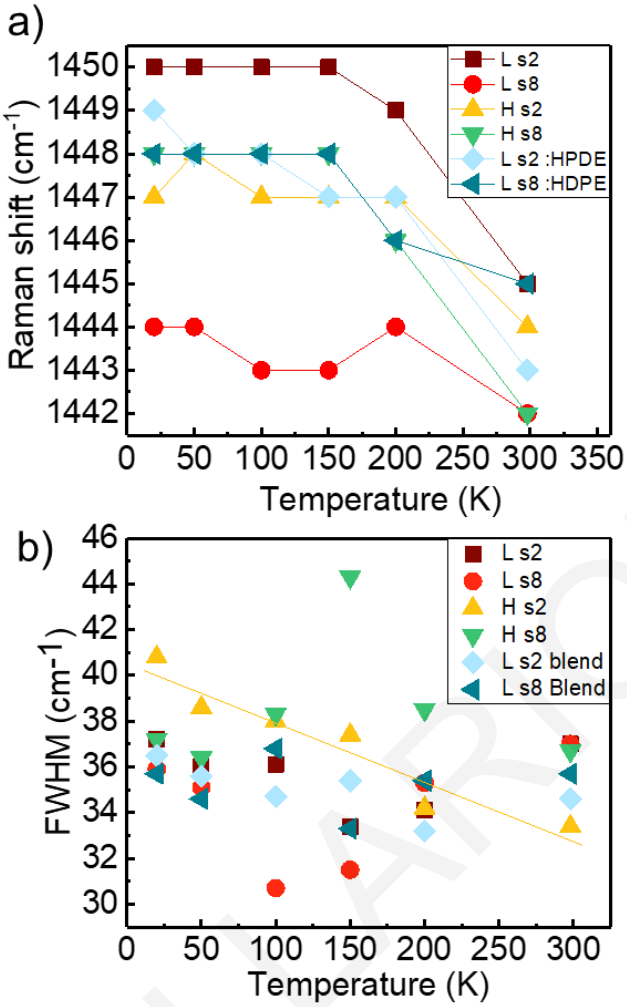

Figure 7.10: *Fitting extracted parameters for: a) the thiophene C=C stretch frequency for the various samples measured as a function of temperature, b) the FWHM of the same mode. Excitation wavelength was 532 nm. L stands for low M_n (55 kg·mol^{-1}), H for high M_n (83 kg·mol^{-1}), s2 for 50 nm film thickness, s8 for 200 nm film thickness (blend is PCE11:HDPE).*

In an endeavour to explain physically those results, in the next sections we focus on one specific sample (high M_n (83 kg·mol^{-1}, 50 nm film thickness) to further elaborate on these findings, considering also the evolution of the absorption spectrum as a function of temperature.

7.2.6 Temperature dependent absorption

We will now focus on the temperature-dependent evolution of the absorption spectrum of PCE11 and explore the nature of the changes observed. In **figure 7.11** we can see that by lowering the temperature from 298 K (RT) to 5 K the spectra of the low energy CT band red-shift gradually and the intensities of the 0-0 and 0-1 transitions are increased. The $A_{0\text{-}0}/A_{0\text{-}1}$ vibronic peak ratio, which is a sensitive probe of the strength of inter- versus intra-

chain coupling, does not however change significantly upon cooling and varies between 1.19 at 298K and 1.12 at 5K (**fig. 7.11**). According to the model developed by Spano for the weakly interacting J aggregate states,[37,38] the $A_{0\text{-}0}/A_{0\text{-}1}$ peak ratio can be used to estimate the magnitude of the intrachain coupling through the relation:

$$\frac{A_{0-0}}{A_{0-1}} \approx \frac{\left[1+ {}^{0.24W}/_{E_p}\right]^2}{\left[1-{}^{0.073W}/_{E_p}\right]^2} \qquad (7.1)$$

where W is the free exciton bandwith of the aggregates and E_p is the energy of the main intramolecular vibration, assumed equal to 0.18 eV in our system as obtained from the average energy of the dominant vibrational modes that couple to the electronic transition (C=C stretches of thiophene and BT). According to this model, the estimated W for all the temperatures is between 16% and 27% of the ω_{vib} (frequency of the main intramolecular vibration), falling within the weak coupling regime ($\leq \lambda^2\omega_{vib}$, where λ^2 is the Huang–Rhys factor ≈1).[39]

Enhanced absorption accompanied by a redshift of the spectrum with decreasing temperature is systematically observed in conjugated polymers.[14,15,11] Those characteristics are often associated with better conjugation and planarization of the backbone; however, this statement usually is not further supported by structural-sensitive characterisation techniques such as Resonance Raman.

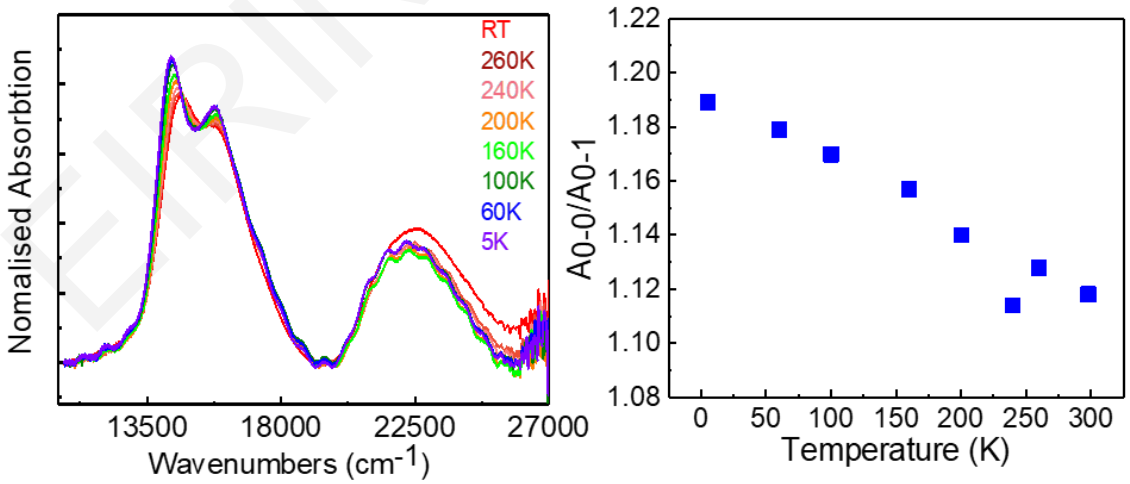

Figure 7.11: *PCE11 film absorption spectra for different temperatures (left) and $A_{0\text{-}0}/A_{0\text{-}1}$ intensity ratio as a function of temperature. The solution spectrum at RT was subtracted from all spectra.*

A combination of photoluminescence, absorption and Raman scattering techniques has been employed previously to systematically study poly(2,5-bis(2'-ethyl-hexyl)–1,4-

phenylenevinylene) (BEH–PPV) films and concluded that effective conjugation length increases at low temperatures.[16] However, results on blends of another PPV-type polymer, poly[2-methoxy-5-(2'-ethylhexyloxy)-p-phenylenevinylene] (MEH-PPV) with 2,4,7-trinitrofluorenone (TNF) forming a charge-transfer complex (CTC) do not show a direct connection to increased molecular order at low temperatures.[17] Differences observed in PCE11, would suggest a higher degree of order upon cooling, those changes however are marginal to draw safe conclusions, and thus will be accompanied by temperature-dependent Resonance Raman measurements.

The last feature of interest in the temperature evolution of the absorption spectrum is the substantial change in vibronic spacing, $\Delta_{10,}$ from 1021 cm^{-1} at 298K to 1466 cm^{-1} at 5K, far beyond theoretical predictions described by the Spano model for J aggregates.[38] (see **fig. 7.12**).

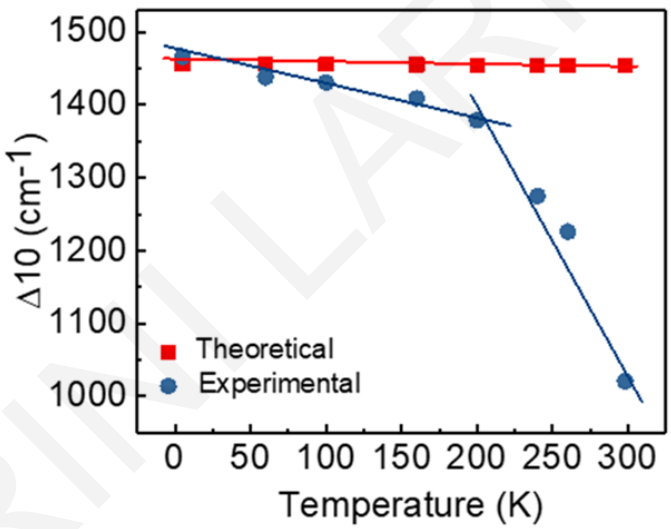

Figure 7.12: *Theoretical (red) and experimental (blue) values of vibronic spacing as a function of temperature.*

This irregular change is additionally reflected by the slope in the graph, which between 298 and 200 K is steep, while below 200 K it is much shallower. The theoretically expected value (based on the J aggregate model) for this energy difference is 1466 cm^{-1}, as calculated from the relation:

$$\frac{\Delta_{10}}{\omega_0} = 1 + 0.033\frac{J_\varphi}{\omega_0} + 0.133\frac{J_\varphi^2}{\omega_0^2} \qquad (7.2)$$

Here, ω_0 is assumed the average frequency of the dominant vibrational modes that couple to the electronic transition, J_φ is the excitonic contribution to the energy of the optically

allowed degenerate excitons with wave vectors, $k = \pi\varphi/180$, with φ expressed in degrees, and is extracted from the $A_{0\text{-}0}/A_{0\text{-}1}$ ratio since $J_\varphi = W/4$. The theoretical value of Δ_{10} is indicative of coupling of strong vibrational bands in the high frequency region, such as the thiophene and the BT C=C stretches, to the electronic transition. Since the experimental value of Δ_{10} reduces to 1021 cm^{-1} at low temperatures, a logical assumption would be that vibrational bands of lower frequency couple to the electronic transition or that the phonons responsible for the vibrational modes vary with temperature. This statement will be investigated through temperature dependent RR measurements, recorded at an extensive frequency region in the next section. One thing that is certain though is that there is a huge discrepancy between the theoretical and the experimental spacing value with temperature.

7.2.7 Temperature Dependent RR

Focusing on the CT transition due to its potential impact on photovoltaic processes, we further explore with RR the structural evolution of PCE11 as a function of temperature. Having as a guideline the evolution of the absorption spectrum in the CT transition with temperature, we obtained RR spectra in the same temperature range from 298 K down to 20 K and employed two excitation wavelengths this time: 532 and 633 nm. In **figure 7.13** we observe the effect of temperature on the RR spectra of PCE11 excited at 532 nm. This excitation wavelength is located at the high energy edge of the absorption band of the CT transition (see **fig. 7.1**), thus it can effectively probe the presence of disordered populations within the polymer. Focusing on the extended frequency region this time -to explore the potential contribution of low frequency modes to the coupling with the electronic transition- we observe that the intensity of the 428 cm^{-1} BT mode is diminished at low temperatures, the intensity of the N-S-N vibration of the BT at 852 cm^{-1} is unchanged, while no other mode appears around 1021 cm^{-1}. This shows an apparent contradiction to our effort to relate the change in vibronic spacing to a different contribution of vibrational modes at low temperatures. Moving to the high frequency region, by decreasing the temperature to 200 K we observe a 5 cm^{-1} shift of the thiophene C=C stretching mode to higher frequencies and increased FWHM which persists in all spectra down to 20 K. The broadening of the thiophene mode is indicative of the coexistence of different conjugation lengths,[40] while the shift resembles a transition-like behavior that could possibly be occurring upon cooling between 298K and 200K. A temperature-activated transition that could describe this kind of "freezing" of the polymer backbone to a locked-in configuration is the glass transition (T_g). Due to its thermomechanical character, T_g can be determined using various experimental techniques, the most popular of which are broadband dielectric spectroscopy (BDS),

dynamic mechanical analysis (DMA) and differential scanning calorimetry (DSC).[41] However, these well-developed techniques can only measure the bulk T_g of polymeric materials and it's challenging to be applied on thin films due to their limited mass that results in poor thermal signal.[42,43] Moreover, ordered phases of polymeric materials do not display T_g, making this study even harder in crystalline polymers. Other techniques such as variable-temperature ellipsometry (VTE)[44] and small angle X-ray scattering[45] have also been employed for measuring T_g in crystalline polymer thin films. Raman spectroscopy can be an indirect yet sensitive indicator of phase transitions as it follows structural changes that usually accompany such transitions and has been employed for this purpose by previous studies in the past. [43,46, 47,48]

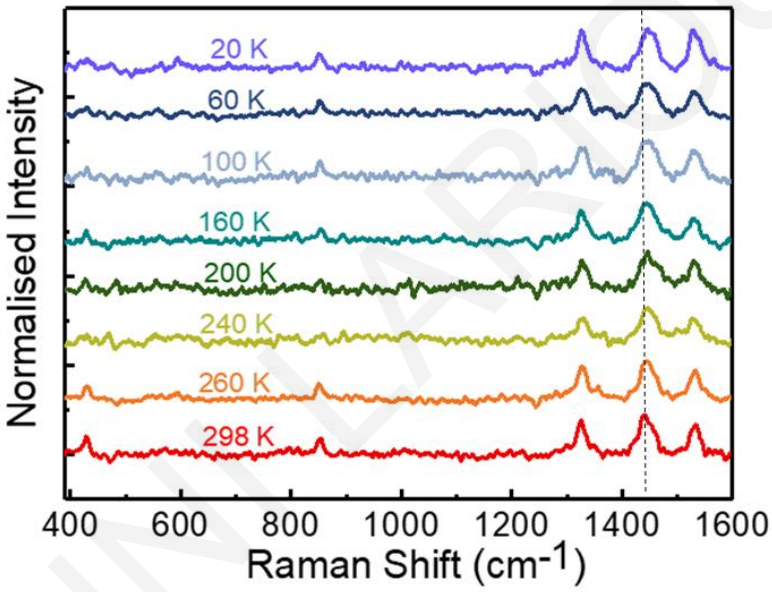

Figure 7.13: *Temperature dependent Raman spectra, acquired at an extended frequency region 390 – 1600 cm^{-1}. Excitation wavelength is 532 nm.*

More specifically, Liem et al. [43] have introduced Raman spectroscopy as a complementary technique to study T_g in thin polymer films causing Raman shifts, FWHM and relative intensity variations as a function of temperature. To further explore the possibility of a phase transition occurring between 298 K and 200 K we return to the weakly interacting J aggregate model by Spano[38,49] and having calculated the free exciton bandwidth (W) through relation 7.1, we employ the inverse free exciton bandwidth (1/W) as a proportional indicator of the conjugation length and intra-chain order of the interacting chromophores.[50,51] By plotting the 1/W as a function of temperature (**Fig. 7.14**) we notice a change in the slope around 200 K, near the temperature where the thiophene C=C stretch shift is observed, suggesting a potential correlation between them. A similar transition was reported by Root

et.al.[42] who first related this change to the T_g and Yazawa et al.,[52] who correlated the glass transition of poly(3-butylthiophene) (P3BT) with the thermal activation of the dihedral twist between two thiophene rings. Despite, however, the considerable evidence that a conformational transition occurs around 200 K, the assignment of this change to the T_g would require the confirmation by additional characterisation techniques and should not be straightforward.

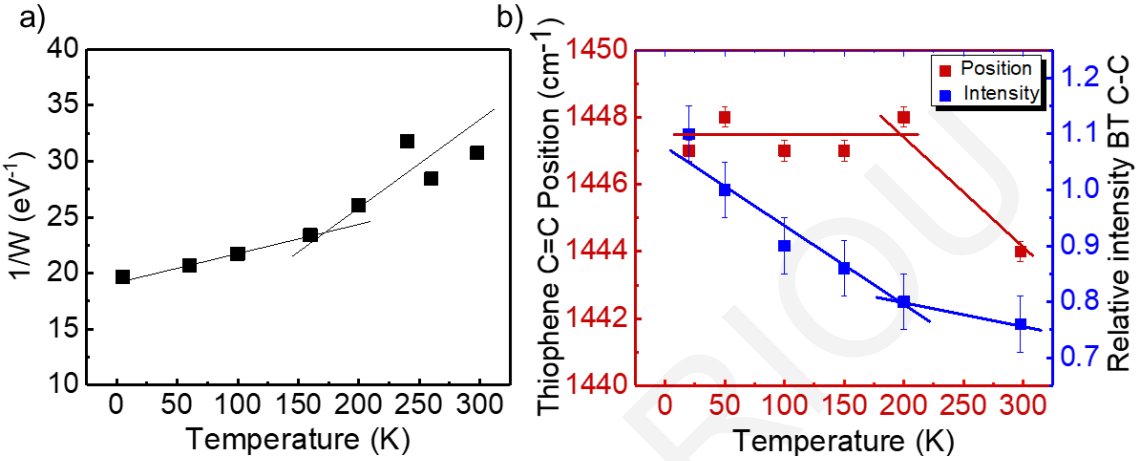

Figure 7.14: *Temperature dependent a) inverse exciton badwidth calculated by weakly interacting J aggregate analysis b) Temperature-dependent shifts of the thiophene C=C stretch (red) and relative intensity (with respect to the thiophene) of the BT C-C stretch (blue) extracted from the RR spectra excited at 532 nm.*

Together with the thiophene shift, there is a gradual enhancement of the BT C-C stretch with respect to the thiophene C=C stretch. DFT calculations confirm that those characteristics are signs of larger torsional angle between donor-acceptor units, corresponding to a less planar geometry. Reduced planarity at low temperatures has been reported in the past for the case of *para*-hexaphenyl, PHP.[53,54] Conclusively, at low temperatures, reduced motions such as torsional rotations of the thiophene rings are expected, but this is reflected in the Raman spectra by an increase in the dihedral angle between the donor and acceptor unit, suggesting a conformational transition (possibly relevant to the glass transition) occurring around 200 K.

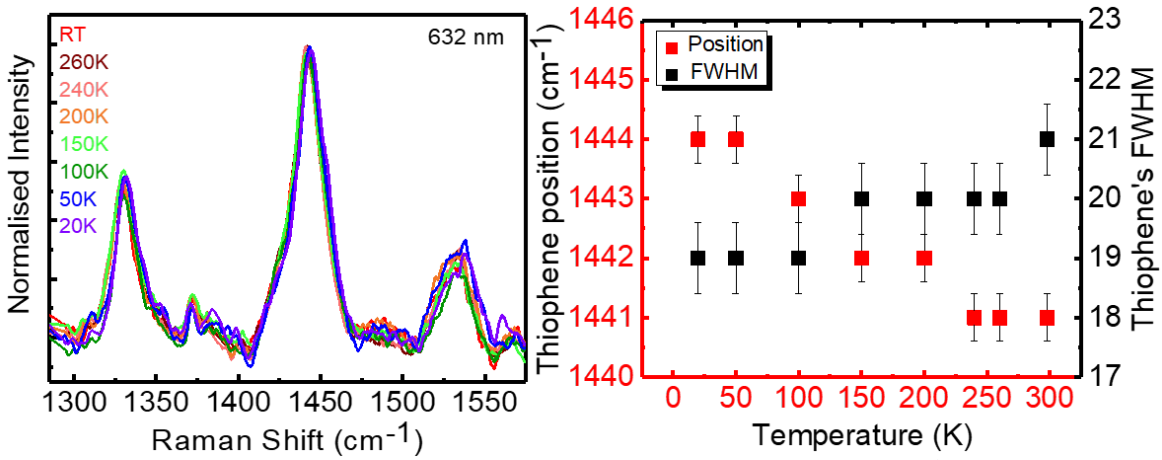

Figure 7.15: *Temperature dependent Raman spectra in the region 1280 – 1580 cm^{-1} with excitation at 632 nm (left). Fitting extracted parameters for the position and FWHM of the thiophene's C=C stretching mode (right).*

Excitation at 632 nm, despite being at the absorption maximum of the CT transition, showed significantly reduced temperature dependence in the RR spectra (see **Figure 7.15**) compared to 532 nm probably due to low sensitivity of this wavelength to disordered conformations. Although the position of the thiophene C=C stretch shifts to higher frequencies (by 2 cm^{-1}) with reducing temperature (**Figure 7.15** right), this shift is by 3 cm^{-1} more pronounced at 532 nm. Another interesting feature is the significantly lower FWHM of the thiophene's C=C stretch for all temperatures measured compared to the 532 nm excitation (the trend on the FWHM of the C=C stretch at 532 nm is shown in **Figure 7.10**). This feature suggests greater homogeneity and reinforces the argument that changes observed at 532 nm can be related to the T_g, as only disordered fractions of polymers undergo glass transition.[55]

7.2.8 Resonance Raman Intensity Analysis

Having obtained a good account of the ground state behavior, by combining the experimental data obtained by absorption and Raman, we can proceed further and access information about the early (~tens of femtoseconds after photoexcitation) excited state structure.[56] CT processes are taking place within these timescales and are often hardly detectable through conventional pump-probe spectroscopic techniques. Exploring this structural evolution in the Frank-Condon region is possible by a theoretical tool, RRIA, that allows us to directly quantify the distortion of the excited state geometry with respect to that of the ground state through the RR intensities.[57] The displacements of the potential wells from the equilibrium position (Δ) determine the shape of the absorption spectrum, providing additional insights on the resonant electronic transition. The excited state potential energy surface parameters

for PCE11 can be extracted by simultaneous modelling of the absorption spectrum and the RR relative intensities. While RR spectra are sensitive only to intra-chain structural characteristics and can be modelled as measured, to be able to reproduce the absorption experimental spectra we had to subtract the solution spectrum. The contribution from the random coil phase remains unchanged with temperature thus can be subtracted without affecting the temperature-specific characteristics. Returning to the increasing vibronic spacing observed at low temperatures (**Fig 7.12**), although it has been reported to indicate the presence of J-aggregates, knowing that the exciton coupling in our case falls within the weak regime ($W \leq \lambda^2\omega_{vib}$), where limited intra-chain interactions contribute to the absorption spectrum lineshape, we are able to consider simple models of isolated chains to reproduce theoretically the experimental spectra.

We modeled the absorption spectrum together with the RR intensities in the calculated excitation profiles (REPs) of five vibrational modes (428, 853, 1323, 1443 and 1532 cm^{-1}) for eight different temperatures: 298K, 260K, 240K, 200K, 160K, 100K, 60K and 20K. The calculated spectra of the absorption were in good agreement with the experimental ones for each temperature studied and the calculated REP curves reproduced the experimental relative RR intensities for each mode. An indicative example is shown in **figure 7.16** depicting the room temperature results while modelling results for each temperature can be found in the Appendix. The calculation extracted parameters are reported in **Table 7.4**.

It is worth mentioning that to be able to theoretically reproduce the large vibronic spacing at 20 K, it was necessary to increase the excited state frequency ω_e of three vibrational modes of the acceptor unit. Specifically, the 429 cm^{-1} bending mode of the BT and the two C=C stretching modes of the BT were increased to 600, 1600 and 1800 cm^{-1} respectively. This change is reasonable considering that acceptor modes play a dominant role in the CT transition where the π electron density in the excited state is localised on specific bonds involved in these modes (see **fig. 7.1**), causing them to adopt a double-bond character. These increased excited state frequencies were maintained for all the temperatures modelled here, with the reduced vibronic spacing at higher temperatures reproduced through increase in the spectral broadening (inhomogeneous broadening).

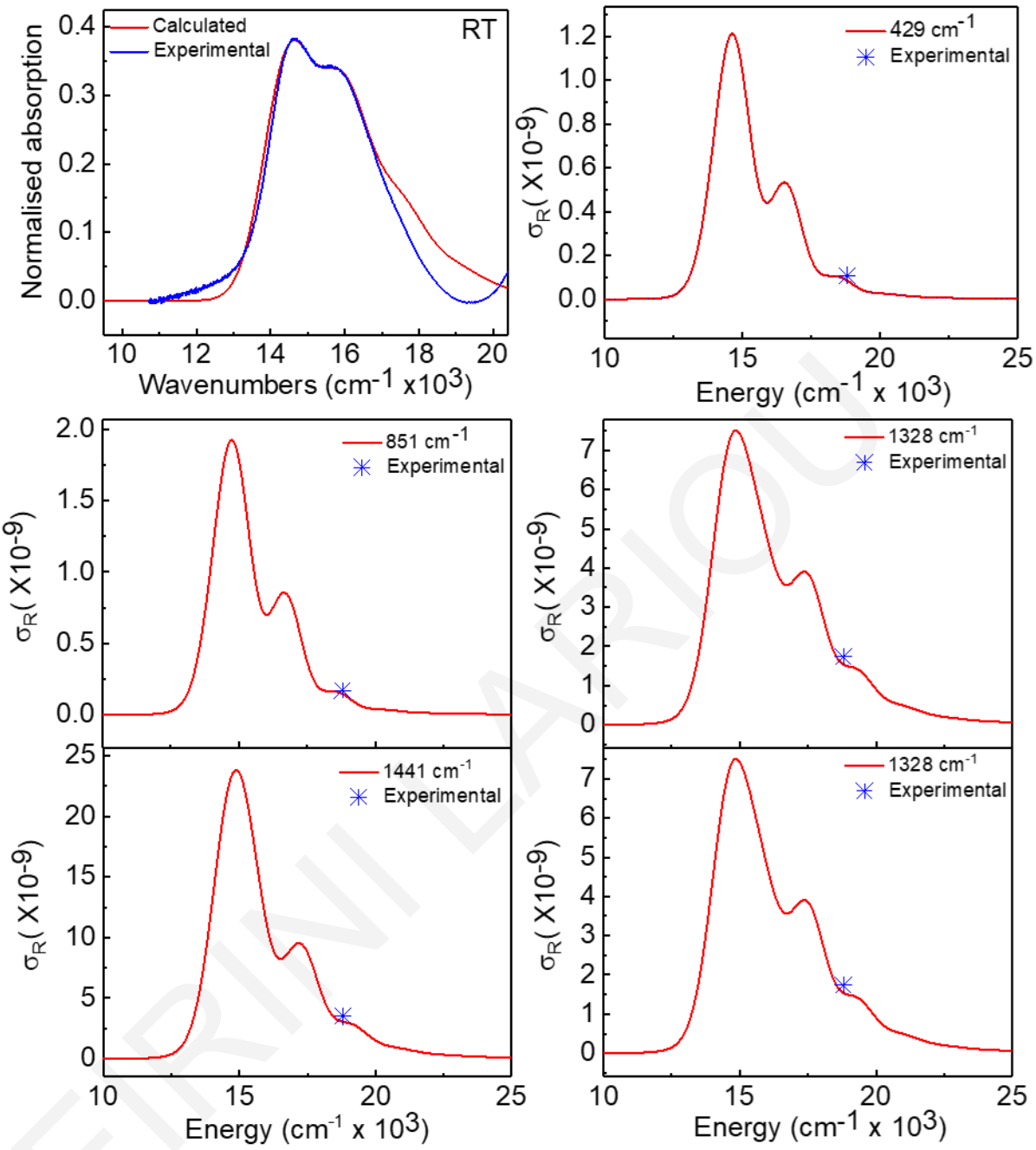

Figure 7.16: *Results of the simultaneous modelling of the room temperature absorption spectrum and the RR intensities (σ_R: Raman cross sections).*

Table 7.4: *Parameters used to computationally model absorption and RR spectra.*

	ω_g [a]	ω_e [a]	Δ_{298} [b]	Δ_{260} [b]	Δ_{240} [b]	Δ_{200} [b]	Δ_{160} [b]	Δ_{100} [b]	Δ_{60} [b]	Δ_{20} [b]
ν_1 [c]	429	600	0.26	0.24	0.25	0.22	0.22	0.22	0.25	0.25
ν_2 [c]	851	851	0.31	0.34	0.28	0.31	0.33	0.32	0.32	0.3
ν_3 [c]	1326	1600	0.52	0.54	0.47	0.47	0.5	0.46	0.48	0.5
ν_4 [c]	1443	1443	1.0	0.97	1.0	1.0	0.99	0.98	0.946	0.925
ν_5 [c]	1532	1800	0.47	0.5	0.53	0.51	0.49	0.54	0.58	0.61
Γ (cm^{-1})			250	280	320	325	295	275	255	250
Θ (cm^{-1})			545	500	440	400	415	430	450	450
E_{00}(cm^{-1})			14000	13950	13950	13950	13850	13850	13800	13770
M (A)			1.17	1.175	1.18	1.18	1.18	1.195	1.205	1.21

[a] Ground (ω_g) and excited state frequencies (ω_e)
[b] Displacements along each normal coordinate at each temperature studied
[c] Vibrational modes included in the calculation
Γ: Homogeneous broadening
Θ: Inhomogeneous broadening
E_{00}: The difference between the v = 0 in the ground and excited electronic states
M(A): The electronic transition dipole moment

In **Figure 7.17** we observe the temperature dependent evolution of the values extracted for the dimensionless displacements (Δ) for all vibrational normal modes that reflect structural changes between the ground and excited state. Thiophene modes exemplify the largest Δ values, showing a gradual decrease as we lower the temperature. The fact that Δ is reduced in the case of thiophene suggests that this distortion between the ground and excited state is less at low temperatures, i.e. the excited state conformation is closer to the ground state structure, possibly due to limited flexibility of the chains to move.

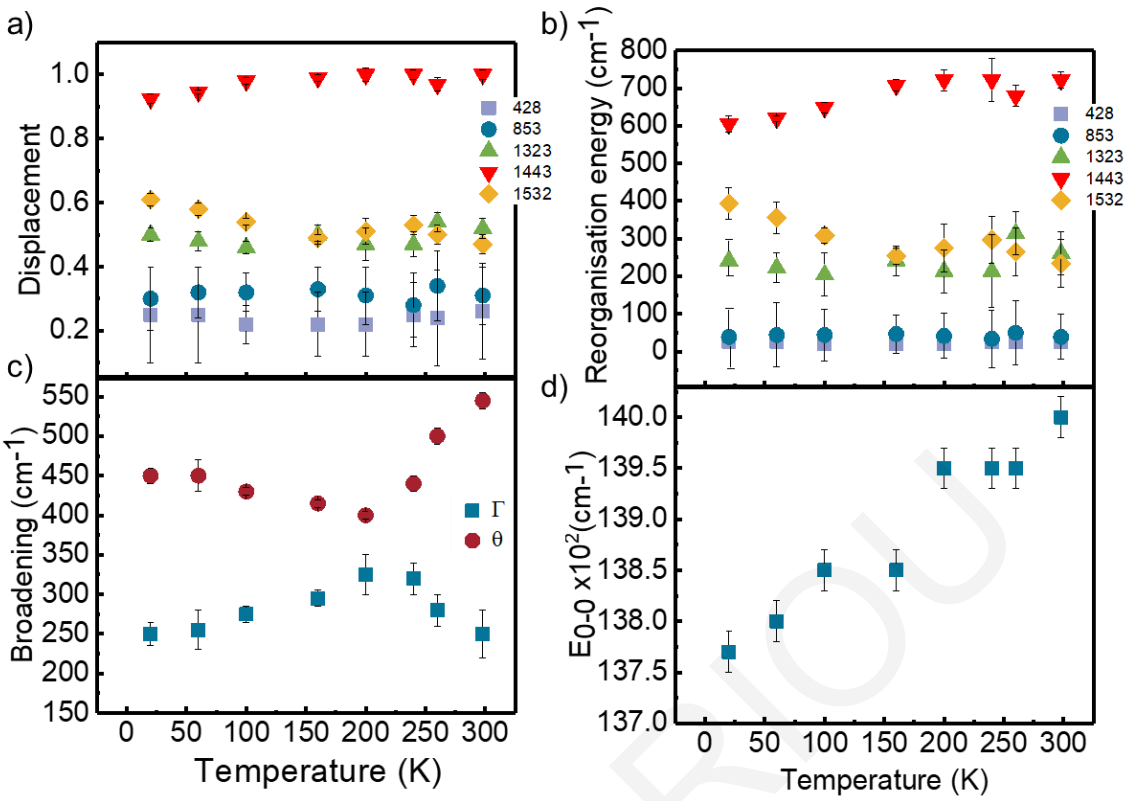

Figure 7.17: *a) Computationally extracted values for the displacements of the coordinate-dependent excited state potential well equilibrium position as a function of temperature. b) Calculated values for the reorganisation energy as a function of temperature. c) Calculated values for the homogeneous (θ) and inhomogeneous (Γ) broadening as a function of temperature. d) Calculated $E_{0\text{-}0}$ values as a function of temperature.*

The Δ values of the acceptor modes are in general constant with decreasing temperature except of the C=C stretch at 1532 cm^{-1} which shows a linear increase with decreasing temperature, in good agreement with the increased intensity of that mode upon cooling observed in the experiment. From the values for the displacement we can determine the mode specific reorganization energy though the expression: $\lambda_j = (\frac{\omega_e{}^2}{\omega_g}) \frac{\Delta_j^2}{2}$ where ω_e and ω_g are the frequencies of the excited and ground state, respectively. As expected, the temperature-dependent evolution follows the same trend as the Δ and it is clear that the largest contribution to the excited state reorganization stems from the thiophene C=C stretch. We attribute this significant contribution to the low torsional potential barrier between substituted and unsubstituted thiophenes in the backbone as revealed by DFT calculations (Graphs are included in the Appendix). **Figure 7.17c** shows that homogeneous as well as inhomogeneous broadening have a weak temperature dependence. However, one could reason that using relative rather than absolute resonance Raman cross sections in the RRIA limits the constraint and distinction of the contribution of the two types of broadening to the

absorption and Raman spectra. However, both the temperature dependence and the value of these two types of broadening have been measured through 2D PL excitation in collaboration with the group of Prof. Carlos Silva at the Georgia Institute of Technology, and those experiments confirm both the weak dependence of each on temperature, but also the magnitude of the values. The 2D results are shown in the appendix. Finally, **Figure 7.17d** $E_{0\text{-}0}$ shows a marginal shift to lower energies upon cooling, with a sharp step at 200 K, as was also observed above in the experimental spectra.

To conclude, RR spectroscopy can provide insights on morphology-dependent excited state features such as vibrational displacements as well as an accurate estimation of broadening characteristics. The apparently contradicting experimental results obtained from RR (suggesting higher torsional disorder upon cooling) and absorption (examined features suggested improved overall ordering of the chains at low temperatures) could be effectively combined to extract early excited state conformational characteristics. The most significant finding of this study was that the thiophene mode has a dominant contribution to the excited state structural distortions, especially at room temperature. This work revealed also an overall weak dependence of the mode-specific displacements (Δ) and reorganization energies with temperature, apart from a variation in the relative contribution of the thiophene mode (1441 cm^{-1}) and the BT mode at 1532 cm^{-1}. As a final note, we can say that RRIA is a very powerful theoretical tool to access information encoded in conventional spectroscopic techniques such as excited state structure and dynamics. It would be interesting to explore further its potential and applicability to other donor-acceptor systems.

References

(1) Liu, Y.; Zhao, J.; Li, Z.; Mu, C.; Ma, W.; Hu, H.; Jiang, K.; Lin, H.; Ade, H.; Yan, H. Aggregation and Morphology Control Enables Multiple Cases of High-Efficiency Polymer Solar Cells. *Nat. Commun.* **2014**, *5* (9), 1–8. https://doi.org/10.1038/ncomms6293.

(2) Zhang, Y.; Parnell, A. J.; Blaszczyk, O.; Musser, A. J.; Samuel, I. D. W.; Lidzey, D. G.; Bernardo, G. Effect of Fullerene Acceptor on the Performance of Solar Cells Based on PffBT4T-2OD. *Phys. Chem. Chem. Phys.* **2018**, *20* (28), 19023–19029. https://doi.org/10.1039/c8cp02195c.

(3) Cha, H.; Wu, J.; Wadsworth, A.; Nagitta, J.; Limbu, S.; Pont, S.; Li, Z.; Searle, J.; Wyatt, M. F.; Baran, D.; et al. An Efficient, "Burn In" Free Organic Solar Cell Employing a Nonfullerene Electron Acceptor. *Adv. Mater.* **2017**, *29* (33), 1–8. https://doi.org/10.1002/adma.201701156.

(4) Duan, L.; Elumalai, N. K.; Zhang, Y.; Uddin, A. Progress in Non-Fullerene Acceptor Based Organic Solar Cells. *Sol. Energy Mater. Sol. Cells* **2019**, *193* (December 2018), 22–65. https://doi.org/10.1016/j.solmat.2018.12.033.

(5) Li, W.; Yang, L.; Tumbleston, J. R.; Yan, L.; Ade, H.; You, W. Controlling Molecular Weight of a High Efficiency Donor-Acceptor Conjugated Polymer and Understanding Its Significant Impact on Photovoltaic Properties. *Adv. Mater.* **2014**, *26* (26), 4456–4462. https://doi.org/10.1002/adma.201305251.

(6) Osaka, I.; Saito, M.; Mori, H.; Koganezawa, T.; Takimiya, K. Drastic Change of Molecular Orientation in a Thiazolothiazole Copolymer by Molecular-Weight Control and Blending with PC 61BM Leads to High Efficiencies in Solar Cells. *Adv. Mater.* **2012**, *24* (3), 425–430. https://doi.org/10.1002/adma.201103065.

(7) Bartelt, J. A.; Douglas, J. D.; Mateker, W. R.; Labban, A. El; Tassone, C. J.; Toney, M. F.; Fréchet, J. M. J.; Beaujuge, P. M.; McGehee, M. D. Controlling Solution-Phase Polymer Aggregation with Molecular Weight and Solvent Additives to Optimize Polymer-Fullerene Bulk Heterojunction Solar Cells. *Adv. Energy Mater.* **2014**, *4* (9), 1–11. https://doi.org/10.1002/aenm.201301733.

(8) Sundberg, M.; Inganäs, O.; Stafström, S.; Gustafssön, G.; Sjögren, B. Optical Absorption of poly(3-Alkylthiophenes) at Low Temperatures. **1989**, *71* (6), 435–439.

(9) Panzer, F.; Sommer, M.; Bässler, H.; Thelakkat, M.; Köhler, A. Spectroscopic Signature of Two Distinct H-Aggregate Species in poly(3-Hexylthiophene). *Macromolecules* **2015**, *48* (5), 1543–1553. https://doi.org/10.1021/acs.macromol.5b00129.

(10) Martin, T.; Wise, A.; Busby, E.; Gao, J.; Roehling, J. D.; Ford, M. J.; Larsen, D. S.; Moulé, A. J.; Grey, J. K. Packing Dependent Electronic Coupling in Single Poly (3-Hexylthiophene) H-and J-Aggregate Nanofibers. *J. Phys. Chem. B* **2013**, *117* (16), 4478–4487. https://doi.org/10.1021/jp308586k.

(11) Kanemoto, K.; Akai, I.; Sugisaki, M.; Hashimoto, H.; Karasawa, T.; Negishi, N.; Aso, Y. Temperature Effects on Quasi-Isolated Conjugated Polymers as Revealed by Temperature-Dependent Optical Spectra of 16-Mer Oligothiophene Diluted in a Sold Matrix. *J. Chem. Phys.* **2009**, *130* (23). https://doi.org/10.1063/1.3152447.

(12) Köhler, A.; Hoffmann, S. T.; Bässler, H. An Order-Disorder Transition in the Conjugated Polymer MEH-PPV. *J. Am. Chem. Soc.* **2012**, *134* (28), 11594–11601. https://doi.org/10.1021/ja302408a.

(13) Kong, F.; Wu, X. L.; Huang, G. S.; Yuan, R. K.; Yang, C. Z.; Chu, P. K.; Siu, G. G. Temperature-Dependent Photoluminescence from MEH-PPV and MEH-OPPV Containing Oxadiazole in the Main Chain. *Appl. Phys. A Mater. Sci. Process.* **2006**, *84* (1–2), 203–206. https://doi.org/10.1007/s00339-006-3601-5.

(14) Hedström, S.; Henriksson, P.; Wang, E.; Andersson, M. R.; Persson, P. Temperature-Dependent Optical Properties of Flexible Donor-Acceptor Polymers. *J. Phys. Chem. C* **2015**, *119* (12), 6453–6463. https://doi.org/10.1021/jp511246n.

(15) Panzer, F.; Bässler, H.; Köhler, A. Temperature Induced Order-Disorder Transition in Solutions of Conjugated Polymers Probed by Optical Spectroscopy. *J. Phys. Chem. Lett.* **2017**, *8* (1), 114–125. https://doi.org/10.1021/acs.jpclett.6b01641.

(16) Oliveira, F. A. C.; Cury, L. A.; Righi, A.; Moreira, R. L.; Guimarães, P. S. S.; Matinaga, F. M.; Pimenta, M. A.; Nogueira, R. A. Temperature Effects on the Vibronic Spectra of BEH-PPV Conjugated Polymer Films. *J. Chem. Phys.* **2003**, *119* (18), 9777–9782. https://doi.org/10.1063/1.1615959.

(17) Osotov, M. O.; Bruevich, V. V.; Paraschuk, D. Y. Thermal Vibrational Disorder of a Conjugated Polymer in Charge-Transfer Complex. *J. Chem. Phys.* **2009**, *131* (9). https://doi.org/10.1063/1.3216106.

(18) Wu, Z.; Petzold, A.; Henze, T.; Thurn-Albrecht, T.; Lohwasser, R. H.; Sommer, M.; Thelakkat, M. Temperature and Molecular Weight Dependent Hierarchical Equilibrium Structures in Semiconducting poly(3-Hexylthiophene). *Macromolecules* **2010**, *43* (10), 4646–4653. https://doi.org/10.1021/ma902566h.

(19) Myers, A. B. Resonance Raman Intensity Analysis of Excited-State Dynamics. *Acc. Chem. Res.* **1997**, *30* (12), 519–527. https://doi.org/10.1021/ar960240c.

(20) Myers, A. B. Resonance Raman Intensities and Charge-Transfer Reorganization Energies. *Chem. Rev.* **1996**, *96* (3), 911–926. https://doi.org/10.1021/cr950249c.

(21) Myers, A. B. "Time-Dependent" Resonance Raman Theory. *J. Raman Spectrosc.* **1997**, *28* (6), 389–401. https://doi.org/10.1002/(sici)1097-4555(199706)28:6<389::aid-jrs128>3.3.co;2-d.

(22) Dantanarayana, V.; Fuzell, J.; Nai, D.; Jacobs, I. E.; Yan, H.; Faller, R.; Larsen, D.; Moule, A. J. Put Your Backbone into It: Excited-State Structural Relaxation of PffBT4T-2DT Conducting Polymer in Solution. *J. Phys. Chem. C* **2018**, *122* (12), 7020–7026. https://doi.org/10.1021/acs.jpcc.8b01356.

(23) Spano, F. C.; Introduction, I. The Spectral Signatures of Frenkel Polarons in H and J Aggregates. *Acc. Chem. Res.* **2009**, *43* (3), 429–439.

(24) Reish, M. E.; Nam, S.; Lee, W.; Woo, H. Y.; Gordon, K. C. A Spectroscopic and DFT Study of the Electronic Properties of Carbazole-Based D-A Type Copolymers. *J. Phys. Chem. C* **2012**, *116* (40), 21255–21266. https://doi.org/10.1021/jp307552z.

(25) Martin, E. J. J.; Bérubé, N.; Provencher, F.; Côté, M.; Silva, C.; Doorn, S. K.; Grey, J. K. Resonance Raman Spectroscopy and Imaging of Push–pull Conjugated Polymer–fullerene Blends. *J. Mater. Chem. C* **2015**, *3* (23), 6058–6066. https://doi.org/10.1039/C5TC00847F.

(26) Koppe, M.; Brabec, C. J.; Heiml, S.; Schausberger, A.; Duffy, W.; Heeney, M.; McCulloch, I. Influence of Molecular Weight Distribution on the Gelation of P3HT and Its Impact on the Photovoltaic Performance. *Macromolecules* **2009**, *42* (13), 4661–4666. https://doi.org/10.1021/ma9005445.

(27) Ma, W.; Kim, J. Y.; Lee, K.; Heeger, A. J. Effect of the Molecular Weight of poly(3-Hexylthiophene) on the Morphology and Performance of Polymer Bulk Heterojunction Solar Cells. *Macromol. Rapid Commun.* **2007**, *28* (17), 1776–1780. https://doi.org/10.1002/marc.200700280.

(28) Fetters, L. J.; Lohse, D. J.; Richter, D.; Witten, T. A.; Zirkel, A. Connection between Polymer Molecular Weight, Density, Chain Dimensions, and Melt Viscoelastic Properties. *Macromolecules* **1994**, *27* (17), 4639–4647. https://doi.org/10.1021/ma00095a001.

(29) Brabec, C. J.; Heeney, M.; McCulloch, I.; Nelson, J. Influence of Blend Microstructure on Bulk Heterojunction Organic Photovoltaic Performance. *Chem. Soc. Rev.* **2011**, *40* (3), 1185–1199. https://doi.org/10.1039/c0cs00045k.

(30) Noriega, R.; Rivnay, J.; Vandewal, K.; Koch, F. P. V; Stingelin, N.; Smith, P.; Toney, M. F.; Salleo, A. A General Relationship between Disorder, Aggregation and Charge Transport in Conjugated Polymers. *Nat. Mater.* **2013**, *12* (11), 1038–

1044. https://doi.org/10.1038/nmat3722.

(31) Morvillo, P.; Bobeico, E.; Esposito, S.; Diana, R. Effect of the Active Layer Thickness on the Device Performance of Polymer Solar Cells Having [60]PCBM and [70]PCBM as Electron Acceptor. *Energy Procedia* **2012**, *31*, 69–73. https://doi.org/10.1016/j.egypro.2012.11.166.

(32) Mouĺ, A. J.; Bonekamp, J. B.; Meerholz, K. The Effect of Active Layer Thickness and Composition on the Performance of Bulk-Heterojunction Solar Cells. *J. Appl. Phys.* **2006**, *100* (9). https://doi.org/10.1063/1.2360780.

(33) Ferenczi, T. A. M.; Müller, C.; Bradley, D. D. C.; Smith, P.; Nelson, J.; Stingelin, N. Organic Semiconductor: Insulator Polymer Ternary Blends for Photovoltaics. *Adv. Mater.* **2011**, *23* (35), 4093–4097. https://doi.org/10.1002/adma.201102100.

(34) Jahnke, A. A.; Yu, L.; Coombs, N.; Scaccabarozzi, A. D.; Tilley, A. J.; Dicarmine, P. M.; Amassian, A.; Stingelin, N.; Seferos, D. S. Polytellurophenes Provide Imaging Contrast towards Unravelling the Structure-Property-Function Relationships in Semiconductor: Insulator Polymer Blends. *J. Mater. Chem. C* **2015**, *3* (15), 3767–3773. https://doi.org/10.1039/c5tc00158g.

(35) Razzell-Hollis, J.; Fleischli, F.; Jahnke, A. A.; Stingelin, N.; Seferos, D. S.; Kim, J. S. Effects of Side-Chain Length and Shape on Polytellurophene Molecular Order and Blend Morphology. *J. Phys. Chem. C* **2017**, *121* (4), 2088–2098. https://doi.org/10.1021/acs.jpcc.6b11675.

(36) Kumar, A.; Baklar, M. A.; Scott, K.; Kreouzis, T.; Stingelin-Stutzmann, N. Efficient, Stable Bulk Charge Transport in Crystalline/crystalline Semiconductor-Insulator Blends. *Adv. Mater.* **2009**, *21* (44), 4447–4451. https://doi.org/10.1002/adma.200900717.

(37) Spano, F. C. Modeling Disorder in Polymer Aggregates: The Optical Spectroscopy of Regioregular poly(3-Hexylthiophene) Thin Films. *J. Chem. Phys.* **2005**, *122* (23). https://doi.org/10.1063/1.1914768.

(38) Spano, F. C. Analysis of the UV/Vis and CD Spectral Line Shapes of Carotenoid Assemblies: Spectral Signatures of Chiral H-Aggregates. *J. Am. Chem. Soc.* **2009**, *131* (12), 4267–4278. https://doi.org/10.1021/ja806853v.

(39) Spano, F. C. Absorption in Regio-Regular poly(3-Hexyl)thiophene Thin Films: Fermi Resonances, Interband Coupling and Disorder. *Chem. Phys.* **2006**, *325* (1), 22–35. https://doi.org/10.1016/j.chemphys.2005.08.019.

(40) C.Heller; G.leising; C.Godon; S.Lefrant; W.Fischer; F.Stelzer. Raman Excitation Profiles of Conjugated Segments in Solution. *Phys. Rev. B* **1995**, *51* (13), 8107–8114.

(41) Qian, Z.; Cao, Z.; Galuska, L.; Zhang, S.; Xu, J.; Gu, X. Glass Transition Phenomenon for Conjugated Polymers. *Macromol. Chem. Phys.* **2019**, *1900062*, 1–30. https://doi.org/10.1002/macp.201900062.

(42) Root, S. E.; Alkhadra, M. A.; Rodriquez, D.; Printz, A. D.; Lipomi, D. J. Measuring the Glass Transition Temperature of Conjugated Polymer Films with Ultraviolet-Visible Spectroscopy. *Chem. Mater.* **2017**, *29* (7), 2646–2654. https://doi.org/10.1021/acs.chemmater.7b00242.

(43) Liem, H.; Cabanillas-Gonzalez, J.; Etchegoin, P.; Bradley, D. D. C. Glass Transition Temperatures of Polymer Thin Films Monitored by Raman Scattering. *J. Phys.*

Condens. Matter **2004**, *16* (6), 721–728. https://doi.org/10.1088/0953-8984/16/6/003.

(44) G.Beaucage; R.Composto; R.S.Stein. Ellipsometric Study of the Glass Transition and Thermal Expansion Coefficients of Thin Polymer Films C. *J. Polym. Sci. Part B Polym. Phys.* **1993**, *31*, 319–326.

(45) Fischer, E. W. Small Angle X-Ray Scattering Studies of Phase Transitions in Polymeric and Oligomeric Systems. *Pure Appl. Chem.* **2008**, *26* (3–4), 385–422. https://doi.org/10.1351/pac197126030385.

(46) Abramczyk, H.; Paradowska-Moszkowska, K. Crystallization and Glass Formation Processes in Methylcyclohexane: Vibrational Dynamics as a Possible Molecular Indicator of the Liquid-Glass Transition. *J. Chem. Phys.* **2001**, *115* (24), 11221–11227. https://doi.org/10.1063/1.1420490.

(47) Menezes, D. B.; Reyer, A.; Musso, M. Verifying the Glass Transition Temperature of Polymers (Ps, Pmma and Pet) By Raman Spectroscopy. *I.J.E.M.S.* **2016**, *7* (2), 84–90.

(48) Samith, V. D.; Ramos-Moore, E. Study of Glass Transition in Functionalized Poly(itaconate)s by Differential Scanning Calorimetry, Raman Spectroscopy and Thermogravimetric Analysis. *J. Non. Cryst. Solids* **2015**, *408*, 37–42. https://doi.org/10.1016/j.jnoncrysol.2014.10.009.

(49) Clark, J.; Silva, C.; Friend, R. H.; Spano, F. C. Role of Intermolecular Coupling in the Photophysics of Disordered Organic Semiconductors: Aggregate Emission in Regioregular Polythiophene. *Phys. Rev. Lett.* **2007**, *98* (20), 1–4. https://doi.org/10.1103/PhysRevLett.98.206406.

(50) Clark, J.; Chang, J. F.; Spano, F. C.; Friend, R. H.; Silva, C. Determining Exciton Bandwidth and Film Microstructure in Polythiophene Films Using Linear Absorption Spectroscopy. *Appl. Phys. Lett.* **2009**, *94* (16), 3–6. https://doi.org/10.1063/1.3110904.

(51) Spano, F. C.; Silva, C. H- and J-Aggregate Behavior in Polymeric Semiconductors. *Annu. Rev. Phys. Chem.* **2014**, *65*, 477–500. https://doi.org/10.1146/annurev-physchem-040513-103639.

(52) Yazawa, K.; Inoue, Y.; Yamamoto, T.; Asakawa, N. Twist Glass Transition in Regioregulated poly(3-Alkylthiophene). *Phys. Rev. B - Condens. Matter Mater. Phys.* **2006**, *74* (9), 1–12. https://doi.org/10.1103/PhysRevB.74.094204.

(53) Guha, S.; Graupner, W.; Resel, R.; Chandrasekhar, M.; Chandrasekhar, H. R.; Glaser, R.; Leising, G. Planarity of Para Hexaphenyl. *Phys. Rev. Lett.* **1999**, *82* (18), 3625–3628. https://doi.org/10.1103/PhysRevLett.82.3625.

(54) Guha, S.; Graupner, W.; Resel, R.; Chandrasekhar, M.; Chandrasekhar, H. R.; Glaser, R.; Leising, G. Tuning Intermolecular Interactions: A Study of the Structural and Vibrational Properties of P -Hexaphenyl under Pressure. *J. Phys. Chem. A* **2001**, *105* (25), 6203–6211. https://doi.org/10.1021/jp0045540.

(55) Müller, C. On the Glass Transition of Polymer Semiconductors and Its Impact on Polymer Solar Cell Stability. *Chem. Mater.* **2015**, *27* (8), 2740–2754. https://doi.org/10.1021/acs.chemmater.5b00024.

(56) Mondal, S.; Puranik, M. Sub-50 Fs Excited State Dynamics of 6-Chloroguanine upon Deep Ultraviolet Excitation. *Phys. Chem. Chem. Phys.* **2016**, *18* (20), 13874–

13887. https://doi.org/10.1039/c6cp01746k.

(57) Myers, A. B.; Mathies, R. A. Resonance Raman Intensities: A Probe of Excited-State Structure and Dynamics. *Biological Applications of Raman Spectroscopy*. 1987, pp 1–58.

Chapter 8

Conclusions

The overall aim of this work was to establish a fundamental understanding on how film processing affects molecular conformation in organic semiconductors. Moreover, the connection between structure and optical properties was discussed. Two different conjugated systems were studied within this doctoral dissertation. P3HT, a polymer that although it is not a promising candidate for high performance devices, it has long served as a reference system, thus its contribution to understanding the behaviour of conjugated polymers in general is valuable. PCE11 on the other hand, is a polymer that holds enough promise for its integration in OPV applications, yet it is still not sufficiently understood. The common ground between these two systems is that molecular ordering can be easily manipulated by means of processing. Each chapter of this work, provided through different perspectives solid evidence on the sensitivity of molecular conformation to various parameters such as molecular weight, casting conditions and blending with additives. A summary of the most important findings as well as their contribution to the state of the art fundamental understanding of the structure-processing relation is presented in this chapter.

8.1 Controlling local ordering via polarity contrast

In this chapter, the effect of commonly employed approaches on controlling local features was investigated and quantified. Moreover, a common approach which is blending the active material with insulating commodity plastics was extended through considering polarity differences between the semiconductor backbone, its side chains and the additive. The key findings are outlined below:

- By employing the P3HT:PEO blend, we explored the effect of different molecular weight combinations on the optical properties of the blend, a study that highlighted the importance of molecular weight of the additive. Molecular weight of the active material is undoubtedly crucial to the overall properties of conjugated systems, however, in order to fully exploit the potential of blend systems, molecular weight of the additive is a key factor that should be judiciously considered.
- The casting conditions and specifically casting temperature has a substantial effect on the optical and structural properties of blend films (P3HT:PEO). By employing different casting temperatures while wire-bar coating the film, we observed a pronounced

threshold in absorption characteristics around 15^{o}C, where the character of aggregation changed from H-like to J-like, possibly suggesting different phase separation behavior that could be exploited during device fabrication.

- By blending polar P3HT derivatives with insulating commodity plastics, we showed that polarity-driven interactions between the semiconductor and the polymer additive can lead to controlled manipulation of the semiconductor backbone planarity. Polar side chains, often responsible for torsional disorder, can actually promote aggregation and reduce disorder while matched with a polar additive. The enthalpically favourable interactions between additive and side chains 'expel' side chains away from the backbone, reducing steric hinderance and facilitating the re-emergence of backbone order. As it is often hard to achieve all functionality exclusively via chemical design, these findings open a simple alternative pathway to structural control providing a platform for future material selection and processing criteria.

8.2 Photo-active layer morphology and organic metal interface

In this chapter, the conformation of the OPV's photoactive layer (consisting of the archetypal P3HT:PCBM mix) was considered from both the bulk's perspective as well as the interface's with a metal electrode. The correlation of structure with organic solar cell (OSC) characteristics was additionally discussed. The most important findings and conclusions are summarised below:

- P3HT polymorph distribution ("densely" and "non-densely" packed structural motifs) has impact on the energetic disorder of the blend. The distribution of polymorphs was controlled by varying the number-averaged molecular weight (M_n) of the P3HT polymer matrix with low-M_n-P3HT-based blends exhibiting a bimodal distribution (coexistence of "densely" and non-densely" packed polymorphs) and high-M_n P3HT-based P3HT:PCMB blends a uniform distribution of "non-densely" packed polymorphs. RR spectroscopy was sensitive enough to probe some energetic disorder which persists despite the annealing treatment in the absence of densely packed polymorphs. This finding contributes to the overall understanding of those two systems and can be related to the device performance, as the presence of densely packed polymorphs lead to increased PCE. The knowledge gained by these results regarding the impact of polymorphism distribution on charge carrier motilities can potentially be useful in the optimisation of different types of optoelectronic devices such as fullerene-free OPVs and organic light emitting diode (OLED) devices.

- The presence of a metal electrode inhibits short-range ordering of P3HT:PCBM systems as the proximity with a rough metal surface is likely to disrupt the order of P3HT chains. Incorporating specific additives, HEG-DT and BDMT, in the P3HT:PCBM photoactive layer, has a positive effect on the microscopic ordering of the chains both at the bulk of the films and the organic-metal interface. Possibly the formation of the interlayer (caused by the favourable interactions of the additive's thiol end groups and silver) prevents the disruption observed for P3HT:PCBM but only when the additives are blended in the organic layer and not if deposited separately. The interfacial morphology probed by SERRS could not be correlated in this case with device performance as the interfacial energy level alignment was possibly determined by the different chemical environments imposed by the different additives at the organic/metal interface. This contradicts with the current understanding on the direct correlation between morphology and device performance and highlights that this conclusion should not be straightforward.

8.3 Spectroscopic and computational study of the donor-acceptor polymer PCE11

In this chapter, a fundamental study on PCE11, a new generation donor-acceptor polymer was performed, showing a processing dependence of its molecular conformation. Moreover, ground as well as excited state structure was monitored through a spectroscopic and computational temperature dependent study. A summary of the drawn conclusions is presented below:

- RR experiments provide evidence that high M_n PCE11 films (83 $kg{\cdot}mol^{-1}$) can relate to improved backbone planarity compared to low M_n ones (55 $kg{\cdot}mol^{-1}$), following our understanding for other donor-acceptor polymers regarding the impact of molecular weight. Film thickness has a significant impact on backbone conformation (thick films of 200 nm showed a substantially improved chain planarity compared to thinner ones (50 nm)). These findings suggest that M_n and thickness can be potentially exploited as a way to control morphological characteristics, thus their impact on photoactive layer morphology should be further explored considering blends with fullerenes or other small molecule acceptors.
- Evidence on increased torsional disorder of the PCE11's chains at low temperatures stimulated a systematic study of the properties of this systems at cryogenic temperatures. Absorption measurements showed a weak dependence of the 0-0/0-1 intensity ratio – sensitive indicator of the strength of inter-versus intra-chain coupling- with temperature while RR data provide clear evidence of a transition-like twisting of the chains around

200K. This structural change at low temperatures contradicts with the state of the general assumption of chain planarization upon cooling, established through temperature dependent absorption experiments, which was not usually supported by structurally sensitive techniques. This is especially an issue in the case when the optical changes are small as other contributions could be at work.

- A simultaneous modelling of absorption and RR excitation profiles (REPS) was performed to access the excited state structure and it was shown than that largest contribution to the excited state reorganization stems from the thiophene C=C stretch, due to the low torsional potential barrier between substituted and unsubstituted thiophenes in the backbone. These findings shape a fundamental understanding regarding the excited state behaviour of PCE11 and can potentially describe the structural behaviour of similar donor-acceptor systems.

Chapter 9

Future perspectives

Exploring the structure-processing relation in organic semiconductors is a process with unlimited sources for research, from the choice of the appropriate solvents and additives to post deposition treatment techniques. The present work provided unambiguous evidence regarding the sensitivity of structure to various processing parameters (deposition temperature, blend additives, film thickness etc.). which could serve as a useful scientific basis for further research. Considering the conclusions drawn, some suggestions for the orientation of the future research are provided below:

P3HT-based systems are in general well-characterised and a satisfactory level of understanding has been built over the past decades of research. However, a major hurdle towards commercial reality is the long-term stability of devices and future research should definitely address this issue. Stability is tightly connected to morphological degradation and various parameters such as temperature, power cycling or radiation can contribute to this. The present study addressed the effect of exposure to humidity at P3BEOT and P3BEOT:PEO blends. Humidity was shown to alter their structural and optical properties. Moreover, while left to ambient conditions for 4 months, structural degradation was observed in the case of P3BEOT.Those findings suggest that Raman spectroscopy can be a sensitive probe of morphological changes observed over time or under exposure to high/low temperatures, humidity, illumination or mechanical stress, thus, such experiments would be a reasonable continuation of this work. The stability issue can be also addressed by means of processing such as testing specific additives (ex. HDPE) that can provide local encapsulation.[1] In general, the most significant operational stabilities reported so far are up to only a few years.[2,3] A specific intrinsically stable system however, was recently tested under high intensity illumination, showing promise for the future.[4]

Another meaningful direction of future research discussed in the 6th chapter of this work, would be the exploitation of SERRS in the study of interfacial properties. Interfacial phenomena between organic materials and metals, although are crucial for improving device performances, are not easily accessible by other experimental techniques. SERRS is a

powerful tool to quantify and understand these phenomena with high sensitivity and selectivity, and can serve as a way to unravel the impact of morphology to device characteristics. Moreover, it can be applied to various different systems, not limited to OSCs, but also field effect transistors, sensors etc., while a different perspective would be the study of plasmonic phenomena that lead to increased absorption within the active layer.

Regarding PCE11, the potential research paths are numerous, as several issues are still open. First of all, although the present work provides some preliminary results regarding the effect of specific parameters, the structure-processing relation should be established based on a large number of samples, prepared by different deposition techniques additionally to wire-bar coating (as the results presented here) and moreover, tested over time to ensure reliability. This fundamental research is required, before mixing with any acceptor and explore their potential correlation with device performance. Temperature-dependent measurements performed within this study offer valuable insides on the evolution of structural and optical properties upon cooling, however, they do not answer the fundamental question regarding the abnormal increase of vibronic spacing observed in absorption spectra upon cooling. Finally, to relate our fundamental understanding regarding excited state properties with the end applications in OSCs, a direct experimental observation of lifetimes and dynamics through transient spectroscopic techniques such as transient absorption (TA) and time-resolved Resonance Raman (TRRR) would we valuable. PCE11 combined with PCBM or other acceptors can be monitored to extract lifetimes for photophysical processes such as exciton generation and recombination, polaron formation etc. Some preliminary studies on PCE11:PCBM blends as well as a blend with non-fullerene acceptor do exist, revealing exciton lifetimes and exciton diffusion lengths through TA experiments.[5] Polaron lifetimes of PCE11:PCBM blends can additionally be inferred by those data, estimated to occur at nanosecond time scales. Those long-lived polarons should be detectable by TRRR through ours group setup by employing near-IR excitation wavelengths. An initial effort to set up this experiment has already been attempted, the challenge however rests on the alignment of the invisible 953 nm laser beam. If this is overcome, we'll be able to obtain a dinstict signature of the polaron formation in the vibrational modes of the polymer and access molecular conformation dynamics of this fundamental photophysical process.

References

(1) Kumar, A.; Baklar, M. A.; Scott, K.; Kreouzis, T.; Stingelin-Stutzmann, N. Efficient, Stable Bulk Charge Transport in Crystalline/crystalline Semiconductor-Insulator Blends. *Adv. Mater.* **2009**, *21* (44), 4447–4451. https://doi.org/10.1002/adma.200900717.

(2) Cha, H.; Wu, J.; Wadsworth, A.; Nagitta, J.; Limbu, S.; Pont, S.; Li, Z.; Searle, J.; Wyatt, M. F.; Baran, D.; et al. An Efficient, "Burn In" Free Organic Solar Cell Employing a Nonfullerene Electron Acceptor. *Adv. Mater.* **2017**, *29* (33), 1–8. https://doi.org/10.1002/adma.201701156.

(3) Baran, D.; Ashraf, R. S.; Hanifi, D. A.; Abdelsamie, M.; Gasparini, N.; Röhr, J. A.; Holliday, S.; Wadsworth, A.; Lockett, S.; Neophytou, M.; et al. Reducing the Efficiency-Stability-Cost Gap of Organic Photovoltaics with Highly Efficient and Stable Small Molecule Acceptor Ternary Solar Cells. *Nat. Mater.* **2017**, *16* (3), 363–369. https://doi.org/10.1038/nmat4797.

(4) Burlingame, Q.; Huang, X.; Liu, X.; Jeong, C.; Coburn, C.; Forrest, S. R. Intrinsically Stable Organic Solar Cells under High-Intensity Illumination. *Nature* **2019**, *573* (7774), 394–397. https://doi.org/10.1038/s41586-019-1544-1.

(5) Cha, H.; Wheeler, S.; Holliday, S.; Dimitrov, S. D.; Wadsworth, A.; Lee, H. H.; Baran, D.; McCulloch, I.; Durrant, J. R. Influence of Blend Morphology and Energetics on Charge Separation and Recombination Dynamics in Organic Solar Cells Incorporating a Nonfullerene Acceptor. *Adv. Funct. Mater.* **2018**, *28* (3), 1–11. https://doi.org/10.1002/adfm.201704389.

APPENDIX

Supplementary figures

Figure S1*: Results of the simultaneous modelling of the PCE11 absorption spectrum together with the RR intensities that coincide with the REPs of each mode. The data where acquired at 260 K.*

Figure S2*: Results of the simultaneous modelling of the PCE11 absorption spectrum together with the RR intensities that coincide with the REPs of each mode. The data where acquired at 240 K.*

Figure S3*: Results of the simultaneous modelling of the PCE11 absorption spectrum together with the RR intensities that coincide with the REPs of each mode. The data where acquired at 200 K.*

Figure S4*: Results of the simultaneous modelling of the PCE11 absorption spectrum together with the RR intensities that coincide with the REPs of each mode. The data where acquired at 160 K.*

Figure S5*: Results of the simultaneous modelling of the PCE11 absorption spectrum together with the RR intensities that coincide with the REPs of each mode. The data where acquired at 100 K.*

Figure S6*: Results of the simultaneous modelling of the PCE11 absorption spectrum together with the RR intensities that coincide with the REPs of each mode. The data where acquired at 60 K.*

Figure S7*: Results of the simultaneous modelling of the PCE11 absorption spectrum together with the RR intensities that coincide with the REPs of each mode. The data where acquired at 20 K.*

Figure S8*: PCE11 dimer's calculated surface potential as a function of torsion angle.*

Figure S9: *Experimentally extracted linewindths (by 2D PL measurements). (Fluence 157 nJ/cm^2)*

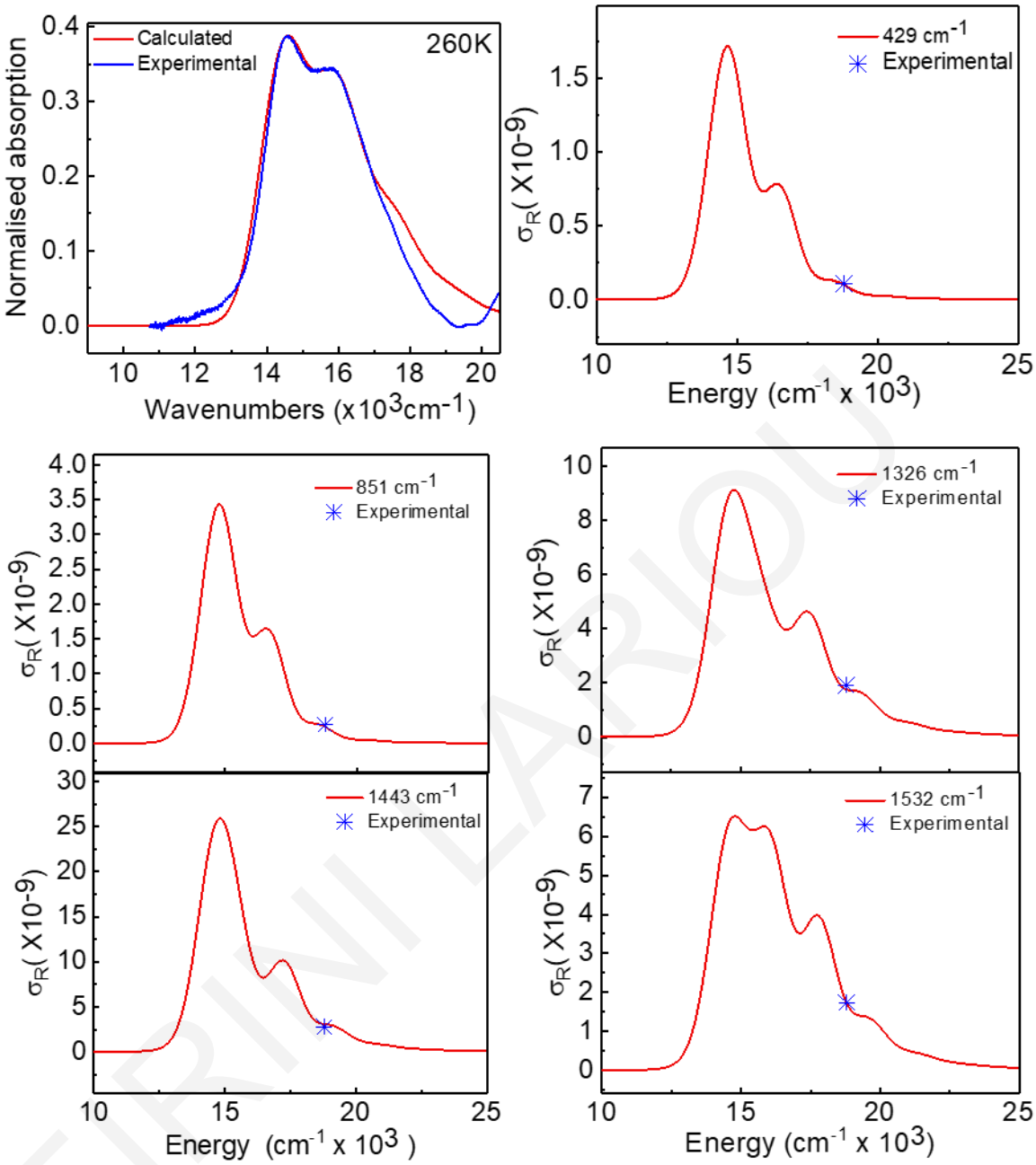

Figure S1: *Results of the simultaneous modelling of the PCE11 absorption spectrum together with the RR intensities that coincide with the REPs of each mode. The data where acquired at 260 K.*

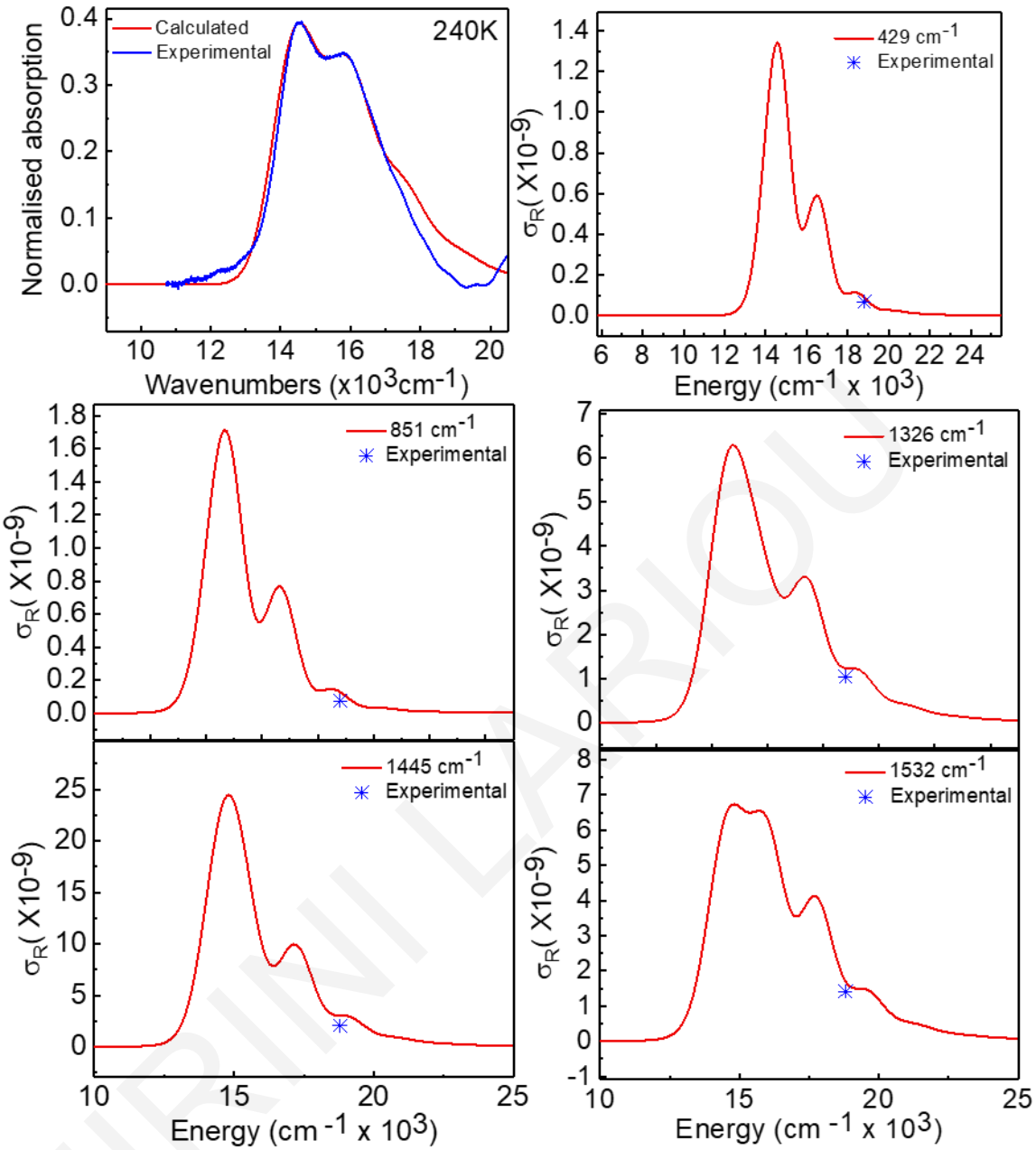

Figure S2: *Results of the simultaneous modelling of the PCE11 absorption spectrum together with the RR intensities that coincide with the REPs of each mode. The data where acquired at 240 K.*

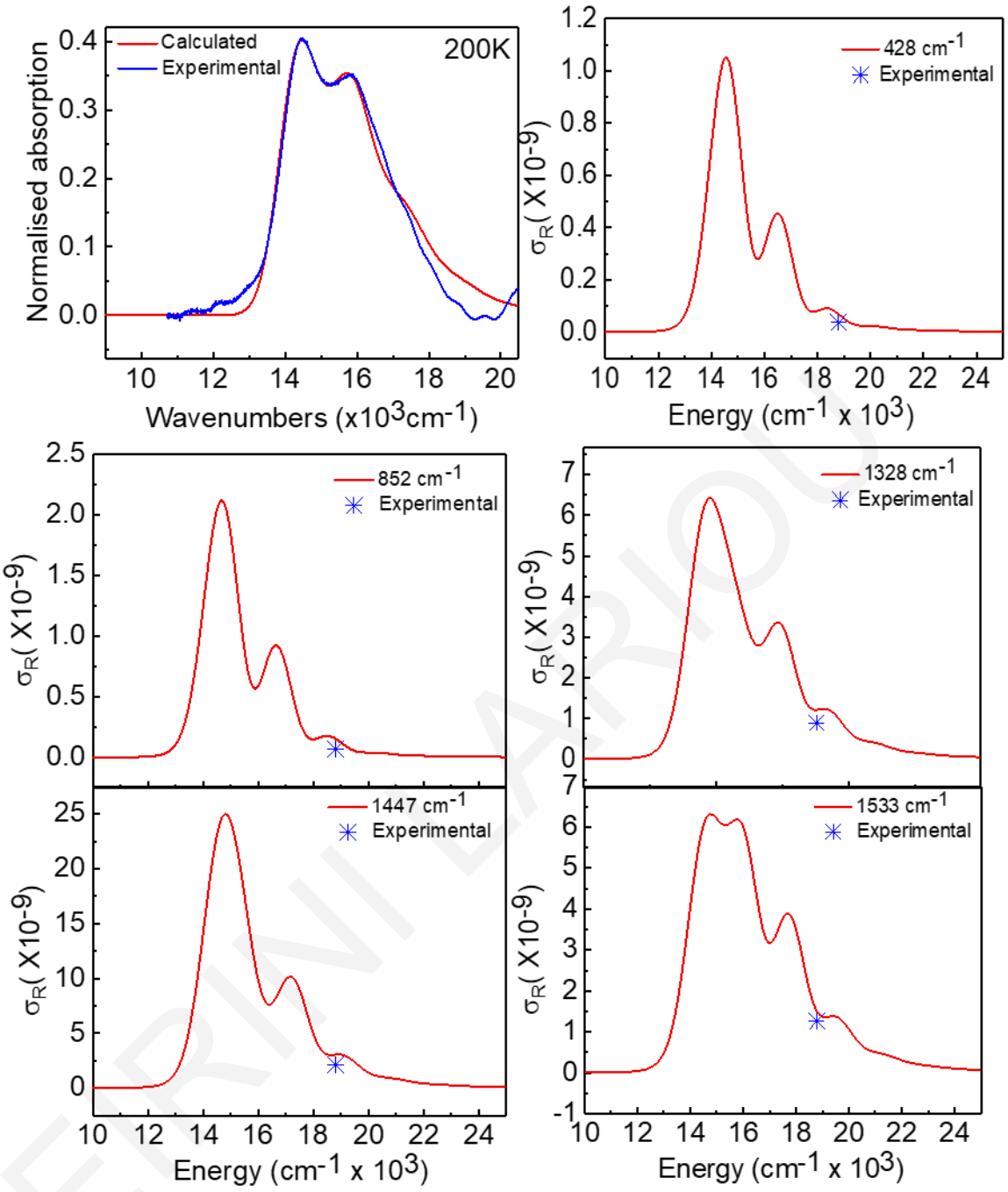

Figure S3*: Results of the simultaneous modelling of the PCE11 absorption spectrum together with the RR intensities that coincide with the REPs of each mode. The data where acquired at 200 K.*

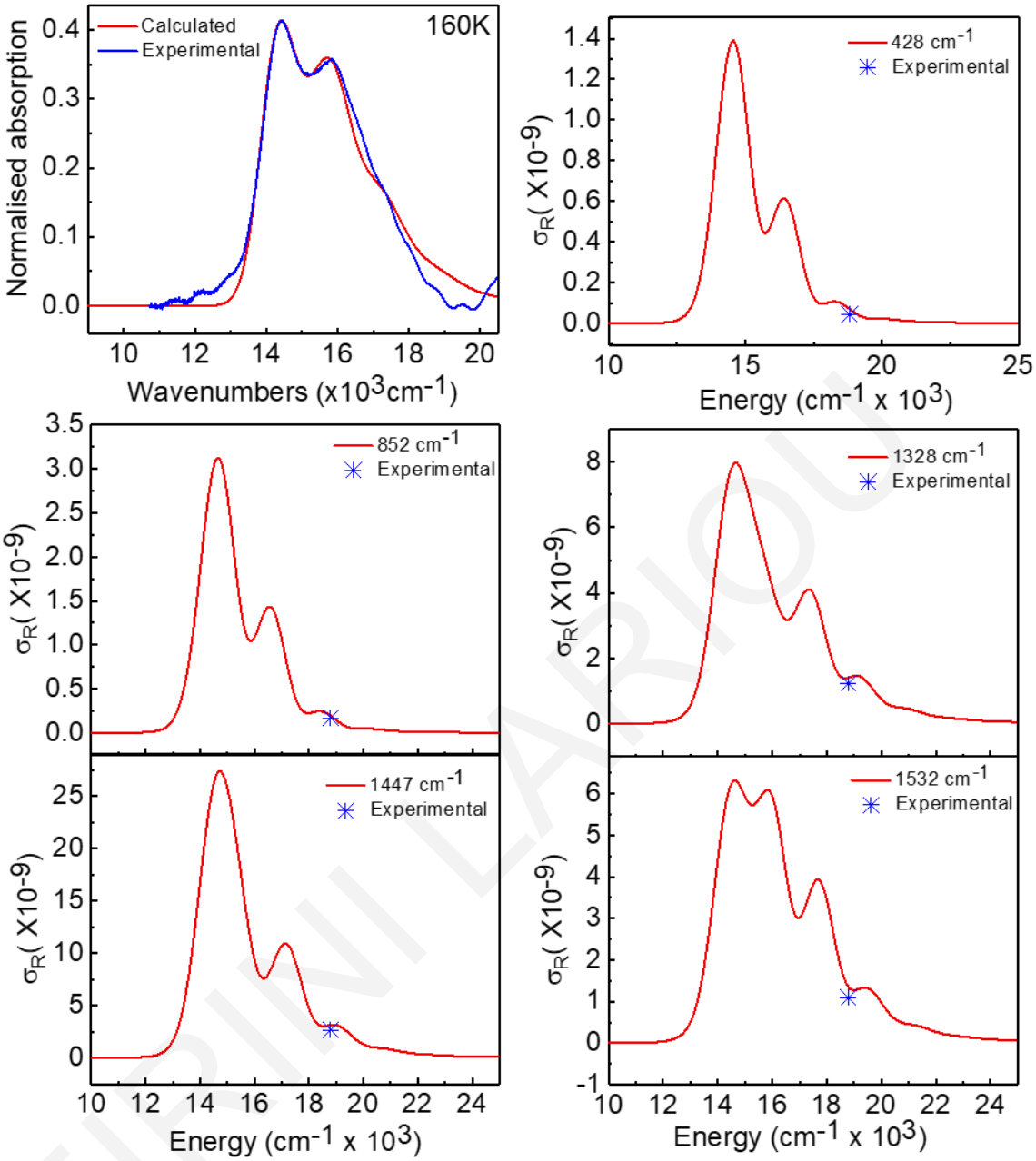

Figure S4*: Results of the simultaneous modelling of the PCE11 absorption spectrum together with the RR intensities that coincide with the REPs of each mode. The data where acquired at 160 K.*

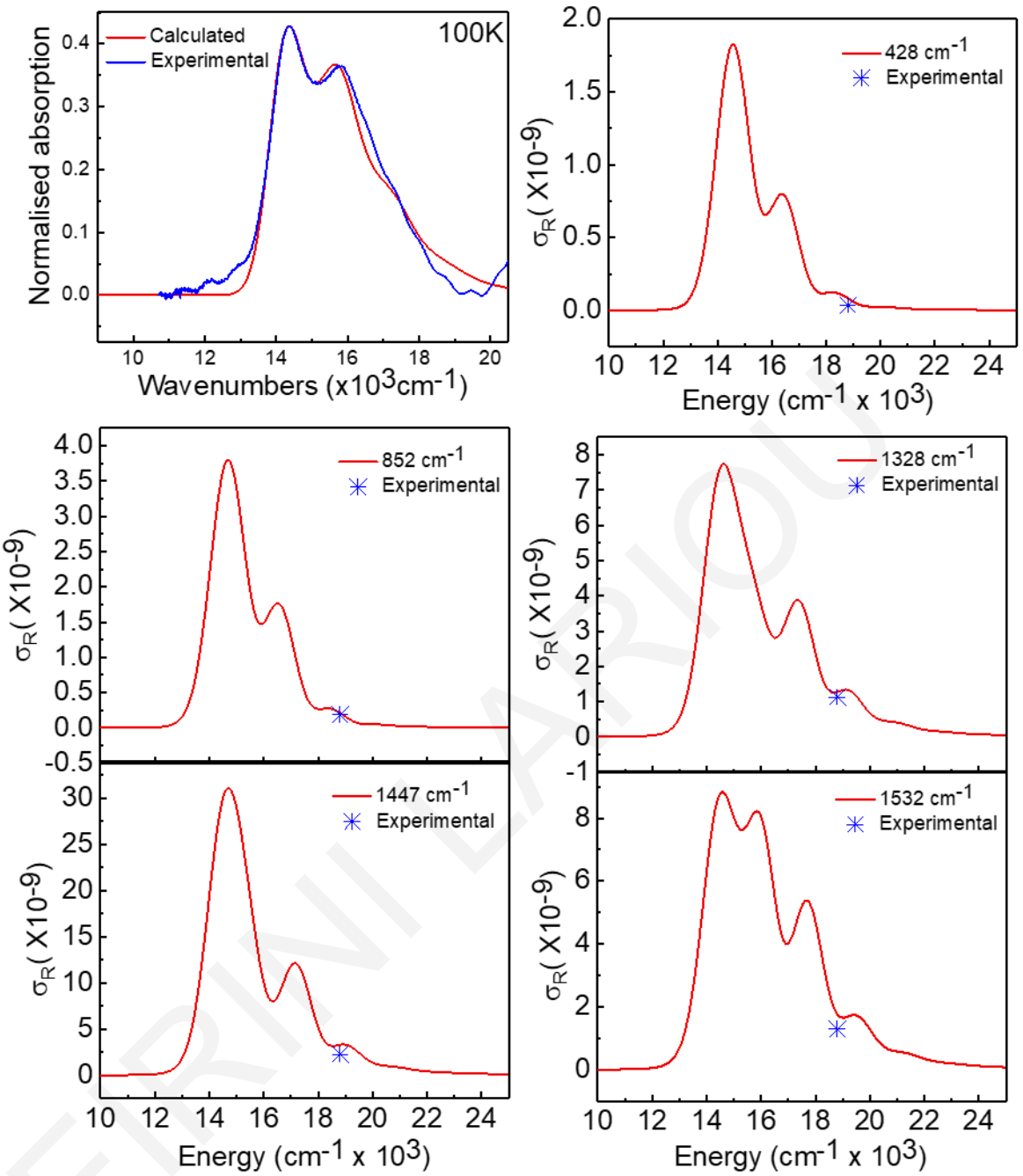

Figure S5: *Results of the simultaneous modelling of the PCE11 absorption spectrum together with the RR intensities that coincide with the REPs of each mode. The data where acquired at 100 K.*

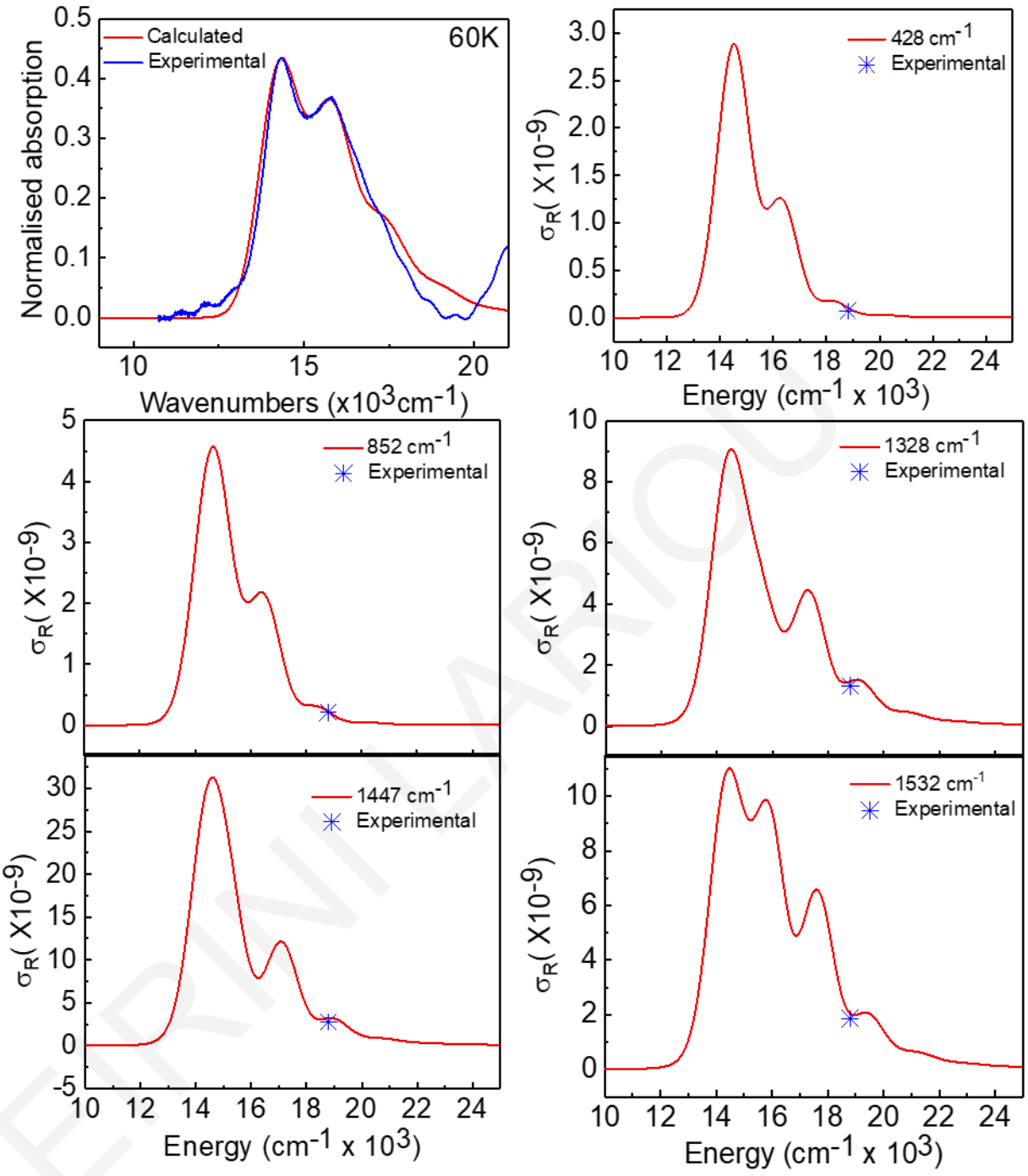

Figure S6: *Results of the simultaneous modelling of the PCE11 absorption spectrum together with the RR intensities that coincide with the REPs of each mode. The data where acquired at 60 K.*

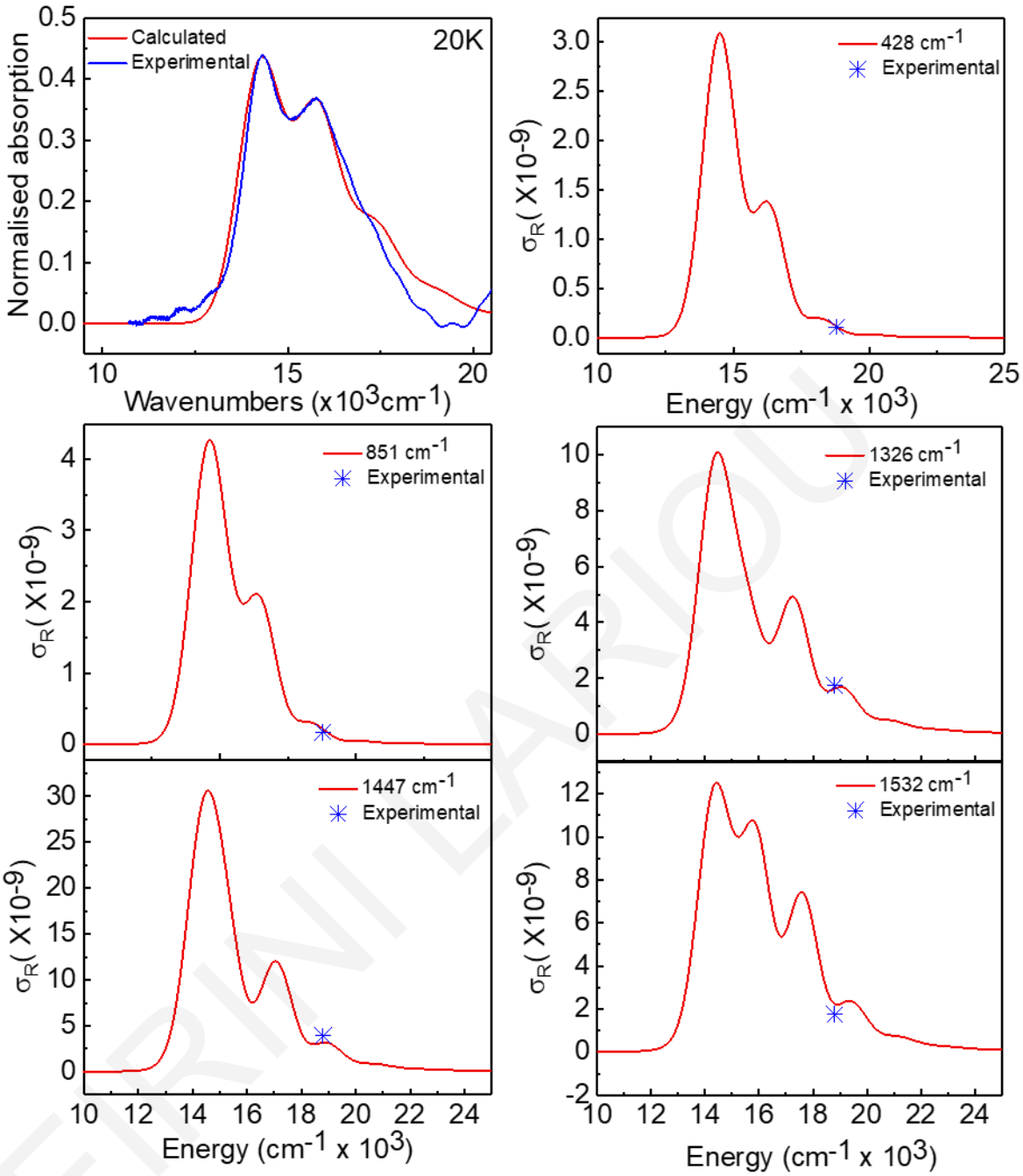

Figure S7*: Results of the simultaneous modelling of the PCE11 absorption spectrum together with the RR intensities that coincide with the REPs of each mode. The data where acquired at 20 K.*

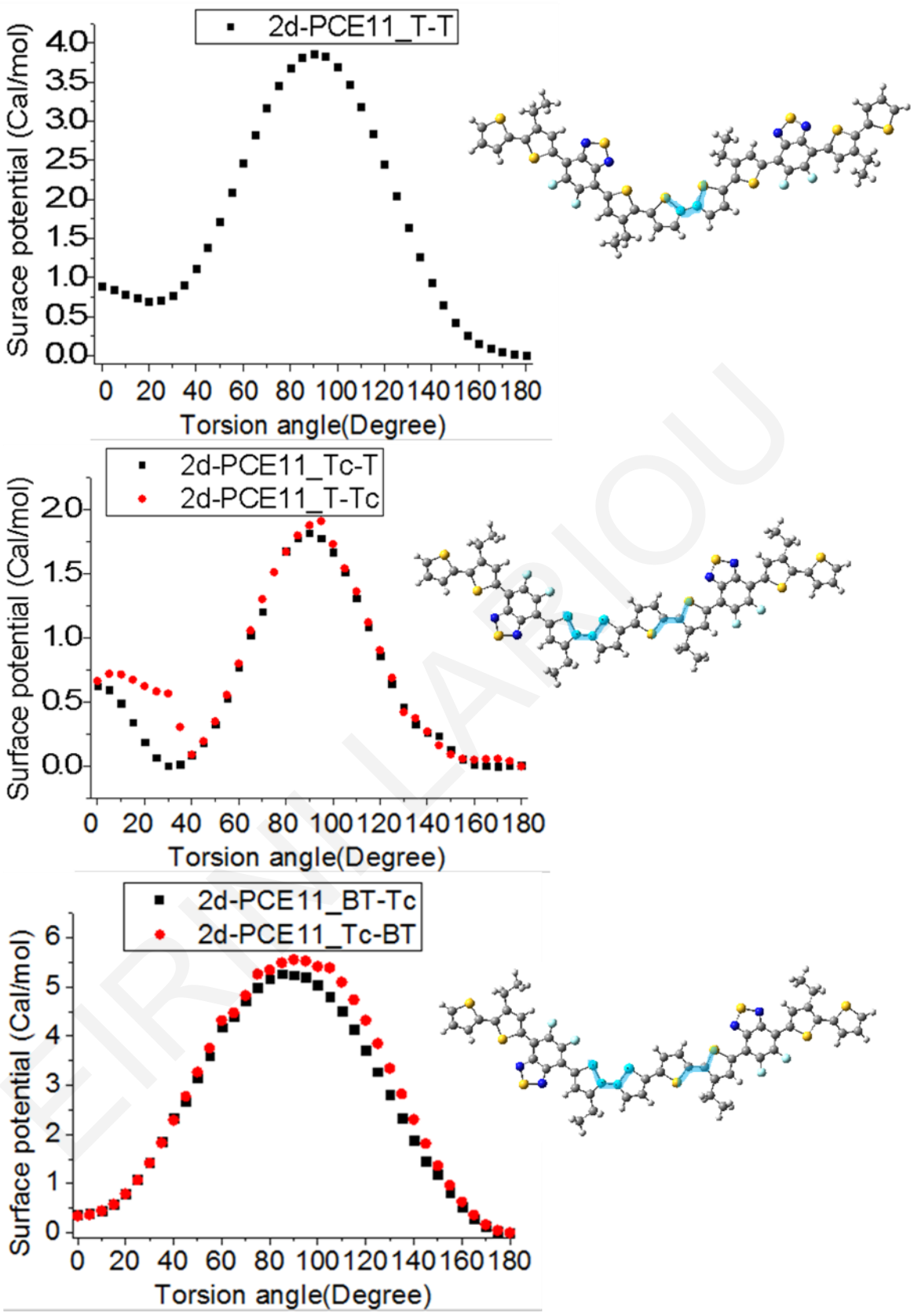

Figure S8: *PCE11 dimer's calculated surface potential as a function of torsion angle for the polymer under vacuum.*

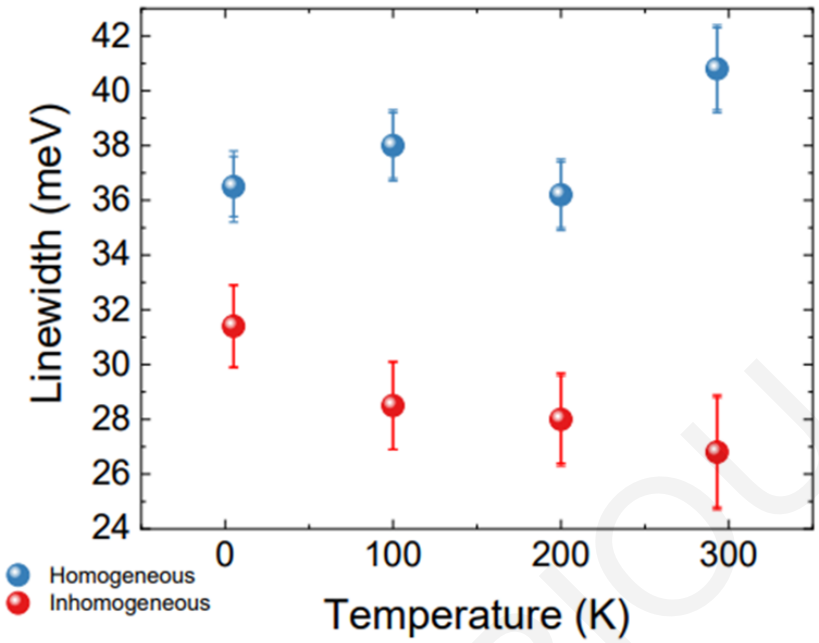

Figure S9: *Experimentally extracted linewidths (through 2D PL measurements). (Fluence 157 nJ/cm^2)*